# New Methods of Coherent Anti-Stokes Raman Spectroscopy Based on Broadband Pulses

by

Xiaoji Xu

B.Sc., Peking University, Beijing, 2004

A THESIS SUBMITTED IN PARTIAL FULFILLMENT OF
THE REQUIREMENTS FOR THE DEGREE OF

DOCTOR OF PHILOSOPHY

in

The Faculty of Graduate Studies

(Chemistry)

THE UNIVERSITY OF BRITISH COLUMBIA

(Vancouver)

May 2009

# Abstract

The research work of this Ph.D. thesis is centered on coherent anti-Stokes Raman spectroscopy (CARS) with broad band coherent pulses. After a mathematical derivation of the formula that is responsible for CARS, four new approaches were proposed. The first method of *Noise-autocorrelation spectroscopy with coherent Raman scattering* utilizes spectral noise to reveal vibrational level spacings through autocorrelation. Its variation of *Narrowband spectroscopy by all-optical correlation of broadband pulses*, uses the technique of optical processing based on noisy probe pulse of special shape to obtain high resolution CARS spectra. The method of *complete characterization of molecular vibration*, can measure the phase of laser induced vibration through amplitude and phase retrieval on a time-frequency spectrogram. It is also a high resolution method. The final method *Background free coherent Raman spectroscopy by detecting spectral phase of molecular vibrations* is the spectroscopic application of detected spectral phase of laser induced vibration.

# Table of Contents

## Appendices

# List of Figures

# List of Programs

# Glossary

**BBO** $\beta$-Barium Borate

**CARS** Coherent anti-Stokes Raman Scattering

**CCD** Coupled Charge device

**FROG** Frequency Resolved Optical Gating

**FWM** Four Wave Mixing

**FWHM** Full Width at Half Maximum

**LBO** Lithium Triborate

**MIIPS** Multiphoton Intrapulse Interference Phase Scan

**NASCARS** Noise Auto-correlation Spectroscopy with Coherent anti-Stokes Raman Scattering

**OPA** Optical Parametric Amplifier

**PMT** Photomultiplier Tube

**SFG** Sum Frequency Generation

**SHG** Second Harmonic Generation

**SLM** Spatial Light Modulator

**XFROG** Cross-correlation Frequency Resolved Optical Gating

# Acknowledgments

First and foremost, I want to express my cordial thanks to my Ph.D. advisor Dr. John W. Hepburn. As an established chemical physicist, his advice has been the beacon of light guiding me through the whole period of my research. His profound knowledge in spectroscopy, his zeal on research and his kind encouragement inspire me to be a better researcher. I enjoy every discussion with him, for each constructive conversation sparkles new ideas.

I want to thank my "de facto" co-advisor Dr. Valery Milner for his extensive advices during my research. He is a truly researcher with both creativity and diligence. Detailed discussions with him and advices from him turn a flash of idea into a reality. His high standard on research, meticulous theoretical derivations and numerical simulations drive our experiments towards perfection.

I hold deep gratitude to my colleague and coworker, Dr. Stanislav (Stas) O. Konorov. We collaborated on most of experiments presented in this thesis. His knowledge and skill on optics helps me immensely during the experiment. His intrinsic sense of humor always makes a happy experiment even if sometimes experimental results turn out to be negative.

I want to express my special thank to Dr. Moshe Shapiro. His course on quantum mechanics at the beginning of my study turned me from an analytical chemistry undergraduate to a chemical physicist. Besides his course, I am greatly benefited from the academic atmosphere of coherent control he has created at University of British Columbia.

I would like to thank current and previous members of Hepburn group for the support during my study, the Laboratory for Advanced Spectroscopy and Imaging Research (LASIR) for its state of art research facility and chemistry department of U.B.C. for the teaching assistantship and University Graduate

Fellowship.

# Dedication

Dedicate this thesis to my parents and my enlightenment physics teacher, Mrs. Zhou, Shou-Kang, who opened the door of science to me.

# Statement of Co-Authorship

This Ph.D. thesis includes several published and in press articles in peer-reviewed journals (chapter 2 to 5 and appendix D). I am coauthored in these articles with my supervisors Dr. John W. Hepburn and Dr. Valery Milner, my co-worker Dr. Stanislav O. Konorov, who is a postdoctoral fellow. In all articles in this thesis, I contributed the conception of the idea, played a key role in building all experimental setup, data collections and result analysis. In the article of chapter 4, the pulse shaper used in experiment is built by Mr. Sergey Zhdanovich, a fellow Ph.D. student from the same research group.

# Chapter 1

# Introduction to Coherent Anti-Stokes Raman Scattering

## 1.1 Introduction

### 1.1.1 Raman Effect

The Raman process is a type of inelastic scattering of light which involves the generation of new frequencies during light matter interaction. It was observed by C. V. Raman[1] and independently by Grigory Landsberg and Leonid Mandelstam[2]. Because the generated light frequencies reflect the property of the scattering media, Raman scattering is of great significance for the diagnosis of the chemical composition and structure of molecules.
When light is scattered by particles, the majority of photons do not change their frequency, which is elastic and known as the Rayleigh scattering. However in Raman scattering, a small fraction of photons are scattered inelastically, changing their frequency during the light matter interaction. In one type of such scattering, the frequencies of the scattered photons are red-shifted by the energy difference between the ground state and the vibrationally excited states, which is known as Stokes scattering. There is another type of Raman scattering, especially for high temperature samples that have considerable population in the excited vibrational states, the frequencies of the scattered photons are blue-shifted by the energy difference between the ground state and vibrational excited states. It is known as anti-Stokes scattering.Figure 1.1 shows the energy scheme of these three types

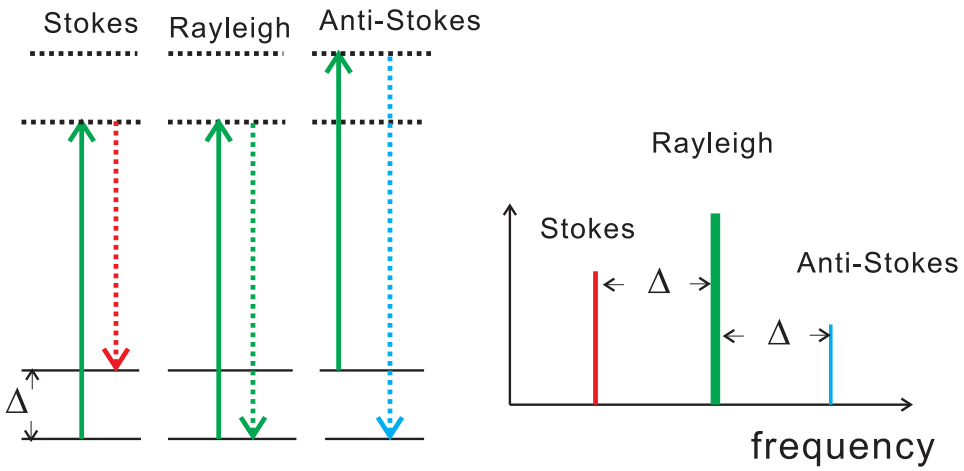


Figure 1.1: This figure shows the Stokes scattering, anti-Stokes scattering and Rayleigh scattering

of scattering. Stokes Raman scattering and anti-Stokes Raman scattering are both called spontaneous Raman scattering. In Stokes scattering, the population of the ground state is transferred into excited states, whereas in anti-Stokes scattering the population of excited states is transferred to the ground state. The intensity of spontaneous Raman scattering is linearly proportional to the concentration of the sample and reflects the population of energy states.

Because the position of vibrationally excited states determines the frequency shift between the incident light and Raman scattered photons, the spectrum of spontaneous Raman therefore has a profile of the energy levels structure of the sample, and the corresponding spectroscopic method is called Raman spectroscopy. Unfortunately, the weak signal of spontaneous Raman constitutes main disadvantage of this method. Sir Raman admitted that Raman effect has "the excessive feebleness " in his initial article [1].

### 1.1.2 Discovery of Coherent Anti-Stokes Raman Scattering (CARS)

Light amplification by stimulated emission of radiation (laser) was achieved by Schawlow and Townes [3]. The invention of the laser is a cornerstone for spectroscopy. With the development of high power pulsed laser technology, Maker and Terhune[4] at Ford Motor Laboratory discovered the nonlinear optical process that is now known as Coherent anti-Stokes Raman scattering (CARS). They used a pulsed ruby laser to systematically investigate third order polarization $\chi^{(3)}$ responses of benzene, and among those third order processes was CARS. To do the experiment, they used a Raman cell to generate a frequency-shifted beam, then they combined ruby radiation with the frequency-shifted beam and focused the beams in benzene. A Blue shifted signal was observed. They also discussed the signal amplification if the energy difference of the beams matching the vibrational levels of the sample. As a result, the spectrum of CARS reflects the energy levels of the sample. The final name "Coherent anti-Stokes Raman Scattering" (CARS), which reflects the spectroscopic utilization of this process, was given by

Begley et. al. [5]. In the literature, CARS also stands for "Coherent Anti-Stokes Raman Spectroscopy".

CARS is the nonlinear optical version of Raman scattering: CARS and Raman share the same selection rules[6]; in the ideal case, both yield spectra that correspond to vibrational resonance structures. However CARS gives much higher signal strength ($10^6$ times higher)[7] than spontaneous Raman scattering. It is better for those applications that require Raman spectra but the sample is too dispersed to yield a measurable signal. The CARS technique has been widely used for chemical diagnosis, combustion temperature measurement and biological imaging. It is also proven to be useful in remote chemical detection [8, 9], where it is nearly impossible to use spontaneous Raman techniques. The implementation of CARS microscopy by X.S. Xie and coworkers [10] is another significant achievement for CARS, which enables noninvasive chemical-specific imaging.

### 1.1.3 Coherent Anti-Stokes Raman Scattering at Glance

Under pulsed laser excitation, the CARS process can be conveniently separated into two steps according to the interaction time of the pulses. Figure 1.2 shows the scheme of CARS. During the vibration preparation step, two laser pulses simultaneously arrive at the sample. If the difference between their frequencies covers vibration resonances, a fraction of molecules are excited into vibrationally excited levels. Due to the coherence of laser fields, the excited state vibrates "coherently" with the ground vibration state. The excitation laser with higher frequency is called the *pump* pulse and the one with lower frequency is called the *Stokes* pulse.

The expression for creating the vibrational coherence has the following form, which will be derived in section 1.3:

$$R(\Omega) = [\sum_v \frac{C_v}{(\omega_v - \Omega) - i\gamma_v} + C_{nR}] \cdot \int E_p(\omega) E_S^*(\omega - \Omega) d\omega \qquad (1.1)$$

Where $R(\Omega)$ is called vibrational coherence function, and it carries the strength of the excitation and reflects the profile of the vibrational reso-

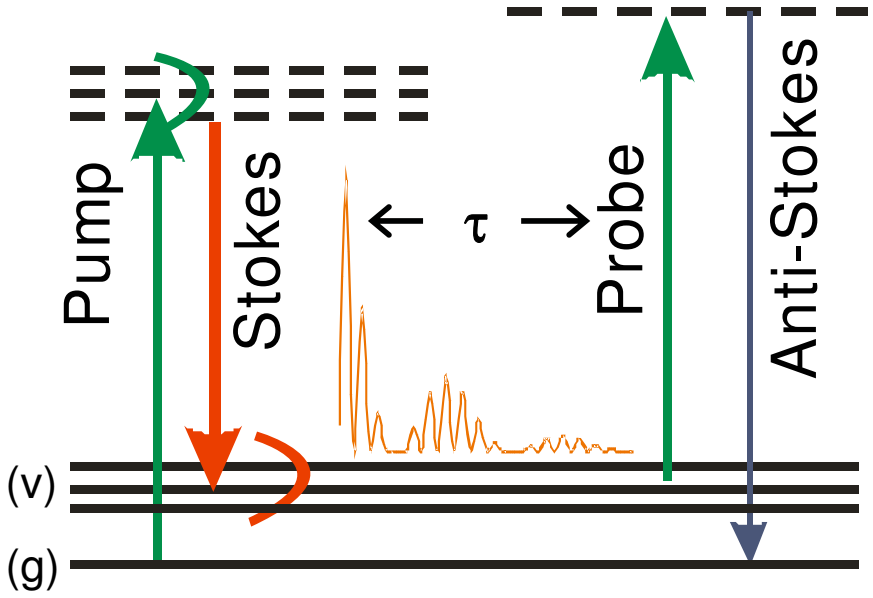


Figure 1.2: This figure shows the scheme of CARS signal generation: coherent vibration excitation by simultaneous arrival of pump and Stokes pulses and coherent scattering of probe pulse at anti-Stokes frequencies of vibrational levels.

nances. $C_v$,$\omega_v$ and $\gamma_v$ are the strength, frequency and line width of vibrational resonant levels, $E_p$ and $E_s$ are the pump and Stokes excitation fields respectively.

The next step is coherent scattering, where a *probe* pulse interacts with the prepared coherent vibrational level and generates a coherent, directional signal at the anti-Stokes frequency of the probe frequency. The scattered anti-Stokes light carries the information of vibrational coherence and is recorded by a spectrometer.

The generation of the CARS signal through probing follows the expression (1.2):

$$E_{CARS}(\omega) \propto \int R(\Omega) E_{pr}(\omega - \Omega) d\Omega \tag{1.2}$$

The generation of CARS spectrum is a convolution between the probe field $E_{pr}$ and vibrational coherence function $R(\Omega)$. Such a convolution plays a central role in the discussion of this thesis. For CARS with a broadband probe pulse, the convolution leads to poor spectral resolution in the CARS spectrum. Methods have been created to recover or partial recover the $R(\Omega)$ from the CARS spectrum with broad band excitation pulses and they will be discussed.

### 1.1.4 Coherent Spectroscopy

CARS is a typical coherent spectroscopy technique. The technique of coherent spectroscopy is based on either the coherent excitation of atoms and molecules or the superposition of coherent light scattered by molecules and particles [11]. The coherent excitation from laser pulses establishes definite phase relation between the amplitude of the atomic or molecular wave functions. Such a definite phase relation in turn determines the total amplitudes of the emitted, scattered or absorbed radiation. During the excitation step of a coherent spectroscopy, two or more vibrational levels are excited coherently by a coherent broad pulse. The wave functions of the excited levels have fixed phase relations and can form a wavepacket that propagates in time. In addition, a whole ensemble of many molecules is coherently excited simultaneously to identical level, and such excitation also creates a spatial

distribution of coherent excited molecules.

The coherent property constitutes the major difference between CARS and its incoherent counterpart, spontaneous Raman. The coherence between multiple excited levels in the time domain often means the observed CARS signal is also a function of the relative time delay between excitation pulses. In spontaneous Raman, there is no control over time. The time dependence of CARS enables time-resolved CARS studies (see section 1.2.3). The spatial coherence of CARS leads to a directional signal, whereas the signal of spontaneous Raman scattering is distributed over $4\pi$ steradian solid angle. Such a directional signal benefits the experimental detection of CARS. When the three excitation beams of CARS are placed properly, the generated anti-Stokes signal is automatically separated from the incident beams (see section 1.3.5), and with proper collimating optics, the full intensity of CARS signal can be detected. For the experiment of spontaneous Raman, only a fraction of scattered signal is detected.

In terms of the density dependence, the incoherent spontaneous Raman measures the population density of the sample, while CARS has a quadratic dependence on the particle density. In quantum mechanics, incoherent spectroscopy measures the square $|\psi|^2$ of the wave function $\psi$, whereas the coherent spectroscopy, such as CARS, is related to wave function $\psi$ itself, therefore yielding additional information on the phase and amplitude [11] (for detail see chapter 4).

From the experiment point of view, the preparation of coherently excited levels is best done by a broad band coherent laser, typically a Ti:sapphire femtosecond laser. The definite phase relations between excited vibrational levels also allow the technique of Coherent Control [12] (see below) in coherent spectroscopy.

### 1.1.5 Coherent Broad Band Laser

The implementation of solid state Ti:sapphire femtosecond laser systems [13] in the early 1990s greatly boosted the innovation of CARS methods. The availability of sub 100fs pulses enabled time-resolved CARS experiments,

which were done in the time domain with pump/Stokes pulses exciting the molecular vibration and a probe pulse checking the excited states after a time delay[14]. The broad bandwidth of the femtosecond excitation pulses enables simultaneously preparation of multiple vibrational levels. The coherent property of the laser field is then transferred to the vibrational levels and a wavepacket is formed. The wavepacket beats in time and generates the detectable anti-Stokes signal when interacting with a probe pulse. Fourier transform is then used to convert the time domain vibrational beatings to the vibrational level spacing.

In addition to the availability of direct time domain research, femtosecond lasers with the high peak intensity leads to high signal strength in the CARS signal. For example, given the same average output power, the 100fs Ti:Sapphire regenerative laser system has 100 times higher peak power than that of 10ps Nd:YAG of same repetition rate. The femtosecond laser has $10^4$ times higher total CARS signal than that from the Nd:YAG laser.

Femtosecond laser systems also provide a more convenient frequency conversion than the Nd:YAG laser pumped dye lasers. The optical parametric amplifier (OPA) used with Ti:Sapphire femtosecond laser can provide frequency conversion from a wavelength of 300nm to 2000nm. In terms of efficiency, an OPA can convert about 25% of the input light into tunable light. Wide range tunability facilitates CARS studies. With an OPA, the CARS experiment can conveniently work with three separate frequencies as pump, Stokes and probe pulses, and this adds flexibility to the experiment. For example, pulse shaping can be done independently on the three pulses, and the relative time delay between probe and the pump/Stokes pair can be adjusted as well.

From a broader perspective, the broad bandwidth of the Ti:Sapphire laser also enables an easy way to implement the coherent control technique. Coherent control is a family of quantum mechanical based methods that use quantum interference of two or more different pathways to control the final state of dynamic processes controlled by light fields. The general concept was first proposed in 1986 by P. Brumer and M. Shapiro [15]. Numerous experiments [16] have been done in coherent control, such as controlling

the direction of electron motion in semiconductors [17], and the breaking of chemical bonds [18]. Femtosecond Ti:Sapphire laser pulses come with a broad bandwidth and definite spectral phase which can be used to construct the multiple pathways required in coherent control. Control of chemical reactions by feedback-optimized phase-shaped femtosecond laser pulses was demonstrated by G. Gerber and colleagues [19], where the spectral phase of a broad band coherent pulse was pulse shaped to control the outcome of organometallic photo-dissociation reactions. A comprehensive discussion of coherent control can be found in the book "Principles of the Quantum Control of Molecular Processes" by M. Shapiro and P. Brumer [12]. In the actual CARS experiments of this thesis, the concept of coherent control heavily influenced the way the experiment was done and particularly, the way that pulse shaping technique was used, even though the experiments per se were not done for the aim of applying coherent control or a new demonstration of coherent control technique in CARS.

### 1.1.6 Pulse Shaping Technique

Because femtosecond lasers possess a broad bandwidth, the phase of spectral components across the bandwidth can have different values. Spectral phases across the broad band pulse now become a controllable parameter in CARS experiments. The pulse shaping technique[20] is a powerful tool to control the spectral phase as well as the amplitude of the pulse. Pulse shaping is done through an assembly of optical devices collectively called a pulse shaper, as shown in figure 1.3. In a pulse shaper, the input pulse is spectrally dispersed into frequency components by a grating. Then the frequency components are collimated by a lens and passing through a spatial light modulator (SLM). The amplitude and spectral phase of each frequency components are controlled independently according to each pixel of the SLM (for detail see section 1.4.3). An exact replica of the lens and the grating is used to reconstruct the dispersed light into a pulse and give an output. The pulse shaper controls the amplitude and phase of light in the frequency domain. Because the frequency and time domain response of a broad band

pulse is linked by Fourier transform, the phase and amplitude manipulation in the frequency domain also leads to the full profile control in the time domain. Controllable chirp or a train of small pulses can be created from a coherent broad band pulse with a pulse shaper.

In CARS, the pulse shaping technique has been used to improve spectral resolution [21] and selectively excite one resonance from serval adjacent levels[22]. The state-of-the-art pulse shaping technique also enables single pulse CARS techniques. By properly tailoring a single broadband pulse, different frequency components can serve as pump, Stokes and probe pulse respectively and generate the CARS signal[23, 24].

The following sections 1.2 to 1.4 provide a detailed background knowledge to CARS. Section 1.2 gives a review of the literature. It briefly describes the development of CARS methods and discusses respective strengths and weaknesses of current methods. In section 1.3, the analytical expression for CARS signal generation is derived using the time domain representation. The discussion of the effect of non-resonant background and requirement of phase matching is presented. section 1.3 also includes a numerical simulation of CARS signal. In section 1.4, the experimental techniques are discussed. The Ti:Sapphire laser and OPA are described. A detailed recipe for construction of a pulse shaper is included as well as some useful tips for CARS signal generation.

## 1.2 Review on Current Coherent Anti-Stokes Raman Scattering Methods

A review of current CARS techniques and applications can help readers understand the background of this thesis work. Since the discovery of coherent anti-Stokes scattering, CARS techniques have been widely used for various applications from chemical and combustion diagnosis to biological imaging. Understanding the mechanism, strengths and weaknesses of each CARS method can provide guidance to the research of this thesis.

For the convenience of discussion, CARS methods are categorized into

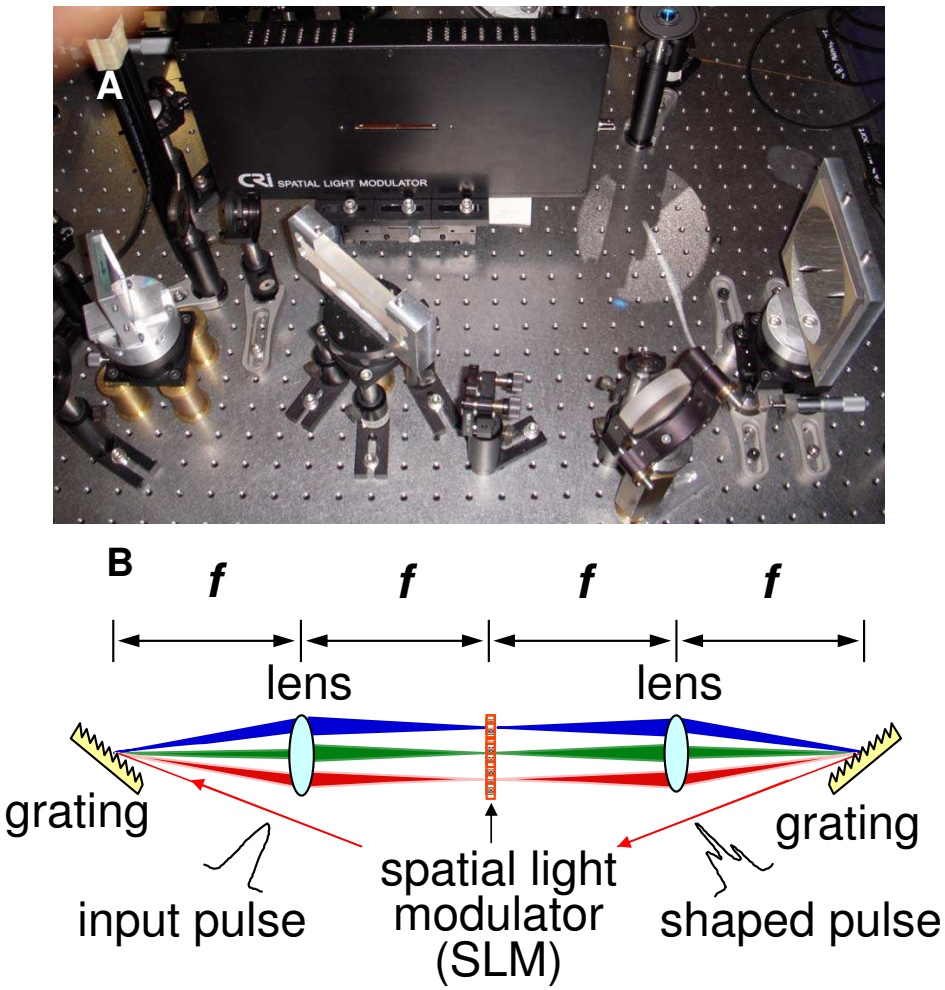


Figure 1.3: (A) shows a photograph of a pulse shaper. (B) shows the scheme of optical elements. f is the focal length of the lenses.

two types in this thesis discussion: frequency domain methods and time domain methods. The initial CARS discovery and development used frequency domain methods. The equipment was based on narrow band laser systems and the purpose of the spectroscopy was to resolve the resonances of the sample. Later, especially after the invention of solid state femtosecond lasers, time domain methods became common in the chemical physics community. Time domain methods are capable of investigating the time dynamics of excited resonant states, and through Fourier transform, giving the spectroscopic information on level spacings and lifetimes. The solid state femtosecond laser also provides coherent broad band pulses which can be used to access multiple resonances in frequency domain methods.

### 1.2.1 Traditional Narrow Band CARS

The Coherent anti-Stokes Raman scattering effect was first observed by Maker and Terhune[4] in 1965. Their experiment was done with a ruby laser system with 100mJ per pulse of 30 ns duration. The output pulse of the ruby laser was guided through a cell filled with benzene to generate a frequency shifted beam through stimulated Raman emission. Then the generated beam interacted with ruby radiation again and generated the anti-Stokes frequency signal from the same benzene sample. Retrospectively, this experiment was a milestone for the CARS spectroscopy. However, the lack of tunable laser sources at that time limited its real spectroscopic applications.

With the development of tunable dye laser sources [25], CARS spectroscopy developed considerably during 1970s [26] from the original Maker and Terhune experiment. It became a very attractive method in the field of chemical diagnosis, particularly in situations where normal spontaneous Raman gives very low signal or high background, such as fuel combustion. During this period, besides the task of obtaining spontaneous Raman equivalent spectra, one major application of the CARS method was to measure the temperature of combustion. This involved of the measurement rotational lines intensities with good spectral resolution, and calculation of gas temperatures through the rotation state partition function.

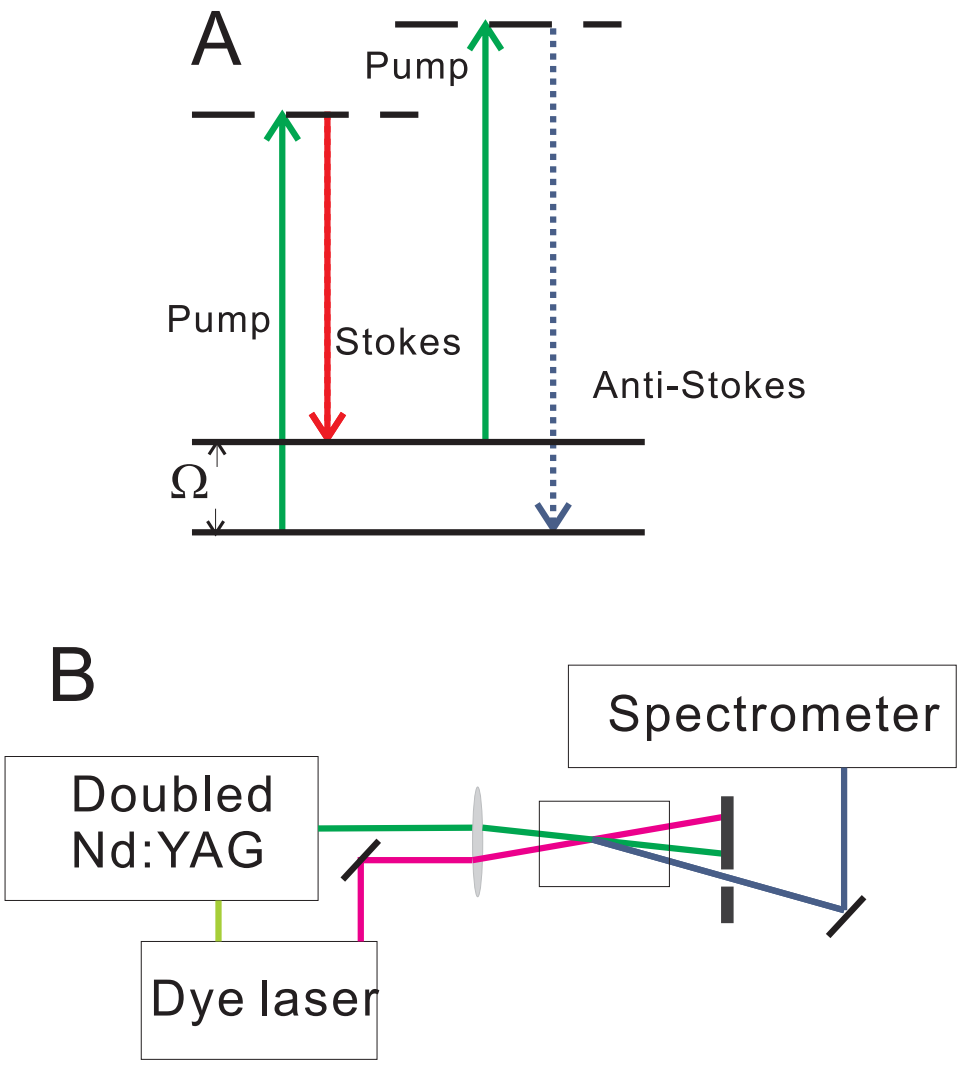


Figure 1.4: (A) shows the energy diagram for CARS. (B) shows a typical experimental setup of narrow band CARS. The spectrum is obtained through scanning the frequency of the dye laser system. In this setup, the pump pulse also acts as probe.

The typical frequency domain CARS experiment utilizes two laser frequencies to generate detectable CARS signal at the anti-Stokes frequency as figure 1.4A shows. A typical setup includes a frequency doubled Nd:YAG laser pumping a dye laser to provide frequency tunable output. One laser frequency from either the Nd:YAG laser or dye laser serves as both pump *and* probe beam, the other serves as the Stokes beam. To obtain a CARS spectrum, the frequency of the dye lasers is scanned and the CARS signal intensity is recorded as a spectrum. A spectrometer with a photomultiplier tube (PMT) detector is often used to detect the weak CARS signal.

During 1970s to 1980s, CARS spectroscopy was treated as an extension of traditional Raman spectroscopy. The theoretical discussions on CARS were presented in the context of nonlinear optics. In nonlinear optics, CARS is treated as a type of resonant four-wave-mixing. The signal is described by the phenomenological third order susceptibility $\chi^{(3)}$ by

$$E_{as} \propto \chi^{(3)} E_s^* E_p^2 \tag{1.3}$$

The $E_{as}$ is the anti-Stokes field and $E_p$ and $E_s$ are the input fields of pump and Stokes pulse respectively, with frequencies at $\omega_{pu}$ and $\omega_S$. The $\chi^{(3)}$ has two parts, the resonant part $\chi_R$ and non-resonant part $\chi_{nR}$ (see below). When the frequency difference between pump and Stokes matches a resonance, the value of differential Raman cross-section $d\sigma/d\Omega$ is related to the resonant part of $\chi^{(3)}$ by expression:[5]

$$\chi_R = \frac{\pi c^4}{\hbar \omega_{pu} \omega_s^3 \Gamma} \frac{d\sigma}{d\Omega} \tag{1.4}$$

with $\Gamma$ being the linewidth of the resonant level. $\chi^{(3)}$ can be experimentally measured by recording energies of CARS signal and input pump/Stokes beams [5]. Experiments were carried to measure the Raman cross-section of methane [27, 28].

Because lasers can probe samples non-invasively and are capable of penetrating very high temperature gas samples, CARS has been used in combustion investigations [29, 30] and plasma probing [31]. CARS thermometry

[32, 33] was developed to measure the temperature of rapidly flowing gas. This method relies on the rotational line intensities in the high resolution CARS [34, 35] spectrum. The intensity of rotational lines reflects the population of that rotational level. The rotational population can be used to extract the gas temperature T through a calculation involving the Boltzmann distribution equation:

$$\frac{N_1}{N_2} = \frac{2j_1 + 1}{2j_2 + 2} e^{\Delta E/(k_B T)} \tag{1.5}$$

with $N_1/N_2$ being the population ratio of two rotational lines and $\Delta E$ being the energy difference between two rotational levels. $j_1$ and $j_2$ are the rotational quantum number of rotational states. This technique was used in the diagnosis of internal combustion engine [36, 37] and monitoring of jet engine exhaust [38].

It should be noted that peak positions in CARS are sometimes shifted from the vibrational resonances due to the presence of non-resonant background. The non-resonant background of CARS is from the non-resonant four-wave-mixing of the pump and Stokes pulses and does not reflect the profile of the vibrational resonance. Because the resonant CARS signal and the non-resonant background are both coherent, they optically interfere and lead to a distorted CARS spectrum of dispersion profiles. Figure 1.5 shows the comparison between the profile of CARS with non-resonant background and the profile of vibrational resonances. Additional fitting procedures are often required for data interpretation of CARS spectra with non-resonant background [39, 40]. Detailed discussion on the origin of non-resonant background will be discussed in section 1.3.3.

### 1.2.2 Multiplex CARS Method

Measuring spectra from turbulent gases in combustion requires faster measuring speed than that from a stable gas phase sample. The narrow band CARS methods described in the previous section requires scanning of one laser frequency, which is time consuming. Researchers need a fast method to

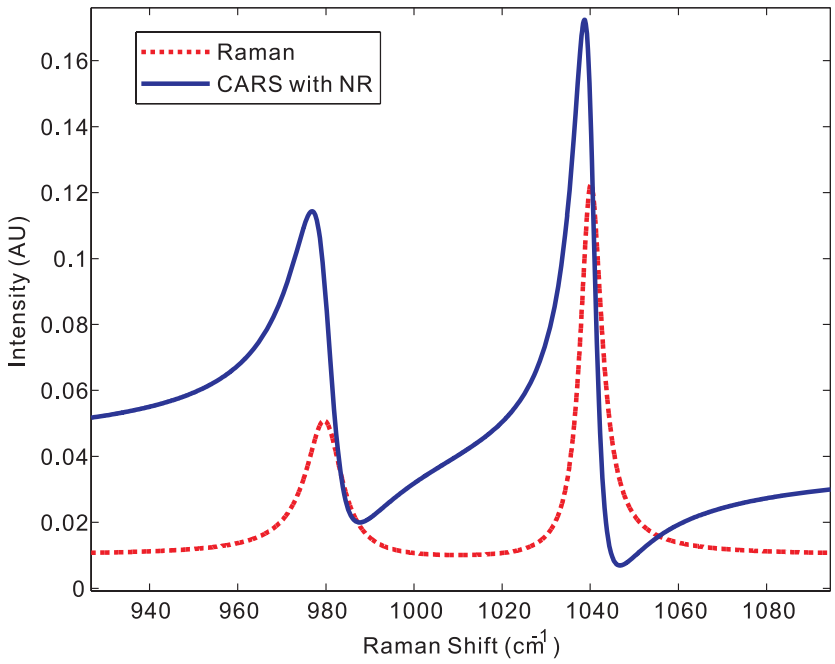


Figure 1.5: This numerical simulation figure shows the comparison between the CARS spectrum with non-resonant background (blue line) and profile of vibrational resonances (red dashed line). There are two resonances at 980 and $1040cm^{-1}$ in the simulation. The strength of the non-resonant background equals 30% of the intensity of the $1040cm^{-1}$ peak. When the non-resonant background is present, the CARS spectrum shows shifted peak position with a dispersive profile due to interference between resonant signal and non-resonant background.

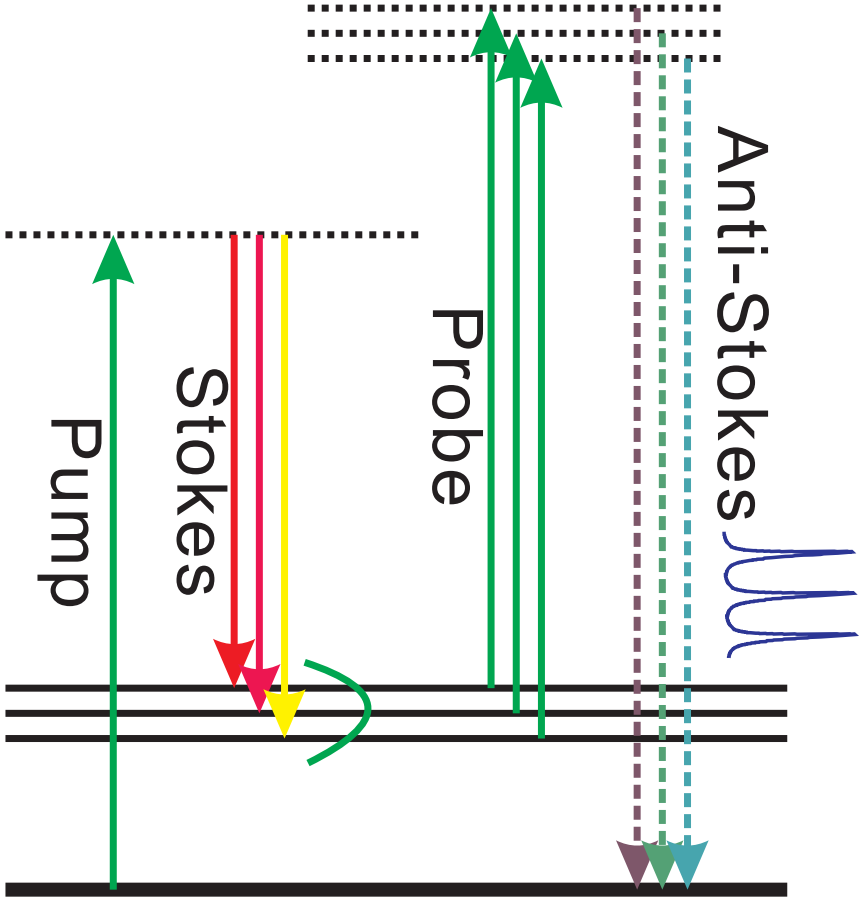


Figure 1.6: This figure schematically shows the energy scheme of multiplex CARS using one narrow band laser as pump and probe, and a broad band pulse as Stokes. The narrow band pump and broadband Stokes pulses excite multiple resonant states simultaneously, and excited states are probed by the narrow band probe pulse to give multiplex CARS spectrum. Dye lasers are used for the broad band Stokes pulse in early experiments. Then solid state broad band lasers later replaced dye lasers as broad band light source for multiplex CARS applications.

obtain high resolution spectra without tuning the frequency of the laser. The invention of multiplex CARS [41] satisfied such a need. Multiplex CARS is associated with broad band lasers, which may not necessarily be coherent. The idea is to use broadband pulse(s) to excite multiple levels and simultaneously "read out" the CARS spectrum. The early multiplex CARS was done using modeless dye lasers [42], where a Nd:YAG laser pumped dye laser gives broad band incoherent radiation. This broad band emission serves as the Stokes pulse and a narrow band frequency doubled Nd:YAG pulse serves as the pump and probe pulse in CARS. The field correlation between the narrow band pump and the broad band Stokes pulse has broad frequency bandwidth and can simultaneously cover multiple levels. When the probe pulse has narrow bandwidth, the CARS spectrum is a replica of the profile of the prepared ro-vibrational levels without frequency scanning. Figure 1.6 shows the energy scheme of one multiplex CARS method.

Because of the ability to read out the rotational CARS spectrum in one shot, multiplex CARS further improved gas temperature measurement[43–46] for combustion diagnosis and temperature measurement. For the multiplex CARS method shown in figure 1.6, the bandwidth of the Stokes determines the vibration resonance "read out" window and the narrowness of the probe pulse determines the spectral resolution.

Multiplex CARS has been gaining strength with the development of laser technologies. The invention of solid state Ti:Sapphire lasers [13, 47, 48] greatly improved the application of the CARS method. The amplified Ti:Sapphire laser can conveniently provide 35fs duration broad band pulses of $450cm^{-1}$ bandwidth centered around 800nm wavelength. Ti:Sapphire lasers are more stable and easier to maintain than organic dye lasers. With the broad bandwidth, it becomes feasible to create a narrow band probe pulse from broad band radiation. In Prince et. al. [49], grating pairs are used to create a pulse of about $10cm^{-1}$ bandwidth from a broad band pulse, and the created narrow band pulse is used as the probe pulse in CARS. An important application of multiplex CARS is the microscopy of living cells (see works of Cheng et.al. [50] and Müller et.al.[51]). In these experiments, a picosecond laser system is synchronized with a femtosecond

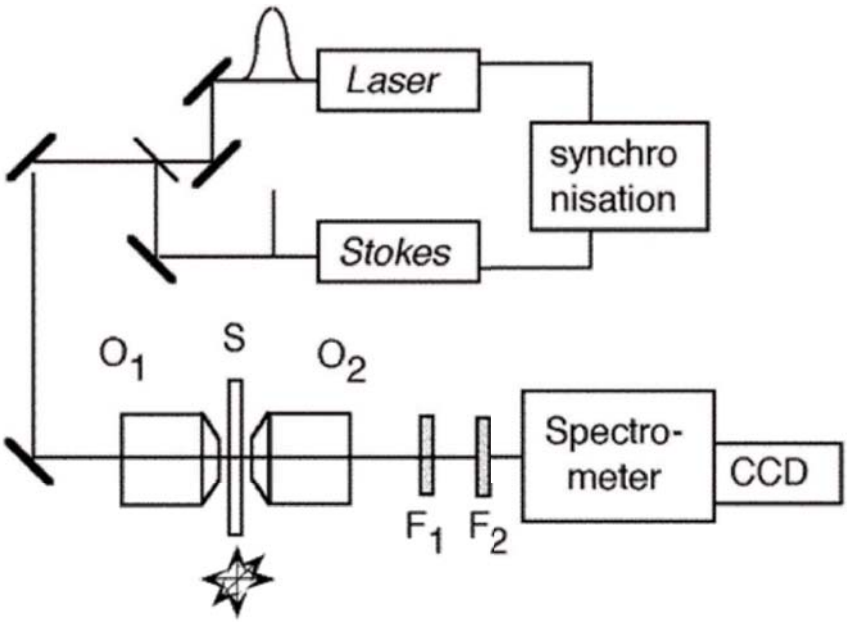


Figure 1.7: This figure shows a schematic of the experimental setup for multiplex CARS microscopy. Two laser systems, a 10 ps and a 80 fs modelocked Ti/sapphire lasers were used to provide narrow band pump and broad band Stokes pulses. Microscope objectives $O_1$,$O_2$ were used to focus and collimate the beams ; Signal generated from sample (S) was filtered by a band pass filter. The laser pulses from the two lasers were actively synchronized. (from M. Müller et. al. J. Phys. Chem. B 2002, 106, 3715-3723)

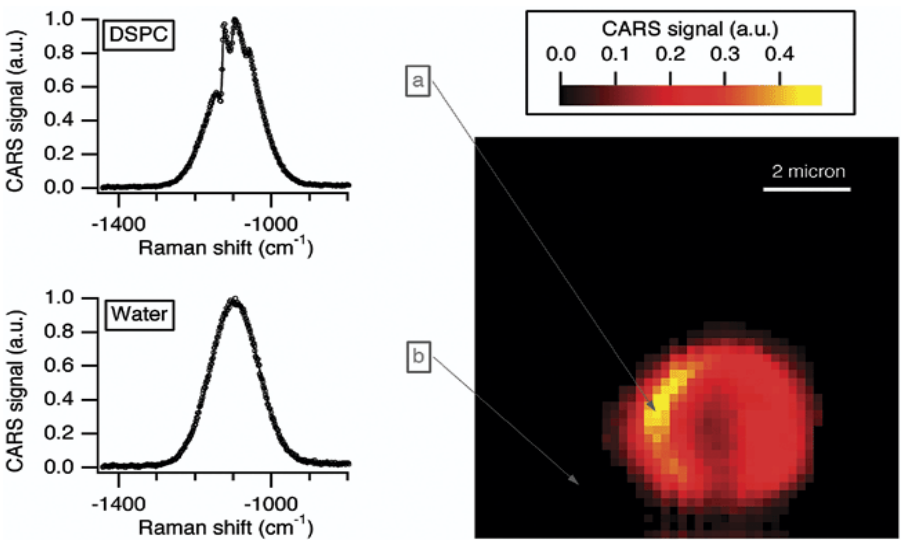


Figure 1.8: This figure shows multiplex CARS image of a multi-lamellar vesicle using the $1128cm^{-1}$ resonance. The acquisition time per pixel was 200 ms, and the image has $50 \times 50$ pixels. The insets show the CARS spectrum of the lipids (a) and the surrounding water (b).(from M Müller et. al. J. Phys. Chem. B 2002, 106, 3715-3723).

Ti:Sapphire laser to provide pump and Stokes pulses for CARS excitation. Figure 1.7 schematically shows the setup. With a tight beam focus using a high numerical aperture microscope objective[10] to satisfy the phase matching condition (details see section 1.3.5), the pump and the Stokes pulses generate a CARS spectrum inside living cells. In Cheng et.al [50], the spectrum of cellular lipids was obtained. By scanning the focus spot across different parts of the cell, an image of three-dimensional distributions of cellular lipids was measured and reconstructed. In the work of Müller et.al.[51], the image of a multi-lamellar vesicle was obtained by multiplex CARS microscopy as shown in figure 1.8. Multiplex CARS microscopy has the potential of obtaining the spectrum when doing imaging, therefore providing better information on chemical-specific distributions. The major

challenge for multiplex CARS microscopy is its acquisition time. For example, an image of $100 \times 100$ pixels has $10^4$ points. If the exposure time of CCD for one spectrum can be as fast as 20ms, the total acquisition time for one image is 200s. It is hard to obtain a realtime image with CARS. In the work of Müller et.al.[51], each pixel took 200ms to acquire. Faster detectors can improve the performance. In the work of Cheng et.al. [50], a PMT dector is used to reduce the acquisition time. For the particular experiment setup that requires synchronization between two lasers [50, 51], time synchronization between a femtosecond laser system and a picosecond laser system requires special feedback control system and susceptible to instability [52].

Multiplex CARS is an improvement on narrow band CARS methods because of its ability to obtain CARS spectra without scanning the frequency of the excitation laser. It dramatically reduces the measurement time of CARS. However, multiplex CARS still suffers from two major disadvantages: firstly, the spectral resolution is limited by the bandwidth of the probe pulse, as the CARS spectrum is still a frequency domain convolution between profiles of vibrational resonances and the probe bandwidth. Secondly, from the signal strength point of view, a narrow band pulse coming with a low peak power yields less signal in a nonlinear process such as CARS. Figure 1.9 shows the numerical comparison between signal strength from probe pulses of different bandwidth cut from the same broad band source: $100cm^{-1}$(thick blue), $10cm^{-1}$(dashed green) and $1cm^{-1}$(thin red). Trimming the bandwidth from $100cm^{-1}$ to $1cm^{-1}$ reduces the total intensity by approximately two orders of magnitude.

### 1.2.3 Time-resolved CARS method

In the early 1980s, scientists successfully brought down the duration of laser pulses into the femtosecond range using dye laser systems [53]. The later discovery of the solid state Ti:Sapphire laser[13] in the early 1990s further shortened the pulse duration to even sub 10fs and greatly amplified the pulse power. A typical commercially available Ti:Sapphire laser system can con-

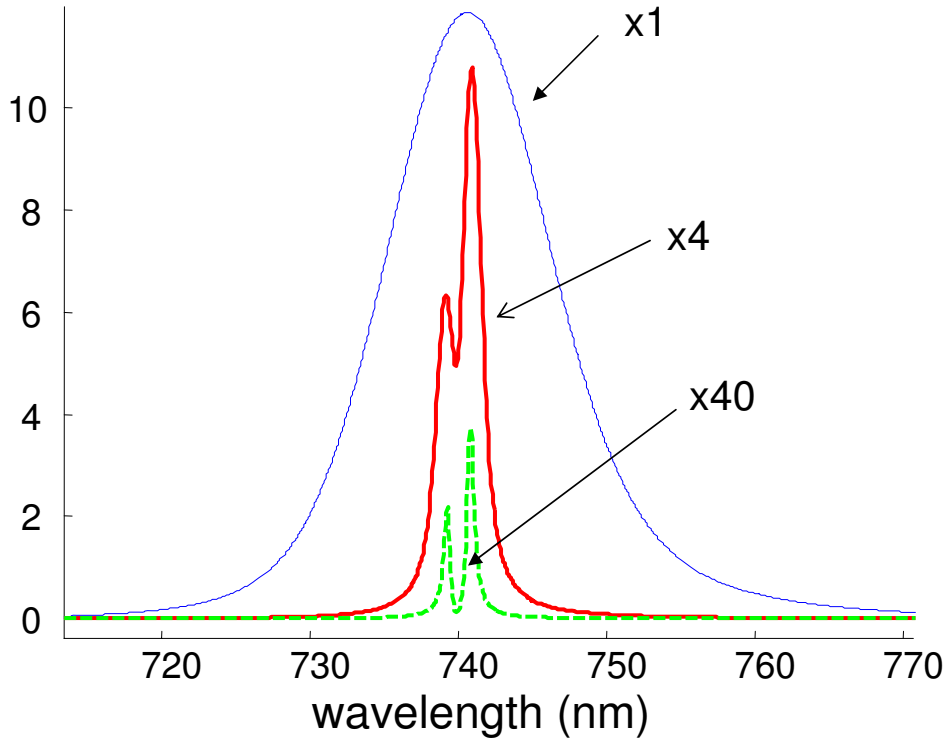


Figure 1.9: This figure shows the CARS signal intensity comparison between difference bandwidth of the probe pulses. Probe pulses have the same spectrum peak intensity. The CARS spectrum using a raw $100cm^{-1}$ transform-limited bandwidth probe pulse (thin blue line), the CARS spectrum using a probe pulse of $10cm^{-1}$ bandwidth, trimmed from the raw $100cm^{-1}$ pulse (red thick line) and the CARS spectrum using a probe pulse of $1cm^{-1}$ bandwidth, trimmed from the raw $100cm^{-1}$ pulse (green dashed line). Two vibrational levels are used in this simulation.

veniently provide below 100fs radiation. The availability of short duration pulses has facilitated the temporal domain investigation of CARS.

With femtosecond duration laser pulses from dye lasers, Zewail and his colleagues pioneered the field of *femtochemistry*[54]. Their work on ultrafast dynamics contributed to the field of time domain spectroscopy and caught the attention of the scientific community. By means of coherent ultrafast lasers, temporal domain molecular coherence was revealed and interpreted. Through a series of pump/probe experiments, it was shown that the temporal domain vibrational wave packet can as well reflect the vibration spacing through means of Fourier transform [55–57]. "Pump/probe" is the most commonly used scheme in femtochemistry: a broad band coherent pump pulse excites the molecular system, preparing a wave packet, and a second pulse coming after a variable delay probes the prepared system.

Time-resolved CARS can be treated as a generalized "pump/probe" experiment. The function of the pump/Stokes pulse pair can be regarded as the "pump", and the probe pulse in CARS serve as the "probe". In CARS, the simultaneous interaction of pump and Stokes pulses prepares a Raman wave packet. The subsequent probing pulse generates CARS signals that reflect the propagation of the prepared vibrational wave packet. Figure 1.2 schematically depicts such a process. In the experimental realization, a time-resolved CARS experiment utilizes three broadband femtosecond excitation pulses. Short duration pump and Stokes pulses overlap in time followed by a probe pulse with variable time delay, and the modulation of CARS signal is recorded. After obtaining the CARS signal vs. time delay response, a Fourier transform is used to obtain the resonance spacing in the frequency domain. Figure 1.10 (B) and (D) shows the simulation of vibration beating of toluene and its Fourier transform revealing the vibrational level spacing.

The Time-resolved CARS method was used initially to investigate the dephasing of vibrational levels [58, 59]. Dephasing of vibrational levels leads to a decrease of CARS signal and provides insight into molecular structure and its solvent environment [60]. The direct time domain measurement can provide more accurate data on the time domain behavior of dephasing, comparing to linewidth methods. The spectral resolution of the narrow band

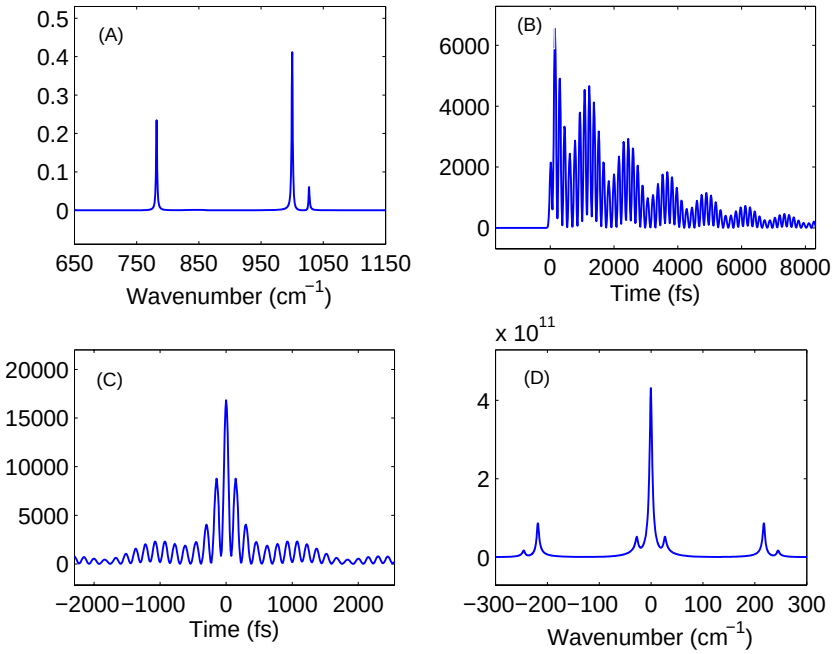


Figure 1.10: (A) shows a simulation of the vibrational spectrum of toluene with resonances at $782cm^{-1}$,$1000cm^{-1}$ and $1027cm^{-1}$. (B) shows the simulation of time domain beating of toluene excited by 100fs pump and Stokes pulses with a frequency difference centered at $900cm^{-1}$. (C) shows the direct Fourier transform of the spectrum in (A). (D) shows the Fourier transform of the time domain beating in (B)

CARS method limits the accuracy of the linewidth measurement. For example, if the probe pulse bandwidth is $0.5\text{cm}^{-1}$, when measuring an energy level with $1\text{cm}^{-1}$ linewidth, the error on the lifetime is quite high due to spectral resolution (5.3 ps for $1cm^{-1}$, comparing to 3.5ps for $1.5cm^{-1}$). On the other hand, the error associated with direct measurement in the time domain is only limited by the duration of the probe pulse, which is often sub 100fs in typical time-resolved CARS experimental setup.

When multiple levels exist within the excitation bandwidth [61], a vibrational wave packet is prepared and resonant level spacing can be calculated through the Fourier transform of the vibrational beating. Time resolved CARS can also be used to perform temperature and pressure measurements. Motzkus and coworkers performed a time resolved CARS experiment on $H_2$ gas [62]. The experimental signal showed detailed beating behavior in the time domain, reflecting the rotational dynamics of all thermally populated rotational levels. Modeling of the experimental time domain response gave the temperatures of the gas (see figure 1.11).

Time-resolved CARS is the temporal domain counterpart to the previously discussed frequency resolved methods. The high peak power of ultrafast pulses used in time resolved CARS gives high signal strength. When recording the beating response, it does not require high resolution spectrometer, and the method is capable of detecting dilute gas samples because of high signal strength. The core of this method is to obtain the vibrational beating and perform Fourier transform to obtain resonance spacing information.

However, the reliance on Fourier transform leads to an underlying problem. Time domain CARS beating measurements and frequency domain CARS spectra are not equivalent [63]. The Fourier relations between spectra, vibrational beating and their corresponding Fourier transforms are compared in figure 1.10. It shows that the fourier transform of vibrational beating does not equal the spectrum and vice versa. The Fourier transform of time domain beatings (figure 1.10B) gives a symmetrical frequency domain response (figure 1.10D) which is different from the actual spectrum of vibrational resonances (figure 1.10A). The Fourier transform of the fre-

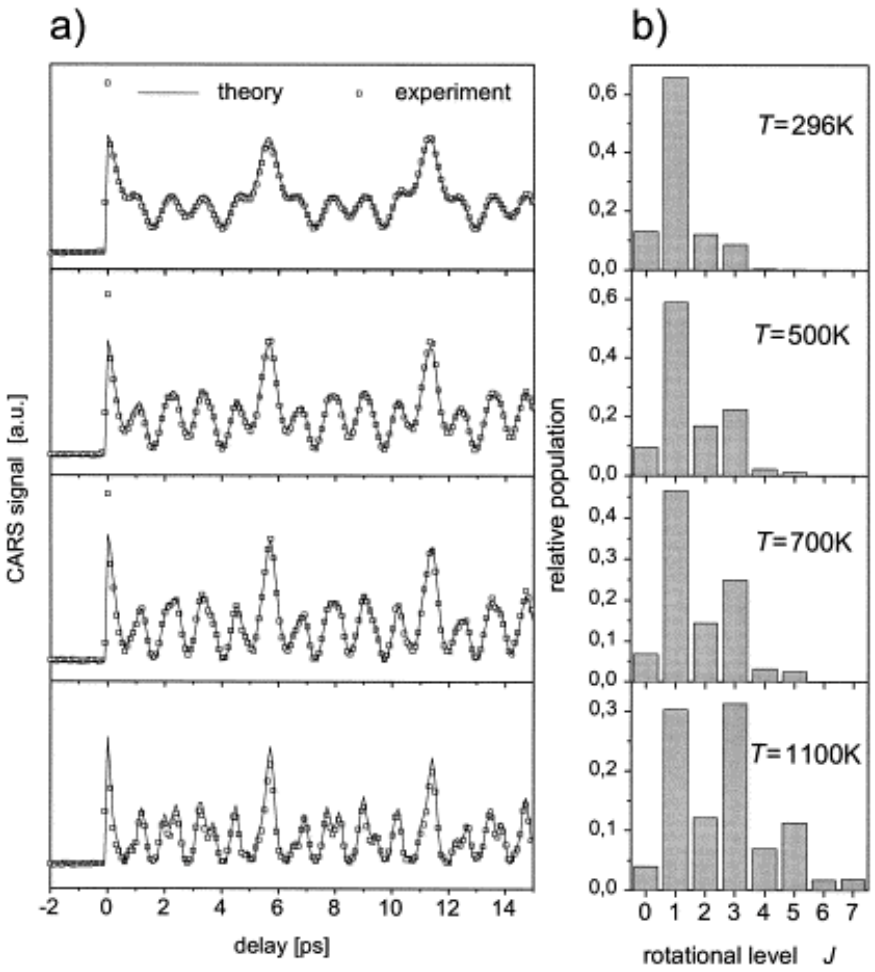


Figure 1.11: (A) Time resolved CARS signal of $H_2$ gas at four different temperatures. (b) Rotational level populations can be calculated through fitting. (from T. Lang et. al. Phys. Chem. Lett. 1999, 310, 65-72)

quency domain spectrum figure (figure 1.10A) gives symmetric time domain profiles (figure 1.10C), which is contradictory to the direct time domain beating measurement. This is a problem of the Fourier transform in linking experimental results of the time domain to the frequency domain and vice versa. The reason this problem exists is the lack of phase information in the measurement. Photon detectors, such as a PMT, or a CCD cannot record the phase of the optical field, only records the intensity of the field, which is the modulus square of field amplitude. The Fourier transform of a real quantity from experimental measurement gives a symmetric response in the conjugated domain. However, if the phase factor is considered into the Fourier transform, the complex spectrum will be equivalent to the vibrational beating, and the Fourier transform of beating signal with phase will give the actual CARS spectrum. This raises the question of how to obtain the phase of vibrational responses. In chapter 4, a tentative approach will be presented.

### 1.2.4 Pulse Shaping in CARS Methods

Beside having a broad bandwidth, Ti:Sapphire lasers also provide *coherent* broad band radiation. The concept of coherence describes the correlation properties between physical quantities of a wave. Spectral components in broad band coherent radiation maintain stable phase relations. This is the fundamental difference between a femtosecond Ti:Sapphire laser and a modeless dye laser: a dye laser gives a sum of shifting spectral lines within bandwidth from shot to shot, while a Ti:sapphire laser gives a stable broadband output every shot. Such stable qualities of both amplitude and spectral phase of coherent lasers lead to the possible utilization of interference effects. To manipulate the spectral phase of a broad band pulse, the technique of pulse shaping is often implemented to control interference effect.

The functions of the pulse shaping technique in CARS can be categorized into two types. In the first type, the pulse shaper tailors broad band spectral components to fulfil the vibrational excitation task and the probing task. It is primarily used for single pulse CARS experiments. In the second type, the

pulse shaper controls the phase and sometimes the amplitude of excitation pulse pairs or the probe pulse to achieve selective excitations or selective probing.

### Single Pulse CARS method

Single pulse CARS utilizes the pulse shaping technique on broad band radiation to include the vibrational excitation and coherent probing within one broad band pulse.

The preparation of molecular vibrations through a single broad band femtosecond pulse is known as impulsive stimulated Raman scattering [64, 65]. Impulsive stimulated Raman scattering was used for vibrational excitation in a single pulse CARS method. Due to the broad bandwidth of femtosecond pulses, if the frequency difference between the red edge and the blue edge of a pulse coincides with a vibration resonance of sample, a vibrational coherence is prepared. The impulsive stimulated Raman process can be treated as a special case of coherent stimulated Raman with a single pulse acting as both pump and Stokes pulses.

The amplitude and phase control ability of the pulse shaper is used to include the probe function into one single broad band pulse. A narrow band spectral component at the blue edge of the spectrum is shaped with different spectral phase from the rest of the spectrum to serve as the probe pulse. The pulse shaping of such a broad band pulse is shown in figure 1.12. It was first demonstrated by Y. Silberberg and coworkers [21]. The pulse shaper blocks the blue edge of broad band spectrum using an amplitude mask. The function of this amplitude mask is to remove the potential spectral overlap between the excitation pulse and the generated CARS signal. Then, at the remaining blue edge of the spectrum, a spectral phase shift is applied to a narrow window of the spectrum. This out of phase spectral component serves as the function of probe pulse, because in the time domain it corresponds to a long time duration. The pulse after the pulse shaper was then focused by a high numeric aperture microscope objective at the sample to generate CARS signals in the collinear geometry. With proper bandpass

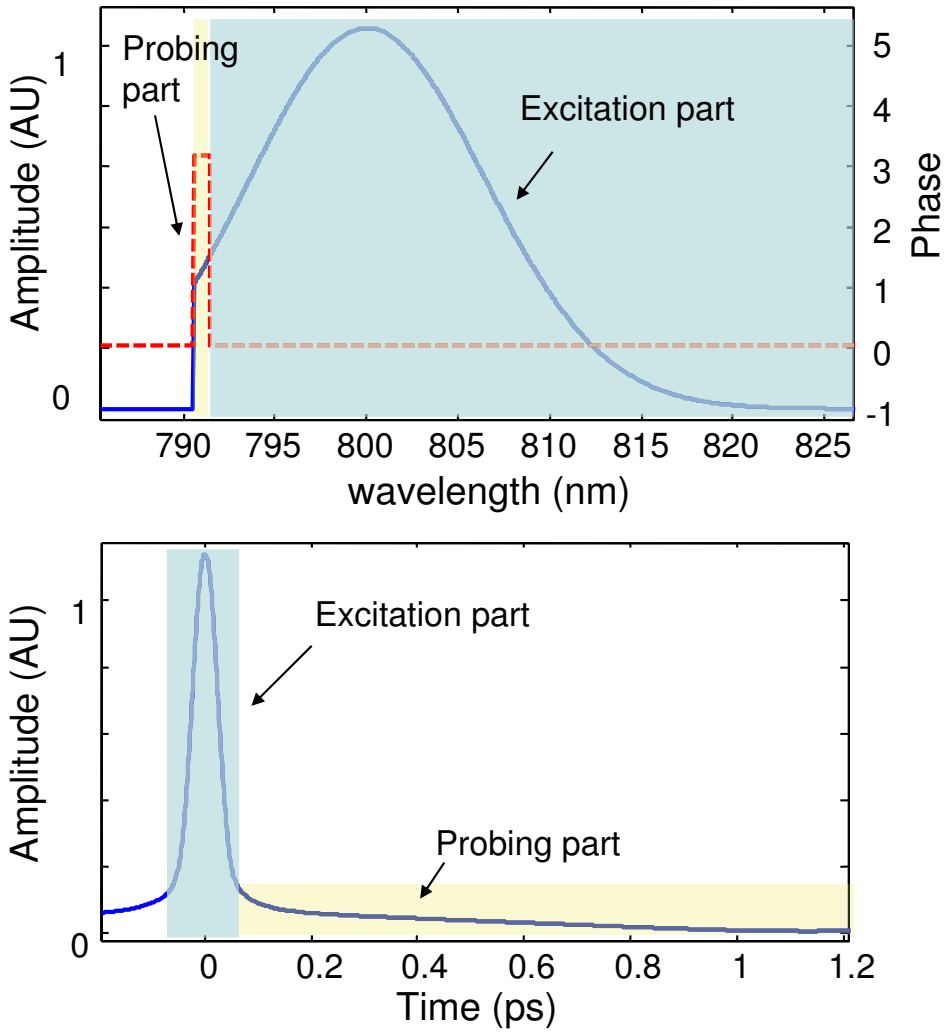


Figure 1.12: The pulse shape of the excitation pulse in single pulse CARS experiment is shown in these plots. The upper plot is the frequency domain representation of broadband pulse amplitude and spectral phase. The narrow spectral phase flipped region serves as the probe pulse. The flat phase region serves as the excitation part. The bottom plot shows the time domain plot of the pulse.

filters to remove the excitation pulse, the CARS signal was then coupled into a spectrometer to give the spectrum. In Oron et. al. [21], the spectral phase shift of the probing spectral component was set alternatively to $\pi$ and 0. The difference between CARS spectra from these two phase patterns was recorded and the resonant level positions of sample were obtained. In continuing work of Y. Silberberg and coworkers [23] and S.R. Leone and coworkers [24] this method was further developed by introducing heterodyne and polarization techniques for detection.

The bandwidth of the femtosecond pulse after shaping usually determines the bandwidth of resonances that single pulse CARS methods can detect. In Lim et. al.[24], a 11fs Ti:sapphire oscillator was used and the measurable spectral range was from 400 to $1500cm^{-1}$. The lower range is determined by the efficiency of spectral filtering, background subtraction as well as the probe pulse band width. The upper limit is determined by the total pulse bandwidth. The resolution of the single pulse CARS method is determined by the width of the probe phase window, and phase window size is limited by the pulse shaper resolution. In Lim et. al.[24], two pixels of the pulse shaper were used to create the probe phase window, and the resulting resolution was about $35cm^{-1}$. Reducing the size of the probe window can give better spectral resolution at the cost of signal strength.

Single pulse methods have the edge over traditional CARS methods in a way that it greatly simplifies the experimental setup. Comparing to traditional requirement of multiple laser frequencies, the single pulse CARS method requires only a femtosecond oscillator, a pulse shaper and a spectrometer. It also removes the time and effort on beams temporal synchronization and spatial overlap. The acquisition speed of the single pulse CARS technique can be shortened to milliseconds as well, since it is only limited by the response time and sensitivity of CCD detector.

#### Selective Excitation through Pulse Shaping

With the utilization of pulse shaping, selective preparation of vibration resonances within the excitation bandwidth became a possibility. In the narrow

band CARS method, vibrational state selection is done by tuning the frequency of excitation lasers. Frequency tuning of a narrow band laser means long operation time and possible instrument instability. Pulse shapers can manipulate the frequency components within the bandwidth of laser. It enables the possibility of fast selection of vibration excitation without tuning the laser frequency.

An early experiment of bandwidth selectivity on the CARS excitation was done through chirping. Chirp is a special phenomenon associated with ultrafast laser pulses. Due to the linear dispersion of light transmitting media, ultrafast pulses extend in duration along the propagation direction. Usually, red frequency components travel faster than blue frequency components in normal dispersion media. If such a chirped pulse is shone on a sample, the low frequency part will arrive earlier than the high frequency part. Hence, the instantaneous frequency that the sample feels gradually shifts toward higher frequency. Such frequency shifting resembles a bird's chirp in an acoustic wave, so it is given the name "chirp". Mathematically, a chirped pulse has a quadratic spectral phase dependence on frequency and can be accurately created by a pulse shaper.

The special property of time-frequency dependence of a chirped pulse enables a way of controlling the excitation bandwidth of vibrational excitation. For pump and Stokes pulses, if either one is chirped, by varying the time delay between two pulses, the central frequency of the field correlation will shift accordingly. Figure 1.13 is a numerical simulation of the frequency correlation between two chirped pulses. It can be seen that by tuning the relative time delay between pulses, the selection of instantaneous frequency of coherent vibration excitation is achieved.

One selective excitation scheme based on chirp was proposed by Zheltikov and coworkers[66] and experiment was done later by Pestov et al.[67] on a solid power sample.

Chirp is not the only way of vibrational selection. Any pulse shaping that can affect the spectrum of pump/Stokes field correlation has the potential of selective excitation . Silberberg and his coworkers explored shaping based on single pulse impulsive Raman process[22, 68]. In their work, sinusoidal

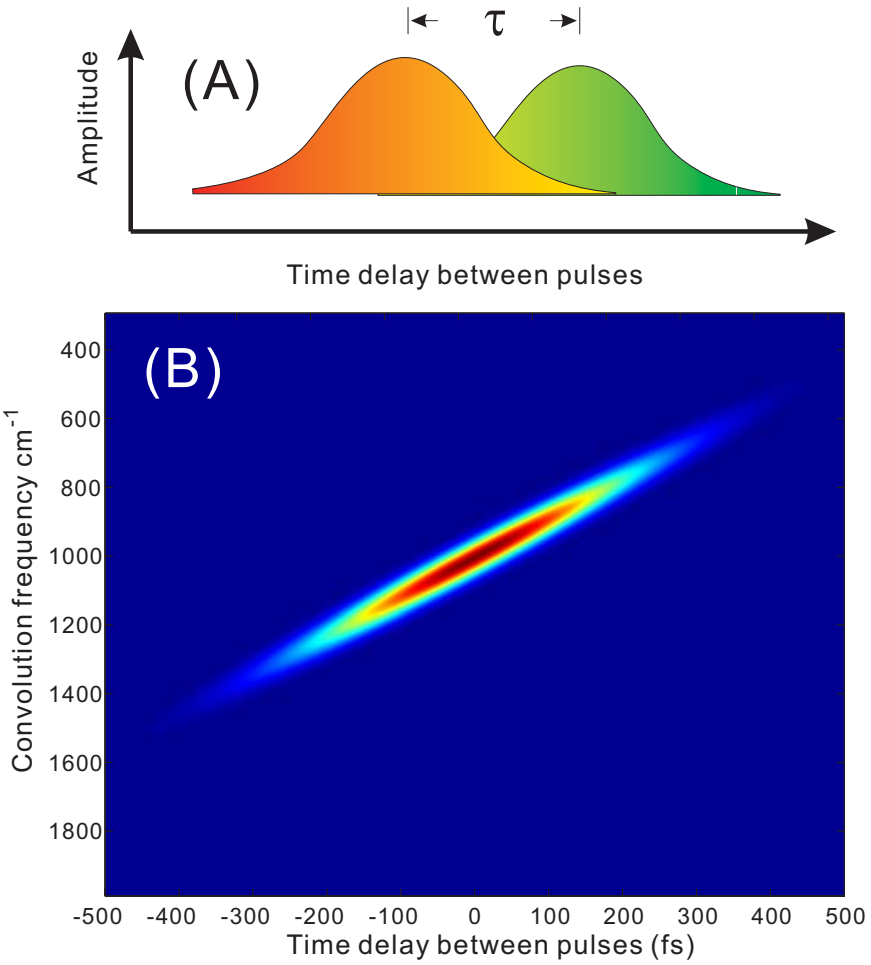


Figure 1.13: (A) schematically shows the overlapping between two chirped pulses in the time domain; $\tau$ is the time difference between center of pulses. (B) shows the numerical simulation of the instantaneous frequency of field correlation. We can see that the convolution frequency now has narrow bandwidth and is a function of relative time delay $\tau$ between pulse and Stokes pulse.

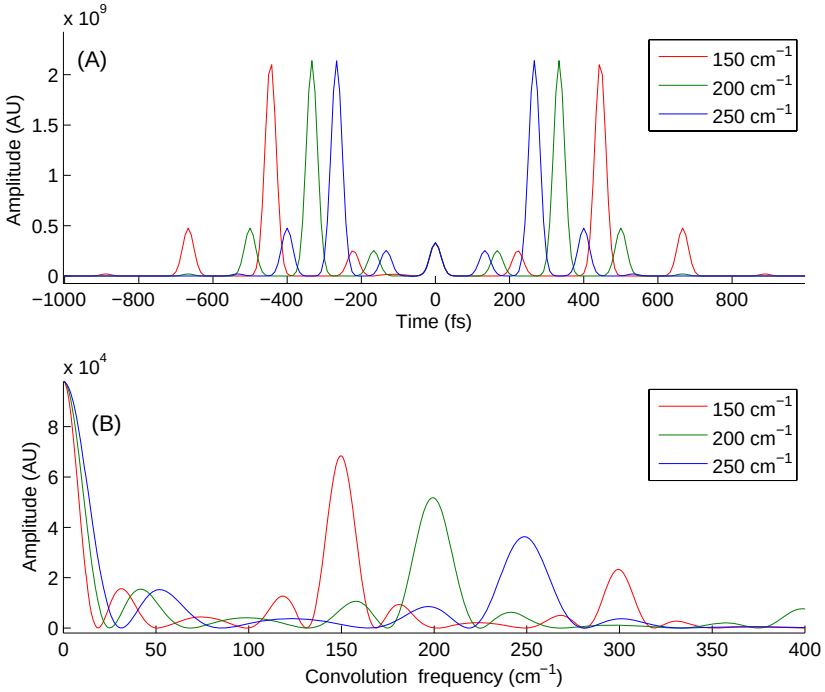


Figure 1.14: The figures show the numerical simulation of femtosecond pulse under sinusoidal spectral phase modulation of 150, 200 and 250 $cm^{-1}$ period. (A) shows the pulse train in the time domain with spectral phase sinusoidal period of 150, 200 and 250$cm^{-1}$ respectively. (B) shows the frequency domain convolution field spectrum. We can see 150, 200 and 250$cm^{-1}$ period modulations also generate frequency component at corresponding frequency as well as its multiple frequency e.g. 150$cm^{-1}$ also generate peak at 300$cm^{-1}$.

phase shaping was applied on the excitation part of single broadband pulse. The excitation part position is shown in figure 1.12 for single pulse CARS. In the time domain, the shaped pulse splits into a pulse train. If the pulse train matches the period of a vibrational resonance, it can effectively excite it. In the frequency domain, the self-correlation of such sinusoidal modulated pulse shows maxima at certain frequency and minima at others. This means excitation for certain resonances and suppression for others. A numerical simulation on sinusoidal shaping of a 150fs pulse is presented as figure 1.14. The effect of sinusoidal spectral phase modulation in the frequency domain generates modulation on the field correlation of pump and Stokes pulses and achieves the selective excitation.

With this scheme, a good resolution pulse shaper can be used to create sinusoidal modulation on a broad band pulse to selectively excite vibration resonances. After the excitation of coherent vibration and probing, the total CARS signal is recorded with respect to the sinusoidal modulation period and is used to generate CARS spectrum. Y. Silerberg and his coworkers [22] further implemented this vibration selection CARS into single beam CARS microscopy. A.G. Motzkus and coworkers [69] further implemented it for low-wavenumber vibration mode (from 50 to 400 $cm^{-1}$) spectroscopy.

The disadvantage of both chirped approach and sinusoidal modulation approach is still the spectral resolution. In both approaches, the spectral resolution is determined by the excitation selectivity over resonances. Therefore it is limited by the pulse shaping ability. It cannot be better than the SLM pixel bandwidth which is around 10 to $20cm^{-1}$. Secondly, both approaches require certain scanning. The chirped pulse approach needs scanning of the time delay and a calibration on the relation between time delay and the excitation frequency for differently chirped pulses. The sinusoidal modulation approach needs to scan the period of sinusoidal phase patterns. The speed of measurement is therefore determined by the pulse shaper response time (The SLM that was used in this thesis work has around a 100ms response time per phase pattern).

### 1.2.5 Summary and Comparison of Current Methods

The narrow band CARS scheme has straightforward spectrum/resonance interpretations. Due to the long duration of narrow band pulses (from picosecond up to nanosecond), time synchronization between excitation lasers is not a difficult problem. With the narrow band probe pulse, the CARS spectrum reflects the profile of vibration resonances when the non-resonant background is low. The disadvantage of the narrow band CARS methods is its low signal strength. Narrow band lasers come with lower peak power than that of short pulse duration lasers, and low peak power laser generates low signal in the third order nonlinear optical process of CARS. To obtain detectable signal, laser power has to be set at high level, which could lead to the possible degradation of samples. The narrow band CARS method requires two lasers of different frequency: typical Nd:YAG laser and a dye laser. It requires frequency tuning of the dye laser, which is time-consuming and susceptible to mechanical instability. The spectral resolution of narrow band CARS is determined by the bandwidth of the excitation pulses, narrow bandwidth leads to high spectral resolution.

Multiplex CARS improves the acquisition speed of narrow band CARS by simultaneously accessing multiple resonant levels while maintaining the straight forward spectrum interpretation. It removes the scanning of laser frequencies. The interpretation of the multiplex spectrum is the same as that obtained by narrow band CARS. In terms of experimental setup, the narrow band Nd:YAG laser is used as pump/probe pulse. A broad band dye laser that is pumped by the narrow band laser provides the broad band Stokes frequency. After the invention of the solid state Ti:sapphire laser, narrow band probe pulses could be created from spectral cutting of broad band pulse[49]. Nonlinear optical parametric process became more effective for high peak power laser pulses, making the frequency conversion convenient. Broad band pulses are used as both pump and Stokes pulse. In both dye laser system and Ti:Sapphire system, the setup of multiplex CARS is based on one source laser, therefore eliminating the fluctuation that is associated between two laser devices. However, the disadvantage of multiplex CARS

is still inherited from the narrow band CARS method: it has low signal strength because of the low peak power of one or two beams. Creating a narrow band probe pulse from broad band femtosecond laser reduces the total signal in multiplex CARS. Moreover, for multiplex CARS methods that involve the usage of narrow band probe cut from broad band radiation, the spectral resolution of CARS spectrum is coupled with the signal intensity. The narrower the probe bandwidth is, the better the spectral resolution, but the lower the signal strength (see figure 1.9).

The above situation describes a "resolution vs. intensity" dilemma of achieving good spectral resolution versus obtaining high signal strength. A similar and simple example of this dilemma is given by the slit choice of a spectrometer: narrow slits give high resolution but low intensity on the detector. In a frequency domain CARS experiment, the spectral resolution is strictly limited by the bandwidth of the probe pulse. For the experiment that the narrow band probe pulse is obtained through cutting of broad band radiation, a probe pulse of small bandwidth gives good spectral resolution, but reduces the signal strength, thus prolonging the required acquisition time. Probing the vibrational coherence with broad band femtosecond pulse, on the other hand, gives strong signal but very poor, if any, spectral resolution. This dilemma is common for multiplex CARS type of methods, including single pulse CARS techniques [21, 23, 63].

Time-resolved CARS methods provide a fresh approach of temporal domain vibrational spectroscopy. They utilize three ultrafast pulses to obtain the time domain beating response of a vibrational coherence, and give high signal strength by using high peak power broad band pulses. The interpretation on the resonant levels is done by the Fourier transform of the temporal beating. The peaks on the Fourier-transformed have better spectral resolution than the bandwidth of probe pulse. For a Fourier method, the spectral resolution of time-resolved CARS is limited by the duration of time scan, rather than the bandwidth of the probe pulse. However, there is one significant difference between time-resolved CARS and frequency domain methods. The vibrational beatings retrieved from Fourier analysis is the autocorrelation of the spectrum rather than the spectrum itself (see fig-

ure 1.10). In addition, autocorrelation of a spectrum gives a poor indication of the linewidth of resonances comparing to the spectrum itself, because the line width of peaks are convolved to give the width of the autocorrelation peak in the autocorrelation spectrum. The comparison between figure 1.10A and figure 1.10D shows this broadening effect.

Combination of femtosecond laser sources with pulse shaping techniques open a door to a group of creative CARS methods. The manipulation of a broad band laser field by pulse shaping can assign certain functions to frequency components or lead to possible interference in multi-photon processes. Single pulse CARS greatly simplified the experimental setup, simplifying the total instruments to perform CARS measurement to an oscillator and a pulse shaper. With pulse shaping, selective excitation is feasible without tuning laser frequencies. However, the spectral resolution of pulse shaping CARS methods is limited by the resolution of the pulse shaper, and the acquisition time is often limited by the response time of the pulse shaper as well.

The above discussion provides readers a broad profile of the CARS research. To gain a further insight into the CARS process, a theoretical analysis is necessary and will be presented in the next section.

## 1.3 Theory of Coherent Anti-Stokes Raman Scattering

The purpose of spectroscopy in general is to exploit light-matter interactions to reveal the energy level structure of atoms or molecules. The matter interacts with light fields and this interaction affects the properties of light fields, whether it is intensity gaining, propagation direction altering or the creation of new frequencies. By measuring the optical fields that take part in the interaction, researchers can deduce structural information of the sample. When this general spectroscopy model comes to the specific case of coherent anti-Stokes Raman scattering (CARS), two questions are immediately raised: how does the resonance structure affect the generation of

the CARS field? and how are spectra of the anti-Stokes field interpreted to give information on resonance structure of samples? Equation (1.1) provides a general formula for CARS signal generation. In this section, detailed analytical discussions on CARS are presented.

### 1.3.1 Brief introduction to Density Matrix

CARS can be treated as a special case of the resonant four-wave-mixing process, therefore it is traditionally described by deriving phenomenological third order susceptibility $\chi^{(3)}$ [70, 71]. However, the line width measured by CARS reflects a *decoherence* process between coherently excited levels, comparing to linewidth of Raman spectroscopy that reflects the relaxation of population. The treatment of density matrix[71, 72] is particularly convenient in describing coherence between laser excited levels and its time evolutions.

The interaction between matter and light is often described by the time-dependent Schrödinger equation:

$$i\hbar\frac{\partial\psi_s(r,t)}{\partial t} = \widehat{H}\psi_s(r,t) \tag{1.6}$$

Where $\widehat{H}$ can be assumed as summation of Hamiltonian of a molecule $\widehat{H}_0$ and interaction Hamiltonian between external optical field and matter $\widehat{V}(t)$

$$\widehat{H} = \widehat{H}_0 + \widehat{V}(t) \tag{1.7}$$

The solution of $\widehat{H}_0$ gives a complete set of basis functions

$$\psi(t,x) = \sum_n C_n(t)\phi_n(x) \tag{1.8}$$

The expansion coefficient $C_n(t)$ gives the probability amplitude of the molecule in energy states n and at time t, and the time evolution of the molecule can be described by the evolution of the expansion coefficients $C_n(t)$.

The real system in experiment consists of many molecules, even in the small interaction region of a tightly focused laser beam, the amount of

molecules (often $> 10^6$) is beyond the computational power to track individually. Moreover, there are often collisions happening among molecules, which modify the actual state of involved molecules. In this situation, the density matrix can be used to conveniently describe the ensemble of molecules in a statistical fashion. The elements of the density matrix are defined by

$$\rho_{nm}(t) = \overline{C_m^*(t)C_n(t)} \tag{1.9}$$

Where the overbar denotes an ensemble average of all molecules. Subscripts n and m represent the energy levels n and m. The density matrix represents an average of coefficient product over all molecules. The diagonal elements of the density matrix $\rho_{nn}$ represents the population of molecules in the state n, and the off-diagonal elements $\rho_{nm}$ represent the *coherence* between states n and m. They are non-zero when the system is in a coherent superposition of energy eigenstates and zero when system is in thermal equilibrium. This can be created by coherent laser radiations but not through population redistribution through temperature changes.

In the density matrix formalism, the expectation value of an observable A is given by the trace of the product between operator matrix $\hat{A}$ and the density matrix $\hat{\rho}$

$$< A >= tr(\hat{\rho}\hat{A}) \tag{1.10}$$

The time evolution of the density matrix follows [71]

$$\frac{d\rho_{nm}}{dt} = \frac{-i}{\hbar}[\hat{H}, \hat{\rho}]_{nm} \tag{1.11}$$

which is known as Liouville equation, which is derived from time dependent Schrödinger equation.

Due to collisions or other interactions that drive the system towards thermal equilibrium, there are relaxation terms in both diagonal (population) and off-diagonal (coherence)terms of the density matrix. The Liouville equation is then modified by adding the statistical damping factor $\gamma_{nm}$

$$\frac{d\rho_{nm}}{dt} = \frac{-i}{\hbar}[\hat{H}, \hat{\rho}]_{nm} - \gamma_{nm}(\rho_{nm} - \rho_{nm}^{eq}) \tag{1.12}$$

Since in thermal equilibrium, the phase of individual molecules in a given energy level is random, the statistical off diagonal density matrix element $\rho_{nm}^{eq}$ is assumed to be zero due to the cancelation of summation over wavefunctions of large number of molecules. The damping factor $\gamma_{nm}$ reflects the rate of relaxation from a coherent superposition of different states to thermal equilibrium and $\gamma_{nm} = \gamma_{mn}$. Using expression (1.7), the commutator can be separated as $[\hat{H}, \hat{\rho}] = [\hat{H}_0, \hat{\rho}] + [\hat{V}, \hat{\rho}]$ and equation (1.12) can then be expressed as

$$\frac{d\rho_{nm}}{dt} = -i\omega_{nm}\rho_{nm} - \frac{i}{\hbar}[\hat{V}, \hat{\rho}]_{nm} - \gamma_{nm}(\rho_{nm} - \rho_{nm}^{eq}) \tag{1.13}$$

where $\omega_{nm}$ is the energy difference between level n and m, which comes from the stationary Hamiltonian $\hat{H}_0$. Equation 1.13 is used as the fundamental equation to describe the behavior of an ensemble of molecules.

### 1.3.2 CARS Expression Derivation Using Density Matrix Formalism

CARS generates a directional coherent signal at the anti-Stokes frequencies. The light emission process is associated with Maxwell's equations with a source polarization term $\widetilde{P}$.

$$-\nabla^2\widetilde{E} + \frac{1}{c^2}\frac{\partial^2}{\partial t^2}\widetilde{E} = -\frac{4\pi}{c^2}\frac{\partial^2\widetilde{P}}{\partial t^2} \tag{1.14}$$

The $\widetilde{P}$ derives from the macroscopic "polarization" of the sample [72], which is directly related to the dipole operator $\hat{\mu}$, by $\widetilde{P} = N < \mu >$, where N is the particle number. Taking a two level system as an example, the dipole operator $\hat{\mu}$ has the form of

$$\hat{\mu} = \begin{bmatrix} 0 & \mu_{12} \\ \mu_{21} & 0 \end{bmatrix} \tag{1.15}$$

note that $\mu_{21} = \mu_{12}^*$ The expectation value of $\hat{\mu}$ is given by expression (1.10). For example if the density matrix of the two level system has the form of

$\begin{bmatrix} \rho_{11} & \rho_{12} \\ \rho_{21} & \rho_{22} \end{bmatrix}$, the expectation value of $\mu$ is then obtained by the trace of $\hat{\rho}\hat{\mu}$.

$$\hat{\rho}\hat{\mu} = \begin{bmatrix} 0 & \mu_{12} \\ \mu_{21} & 0 \end{bmatrix} \begin{bmatrix} \rho_{11} & \rho_{12} \\ \rho_{21} & \rho_{22} \end{bmatrix} \tag{1.16}$$

$$< \mu >= \rho_{12}\mu_{21} + \rho_{21}\mu_{12} \tag{1.17}$$

Even though expression (1.17) represents the situation of a two level system, for multilevel system, the expectation value of the dipole moment has similar form. Thus the macroscopic polarization $\widetilde{P}$ depends on the off-diagonal elements of the density matrix $\rho_{nm}$. Therefore, the following discussion on CARS in this thesis is based on deriving off-diagonal elements of the density matrix resulting from light-matter interaction.

The interaction between matter and light is described by equation (1.13). The energy diagram of CARS is shown in figure 1.15

It contains three resonant levels, the ground state, vibrational state and an intermediate state at much higher energy. Its density matrix can be represented by a $3 \times 3$ matrix spanning the ground state g, vibrational state v and intermediate state i as figure 1.15 shows. To simplify the discussion, the initial state can be assumed to be $\rho_0 = \begin{bmatrix} \rho_{gg}^{eq} & 0 & 0 \\ 0 & \rho_{vv}^{eq} & 0 \\ 0 & 0 & \rho_{ii}^{eq} \end{bmatrix}$. $\rho_{vv}^{eq}$ and $\rho_{ii}^{eq} \ll 1$ for $E_v \gg k_b T$, and $\rho_{gg}^{eq} \approx 1$ which represents the assumption that majority of molecules are in the ground state in thermal equilibrium. Off-diagonal elements of the matrix are also zero, from the assumption of thermal equilibrium.

When interacting with one pulse, off-diagonal elements of $\rho$ are prepared, which can be obtained by solving equation 1.13. With initial condition of $\rho_0$, and using the perturbation method [71] (assuming $\hat{\rho} = \hat{\rho}^{(0)} + \hat{\rho}^{(1)} + \hat{\rho}^{(2)}....$), the linear response term of $\hat{\rho}$ follows

$$\rho_{nm}^{(1)}(t) = e^{-(i\omega_{nm}+\gamma_{nm})t} \int_{\infty}^{t} \frac{-i}{\hbar} [\hat{V}, \rho_0]_{nm} e^{(i\omega_{nm}+\gamma_{nm})t'} dt' \tag{1.18}$$

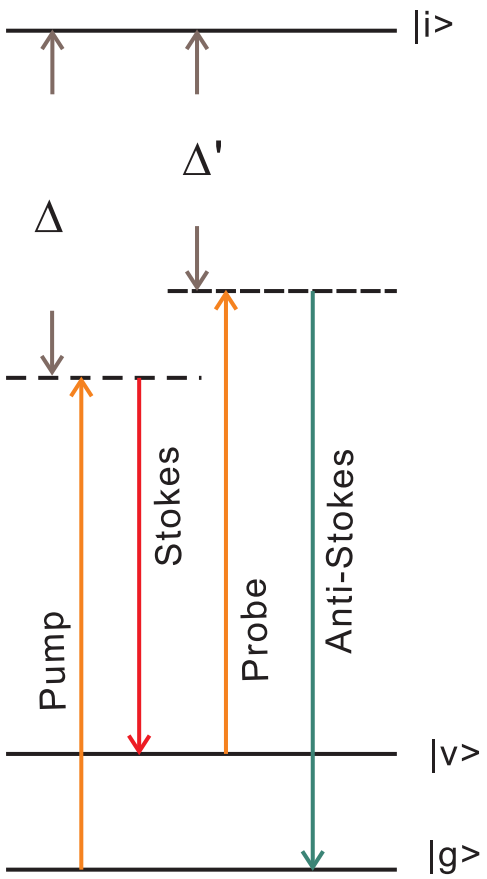


Figure 1.15: The energy diagram of CARS, g v and i are three levels involved in derivation. The intermediate electronic level $|i>$is far from resonance with detuning of $\Delta$ and $\Delta'$

n, m are dummy indices and $\hat{V}(t')$ is the interaction Hamiltonian, which has the form

$$\hat{V} = -\begin{bmatrix} 0 & \mu_{gv}E(t) & \mu_{gi}E(t) \\ \mu_{vg}E(t) & 0 & \mu_{vi}E(t) \\ \mu_{ig}E(t) & \mu_{iv}E(t) & 0 \end{bmatrix} \tag{1.19}$$

Where $\mu_{gv}$ is the dipole moment between state g and v, and $\mu_{gv} = \mu_{vg}^*$.

When interaction involves two pulses, as is the case in the vibration preparation step of CARS, the second order expansion of the density matrix $\hat{\rho}^{(2)}$ is used to reflect such preparation. It can be derived as

$$\rho_{nm}^{(2)}(t) = e^{-(i\omega_{nm}+\gamma_{nm})t}\int_{\infty}^{t}\frac{-i}{\hbar}[\hat{V},\hat{\rho}^{(1)}]_{nm}e^{(i\omega_{nm}+\gamma_{nm})t'}dt' \tag{1.20}$$

The E field in the interaction Hamiltonian $\hat{V}$ contains the incident pulses. When multiple fields exist for excitation, E(t) can take the general form of

$$E(t) = \sum_n \int_0^{\infty} E_n(\omega)e^{-i\omega t}d\omega + c.c. \tag{1.21}$$

This expression contains both positive frequency and negative frequency components, in order to let the electric field in the time domain be real, since it is a measurable observable. To follow the convention of CARS, in the following derivation we use $E_p(t)$ to describe the first optical field (pump) that interacts with the system, $E_s(t)$ to describe the second optical field (Stokes), and $E_{pr}(t)$ to describe the third optical field (probe).

The solution of off diagonal elements of $\hat{\rho}^{(1)}$ in equation (1.20) can be found as

$$\rho_{ig}^{(1)} = \hbar^{-1}\mu_{ig}(\rho_{gg}^{eq}-\rho_{ii}^{eq})\int_0^{\infty}[\frac{E_p(\omega)e^{-i\omega t}}{(\omega_{ig}-\omega)-i\gamma_{ig}}+\frac{E_p^*(\omega)e^{i\omega t}}{(\omega_{ig}+\omega)-i\gamma_{ig}}]d\omega \tag{1.22}$$

$$\rho_{vg}^{(1)} = \hbar^{-1}\mu_{vg}(\rho_{gg}^{eq}-\rho_{vv}^{eq})\int_0^{\infty}[\frac{E_p(\omega)e^{-i\omega t}}{(\omega_{vg}-\omega)-i\gamma_{vg}}+\frac{E_p^*(\omega)e^{i\omega t}}{(\omega_{vg}+\omega)-i\gamma_{vg}}]d\omega \tag{1.23}$$

$$\rho_{vi}^{(1)} = \hbar^{-1}\mu_{vi}(\rho_{ii}^{eq}-\rho_{vv}^{eq})\int_0^{\infty}[\frac{E_p(\omega)e^{-i\omega t}}{(\omega_{vi}-\omega)-i\gamma_{vi}}+\frac{E_p^*(\omega)e^{i\omega t}}{(\omega_{vi}+\omega)-i\gamma_{vi}}]d\omega \tag{1.24}$$

Noted these first order elements $\rho_{nm}^{(1)}$ are very small in the situation of CARS, since the excitation fields are far from being resonant with either the vibrational state $\omega_{gv}$ or intermediate state $\omega_{gi}$. In terms of actual value, $\rho_{gi}^{(1)}$ and $\rho_{gv}^{(1)} \gg \rho_{vi}^{(1)}$, because of initial equilibrium diagonal density matrix element of state i being zero. The actual value of $\rho_{gi}^{(1)}$ and $\rho_{gv}^{(1)}$ depends on the magnitude of detuning $\Delta$ and $\Delta'$.

With these expression of first order perturbation solution of density matrix, we continue to check the second order density matrix $\hat{\rho}^{(2)}$. The density element corresponding to the coherence between the ground state and the vibrational state, $\rho_{vg}^{(2)}$ can be found by solving equation (1.20) as

$$
\begin{aligned}
\rho_{vg}^{(2)} \quad = \quad & \frac{(\rho_{ii}^{eq} - \rho_{vv}^{eq})\mu_{vi}\mu_{ig}}{\hbar^2}\{ \\
& \int_0^\infty \int_0^\infty \frac{E_p(\omega)E_s(\omega')e^{-i(\omega+\omega')t}}{[(\omega_{vg} - \omega - \omega') - i\gamma_{vg}][(\omega_{vi} - \omega) - i\gamma_{vi}]} d\omega' d\omega \\
& + \int_0^\infty \int_0^\infty \frac{E_p^*(\omega)E_s(\omega')e^{i(\omega-\omega')t}}{[(\omega_{vg} + \omega - \omega') - i\gamma_{vg}][(\omega_{vi} + \omega) - i\gamma_{vi}]} d\omega' d\omega \\
& + \int_0^\infty \int_0^\infty \frac{E_p(\omega)E_s^*(\omega')e^{-i(\omega-\omega')t}}{[(\omega_{vg} - \omega + \omega') - i\gamma_{vg}][(\omega_{vi} - \omega) - i\gamma_{vi}]} d\omega' d\omega \\
& + \int_0^\infty \int_0^\infty \frac{E_p^*(\omega)E_s^*(\omega')e^{i(\omega+\omega')t}}{[(\omega_{vg} + \omega + \omega') - i\gamma_{vg}][(\omega_{vi} + \omega) - i\gamma_{vi}]} d\omega' d\omega\} \\
& - \frac{(\rho_{gg}^{eq} - \rho_{ii}^{eq})\mu_{ig}\mu_{vi}}{\hbar^2}\{ \\
& \int_0^\infty \int_0^\infty \frac{E_p(\omega)E_s(\omega')e^{-i(\omega+\omega')t}}{[(\omega_{vg} - \omega - \omega') - i\gamma_{vg}][(\omega_{ig} - \omega) - i\gamma_{ig}]} d\omega' d\omega \\
& + \int_0^\infty \int_0^\infty \frac{E_p(\omega)E_s^*(\omega')e^{-i(\omega-\omega')t}}{[(\omega_{vg} - \omega + \omega') - i\gamma_{vg}][(\omega_{ig} - \omega) - i\gamma_{ig}]} d\omega' d\omega \\
& + \int_0^\infty \int_0^\infty \frac{E_p^*(\omega)E_s(\omega')e^{i(\omega-\omega')t}}{[(\omega_{vg} + \omega - \omega') - i\gamma_{vg}][(\omega_{ig} + \omega) - i\gamma_{ig}]} d\omega' d\omega \\
& + \int_0^\infty \int_0^\infty \frac{E_p^*(\omega)E_s^*(\omega')e^{i(\omega+\omega')t}}{[(\omega_{vg} + \omega + \omega') - i\gamma_{vg}][(\omega_{ig} + \omega) - i\gamma_{ig}]} d\omega' d\omega\}
\end{aligned}
\tag{1.25}
$$

Expression (1.25) is the complete term of vibrational coherence $\rho_{gv}^{(2)}$. According to equation (1.20), only $\rho_{gi}^{(1)}$ and $\rho_{iv}^{(1)}$ enters into $\rho_{vg}^{(2)}$. Still, it has a very complex form. It has to be simplified before being used. Such simplification can be done by analyzing the major contributions. The resonance $\omega_{gv}$ for a typical Raman active sample is from $200cm^{-1}$ to 4000 $cm^{-1}$, the intermediate state normally is an electronic state, which varies depending on specific sample, a typical estimation is $\omega_{ig} > 20000cm^{-1}$. The initial equilibrium state $\rho^{(eq)}$ can also help simplification. $\rho_{ii}^{eq}$ can be considered as zero at equilibrium distribution and $\rho_{vv}^{(eq)} \ll \rho_{gg}^{(eq)}$ which can be estimated by Boltzmann distribution. With those conditions, one can find that the main resonant term of contribution to CARS process is

$$\rho_{vg}^{(2)}(t) = -\frac{\rho_{gg}^{eq}\mu_{ig}\mu_{vi}}{\hbar^2}\int_0^\infty\int_0^\infty \frac{E_p(\omega)E_s^*(\omega')e^{-i(\omega-\omega')t}}{[(\omega_{vg}-\omega+\omega')-i\gamma_{vg}][(\omega_{ig}-\omega)-i\gamma_{ig}]}d\omega' d\omega \tag{1.26}$$

This can be interpreted as a stimulated Raman process, which serves as the first step of CARS excitation (see section 1.1.3). It has the carrier frequency of $\omega-\omega'$. It should be noted that the rest non-resonant terms can create transient coherence of $\rho_{vg}^{(2)}$ between the ground state and vibrational state during the pulse excitation, which contributes to the non-resonant background of CARS. It will be discussed in the next section.

Expression (1.25) is the general perturbation solution to two-photon process, and expression (1.26) is a specialized expression for stimulated Raman process that is responsible for the vibrational excitation in CARS with considerations of energy levels, equilibrium state population and pump/Stokes frequencies.

Expression (1.26) can be further simplified by replacing the $\omega'$ with $\omega-\Omega$.

$$\rho_{vg}^{(2)}(t) = -\frac{\rho_{gg}^{eq}\mu_{ig}\mu_{vi}}{\hbar^2}\frac{\int_0^\infty\int_0^\infty E_p(\omega)E_s^*(\omega-\Omega)e^{-i\Omega t}d\omega d\Omega}{[(\omega_{vg}-\Omega)-i\gamma_{vg}][(\omega_{ig}-\omega)-i\gamma_{ig}]} \tag{1.27}$$

From expression (1.27), we can define the response function $R(\Omega)$ to represent the coherence $\rho_{vg}^{(2)}$ in the frequency domain. $R(\Omega)$ contains the

profile of the vibrational level ($\omega_{vg}$, $\gamma_{vg}$) and is a result of field excitation strength $A(\Omega)$

$$R(\Omega) \equiv \rho_{vg}^{(2)}(\Omega) = \frac{C_{vg} \cdot A(\Omega)}{[(\omega_{vg} - \Omega) - i\gamma_{vg}]} \tag{1.28}$$

with $C_{vg} = -\frac{\rho_{gg}^{eq}\mu_{ig}\mu_{vi}}{\hbar^2}$ which reflects the dipole transition strength, and

$$A(\Omega) = \int_0^\infty \frac{E_p(\omega)E_s^*(\omega - \Omega)}{(\omega_{ig} - \omega) - i\gamma_{ig}} d\omega \tag{1.29}$$

which reflects the preparation power of pump and Stokes pulses. In typical CARS experiment, the pump field is often far off resonant from the intermediate electronic resonant level with detuning $\Delta = \omega_{ig} - \omega_p \sim 10^4 cm^{-1}$), therefore, the denominator term of $\frac{1}{\omega_{ig} - \omega - i\gamma_{ig}}$ in equation (1.29) can be treated as non-resonant excitation therefore be replaced by a real number $1/\Delta$ and can be grouped into $C_{vg}$ which is now $-\frac{\rho_{gg}^{eq}\mu_{ig}\mu_{vi}}{\hbar^2\Delta}$. Therefore equation (1.29) can be simplified as

$$A(\Omega) = \int_0^\infty E_p(\omega)E_s^*(\omega - \Omega) d\omega \tag{1.30}$$

Note that in some experiments [14, 73], the pump pulse can be resonant with low electronic states, which will increase the preparation efficiency through the resonant denominator.

The vibration coherence response function $R(\Omega)$ prepared by pump and Stokes pulses reflects the resonance information of the vibrational level. Figure 1.16 shows the numerical plot of R(t) and $R(\Omega)$ for a single resonant level (MATLAB simulation script can be found in Appendix A). The resonance is centered at 1000 $cm^{-1}$ and has a FWHM of $12cm^{-1}$. The real part of $R(\Omega)$ figure 1.16A shows dispersive profile. The imaginary part shows the Lorentzian profile. Figure 1.16C is the spectrum and spectral phase representation, it is equivalent to the real and imaginary representation shown on figure 1.16A and figure 1.16B. The spectral phase of $R(\Omega)$ shows a characteristic $\pi$ radian spectral phase shift across resonance according to expression (1.28). Figure 1.16D shows the time domain R(t) (carrier phase factor $e^{i\omega_{vg}t}$ is not shown on this plot). Its amplitude remains zero before the laser pulses

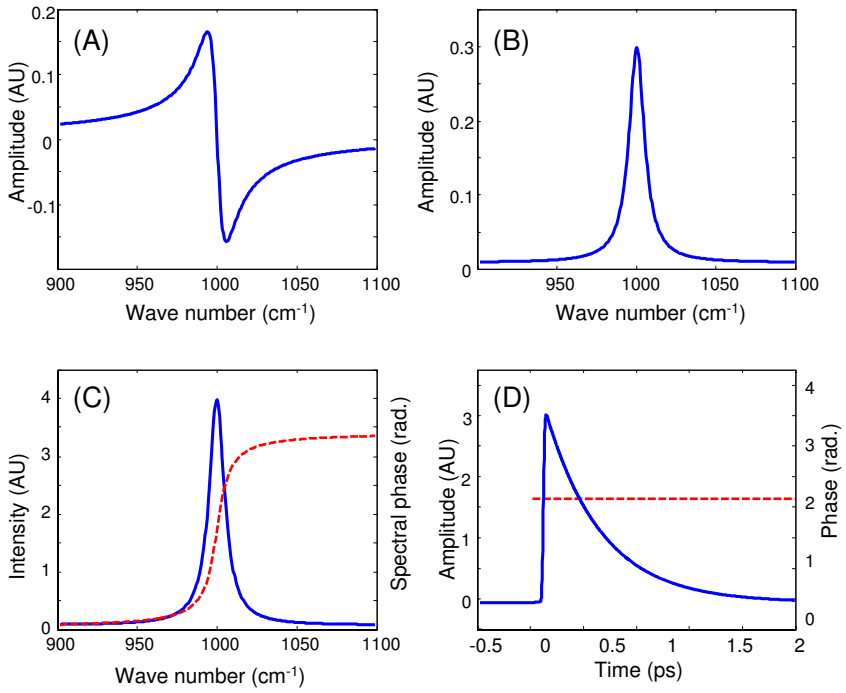


Figure 1.16: This plot is the numerical simulation of one resonant level at $1000cm^{-1}$ with $\Gamma$ of 6 $cm^{-1}$. Plot (A) is the real part of $R(\Omega)$. Plot (B) is the imaginary part of $R(\Omega)$, which has perfect Lorentzian profile. Plot (C) is $R(\Omega)$ (solid line) and spectral phase (dashed line) representation of R(t). Plot (D) is the time domain R(t) with intensity (solid line) and phase (dashed line). Carrier frequency is not shown here.

and free decay after excitation reflecting the decoherence coefficient $\gamma_{vg}$.

For femtosecond lasers, their broad bandwidth is capable of simultaneously exciting multiple vibrational states $v_j$. The individual vibrational coherence that broad laser pulses prepare works collectively in coherent anti-Stokes Raman scattering. The expression(1.28) for the vibrational coherence between the ground state and one vibrational excited state $v_j$ can be expanded to expression(1.31) that considers multiple vibrational states covered by the excitation bandwidth. It is a summation of resonant part of $\rho^{(2)}_{v_i g}$

$$R(\Omega) = A(\Omega) \sum_j \frac{C_j}{[(\omega_j - \Omega) - i\gamma_j]} \tag{1.31}$$

This expression shows that the vibrational coherence response function $R(\Omega)$ has the form of the spontaneous Raman spectra. Its time domain response $R(t)$ can be obtained through straightforward Fourier transform.

In chapter 4, an approach of complete characterization of vibrational coherence will be presented that can measure R($\Omega$) of laser induced coherent vibrations.

### Generation of Coherent Anti-Stokes Field

After the preparation of the vibrational coherence $\rho^{(2)}_{vg}$ through stimulated Raman, the probe pulse then interacts with the prepared vibrational system to generate signal radiation at the anti-Stokes frequency. From a spectroscopy perspective, the probe pulse measures the prepared system and generates CARS signal carrying the information about the vibrational coherence. In frequency resolved CARS experiments, the bandwidth of the probe pulse is very narrow, thus CARS spectra share the same profile as the vibrational coherence response function $R(\Omega)$. The only difference between them is the CARS spectrum measured is an array of real values, whereas $R(\Omega)$ is a complex quantity. Nevertheless, resonant positions and linewidths can be deduced from CARS spectra. However, when the probe pulse has a broad bandwidth, the resemblance between the CARS spectrum and the vibrational coherence is lost. Additional treatments of fitting are often needed

to extract resonance positions from the CARS spectrum. In this section, the generation of CARS signal from vibrational coherence will be discussed.

The interaction of the probe pulse and the vibrational coherence can also be treated perturbatively, through equation

$$\rho_{nm}^{(3)}(t) = e^{-(i\omega_{nm}+\gamma_{nm})t} \int_{\infty}^{t} \frac{-i}{\hbar}[\hat{V}, \rho^{(2)}]_{nm} e^{(i\omega_{nm}+\gamma_{nm})t'} dt' \tag{1.32}$$

Full expansion of $\rho_{nm}^{(3)}$ can be really complex. In a similar treatment of finding the main resonant term in deriving equation (1.27), equation (1.32) can be solved as

$$\rho_{ig}^{(3)}(t) = \frac{i}{\hbar} e^{-i(\omega_{ig}+\gamma_{ig})t} \int_{-\infty}^{t} \mu_{iv} \rho_{vg}^{(2)} E_{pr}(t') e^{i(\omega_{ig}+\gamma_{ig})t'} dt' \tag{1.33}$$

One can replace the probe pulse field with $E_{pr}(t') = \int_0^\infty E_{pr}(\omega'') e^{-i\omega'' t'} d\omega'' +$ *c.c.* and $\rho_{gv}^{(2)}$ with previous derived expression (1.27), and definition of $R(\Omega)$,

$$\rho_{ig}^{(3)}(t) = \frac{1}{\hbar} \int_0^\infty \int_0^\infty \frac{R(\Omega)(\omega'') e^{-i(\omega''+\Omega)t}}{\omega_{ig} - \Omega - \omega'' - i\gamma_{ig}} d\omega'' d\Omega \tag{1.34}$$

In terms of excitation frequency, the probe pulse generally is not chosen to be resonant with electronic intermediate state. The detuning $\Delta' = \omega_{ig} - \Omega - \omega''$ is much larger than the damping term $\gamma_{ig}$. The factor $1/(\omega_{ig} - \Omega - \omega'' - i\gamma_{ig})$ can be treated as non-resonant as well, replacing it by $1/\Delta'$. With this approximation, equation (1.34) can be re-arranged into an explicit form in the time domain

$$\rho_{ig}^{(3)}(t) = C'_R R(t) E_{pr}(t) \tag{1.35}$$

with $C'_R = 1/(\hbar\Delta')$ and $R(t) = \int_0^\infty R(\Omega) e^{-i\Omega t} d\Omega$. It is clear that in the time domain, $\rho_{ig}^{(3)}(t)$ is a product of vibrational coherence $R(t)$ and probe field $E_{pr}(t)$

CARS signal is generated through the third order polarization $\widetilde{P}^{(3)}$, which can be found by extending expression of laser induced dipole moment

expression (1.17) to the $3 \times 3$ density matrix of our three level systems, where the main contribution terms can be found as

$$< \mu >= \mu_{gi}\rho_{ig}^{(3)} + \mu_{ig}\rho_{gi}^{(3)} \tag{1.36}$$

These two terms oscillates at anti-Stokes frequency and corresponds to CARS process, there exist others contribution that are responsible for other FWM frequencies.

The generated field $E_{as}$ is linearly proportional to the third order polarization $\widetilde{P}^{(3)}$ and $\widetilde{P}^{(3)} = N < \mu >$, where N is the particle number. Therefore the detectable anti-Stokes signal has the form of

$$E_{as}(t) \propto C'_R R(t) E_{pr}(t) + c.c. \tag{1.37}$$

with $C_R = \mu_{gi} C'_R$.

By the convolution theorem, in the frequency domain, the anti-Stokes field is a straightforward convolution relation between $R(\Omega)$ and the probe field $E_{pr}(\omega)$ in the frequency domain.

$$E_{as}(\omega) \propto \int_0^\infty E_{pr}(\omega - \Omega) R(\Omega) d\Omega \tag{1.38}$$

It should be noted that both expressions (1.38) and (1.37) assume that the probe pulse does not link the vibrational state v with the intermediate state i. Otherwise, the exact form of expression (1.34) has to be used to describe the process. As a rule of thumb, if the frequency component of the probe pulse is resonant with the energy difference between vibrational states and electronic states $\omega_{iv}$, there will be additional peaks in the CARS spectrum.

The possibility of preparing multiple resonant levels with broad band pulses is considered through $R(\Omega)$ in equation (1.31).

As a summary, we find that the probing step of CARS is quite simple and straight forward. In the time domain, the CARS signal is the multiplication between the vibrational coherence R(t) and the probe pulse. In the frequency domain, it is a convolution between the vibrational coherence

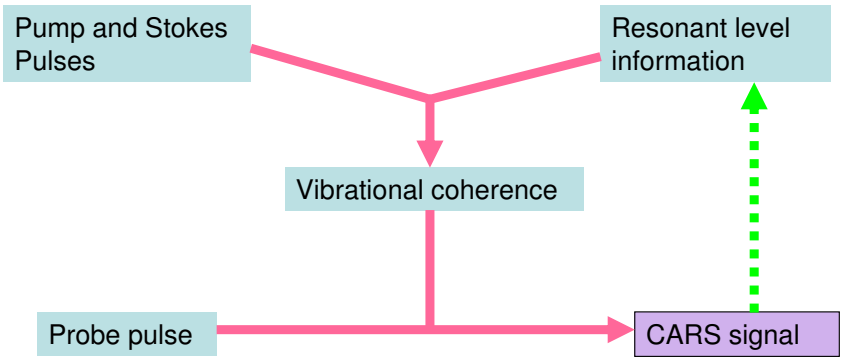


Figure 1.17: The pink arrows show the information flow along physical interactions, and the green dashed arrow shows the information flow of data processing. Pump and Stokes pulses prepare vibrational coherence based on the information of molecular resonant levels. Vibrational coherence contains the information of excitation and resonances. Then, vibrational coherence scatters probe pulse to give detectable CARS signal. The shape of CARS signal is determined by the vibrational coherence and the probe field. The task for spectroscopist is to analyze the CARS spectrum to deduce the vibration resonant structure of molecule in data analysis, where the information flow is from CARS spectrum back to vibrational resonances.

and the probe pulse. From the information point of view, the scattering of the probe pulse can be treated as a transfer of information from the not directly measurable vibrational coherence $R(\Omega)$ to the directly measurable CARS spectrum by frequency convolution. This is a rather general approach in spectroscopy. Considering the fact that the vibrational coherence $R(\Omega)$ contains the structural information of vibrational resonances, the tasks of CARS spectroscopy are first to prepare vibrational coherence $R(\Omega)$ and then to probe $R(\Omega)$ to reveal the profile of vibrational resonances. Figure 1.17 depict such relations.

### 1.3.3 Non-resonant Background

For a spectroscopic method, the measured signal should reflect and preferably only reflect the energy levels of the sample. Photons that are of same frequency as the signal but come from processes that do not involve energy levels of the sample are detrimental to the measurement. A case in point is the fluorescence background of spontaneous Raman spectroscopy that covers the Stokes region of the spectrum. CARS methods do not suffer from fluorescence background as spontaneous Raman does, because the anti-Stokes signal is blue-shifted from the frequency of the probe pulse which most fluorescence is red-shifted from the incident light field. But CARS does suffer from a non-resonant background, which comes from the non-resonant other four-wave-mixing pathways that gives the same frequency photons as the CARS signal that reflects vibrational levels. Figure 1.18 shows the optical pathway of some possible FWM processes that lead to a non-resonant response of anti-Stokes frequency under the interaction of broad band pump, Stokes and probe pulses.

The theoretical interpretation of non-resonant background can be found as the transient coherence that is prepared during laser pulses interaction with sample when all three pulses temporally overlap. More precisely, it is the summation of the non-resonant terms of $\rho_{ig}^{(3)}$ that does not evolve through the resonant state $|v>$. The source of non-resonant background can be separated into two categories: the first one comes from the transient coherence

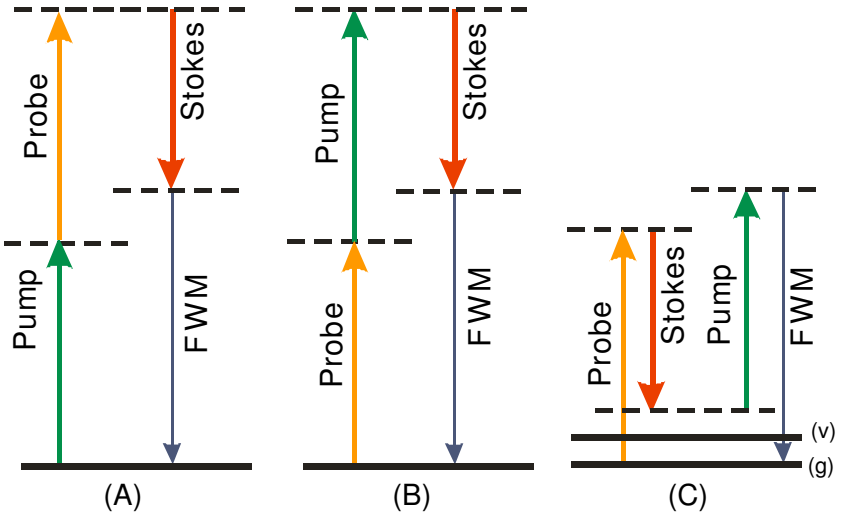


Figure 1.18: Path (A) and (B) are the degenerate pathways that emit photon at CARS signal frequency but do not prepare vibrational coherence. Path (C) is the condition that probe pulse serves as pump pulse and due to their potentially difference in frequency, it does not prepare vibrational coherence in the intended frequency range. All three scenarios can give signal at the anti-Stokes frequency. There are also other pathways that lead to degenerate frequency at anti-Stokes frequency.

of $\rho_{gv}^{(2)}$ and $\rho_{vg}^{(2)}$ from the non-resonant terms of equation (1.25). They are part of the vibrational coherence $\rho_{gv}^{(2)}$ or $\rho_{gv}^{(2)}$, but does not directly reflect the vibrational profile. The second type of non-resonant background comes from other four-wave mixing pathways that prepare transient $\rho^{(3)}$. There is one common behavior of these two sources of non-resonant responses, that is the requirement of all three pulses overlapping in time. Therefore it can be derived from the time field product of pulses.

$$C_{NR}(t) \propto E_p(t)E_s(t)E_{pr}(t) \tag{1.39}$$

where $C_{NR}(t)$ is the time domain response of multiple non-resonant pathways. Note that the time domain optical fields are real and contain both positive frequency and negative frequency $E_n(t) = \int_0^\infty E(\omega_n)e^{-i\omega_n t}d\omega + c.c.$. Thus $C_{NR}(t)$ has multiple terms at different carrier frequencies, such as $\omega_p + \omega_s + \omega_{pr}$ or $\omega_p + \omega_s - \omega_{pr}$. The term that has $\omega_p + \omega_s - \omega_{pr}$ is of the same frequency as CARS signal, and it leads to the non-resonant background of CARS.

Using the convolution theorem and equation (1.30), we can obtain the frequency domain equivalent of equation (1.39) that gives $\omega_p + \omega_s - \omega_{pr}$ as

$$E_{nR}(\omega) \propto \int A(\Omega)E_{pr}(\omega - \Omega)d\Omega \tag{1.40}$$

with $A(\Omega) = \int E_p(\omega)E_s^*(\omega - \Omega)d\omega$. With these expressions, the overall expression for CARS signal including non-resonant response can be found as follows:

$$R_(\Omega) = [\sum_v \frac{C_v}{(\omega_{gv} - \Omega) - i\gamma_{gv}} + C_{nR}]A(\Omega) \tag{1.41}$$

$$E_{CARS}(\omega) \propto \int R(\Omega)E_{pr}(\omega - \Omega)d\Omega \tag{1.42}$$

Where $R(\Omega)$ is the adjusted generalized vibrational coherence between vibration excited states and the ground state with non-resonant background (comparing to equation (1.31)). In the discussion of this thesis, $R(\Omega)$ is assumed to contain the non-resonant background. Hence, the final expressions (1.41) and (1.42) are obtained for CARS. They will serve as basic formulae

for the following chapters of this thesis.

The effect of non-resonant background leads to dispersive profiles in CARS spectra. Due to the coherent nature of CARS signal, the background subtraction of CARS spectra cannot be effectively done. In chapter 5, a new approach based on characterization of vibrational coherence $R(\Omega)$ is introduced to address this problem.

### 1.3.4 Sample Numerical Simulation

This section shows the numerical simulation of broad band CARS using expressions derived in previous section. The simulation starts from a numerical creation of ultrafast pulses as an array of values and coordinates. The original unshaped pulse in the frequency domain is assumed to be Gaussian and transform-limited. as the expression(1.43) shows:

$$E_i(\omega) = exp(-\frac{(\omega - \omega_{ci})^2}{2W^2}) \tag{1.43}$$

with $\omega_{ci}$ being the central frequency and $W$ being the width of the pulse spectrum.

In terms of data structure, $E_i(\omega)$ is stored as an array of complex value corresponding to a coordinate array $\omega$. In the simulation, pump Stokes and probe field arrays are created as $E_p(\omega)$, $E_s(\omega)$ and $E_{pr}(\omega)$ respectively. The simulation code for generating a pulse can be found in appendix A.1.

The effect of pulse shaping on the created pulse arrays is equivalent to applying spectral phase and amplitude masks at the corresponding coordinate. A pulse shaper array can be created according to expression(1.44), with the same coordinate $\omega$ as the pulse that it works on.

$$M(\omega) = M_0(\omega)e^{i\phi_M(\omega)} \tag{1.44}$$

It should reflect the discrete property of shaper pixels (described in section 1.4). The shaping in the simulation is achieved by multiplying shaping array $M(\omega)$ with pulse array $E_i(\omega)$. The frequency domain expression after the pulse shaper is:

$$E_p(\omega) = M(\omega) \cdot E_i(\omega) \tag{1.45}$$

After obtaining the frequency domain pulse array after the pulse shaper, Fourier transform is used to convert it to the time domain array $E_p(t) = fft(E_p(\omega))$ with corresponding coordinate in time domain t. The step size of the time domain coordinate can be calculated by $\Delta t = 1/(max(\omega) - min(\omega))$, where max($\omega$) and min($\omega$) are the maximal and minimal value of the frequency coordinate. To avoid fast phase oscillations, the carrier frequency is tracked separately. Figure 1.19 shows the numerical plot of ultrafast pulses with and without the sinusoidal spectral phase pulse shaping.

The time domain electric field array for pump, Stokes and probe pulses are generated as $E_p(t)$,$E_s(t)$ and $E_{pr}(t)$. The simulation code for pulse shaping can be found in appendix A.2.

The field product A(t) of pump and Stokes pulses in the time domain is given by expression(1.46)

$$A(t) = E_p(t) \cdot E_s^*(t) \tag{1.46}$$

A point worth noting is that the Stokes pulse serves as stimulated emission, so the complex conjugate value is used. Such multiplication is done element by element, and the result is an array.

The vibrational coherence R(t) is the convolution between the resonance Lorentzian and the field product A(t). The MATLAB[74] is very efficient performing discrete Fourier transform and slow on numerical convolutions. To reduce the computational time, the time domain convolution is done in the corresponding frequency domain as multiplication. A(t) is converted to the frequency domain using an inverse Fourier transform $A(\Omega) = \mathit{fft}^{-1}\{A(t)\}$. Its coordinate array is now $\Omega$, centered at the carrier frequency difference of pump and Stokes pulse. The resonances are represented using Lorentzian profile $L(\Omega)$ by expression(1.47):

$$L(\Omega) = [\sum_i \frac{C_i}{(\omega_i - \Omega) - i\gamma_i} + C_{nR}] \tag{1.47}$$

with $\omega_i$ and $\gamma_i$ being the resonant level and line width of respective vibrational resonant levels. The coordinate of this array is $\Omega$, the same as the field correlation array $P(\Omega)$, since the range of frequency difference between pump and Stokes pulses should cover those resonances.

The vibrational coherence $R(\Omega)$ is then given by $R(\Omega) = L(\Omega) \cdot P(\Omega)$. The Fourier transform of $R(\Omega)$ gives vibrational coherence in the time domain R(t), which is then multiplied by the time domain probe field $E_{pr}(t)$ to generate CARS signal in time $E_{CARS}(t)$. If the probe pulse has time delay with respect to pump and Stokes pulses, it can be introduced at this step by shifting its envelope within the coordinate array.

The CARS spectrum then can be obtained by inverse Fourier transform: $E_{CARS}(\omega') = fft^{-1}\{E_{CARS}(t)\}$. Figures 1.20 A and B show the plot of vibrational coherence in both the frequency and the time domains. We can see that the frequency domain $R(\Omega)$ reflects the resonance profile with clear peaks and line width. The simulation code for CARS generation can be found in appendix A.3.

The spectral profile of CARS is dependent on the vibrational coherence ,$R(t)$, and the amplitude and phase shape of the probe pulse, $E_{pr}(t)$. The profile of CARS under broad band excitation of phase shaping may not necessarily reflect the energy level profile. Figure 1.20 shows the comparison of CARS spectra between the probe pulse shaping of $\pi$ phase step (blue line figure 1.20C) and of sinusoidal phase shaping (red dashed line figure 1.20C). They have very different profiles comparing to the spectrum of the vibrational coherence $R(\Omega)$ that is shown in figure 1.20A. Moreover, the spikes in the spectrum do not necessarily correspond to the location of resonances. The CARS spectra with unshaped probe pulse are shown in figure 1.20D as reference. It gives poor spectral resolution due to the broad bandwidth and flat spectral phase of probe pulse.

### 1.3.5 Phase Matching Consideration

CARS signals are coherent. Being coherent has twofold meanings for CARS: firstly, CARS photons propagate along a certain fixed direction. Secondly,

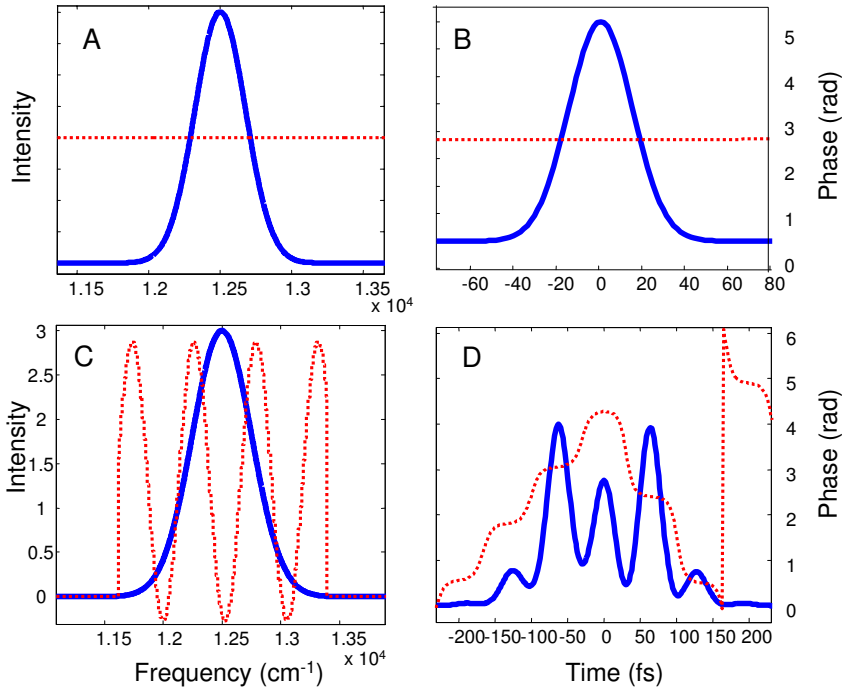


Figure 1.19: (A) is the frequency domain plot of intensity (blue line) of unshaped pulse with $400cm^{-1}$ bandwidth and spectral phase (dashed red line). (B) is the plot of this unshaped pulse in the time domain. (C) shows the plot of intensity (blue line) and shaped spectral phase (dashed line) by pulse shapers. (D) shows the time domain plot for a shaped pulse. The phase jump at 150fs is because for phase 0 equals to $2\pi$ . The carrier frequency is not shown in the time domain plot.

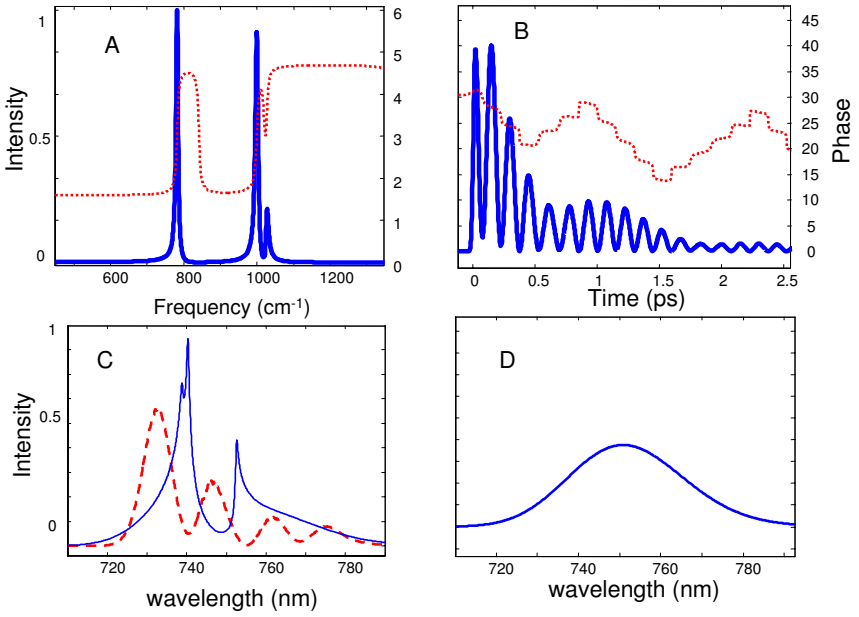


Figure 1.20: (A) is the frequency domain plot of the vibrational coherence of multiple levels prepared by transform limited pump and Stokes pulses with $400cm^{-1}$ bandwidth. Intensity is plotted as thick blue line and spectral phase as dashed red line. (B) is the plot of the vibrational coherence in the time domain. Intensity is plotted as blue line and spectral phase as red dashed line. (C) is the CARS spectra generated with $\pi$ phase step probe pulse (blue line) and with sinusoidal spectral phase shaping (red line). (D) shows the CARS spectrum using a transform-limited probe pulse.

CARS signals generated at different locations in the sample can constructively or destructively interfere with each other. These two facts bring forward questions on determining the signal direction and avoiding destructive interference of signal. The answer to the first question involves the propagation k vector in space, and the answer to second question leads to the phase matching condition[71] consideration.

The typical efficient coherent anti-Stokes Raman scattering process satisfies both the energy conservation expression(1.48) and momentum conservation expression(1.49).

$$\omega_{as} + \omega_s = \omega_p + \omega_{pr} \tag{1.48}$$

$$\overline{k}_{as} + \overline{k}_s = \overline{k}_p + \overline{k}_{pr} \tag{1.49}$$

where $\overline{k}_i$ is the k vector of light fields. The momentum conservation expression(1.49) can be used explicitly to estimate the propagation direction of the CARS signal direction.

However, the sample has its own dispersion property $k_i = n_i\omega_i/c$, satisfying expression(1.48) in a condensed phase leads to

$$|\frac{\overline{k}_{as}}{n_{as}}| + |\frac{\overline{k}_s}{n_s}| = |\frac{\overline{k}_p}{n_p}| + |\frac{\overline{k}_{pr}}{n_{pr}}| \tag{1.50}$$

Where $n_i$ is the respective refractive index at corresponding frequencies.

Both expressions must be satisfied in order to efficiently generate CARS signal. If all pulses are collinearly propagating through the sample, it requires the refractive indices satisfy $n_{as} = n_s = n_{pump} = n_{Stokes}$, which is often not true for condensed matter samples. If the refractive index is not constant across those frequencies, there will be a phase mismatch factor defined as

$$\Delta k = n_p\omega_p/c + n_{pr}\omega_{pr}/c - n_{as}\omega_{as}/c - n_s\omega_s/c \tag{1.51}$$

This enters the spatial terms of Maxwell's equation 1.14, and reflects the mismatch between the phase difference of the generated CARS field and the propagating CARS signal field. The effect of phase mismatch due to the dis-

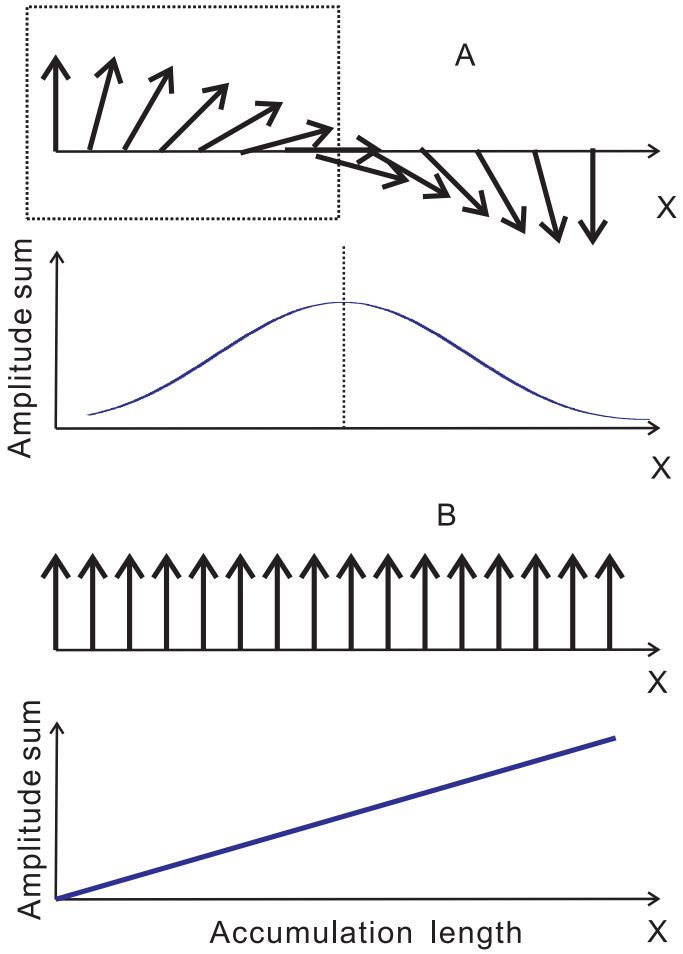


Figure 1.21: (A) shows situation of phase mismatch. The CARS signals generated as different location of sample along the propagation direction have different phase (represented by the direction of arrows) and they add coherently. Such phase mismatch leads to destructive interference at certain distance as the amplitude summation vs. accumulation length plot shows. Figure (B) shows the situation with phase mismatch. All CARS signals add constructively, leads to linear increase of signal amplitude vs. accumulation length.

persion property of sample in the collinear geometry is schematically shown in figure 1.21. We can see the phase mismatch $\Delta k$ leads to destructively interference along the signal accumulation direction.

Under collinear focusing geometry, one way to battle such destructive interference is to shorten the signal accumulation length by using tight focusing. Tight focusing by high numerical aperture lens reduces the CARS interaction length, therefore avoiding the destructive inference. The phase-matching length can be defined as $z_c = 2/\Delta k$ to help the selection of focusing lens. The confocal parameter of lens should be smaller than $z_c$. This tight focus collinear phase-matching scheme has been widely used in single pulse CARS spectroscopy and CARS microscopy.

In non-collinear geometry, expression (1.48) and expression (1.49) can be achieved without strict requirement on focusing condition. The BOXCARS [75] geometry is a popular phase matching geometry for CARS spectroscopy. It arranges the position of three excitation pulses in space such that it occupies three corners of a box (as figure 1.22B shows) before focusing by a lens or mirror. After focused on the sample, the signal should propagate along the remaining corner of the box. The k vectors of the pump, probe and Stokes pulses are not within the same plane spatially. Under such geometry, there exists a solution for $k_{as}$ such that $\Delta k = 0$ and signals generated in the interaction region constructively can interfere to give good signal strength. Figure 1.22 shows the spatial arrangement of the beams.

Either the tight focusing collinear geometry or BOXCARS geometry can generate good strength CARS signals. Due to the advantage of easier signal separation, BOXCARS geometry was used for proof-of-principle experiments in chapter 2 to chapter 5. The tight focus collinear geometry was used for the single pulse Noise-autocorrelation CARS experiment in chapter 2 and in some microscopy experiments that are not included in this thesis.

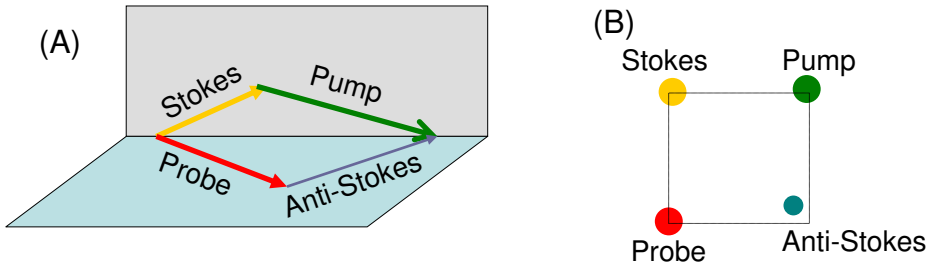


Figure 1.22: (A) schematically shows the direction and amplitude of $\overline{k}$ vector of pump, Stokes and probe photons in BOXCARS geometry and corresponding $\overline{k}$ vector of anti-Stokes photon. (B) shows the spatial position of pulses after interaction on samples. The pump, Stokes, probe pulse and generated anti-Stokes pulse are approximately at four corners of a rectangle.

## 1.4 Experimental Setup and Pulse shaper

### 1.4.1 Overview

This thesis focuses on developing CARS methods with broadband coherent pulses. The experimental setup of CARS with broad band lasers is different from that of traditional CARS methods with narrow band lasers. There are two major differences. Firstly, the excitation and probing pulses are broadband pulses which are from solid state Ti:Sapphire lasers and optical parametric amplifiers (OPA) rather than Nd:YAG and dye lasers. The second difference is the extensive usage of the pulse shaping technique for the phase and amplitude manipulation of broad band coherent pulses. One typical CARS setup is shown in figure 1.23, which consists of a Ti:Sapphire amplifier, an optical parametric amplifier(OPA) and a home-built pulse shaper.

When building an experimental setup for femtosecond CARS with pulse shaping capability, there are four major considerations. Firstly, the choice of light sources, which includes the fundamental laser radiation generation and frequency conversions. Secondly, implementation of pulse shaping on the excitation pulses, which involves the building of pulse shaper devices and calibration of the spatial light modulator (SLM). Thirdly, signal generation,

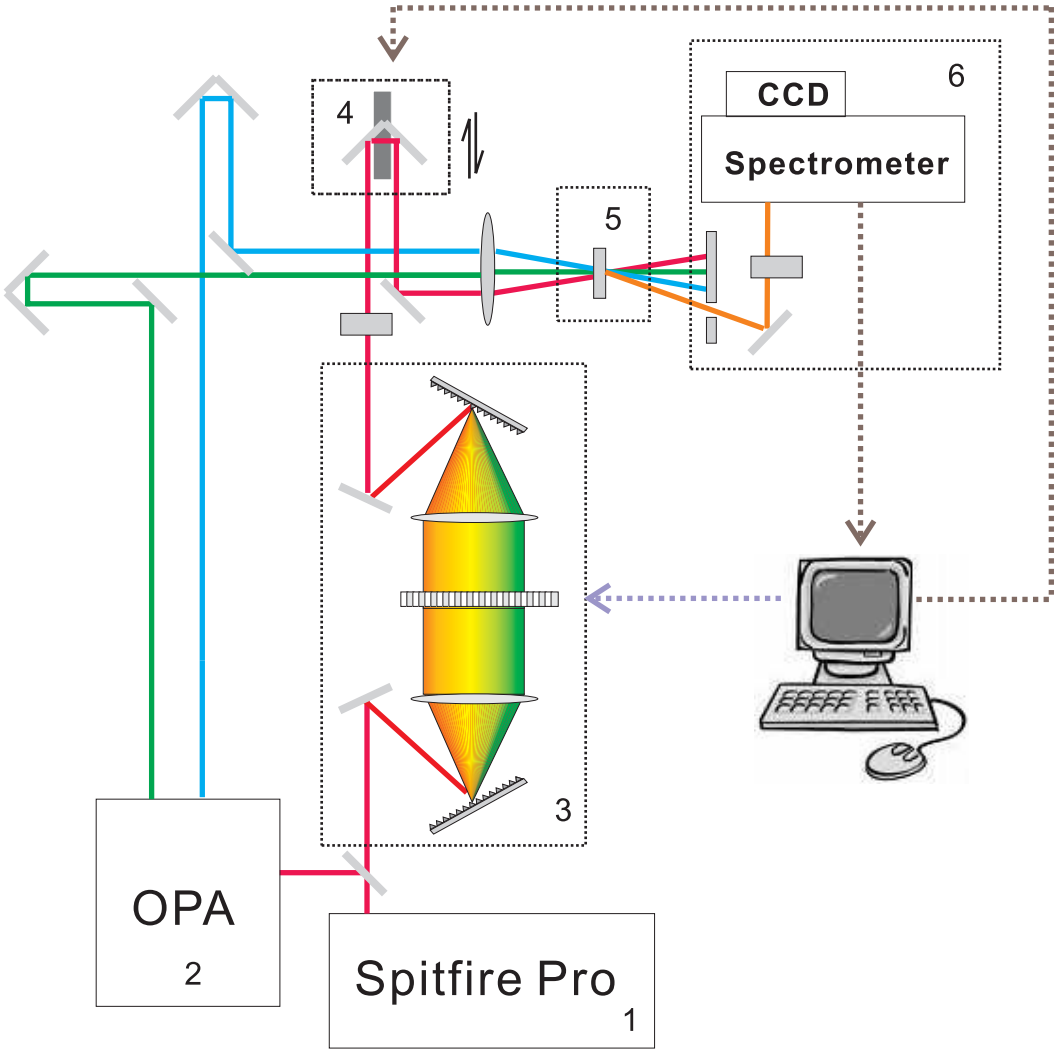


Figure 1.23: This figure shows the setup of a typical BOXCARS geometry CARS experiment with a pulse shaper. The fundamental radiation is generated by a regenerative amplifier (block 1). The optical parametric amplifier provides the new frequencies for CARS (block 2). A pulse shaper modifies the amplitude and phase of laser radiation (block 3). The pulses are synchronized by translation stages (block 4) and are focused on the sample in a noncollinear geometry (block 5). Necessary signal filtering is implemented to improve the quality of the signal which is detected by a spectrometer with CCD (block 6) and the Labview program on a computer records the signal and controls elements of the experiment.

which involves the optical setup and alignment, pulse spatial overlap on the sample and time synchronization. This part varies a lot depending on the actual project. Fourthly, the signal filtering and detection, which can involve spatial filtering, utilization of polarization and dichroic filters.

For the selection of fundamental radiation, the properties of the laser systems need to be considered. These are the central frequency of the output, the duration of pulse, the per pulse energy and the repetition rate. The solid state Ti:Sapphire laser can provide laser radiation from 700nm to 900nm. The pulse duration of Ti:Sapphire lasers can be fewer than two optical cycles (<5.3fs) [76] to picosecond range. There are two kinds of Ti:Sapphire lasers available, the Ti:sapphire oscillator and Ti:Sapphire amplifier. An oscillator system provides high repetition rate ( 80MHz), low pulse energy ( 10 nJ) laser radiation, while the amplifier system provides low repetition rate ( 1kHz), high pulse energy (1 mJ per pulse) laser radiation. Since CARS is a third order nonlinear process, higher peak power gives higher per pulse signal. Even considering the low repetition rate, an amplifier system can generate more signal than an oscillator system for the same amount of total pulse energy.

To provide a broad band tunable radiation, an optical parametric amplifier (OPA) is used. The major advantage of OPA is its easy frequency tunability. It can provide a wide range tunable output (from 300to 2000nm) at good efficiency (about 25% of total input). In CARS, the pulses from the amplifier and OPA are used as pump, Stokes and probe pulses.

The pulse shaping technique can tailor the amplitude and phase profile of the ultrafast pulses to allow sophisticated control over multi-photon processes. When building the pulse shaper, the specifications of optical elements should be considered. The choices of collimating mirrors and gratings are affected by the bandwidth of input laser field and the window width of the spatial light modulator. The spatial light modulator is controlled by the voltage at each pixel. Since the purpose of the pulse shaper is to introduce phase shifts to the light field at different frequencies, it requires calibration to convert the voltage value of each pixel of the SLM into an optical phase shift. Details on pulse shapers will be discussed in the pulse shaping section.

There are two types of CARS experimental setup: BOXCARS geometry setup and single pulse collinear geometry setup. Figure 1.23 shows the scheme of a typical BOXCARS geometry experiment with a pulse shaper. The optical scheme of a common single pulse CARS experiment is shown in figure 1.24. When comparing these two setups, the CARS signal from the BOXCARS geometry is automatically separated from the residual excitation beams, whereas in the collinear geometry the excitation beams have to be filtered out from the signal. From the experiment technique consideration, the BOXCARS geometry setup needs beam alignment and pulse synchronization and the single pulse CARS with collinear geometry does not need pulse synchronization at all and is easier to build. The choice between the BOXCARS geometry and single pulse collinear geometry is based on the experiment needs.

The CARS signal is detected by a spectrometer with a CCD detector. It is straightforward to set up the detection optics. The important part is to improve the signal to noise ratio by implementing spatial filtering, polarization filtering as well as usage of dichroic filters.

### 1.4.2 Ti:Sapphire Generative Amplifier and OPA

#### Regenerative Amplifier

A regenerative amplifier laser system has the ability to provide high energy (>1mJ), short duration (35 to 150fs) laser pulses. The Spitfire regenerative Ti:Sapphire amplifier system (Spectra Physics) is a commercially available regenerative amplifier of 100fs pulse output at 800nm with up to 2w output power (at 1kHz repetition rate). It was used in the first two years of research. The Spectra Physics Spitfire Pro is the upgraded version of Spitfire with shorter output duration (40fs) and higher output power of 3w (at 1kHz repetition rate). It was used in the later half of the research in this thesis. Both systems share a similar design and use the chirped pulse amplification technology [77].

Laser radiation starts as lower energy “seed” pulses from an oscillator at a high repetition rate (80MHz). The peak power of such pulse is below

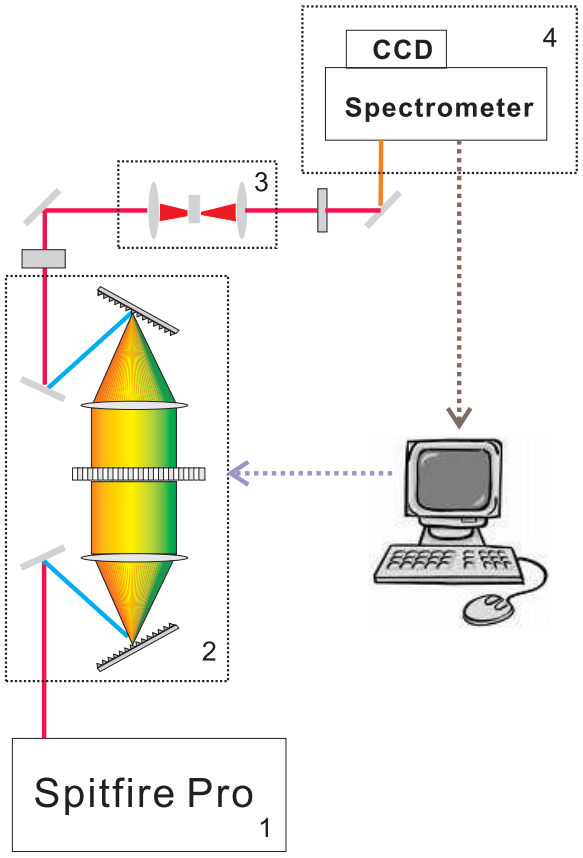


Figure 1.24: This figure shows the optical scheme of a collinear geometry single pulse CARS experiment. It has four key parts, the broadband coherent light source (1), a pulse shaper (2), tight focusing and collimating microscope objectives (3) and spectrometer with proper filters (4).

the damage threshold of the Ti:Sapphire crystal and the mirrors. But the amplified pulse has high peak power (about 5 orders of magnitude higher peak intensity than the seed pulse) and is capable of damaging the optics. The technique of chirped pulse amplification is used to tackle this problem. It first utilizes a grating pair to introduce chirp into the seed pulse. Then the chirped seed pulse undergoes amplification by passing through a Ti:Sapphire crystal multiple times. After amplification, the amplified chirped pulse is re-compressed into a short duration high power pulse by a grating pair compressor. By doing so, the high peak power laser field is only present at the output, therefore avoiding damage to the optics during the amplification. The regenerative amplifier utilizes a laser cavity for multiple pass amplification. The output beam has good beam quality with a diameter of 8mm and pulse energy of 2mJ/3mJ (Spitfire/Spitfire Pro).

The shortest possible output pulse duration of the regenerative amplifier is determined by the bandwidth of the output spectrum. The Spitfire Pro can give around 40fs output duration with 400cm$^{-1}$ FWHM bandwidth. To achieve the shortest possible pulse duration, the grating pair compressor has to be adjusted to compensate the chirp that is introduced by the stretcher grating pair. The distance between the compressor gratings determines the amount of the compensation chirp. In Spitfire Pro, a motorized translation stage was mounted inside the compressor to adjust the chirp compensation. An auto-correlator (Pulsescout, Spectra Physics) was used to monitor the pulse duration of output pulse. If an auto-correlator is not available, a nonlinear type-I BBO crystal can be used to qualitatively monitor the duration of output pulses by adjusting the compressor to find highest second harmonic generation signal from the crystal. Another effective way of grating distance adjustment is using a short focus lens to focus the output beam into the air. The focused femtosecond laser generates plasma when the pulse has a short duration. The sound of the plasma from Spitfire Pro is audible at the frequency of 1k Hz. Therefore, the optimal position of compressor gratings can be found with the maximal sound from plasma.

Operational tips on simple maintenance are included in the user manual of Spitfire Pro. Simply put, the mirrors of the regenerative cavity have to

be kept clean. The seed beam should be efficiently overlapping with cavity optical path of the amplifier and diode pump beams at the amplification crystal.

### Optical Parametric Amplifier

A typical CARS experiment in the BOXCARS geometry requires multiple frequencies to serve as separate pump, Stokes and probe pulses. Even though a single pulse CARS experiment uses only one broad band laser, it cannot be applied to high wave number spectroscopy ( $1000\text{cm}^{-1}$) because of the bandwidth limitation (a 40fs duration laser pulses has FWHM bandwidth of $400\text{cm}^{-1}$). For applications on high wave number spectroscopy, e.g. the C-H stretch at around $3000\text{cm}^{-1}$, a separate tunable frequency source must be included into the CARS experimental setup. The optical parametric amplifier (OPA) is suitable for this task. It can generate radiation from 300nm to 2000nm. The OPA used in our experiment (TOPAS, Light Conversion) gives a total conversion efficiency of 20% to 30%, when it is pumped by the regenerative amplifier (Spitfire Pro) at 1 mJ input. The bandwidth of the OPA output is roughly the same as the bandwidth of the input pump beam ($400\text{cm}^{-1}$).

The OPA working mechanism is based on the nonlinear optical process of different frequency generation (DFG) as shown in figure 1.25A. A high intensity pump laser (800nm) is converted into two infrared lasers (signal $\omega_s$ and idler $\omega_i$) with tunable frequencies. The frequency tunability is done through angle tuning of the nonlinear crystal. The central frequencies of the output beams satisfy the relation of $\omega_f = \omega_s + \omega_i$ with $\omega_f$ being the pump frequency that comes from Spitfire Pro. The polarization of the signal beam is the same as the fundamental pump beam (as both are the ordinary polarization to the optical axis of the nonlinear crystal), and the idler polarization is perpendicular to the pump and signal beam (as it is the extraordinary polarization to the axis of the nonlinear crystal).

Figure 1.25B shows the schematic of an OPA device. The frequency conversion starts from the generation of continuum white light. A small

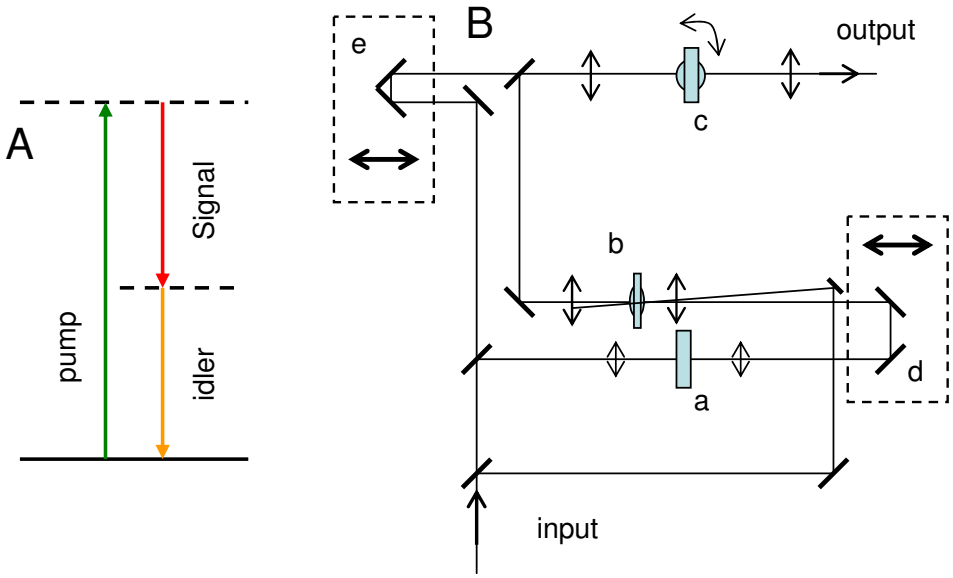


Figure 1.25: (A) shows the difference frequency generation that is used in an OPA. (B) shows the schematics of one OPA. The pump beam generates white light at sapphire plate (a), and it is amplified at an angle-tuned thin BBO nonlinear crystal (b), and finally high intensity amplification is done at a LBO nonlinear crystal (c). The delay lines (d) and (e) are used for the time delay adjustment.

fraction of fundamental radiation (4% of fundamental 800nm from Spitfire Pro) is focused on a sapphire plate to generate uniform and stable white light; then the white light interacts with a fraction of the pump beam intensity (10%) on an angle-tuned BBO ($\beta$-barium borate) nonlinear crystal with good spatial and temporal overlap. The frequency selection is done by tuning the angle of the thin BBO crystal. After the amplification, the seed beam is collimated and synchronized with remaining high intensity fundamental radiation, and the collimated beams propagate collinearly through a second BBO or a LBO (lithium triborate) nonlinear crystal to give the signal and idler infrared radiations.

In CARS experiments, one OPA can be used to provide two frequencies for pump and Stokes pulses. The idler radiation from the OPA is frequency doubled by an additional BBO crystal to give the pump pulse in CARS. Since the polarization of the signal and the idler beams are perpendicular to each other, a BBO crystal is used directly at the output of OPA without using a beam separator. The signal radiation is used as the Stokes pulse in CARS. If the interesting vibrational resonance is at frequency $\Omega$, the angle of BBO crystals in OPA should be tuned to provide the signal beam central frequency $\omega_s$ at $(2\omega_f - \Omega)/3$, and the accompanied idler beam $\omega_i$ at $(\omega_f + \Omega)/3$. In this condition, the frequency difference between the second harmonic of idler and the signal pulses equals to $\Omega$.

### 1.4.3 Pulse Shaping Techniques

#### Principle

The schematic of a common 4-*f*[20] geometry pulse shaper is shown in figure 1.26. Each optical element of the pulse shaper corresponds to a mathematical operation starting with a pulse in time domain $E(t)$. The grating and collimating lens (as figure 1.26(A) shows), perform Fourier transform on the time domain pulse $E(t)$ to the frequency domain $E(\omega)$ along the Fourier plane. This operation breaks the short duration pulse into long time duration frequency components along the Fourier plane and it is equivalent to $\mathit{fft}[E(t)](\omega)$. A spatial Light Modulator(SLM) is placed in the Fourier plane.

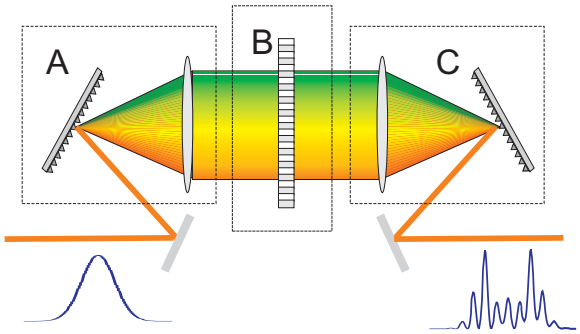


Figure 1.26: This figure schematically shows the configuration of pulse shaper: The optical elements inside box(A) consist of a grating and a collimating lens, their function is to disperse broadband light according to their frequency component. (B) is the liquid crystal based spatial light modulator. It is an array of many independently controllable pixels. The SLM is placed on the Fourier plane of collimating lens, its function is to adjust the amplitude and phase of individual frequency components. Box (C) is the "mirror" setup of (A), its function is to combine beams of different frequency components into a single pulse.

The SLM (figure 1.26(B)) modifies the amplitude and phase of each frequency component independently through the voltages applied on each SLM pixel. This operation mathematically corresponds to $\mathit{fft}[E(t)](\omega)\cdot A(\omega)e^{i\phi(\omega)}$. After amplitude or spectral phase modification, the collimating element and grating of figure 1.26(C) reconstruct the pulse back to a short duration, performing an inverse Fourier transform from the frequency domain back to the time domain. After this operation, the final expression for pulse shaping can be found as:

$$E(t') = \mathit{ifft}[\mathit{fft}[E(t)](\omega) \cdot A(\omega)e^{i\phi(\omega)}](t) \tag{1.52}$$

with $E(t')$ being the field of the output shaped pulse in the time domain. Its profile is now a function of the amplitude mask, $A(\omega)$, and the phase mask, $\phi(\omega)$, which are adjustable through applied voltages on SLM pixels.

A point worth noting is the pixelization of the light field. The SLM

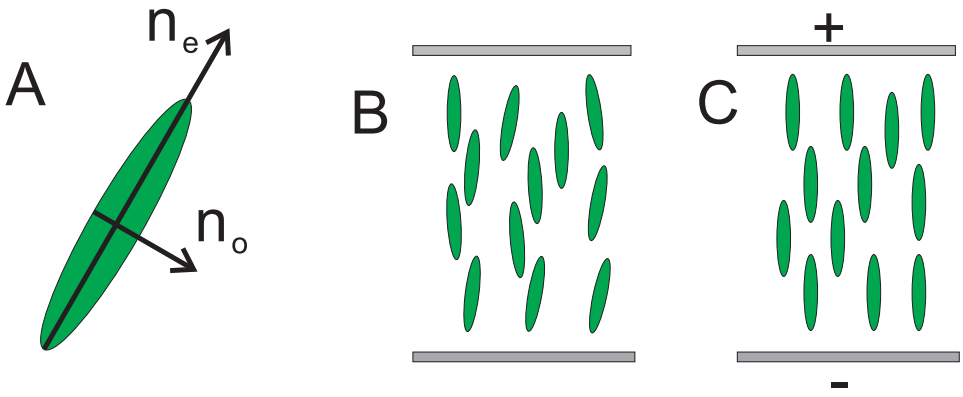


Figure 1.27: Liquid crystal molecules are represented as elliptical rods. (A) shows the anisotropic optical property of nematic liquid crystals. It has two refractive indices along and perpendicular to the averaged molecular orientation. (B) shows the equilibrium orientation of liquid crystal molecules. Figure C shows the liquid crystal orientations under external static electric field with voltages applied.

affects the amplitude and spectral phase of the light in a discrete fashion. The amplitude and phase is independently adjustable for each SLM pixel. But within one pixel, the light experiences the same amplitude and phase. Mathematically, the amplitude mask $A(\omega)$ and $\phi(\omega)$ functions are stepwise. The CRI SLM-128 and CRI SLM-640 are used. In our experiments, they both have a pixel width of 100$\mu$m.

**Properties of Liquid Crystal**

The core elemental of the SLM is a voltage-controlled nematic liquid crystal (NLC) array. Nematic is a phase of the liquid crystal (LC), where LC molecules have directional order but do not have long range periodicity. The NLC molecule has a rod-like shape and is macroscopically anisotropic. For an optical wave, NLC media exhibit two refractive indices $n_o$ and $n_e$. This property allows the polarization rotation of light when it passing through NLC media. In the equilibrium state, the orientation of NLC shows a statistically directional order. A better orientation alignment can be achieved

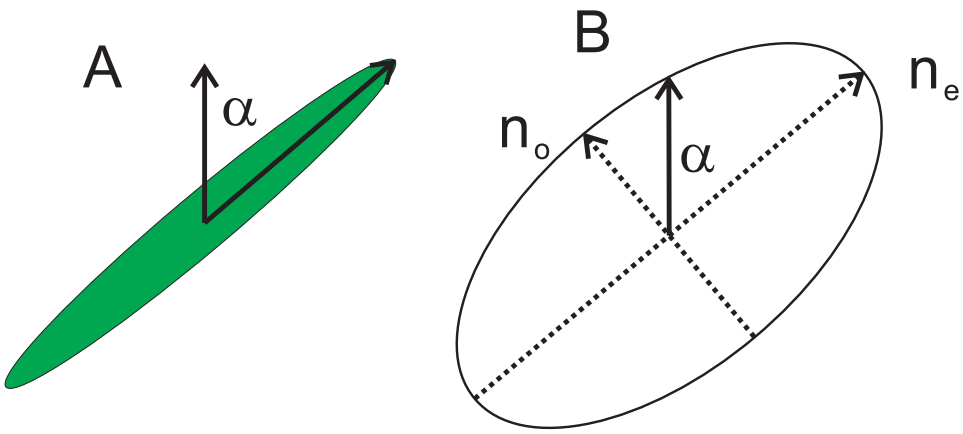


Figure 1.28: When the light passes through liquid crystal molecules, it sees the effective refractive index as a linear combination of $n_o$ and $n_e$. It is dependent on the molecular orientation. $\alpha$ is the angle between the light propagation direction and molecular alignment direction. (A) shows the light propagation direction and liquid crystal molecular alignment. (B) shows the effective refractive index that the light sees on the refractive index sphere.

when molecules are under an external electric field. Figure 1.27 shows this property of NLC.

The phase change introduced by the SLM is connected with the optical path and refractive index. It is given by $\delta\phi = 2\pi\frac{\delta n \cdot l}{\lambda}$ where l being the length of the NLC media, $\lambda$ being the wavelength of light and $\delta n$ being the change of refractive index, which is a function of the average orientation of liquid crystal molecules (figure 1.28). Since the orientation of NLC molecules can be affected by external static electric fields and the refractive index is dependent on the orientation of NLC molecule, the phase is therefore controlled by the external voltage applied on the liquid crystal array.

Since the NLC is also bifringent, when it changes the spectral phase of the light, it also rotates the polarization. This polarization rotation can be used for amplitude shaping with polarizers. However, the spectral phase change and the polarization change are coupled for a single SLM mask. The spectral phase and polarization cannot be shaped separately with only one SLM mask. This disadvantage can be compensated by using a second liquid crystal mask. Two masks introduce the same amount of phase shift but rotate the polarization in the opposite direction. The net effect is then a shift in spectral phase without polarization rotation.

### Calculation on Specifications of Optics

Before building a pulse shaper, the parameters of the optical elements must be considered. Since the spatial light modulator is the central part of a pulse shaper, the choice of gratings and focusing lens/mirrors should fit the specification of the SLM and the input beam size. For example, the CRI SLM-640 (SLM) has a pixel size of $100\mu m$, and the input beam has a diameter of 5mm (an iris is set in front of the pulse shaper entrance to down size the beam). The focus spot can be estimated by equation:

$$d = 1.22f\lambda/D \tag{1.53}$$

with $D$ being the input beam diameter, $\lambda$ being the wavelength of light and $f$ being the focal length. If the central wavelength is 800nm and we assume

the focus spot is equal to the pixel width of the SLM, the calculated focus length $f$ is 50cm. This means 50cm focus length mirrors or lenses should be used as the collimating element.

The next step is the selection of gratings. The main consideration is that the width of the dispersed broad band pulse should fit the width of SLM. Therefore, the ideal dispersing ability of the grating depends on the SLM window width and the laser bandwidth. The width of the CRI SLM-640 SLM window is 5 cm. The maximal allowed angular dispersion width can be calculated as :

$$\theta = w/f \tag{1.54}$$

with $w$ being the width of SLM. The calculated maximal allowed angular dispersion is 0.1 radians. The laser bandwidth out of the Spitfire Pro is 40nm (FWHM) with central wavelength of 800nm, the grating should disperse the spectrum such that the angular spread equals the maximal allowed angular dispersion of 0.1 radians. The solution can be found using the grating equation:

$$\sin\theta_d = n\lambda/d' - \sin\theta_i \tag{1.55}$$

with $\theta_i$,$\theta_d$ being the incident and diffracted angle respectively, n being the order of grating and $d'$ being the grating constant. The calculable form is:

$$\theta = \arcsin(\frac{n(\lambda - B/2)}{d'} - \sin\theta_i) - \arcsin(\frac{n(\lambda + B/2)}{d'} - \sin\theta_i) \tag{1.56}$$

with B being the total wavelength bandwidth of the pulse shaper. It should be bigger than the bandwidth of the laser pulses so as to let the wings of spectrum go through the SLM window. A factor of three is good: with 40nm FWHM laser bandwidth, B will have the value of 120nm. If one assumes that the incident angle of light on the grating is $\pi/6$ radian and the grating is working in first order (n=1), equation (1.56) leads to the selection of 800 grooves per mm grating. Because 800 grooves per mm grating blazed for 800nm was not available at the time when the pulse shaper was built, gratings of either 600 grooves per mm or 1200 grooves per mm were used in our experiments.

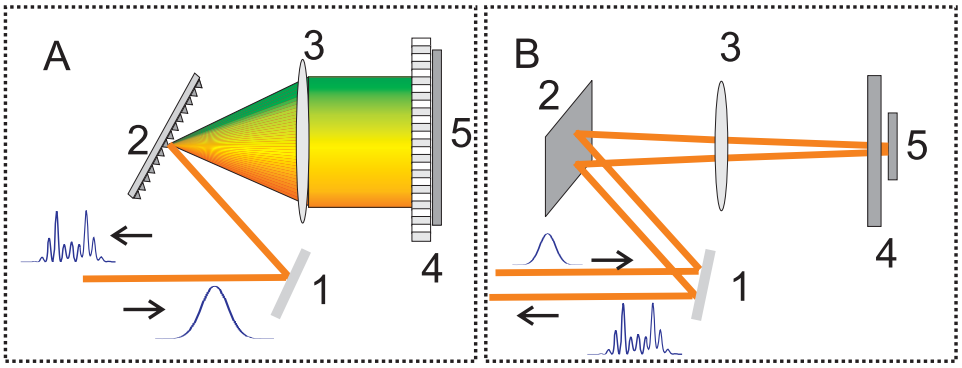


Figure 1.29: (A) shows the top view of folded pulse shaper design. (B) shows the side view of folded pulse shaper design. This design requires only one grating and one lens compared to original design shown in figure 1.26. It reduces the alignment effort on angle and pitch adjustment. 1 is the input/output mirror, 2 is the grating, 3 is the collimating mirror, 4 is the SLM and 5 is the adjustable mirror that mounted behind the SLM.

### Assembly of The Pulse Shaper

The assembly and adjustment of optical elements of the pulse shaper should fulfill the corresponding mathematical functions as expression (1.52) shows. This provides guidelines for pulse shaper adjustment. The grating pairs and collimating lenses should perform the forward and inverse Fourier transform by placing the gratings at the focal distance of the lenses. The SLM should also be capable of changing both amplitude and phase for each frequency component.

First of all, the SLM has to be put in the Fourier plane. The forward Fourier transform introduced by the left side grating and collimating lens (figure 1.26(A)) should be canceled by the inverse Fourier transform introduced by the right side (figure 1.26(C)) optical elements. The distance between lens and gratings should be equal to the focal distance of lens, and the gratings of both sides should be at the same angle. To achieve this, careful alignment of gratings and lenses is required. With the setup shown in figure 1.26, there are two gratings and two lenses in the setup. The po-

sition and pitch of these four optical elements have to be adjusted and pair compensated, which is not easy.

As a result, an alternative design was created to simplify the pulse shaper setup by using a reflective geometry. If a mirror is used after the SLM, light can be reflected back to the same collimating lens and grating. The back reflection guarantees the light goes through the same grating at the same angle, the same lens and the same distance. In this geometry, the only adjustable parameter is on the distance between lens and grating and the angle of the grating. This reduces the alignment of previous four optical elements down to alignment of two. The new design is shown in figure 1.29. A pulse shaper of 128 pixels SLM (CRI SLM-128) was built according to this design.

The folded design occupies a smaller space on optical table than the original design (figure 1.26), because it is only $2f$ in length (twice the focus length). The length of the pulse shaper can be further reduced to $1f$ if a focusing mirror is used instead of a lens. Figure 1.30 shows the setup of a folded pulse shaper based on mirror. A pulse shaper with a 640 pixel SLM and 50cm focus distance was built according to this folded design, and it occupied 60cm by 50cm space of optical table (for photograph of this shaper, see figure 1.3A).

The folded pulse shaper design (figure 1.30) is equivalent to the original $4f$ design(figure 1.26). The advantages of this design are the compactness and elimination of transmissive lenses. As figure 1.30 shows, it occupies only one focal length in terms of the total length of setup. Since a big SLM window width requires long focal length mirror given the same grating dispersion, the compact design avoids occupying excessive optical table space. For example, the CRI SLM-640 has a window size of 5 cm, and the calculated $f$ is equal to 50cm. If the typical $4f$ geometry is used, it will occupy a space of 2 meters length, which means nearly one third to one half of the optical table. Moreover, transmissive lenses introduce dispersion into broad band pulses that has to be corrected afterward, whereas the design with reflective mirror avoids dispersion. The optical alignment procedure of the pulse shaper can be found in appendix B.1.

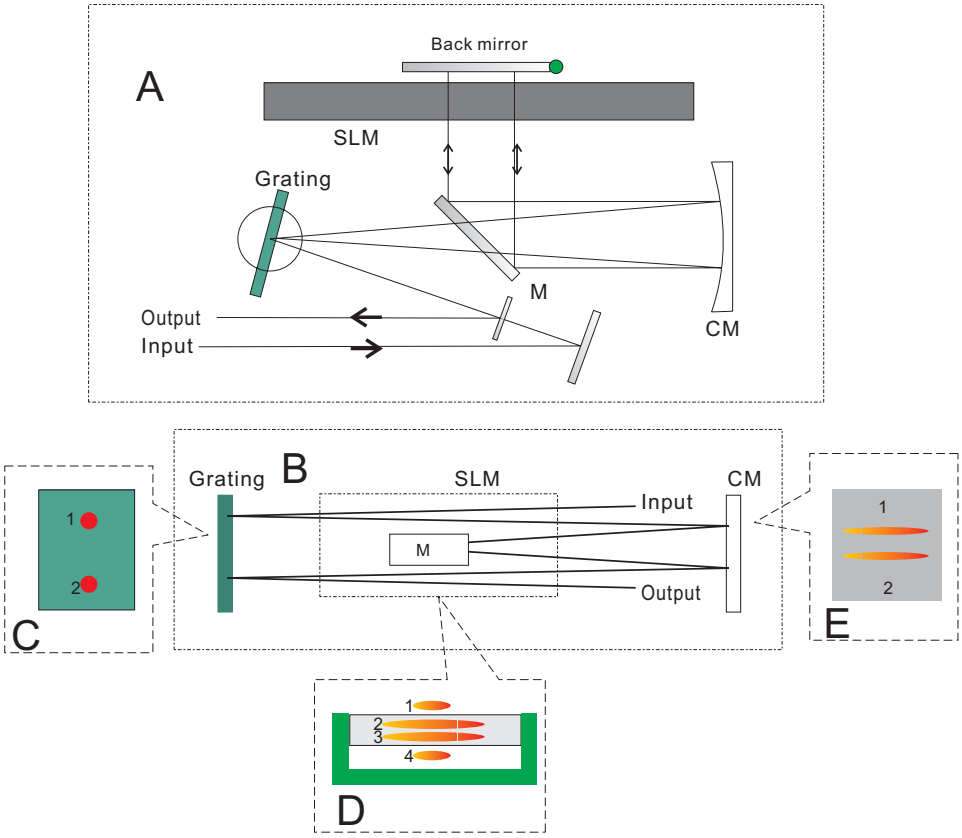


Figure 1.30: The above figures show the setup of a folded pulse shaper with a focusing mirror. The grating in this setup is either 600 or 1200groves/mm, and the cylindrical mirror $f = 50cm$, and CRI SLM-640 has window size about 5cm. (A) shows the top view of the pulse shaper. (B) shows the side view of this pulse shaper. Insets (C) to (E) shows the light profile on corresponding optical elements. The alignment of the pulse shaper can be found in appendix B. A photograph of the pulse shaper of this schematic is shown in figure 1.3A.

### Spatial Light Modulator Calibrations

The ideal input parameters of a pulse shaper are the amplitude and phase. However, the SLM works on voltage. To make the pulse shaper functional, the calibration of voltage vs. phase is necessary. This is done by measuring the transmittance of polarized broadband light. The detailed procedure is included in appendix B.2 After measurement on the transmittance vs. voltage, the phase can be calculated from transmission through equation (1.57)

$$T = \cos^2(\phi/2) \tag{1.57}$$

with T being the transmission and $\phi$ being the phase. This equation can be recast into:

$$\phi = 2\arccos\sqrt{T} + k \cdot 2\pi \tag{1.58}$$

with k being an integer number to reflect the multi value property of phase. The transmission vs. voltage curve then can be converted into a continuous phase vs. voltage curve. A polynomial fitting is used to obtain an analytical form of such a relation, represented as $\phi(V)$, and an inverse function for the voltage vs. phase $V(\phi)$ can be found as well. For a dual-mask SLM, such as CRI SLM-640, calibrations have to be done for both masks.

When the voltage vs. phase calibrations $V(\phi)$ for both masks of the CRI SLM-640 are ready, the next step is to convert the amplitude and phase values into voltage value. For a given pair of amplitude $A$ ($A$ is the square root of the intensity I) and phase shaping $\phi$, the voltage on two masks $V_1$and $V_2$ can be calculated using the following expressions:

$$V_1 = V(\arccos(A) - \phi) \tag{1.59}$$

$$V_2 = V(\arccos(A) + \phi) \tag{1.60}$$

Expression (1.59) and (1.60) can be used to construct the voltage array mask for the masks of the SLM. As the experimental implementation, a Labview script was programmed to automatically convert the amplitude and phase into voltages for both masks.

### 1.4.4 Pulse Characterization

Pulse characterization constituted an important part of the experiments in this thesis. Since the result of the broad band CARS experiment depends on the phase as well as the amplitude profile of the broad band pulse, a careful characterization of pulse profiles is needed for the success of the experiment.

There were two pulse characterization methods used in this thesis work: Frequency Resolved Optical Gating[78] (FROG) and Multi-photon intrapulse interference phase scan (MIIPS) [79]. The FROG technique was initially invented by Trebino and coworkers[78, 80] to recover the phase information of an ultrafast pulse. The idea of FROG is to use an iterative phase-intensity retrieving algorithm on a two-dimensional time-frequency second harmonic spectrogram to recover the phase and intensity information of the unknown pulse. Figure 1.31 shows a typical FROG device setup. The detailed discussion of the FROG technique can be found on literature [78, 80]. For the experiments of this thesis, the phase information of an unknown pulse was obtained through the FROG technique.

The MIIPS technique achieves the pulse characterization through phase compensation. It was invented by Dantus and coworkers [79]. The unknown pulse is coupled into a pulse shaper and then frequency doubled in a nonlinear crystal. The second harmonic signal is measured by a spectrometer. A sinusoidal phase mask is applied to the unknown pulse through the pulse shaper and scanned across the spectrum of the pulse. The profile of the corresponding SHG spectrum is used to deduce the second derivative of the spectral phase of the unknown pulse and create the compensation phase mask. MIIPS characterization works iteratively to obtain a transform-limited pulse. The detailed implementation can be found in the literature[79]. In this thesis work, a Labview program was created to implement the scanning of the sinusoidal phase mask and recovery of the phase profile.

The FROG technique was proposed earlier and it can work without a pulse shaper. The MIIPS technique can achieve a more precise phase characterization than FROG (FROG gives a precision of about 0.05 radian,

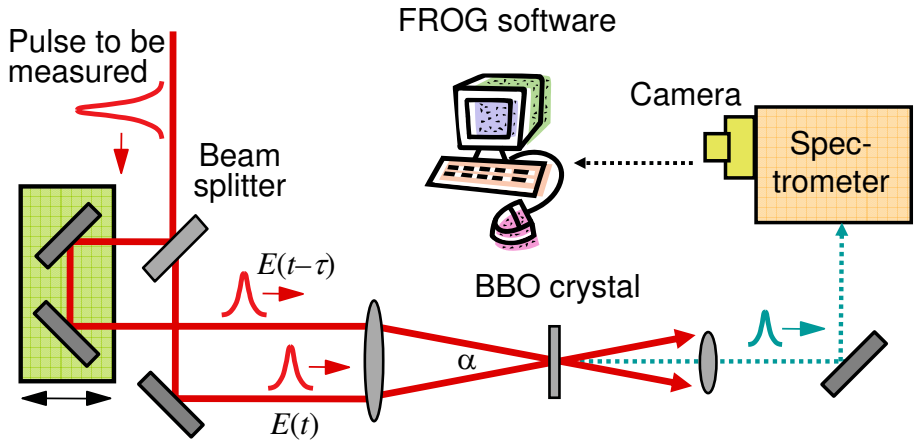


Figure 1.31: This figure shows a FROG setup. The unknown ultrafast laser pulse is beam split into two pulses. One pulse is delayed by $\tau$ using a retro-reflector on translation stage. Then two pulses are combined at a nonlinear crystal for the second harmonic generation (thin type-I BBO cut at 29.2° for 800nm). Scanning $\tau$ and recording spectra of the second harmonic signal to obtain the two-dimensional spectrogram (also known as the FROG trace). Then the trace is analyzed by FROG3 software (Femtosoft technology) to give amplitude and phase information of unknown pulse.

whereas MIIPS can reach precisions better than 0.01 radian). Since the pulse shaper has become a common instrument in modern ultrafast laser labs, MIIPS requires only an additional second harmonics generation setup, therefore it is simpler to implement for a lab with a functional pulse shaper. A combination of these two methods was used in the thesis work. A FROG and a MIIPS setup were built near the output location of the pulse shaper.

### 1.4.5 Generation and Detection of CARS Signal

For single pulse CARS experiments, the generation of signal can be simply achieved by focusing on the sample, if the focusing condition satisfies the phase matching requirement (see section 3.5). A tight focus lens or microscope objective is normally used for single pulse CARS. For the BOXCARS geometry CARS experiment, there are two strict requirements for generating detectable signals: first, all beams should spatially overlap on the sample, and second, excitation pulses should overlap in time. This temporal overlap requirement is different in the femtosecond laser CARS experiment than in CARS with narrow band lasers. For narrow band excitations, the temporal overlap requirement is relaxed, if not automatically satisfied. The following subsections shows some useful simple techniques in femtosecond CARS signal generation.

#### Spatial and Temporal Overlap Adjustment

After placing optical elements on the optical table according to an experimental scheme, a photo diode (DET 210 Thorlabs) is placed in the location of samples and used to detect excitation pulses after attenuation. The signal from the photo diode is displayed on an oscilloscope (TDS 3034B Tektronix). The time of attenuated pulses can be measured with the precision of 0.5ns (about 15cm in distance). The length of optical path of beams can be adjusted by either retro reflectors in the setup or the position of mirrors.

After pre-synchronization, the next step is to achieve spatial overlap. A business card with a small hole (about 50-100$\mu m$) can help alignment. It is mounted on a rigid frame near the sample of CARS experiment. A mirror on

a flipper is used to divert the focusing beams towards the mounted business card. The card is placed at the focal plane of the focusing element. Optical paths of all three beams are adjusted to let the attenuated beams passing through the small hole. An infrared detection card or an infrared viewer is used to view the beams after the hole. This procedure can guarantee good spatial overlap.

The temporal overlap can be obtained by using a nonlinear crystal to generate a "simulated signal" at the CARS frequency. After the pre-synchronization step, the pulse delay difference is within 0.5ns. The femtosecond time scale synchronization is done by adjusting the motorized translation stages. A point worth noting is that the axis of the translation stage should be parallel to the incident beam in order to avoid spatial walk-off during the time delay scanning. Such walk-off can harm the spatial overlap at the focus spot which considerably reduces the signal. In the experiments of this thesis, a $100\mu m$ second harmonic BBO crystal cut at angle of $29.2°$(for 800nm second harmonic generation) was used for pulse synchronization. By placing the BBO crystal at the sample position, the time delay between two beams is scanned to find the sum-frequency or non-resonant four-wave-mixing signal from incident laser pulses. The time delay of two CARS excitation pulses are adjusted to ensure all three pulses arrive at sample at the same time.

**Signal Filtering and Detection**

The nonlinear crystal that is used for synchronizing the pulses can also be used to generate the four-wave-mixing (FWM) signal at anti-Stokes frequency. The FWM signal at CARS frequency can be used for detector alignment. In non-collinear geometry such as BOXCARS, the FWM signal should have the same spatial propagation direction as CARS signal generated by samples (see section 1.3, phase matching section). Therefore aligning the strong, sometimes even visible FMW signal to the spectrometer can give a good pre-alignment for the actual signal. In the experiments a CCD detector (Andor DV400) on a spectrometer (McPherson 2035) was used to detect

the signal.

The scattering of intense excitation beams from samples increase the background in the CARS spectrum. Spatial filtering of the signal is then needed. In experiments, an iris was used to block off the residual excitation beams after the sample. It was placed in such way that the the background was minimized and CARS signal was maximized. After the spatial filtering iris, a dielectric short-wave-pass filter (Semrock) was used to further improve the signal to noise ratio by filtering out the residual scattered excitation beam. In the situation of collinear geometry, since spatial filtering is not possible, multiple short-wave-pass filters are often used to effective block the excitation beams.

Polarization techniques that reduce the non-resonant background can be used to improve signal quality as well. In CARS experiments with BOX-CARS geometry, the polarization of probe pulse can be rotated to 90° related to the polarization of pump and Stokes pulses, which leads to three times reduction on the strength of non-resonant background compared to that of three pulses of the same polarization. This is because $\chi^{(3)}$ for isotropic samples has $\chi_{xxxx} = 3\chi_{xxyy}$ relation[71], with $\chi_{xxxx}$ referring to the component of $\chi^{(3)}$ tensor when all pulses have the same polarization and $\chi_{xxyy}$ referring to the component of $\chi^{(3)}$ tensor when the pump and the Stokes pulses have the same polarization, and the probe pulse and anti-Stokes field are 90° to it.

## 1.5 Structure of Ph.D. Thesis

As a truth in science, every method has its own limitations. The technique of CARS is not an exception. For example, CARS with broad band pulses lacks spectral resolution, which is seen as a serious drawback to its spectroscopic application. The non-resonant background affects the CARS spectrum adversely, which also limits its application. The emphasis of this PhD thesis is on developing new methods to improve the performance of CARS with broad band pulses. The investigations have been done with the combination of broad band laser pulses and the pulse shaping technique.

The PhD thesis is presented in the following structure. The results of the experiments during my PhD study are presented in chapters 2 to 5. In chapter 2, the technique of Noise Auto-correlation Spectroscopy with Coherent Raman Scattering is presented. This is a single pulse CARS approach with the utilization of spectral noise across full pulse bandwidth. In chapter 3, an optical processing experiment of optical correlation on CARS is presented. It can obtain a high spectral resolution CARS spectrum from optical interference of broad band pulses and CARS signal. The method of complete characterization of molecular vibrations is presented in Chapter 4. This method can recover both amplitude and phase of laser-induced coherent vibrations. Chapter 5 is an extension of the chapter 4 technique, where the spectral phase of molecular vibrations is used to provide the vibrational spectrum when the non-resonant background of the sample is high. Chapter 6 gives a summary of these methods and presents possible directions for future research.

# Bibliography


[1] C. V. Raman and K. S. Krishnan, Nature **121**, 501 (1928).

[2] G. Landsberg and L. Mandelstam, Journal of the Russian Physico-Chemical Society, Physics Section **60**, 335 (1928).

[3] A. L. Schawlow and C. H. Townes, Physical Review **112**, 1940 (1958).

[4] P. D. Maker and R. W. Terhune, Physical Review **137**, A801 (1965).

[5] R. F. Begley, A. B. Harvey, and R. L. Byer, Applied Physics Letters **25**, 387 (1974).

[6] B. Hudson, Journal of Chemical Physics **61**, 5461 (1974).

[7] R. F. Begley, A. B. Harvey, R. L. Byer, and B. S. Hudson, Journal of Chemical Physics **61**, 2466 (1974).

[8] C. H. R. Ooi, G. Beadie, G. W. Kattawar, J. F. Reintjes, Y. Rostovtsev, M. S. Zubairy, and M. O. Scully, Physical Review A **72** (2005).

[9] H. W. Li, D. A. Harris, B. Xu, P. J. Wrzesinski, V. V. Lozovoy, and M. Dantus, Optics Express **16**, 5499 (2008).

[10] A. Zumbusch, G. R. Holtom, and X. S. Xie, Physical Review Letters **82**, 4142 (1999).

[11] W. Demtroder, *Laser Spectroscopy* (Springer, 2002), 3rd ed.

[12] M. Shapiro and P. Brumer, *Principles of the Quantum Control of Molecular Processes* (Wiley, New York, 2003).

[13] D. E. Spence, P. N. Kean, and W. Sibbett, Optics Letters **16**, 42 (1991).

[14] M. Schmitt, G. Knopp, A. Materny, and W. Kiefer, Chemical Physics Letters **270**, 9 (1997).

[15] P. Brumer and M. Shapiro, Chemical Physics Letters **126**, 541 (1986).

[16] M. Shapiro and P. Brumer, Reports on Progress in Physics **66**, 859 (2003).

[17] M. U. Wehner, M. H. Ulm, D. S. Chemla, and M. Wegener, Physical Review Letters **80**, 1992 (1998).

[18] S. M. Park, S. P. Lu, and R. J. Gordon, Journal of Chemical Physics **94**, 8622 (1991).

[19] A. Assion, T. Baumert, M. Bergt, T. Brixner, B. Kiefer, V. Seyfried, M. Strehle, and G. Gerber, Science **282**, 919 (1998).

[20] A. M. Weiner, Review of Scientific Instruments **71**, 1929 (2000).

[21] D. Oron, N. Dudovich, and Y. Silberberg, Physical Review Letters **89** (2002).

[22] N. Dudovich, D. Oron, and Y. Silberberg, Nature **418**, 512 (2002).

[23] D. Oron, N. Dudovich, and Y. Silberberg, Physical Review Letters **90** (2003).

[24] S. H. Lim, A. G. Caster, and S. R. Leone, Physical Review A **72** (2005).

[25] I. Itzkan and Cunningh.Fw, Ieee Journal of Quantum Electronics **QE 8**, 101 (1972).

[26] W. M. Tolles, J. W. Nibler, J. R. McDonald, and A. B. Harvey, Applied Spectroscopy **31**, 253 (1977).

[27] P. R. Regnier, F. Moya, and J. P. E. Taran, Aiaa Journal **12**, 826 (1974).

[28] J. J. Barrett and R. F. Begley, Applied Physics Letters **27**, 129 (1975).

[29] R. J. Hall, Combustion and Flame **35**, 47 (1979).

[30] K. Kohsehoinghaus, Progress in Energy and Combustion Science **20**, 203 (1994).

[31] R. F. G. Meulenbroeks, R. A. H. Engeln, J. A. M. vanderMullen, and D. C. Schram, Physical Review E **53**, 5207 (1996), part B.

[32] A. C. Eckbreth, Combustion and Flame **39**, 133 (1980).

[33] D. A. Greenhalgh, F. M. Porter, and W. A. England, Combustion and Flame **49**, 171 (1983).

[34] J. J. Barrett, Applied Physics Letters **29**, 722 (1976).

[35] M. Alden, P. E. Bengtsson, H. Edner, S. Kroll, and D. Nilsson, Applied Optics **28**, 3206 (1989).

[36] I. A. Stenhouse, D. R. Williams, J. B. Cole, and M. D. Swords, Applied Optics **18**, 3819 (1979).

[37] C. Brackmann, J. Bood, M. Afzelius, and P. E. Bengtsson, Measurement Science and Technology **15**, R13 (2004).

[38] A. C. Eckbreth, G. M. Dobbs, J. H. Stufflebeam, and P. A. Tellex, Applied Optics **23**, 1328 (1984).

[39] R. D. Hancock, P. O. Hedman, and S. K. Kramer, Combustion and Flame **87**, 77 (1991).

[40] J. W. Hahn, S. N. Park, E. S. Lee, C. Rhee, K. T. Kang, S. H. Chung, C. Y. Choi, and Y. D. Huh, Applied Spectroscopy **47**, 710 (1993).

[41] W. B. Roh, P. W. Schreiber, and J. P. E. Taran, Applied Physics Letters **29**, 174 (1976).

[42] P. Snowdon, S. M. Skippon, and P. Ewart, Applied Optics **30**, 1008 (1991).

[43] D. R. Snelling, G. J. Smallwood, R. A. Sawchuk, and T. Parameswaran, Applied Optics **26**, 99 (1987).

[44] E. H. van Veen and D. Roekaerts, Applied Optics **44**, 6995 (2005).

[45] S. Roy, T. R. Meyer, and J. R. Gord, Optics Letters **30**, 3222 (2005).

[46] J. Bruebach, E. van Veen, and A. Dreizler, Experiments in Fluids **44**, 897 (2008).

[47] C. P. J. Barty, T. Guo, C. LeBlanc, F. Raksi, C. RosePetruck, J. Squier, K. R. Wilson, V. V. Yakovlev, and K. Yamakawa, Optics Letters **21**, 668 (1996).

[48] S. Sartania, Z. Cheng, M. Lenzner, G. Tempea, C. Spielmann, F. Krausz, and K. Ferencz, Optics Letters **22**, 1562 (1997).

[49] B. D. Prince, A. Chakraborty, B. M. Prince, and H. U. Stauffer, Journal of Chemical Physics **125** (2006).

[50] J. X. Cheng, A. Volkmer, L. D. Book, and X. S. Xie, Journal of Physical Chemistry B **106**, 8493 (2002).

[51] M. Muller and J. M. Schins, Journal of Physical Chemistry B **106**, 3715 (2002).

[52] E. O. Potma, D. J. Jones, J. X. Cheng, X. S. Xie, and J. Ye, Optics Letters **27**, 1168 (2002).

[53] W. Dietel, E. Dopel, D. Kuhlke, and B. Wilhelmi, Optics Communications **43**, 433 (1982).

[54] A. H. Zewail, Science **242**, 1645 (1988).

[55] A. H. Zewail, Journal of Physical Chemistry **97**, 12427 (1993).

[56] A. H. Zewail, *Femtochemistry: Ultrafast Dynamics of the Chemical Bond* (World Scientific, Singapore, 1994).

[57] A. H. Zewail, Journal of Physical Chemistry A **104**, 5660 (2000).

[58] M. Fickenscher and A. Laubereau, Journal of Raman Spectroscopy **21**, 857 (1990).

[59] M. Fickenscher, H. G. Purucker, and A. Laubereau, Chemical Physics Letters **191**, 182 (1992).

[60] R. Inaba, H. Okamoto, K. Yoshihara, and M. Tasumi, Chemical Physics Letters **185**, 56 (1991).

[61] H. Okamoto and K. Yoshihara, Chemical Physics Letters **177**, 568 (1991).

[62] T. Lang, K. L. Kompa, and M. Motzkus, Chemical Physics Letters **310**, 65 (1999).

[63] S. H. Lim, A. G. Caster, and S. R. Leone, Optics Letters **32**, 1332 (2007).

[64] Y. X. Yan, E. B. Gamble, and K. A. Nelson, Journal of Chemical Physics **83**, 5391 (1985).

[65] S. Ruhman, A. G. Joly, and K. A. Nelson, Ieee Journal of Quantum Electronics **24**, 460 (1988).

[66] A. M. Zheltikov and A. N. Naumov, Quantum Electronics **30**, 606 (2000).

[67] D. Pestov, X. Wang, R. K. Murawski, G. O. Ariunbold, V. A. Sautenkov, and A. V. Sokolov, Journal of the Optical Society of America B-Optical Physics **25**, 768 (2008).

[68] T. Polack, D. Oron, and Y. Silberberg, Chemical Physics **318**, 163 (2005).

[69] B. von Vacano, W. Wohlleben, and M. Motzkus, Journal of Raman Spectroscopy **37**, 404 (2006).

[70] Y.R.Shen, *The Principles of Nonlinear Optics* (Wiley-Interscience, 1984), 1st ed.

[71] R. Boyd, *Nonlinear Optics* (Academic Press, 2002), 2nd ed.

[72] D. J. Tannor, *Introduction to Quantum Mechanics, A Time-dependet perspective* (University Science books, 2006).

[73] G. Knopp, I. Pinkas, and Y. Prior, Journal of Raman Spectroscopy **31**, 51 (2000).

[74] `http://http://www.mathworks.com/`.

[75] A. C. Eckbreth, Applied Physics Letters **32**, 421 (1978).

[76] U. Morgner, F. X. Kartner, S. H. Cho, Y. Chen, H. A. Haus, J. G. Fujimoto, E. P. Ippen, V. Scheuer, G. Angelow, and T. Tschudi, Optics Letters **24**, 411 (1999).

[77] P. Maine, D. Strickland, P. Bado, M. Pessot, and G. Mourou, Ieee Journal of Quantum Electronics **24**, 398 (1988).

[78] R. Trebino and D. J. Kane, Journal of the Optical Society of America a-Optics Image Science and Vision **10**, 1101 (1993).

[79] B. W. Xu, J. M. Gunn, J. M. Dela Cruz, V. V. Lozovoy, and M. Dantus, Journal of the Optical Society of America B-Optical Physics **23**, 750 (2006).

[80] K. W. Delong, R. Trebino, J. Hunter, and W. E. White, Journal of the Optical Society of America B-Optical Physics **11**, 2206 (1994).

# Chapter 2

# Noise Auto-correlation Spectroscopy with Coherent anti-Stokes Raman Scattering

## 2.1 Motivation

Noise Auto-correlation Spectroscopy with Coherent anti-Stokes Raman Scattering (NASCARS) is the method that will be introduced in this chapter. In section 1.3, expression (1.2) shows that the CARS signal generation in the frequency domain is a convolution between the probe field $E(\omega)$ and the vibrational coherence $R(\Omega)$. The vibrational coherence $R(\Omega)$ contains the profile of vibrational resonances according to the Lorentzian model equation (1.31). The purpose of CARS spectroscopy is to recover $R(\Omega)$ from the detectable CARS signal. In narrow band CARS or the multiplex CARS method, a narrow band probe pulse is used. With a narrow bandwidth probe pulse, the CARS spectrum has the same profile as the spectrum of the vibrational coherence (including non-resonant background). However, when a broad band coherent probe pulse is used, the CARS signal not only reflects the vibrational coherence, but also reflects the profile of the probe pulse. Therefore, the CARS spectrum cannot be taken as a direct indication of resonant level positions without further interpretation. Figure 1.20

[0] A version of this chapter has been published as Xiaoji G. Xu, Stanislav O. Konorov, John. W. Hepburn and Valery Milner "Noise Auto-correlation Spectroscopy with Coherent anti-Stokes Raman Scattering" *Nature Physics* Vol.4 No.2 page 125-129, 2008

C shows considerable difference in CARS spectra between sinusoidal phase shaping and $\pi$ phase step shaping. The CARS spectra dependence on the probe pulse raises a question: under broad band probe pulse condition, how can the vibrational coherence information be recovered from the broad band CARS signal? This chapter will give one answer to this question.

As discussed in section 1.3, the vibrational coherence $R(\Omega)$ is not directly measurable by the spectrometer. But the CARS signal as well as the optical field of probe pulse is a directly measurable quantity. From the information flow point of view, the information about the vibrational coherence is transferred to the measurable CARS signal through the anti-Stokes scattering of the probe pulse. The CARS spectrum with a narrow band probe pulse (figure 2.1B) reflects the position and linewidth of the vibrational resonances. The CARS spectrum with a broad band probe pulse (figure 2.1A) is broad and structureless. Useful information about the resonant levels is not effectively transferred by the broad band pulse through measurable CARS signals. This is a natural result of the fact that CARS signal is a convolution between the probe field and the vibrational coherence in the frequency domain. A closer look at the time domain gives an alternate but equivalent explanation. The vibrational coherence R(t) interacts with the probe pulse according to equation (1.37). While R(t) has a long lasting time behavior, the transform-limit probe pulse only overlaps with a small part of R(t) (figure 2.1C), whereas the narrow band probe pulse can overlap with the vibrational coherence at all time (figure 2.1D). As a result, only a small part of the time domain response of the vibrational coherence is transferred to the CARS field when the probe pulse has short duration, leading to the loss of structural information of molecules in the CARS spectrum.

The time domain analysis indicates a way to solve the problem. In order to obtain good information transfer from the vibrational coherence to the CARS spectrum, the probe pulse should have a long duration that can cover the whole time domain behavior of the vibrational coherence. However, the probe pulse having a long time duration is only a necessary requirement to the solution but not a sufficient one. Chirping or introducing phase functions to the probe pulse can extend the pulse duration and create sharp features

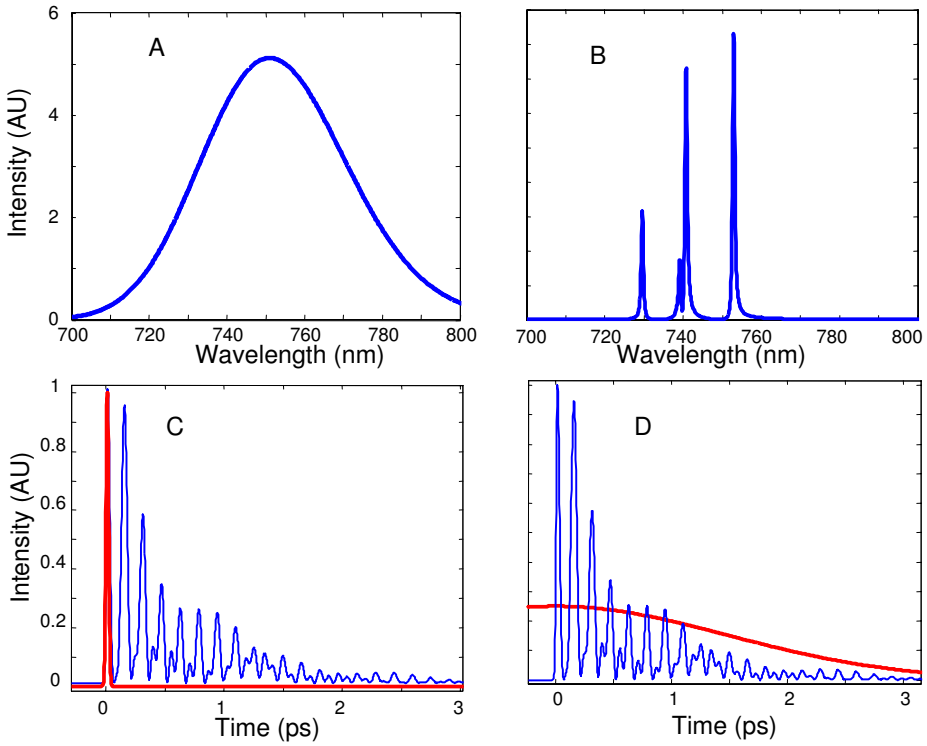


Figure 2.1: These figures show a comparison between a CARS spectrum using a transform-limited broad band probe pulse ($300cm^{-1}$ bandwidth) (A), and a narrow band probe pulse ($3cm^{-1}$ bandwidth) (B). (C) and (D) show the comparison in the time domain of CARS generation by a transform-limited probe pulse (thick red curve in (C))and a narrow band probe pulse (thick red curve in (D)) overlapping with the vibrational coherence (thin blue curve in both (C) and (D) ).

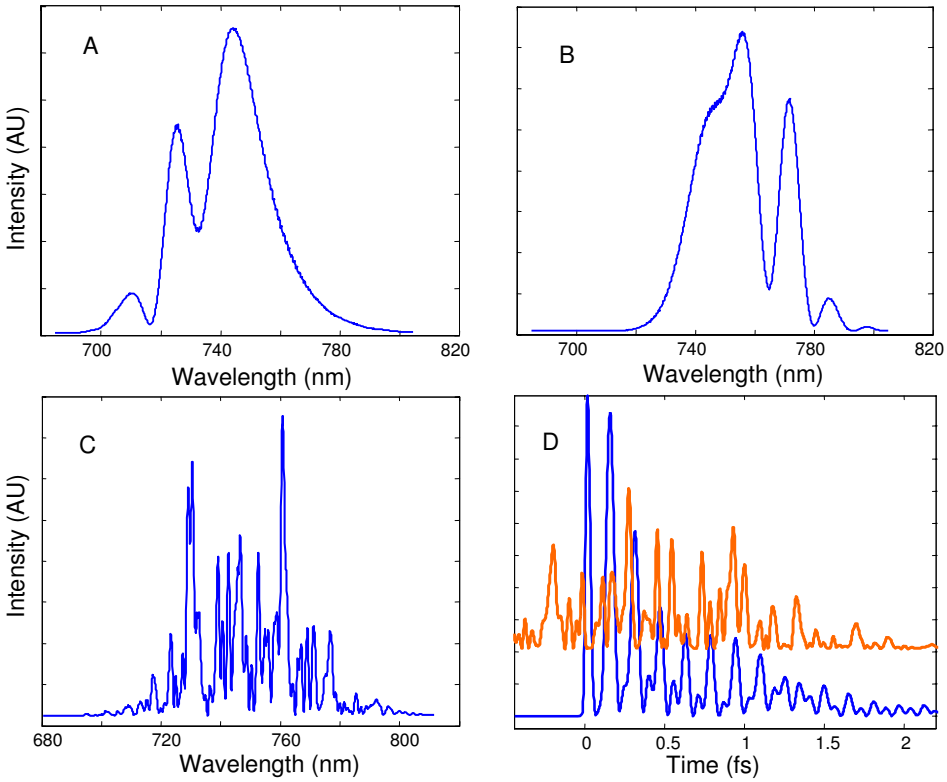


Figure 2.2: (A) shows the CARS spectrum using a positively chirped probe pulse. (B) shows the CARS spectrum using a negative chirped probe pulse. (C) shows the CARS spectrum from a noisy probe pulse. (D) in the time domain shows the vibrational coherence (blue thick line) and the noisy modulated probe pulse (red,thin line). The vibrational coherence in these figures is the same as that of figure 2.1 and the following figure 2.3 .

in the CARS spectrum, but they require additional interpretation as well as the exact knowledge of the probe pulses. As an example, figure 2.2 A and B show spectra of CARS signal generated by a positive chirped and a negative chirped probe pulse. Firstly, the spectra have different shapes from the vibrational coherence (figure 2.1B). Secondly, the CARS spectrum created from a chirped probe pulse is clearly dependent on the sign of the chirp.

There have been some studies [1, 2] done on finding a specific phase shape for broad band probe pulses such that the corresponding CARS spectrum can reflect the resonance structure. In Oron et. al.[1] a $\pi$ phase step and a $0.5\pi$ phase step pulse shaping pattern were used to resolve the resonances in a broad band CARS spectrum. However, such an approach requires exact and accurate pulse shaping of the probe pulse. In this chapter, an alternative approach which does not resort to specific pulse shapes of the probe pulse is presented.

This approach is to introduce uncorrelated spectral noise into the broad band pulse and measure the correlation between spectral peaks in the CARS spectrum. The figure 2.2C shows the CARS spectrum from a noisy probe pulse. The sharp features in the spectrum result from the presence of vibrational resonances and the long time duration component of the probe pulse. Figure 2.2D shows the shape of the vibrational coherence and a noise modulated probe pulse in the time domain. The noise modulated probe pulse has a long time duration that can effectively overlap with the vibrational coherence R(t). Therefore, it satisfies the above mentioned probe pulse requirement. However, the generated noise CARS spectrum contains both the profile of vibrational coherence and the noisy pattern of the probe pulse. It cannot be used directly. However, as will be shown in the following paragraphs, the autocorrelation of the noisy CARS spectrum can reflect the pattern of the vibrational coherence, if the patterns are uncorrelated.

Consider the intensity of the time domain anti-Stokes field:

$$I_{as}(t) = E_{as}(t)E_{as}^{*}(t) \tag{2.1}$$

From equation (1.37) of section 1.3, the expression of the time domain field $E_{as}(t)$ can be treated as $C \cdot E_{pr}(t)R(t)$. The product of vibrational coherence R(t) and the probe field $E_{pr}(t)$ times a constant C, which can be assumed as 1, since it is the profile of the signal field, not the total amount of CARS signal that is interesting. Then the time domain intensity of the anti-Stokes becomes:

$$I_{as}(t) = R(t)R^*(t)E_{pr}(t)E^*_{pr}(t) \tag{2.2}$$

The right hand side of equation(2.2) can be separated into two parts: the intensity of the time domain vibrational coherence, $R(t)R^*(t)$, and the intensity of the probe field $E_{pr}(t)E^*_{pr}(t)$. If the probe pulse is noise modulated, the Fourier transform of $E_{pr}(t)E^*_{pr}(t)$ term then contains a narrow band central frequency component.

The Fourier transform of the left hand side of the equation (2.2) gives the autocorrelation of the frequency domain spectrum of the amplitude and the spectral phase .

$$fft\{I_{as}(t)\}(\Omega) = \int_{-\infty}^{\infty} E^*(\omega)E(\omega+\Omega)d\omega \tag{2.3}$$

The Fourier transform of the right hand side of equation(2.2) represents the convolution of the Fourier transform of the time domain intensity of the vibrational coherence $R(t)R^*(t)$ and the time domain intensity of the probe pulse $E_{pr}(t)E^*_{pr}(t)$ according to equation (2.4).

$$fft\{I_{as}(t)\}[\Omega] = fft\{R(t)R^*(t)\}[\Omega] \bigotimes fft\{E_{pr}(t)E^*_{pr}(t)\}[\Omega] \tag{2.4}$$

In a similar fashion to equation (2.3) for the CARS intensity, the $fft\{R(t)R^*(t)\}$ corresponds to the autocorrelation of the vibrational coherence spectrum of amplitude and phase ("of amplitude and phase" means it is a complex quantity rather than a real quantity) by $fft\{R(t)R^*(t)\}[\Omega] = \int_{-\infty}^{\infty} R^*(\omega)R(\omega+\Omega)d\omega$ . The probe pulse part $fft\{E_{pr}(t)E^*_{pr}(t)\}$ corresponds to the autocorrelation of the probe pulse spectrum of amplitude and phase $fft\{E_{pr}(t)E^*_{pr}(t)\}[\Omega] = \int_{-\infty}^{\infty} E^*_{pr}(\omega)E_{pr}(\omega+\Omega)d\omega$.

Numerical simulations can better illustrate the relation between the

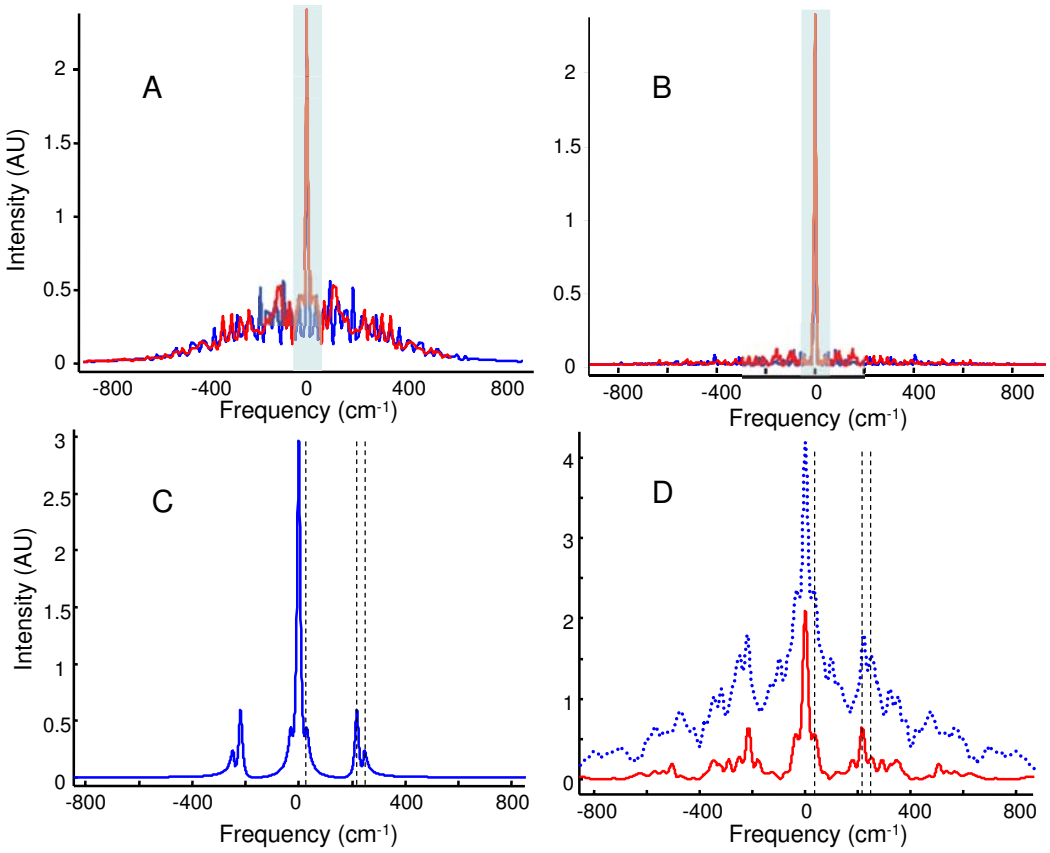


Figure 2.3: (A) shows the plot of the Fourier transform of the probe pulse intensity in time of two low amplitude phase noise patterns (red and blue). (B) shows similar plots but with two high amplitude spectral phase noise patterns (6 times higher than that of (A)). (C) shows the frequency domain Fourier transform of the vibrational coherence intensity $R(t)R^*(t)$, the vibration level spacing is indicated by the vertical dashed lines. (D) shows the Fourier transform of the CARS intensity. Blue dashed curve is from one low amplitude noise pattern of (A). Red continuous line is from one high amplitude noise pattern of (B)).

noisy probe pulse and the vibrational coherence than equations. figure 2.3 shows the autocorrelation of the probe pulse spectrum of amplitude and phase and the autocorrelation of the vibrational coherence spectrum of amplitude and phase. From figure 2.3A and 2.3B, one can find that the phase noise in the probe pulse gives a narrow band central peak in the frequency domain autocorrelation. The high noise level in the probe pulse gives a pedestal in the autocorrelation spectrum. The total autocorrelation of CARS spectrum (expression (2.3)) is shown in figure 2.3D. It is a convolution between the autocorrelation of the vibrational coherence spectrum (figure 2.3C) and the autocorrelation of the probe pulse spectrum (figure 2.3B). Because of the convolution, the narrowness of the central peak of figure 2.3B determines the resolution of total autocorrelation spectrum of figure 2.3D.

However, as figure 2.3D shows, in addition to the peaks that correspond to the autocorrelation of complex vibrational coherence spectrum (vertical lines in figure 2.3D), there are also additional side peaks that come from the residual correlation of spectral noise of the probe pulse. This is due to the fact that no matter how random the probe pulse noise is, the finite bandwidth or duration of the probe pulse always contains residual correlations. To solve this problem, averaging over multiple noise patterns is introduced.

There is also a pedestal in the autocorrelation spectrum of the probe pulse when the amplitude of noise is low (figure 2.3A). Because of the convolution, the pedestal in the autocorrelation of the probe pulse also creates a problem for the final autocorrelation of the spectrum (see figure 2.3D). The autocorrelation pedestal originates from the central short duration part of the probe pulse in the time domain (the profile of pulse is similar to figure 2.4). When the spectral phase noise is high, the time domain pulse is dispersed into irregular pulse trains and the central short duration part is eliminated, leading to a low pedestal in the Fourier transform (figure 2.3B).

For proof of principle NASCARS experiment with BOXCARS geometry, a separate probe pulse is used. It is possible to use the pulse shaper to introduce high amplitude noise into the probe pulse to remove the pedestal. However, for the proposed single pulse NASCARS experiment (see below),

since the pump/Stokes and probe pulses are unified into one single excitation pulse to maintain the short duration central part for the impulsive vibrational coherence preparation (figure 2.4). The high noise amplitude approach is not applicable to the single pulse NASCARS. To solve this problem, subtraction between consecutive noise CARS spectra is used before numerical autocorrelation. Such subtraction is effective for both BOXCARS geometry NASCARS and single pulse NASCARS.

The single pulse NASCARS experiment utilized a broad band excitation pulse of spectral noise of low amplitude to coherently excite the vibrational coherence and probe it. When a broad band pulse contains spectral noises of low amplitude, its time domain representation shows a short duration central peak and a long duration tail of irregular pulse trains (figure 2.4). The long duration tail of the unified pulse can serve as the probe pulse of NASCARS, and the central short duration part serves as the impulsive excitation. The pulse shape of single pulse NASCARS is similar yet different to that of the single pulse CARS method mentioned in section 1.2 (see figure 1.12). In both single pulse experiments, the short duration envelope in the time domain creates the vibrational coherence, and the field of the long tail probes the prepared vibrational coherence. The difference between these two single pulse method is primarily in the probing function. In NASCARS, the probing field is created by the spectral noise of low amplitude, and the spectral noise modulation exists across all parts of the spectrum. In single pulse CARS, the probe field is a narrow band frequency component and specifically allocated at the blue edge of the spectrum. In the frequency domain representation, the autocorrelation of the excitation pulse of single pulse NASCARS contains a pedestal and a central peak of narrow bandwidth. The autocorrelation pedestal covers the bandwidth that is accessible for NASCARS. The central peak of narrow bandwidth in the autocorrelation spectrum determines the spectral resolution (the autocorrelation of excitation pulse in single pulse NASCARS has the same profile shown in figure 2.3A).

In the above derivation, the autocorrelation of the CARS field is treated as $\int_{-\infty}^{\infty} E^*(\omega)E(\omega+\Omega)d\omega$ . In the actual experimental measurement, the

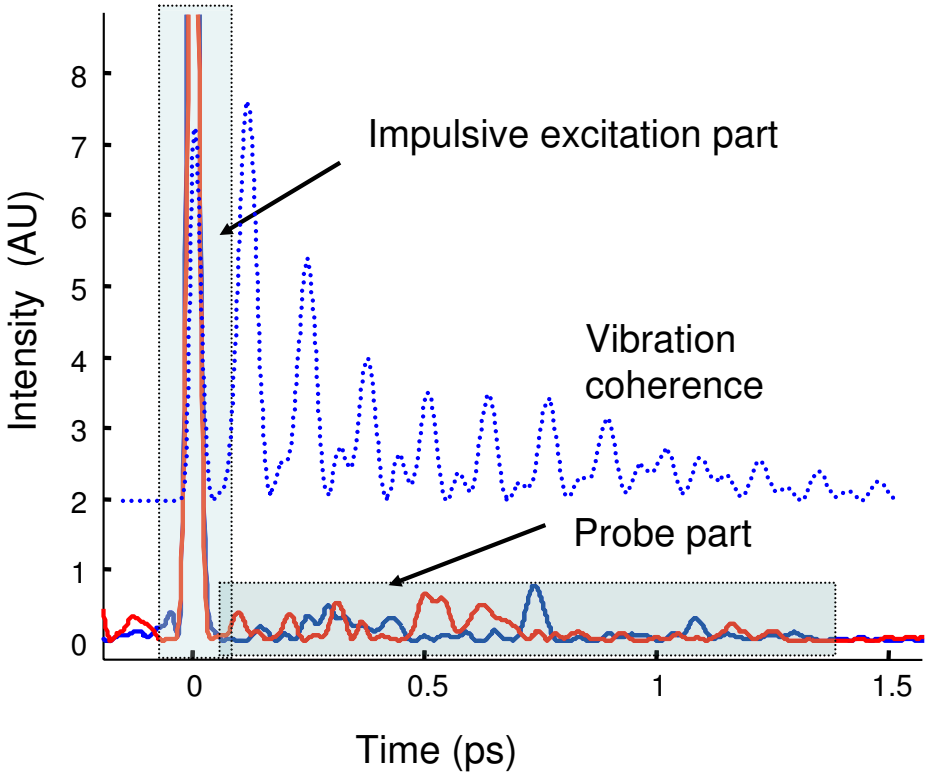


Figure 2.4: This figure shows the time domain representation of a single pulse NASCARS excitation pulse. The low level noise broad band pulse in the time domain has two parts (the high-lighted boxes), the coherent central part and the noise tail part. The coherent central part is capable of generating vibrational coherence(dashed line). The central part is conserved from realization to realization. The continuous thick curves (red and blue) show two of such random low level noisy pulse. The dashed curve represents the vibrational coherence in time.

autocorrelation is done based on the CARS spectrum as $\int_{-\infty}^{\infty} I(\omega)I(\omega+\Omega)d\omega$. The autocorrelation of the CARS spectrum and the autocorrelation of the CARS field of amplitude and phase both can yield the vibrational level spacing of the sample.

The first experiment was done in a BOXCARS geometry using a pulse shaper to introduce high spectral noise to a probe pulse, and then the difference between CARS spectra of two consecutive CARS spectra was measured. An autocorrelation of the difference of CARS spectra was taken and averaged. The averaged autocorrelation spectrum of many different random noise probe pulse patterns shows the vibrational level spacings. After the proof of principle experiment of BOXCARS geometry, a single pulse CARS experiment was demonstrated. We found a convenient way of creating low level noise modulated pulse from a regenerative amplifier by modifying the compressor grating system. With collinear focusing and proper signal filtering, CARS spectra were obtained and consecutively subtracted. The difference of spectra follows the same treatment of autocorrelation and averaging. The experimental detail is shown in the article and method section. The single pulse NASCARS can reveal the vibrational level spacing of low wave numbers resonances. ($< 400\text{cm}^{-1}$), limited by the bandwidth of the excitation broad band pulse.

The single pulse NASCARS can give the spacing of the vibrational levels in a single pulse experiment. It inherits the compactness of the single pulse CARS technique and requires only a regenerative amplifier laser system. Since the exact phase shape of noise is not required, single pulse NASCARS method can work without a pulse shaper. However, NASCARS recovers only the autocorrelation of the vibrational spectrum (2.3C) but not the spectrum itself (figure 2.1B). The autocorrelation spectrum contains less structural information than the actual spectrum, e.g. the line width of resonances is hard to obtain through autocorrelation. Chapter 3 is going to address this autocorrelation problem and give a solution for obtaining the full spectrum using broad band noise pulse.

## 2.2 Method Content

### 2.2.1 Content

Coherent anti-Stokes Raman scattering (CARS) with femtosecond laser pulses has become the method of choice in nonlinear optical spectroscopy and microscopy[3, 4]. As a third-order nonlinear process, femtosecond CARS exhibits high efficiency at low average laser power. High sensitivity to molecular structure enables detection of small quantities of complex molecules[5, 6] and non-invasive biological imaging[7]. Temporal and spectral resolution of CARS is typically limited by the duration of the excitation pulses and their frequency bandwidth, respectively. Broadband femtosecond pulses, though advantageous for time-resolved CARS spectroscopy[8, 9], offer poor spectral resolution. The latter can be improved by invoking optical[10, 11] or quantum[2, 12] interferences at the expense of increasing complexity of instrumentation and susceptibility to noise. Here we present a new approach to coherent Raman spectroscopy in which high resolution is achieved by means of deliberately introduced noise. The proposed method combines the efficiency of a coherent process with the robustness of incoherent light, and does not require any temporal scanning or spectral pulse shaping commonly employed by the frequency-resolved spectroscopic methods with ultrashort pulses.

In CARS, pump and Stokes photons of frequencies $\omega_p$ and $\omega_S$, respectively, excite molecular vibrations at frequency $\Omega = \omega_p - \omega_S$ (Figure a). A probe photon at $\omega_0$ is scattered off the coherent vibrations generating the anti-Stokes signal at frequency $\omega = (\omega_0 + \Omega)$. Special care is usually taken to preserve the coherence of laser pulses as it determines the accuracy of a spectroscopic measurement. The latter can be improved by means of the pulse shaping technique[1, 13] which modifies the amplitudes and phases of the spectral constituents of the pulse[14] (Figure 2.2.1b(i)). It enables selective excitation[2, 12] or selective probing[10, 11] of separate vibrational modes on the frequency scale narrower than the overall pulse bandwidth. Selective excitation is based on the coherent control[15] of nonlinear optical processes [16], whereas selective probing employs the idea of multiplex CARS[7] in

which a small part of the pulse spectrum is modified (in amplitude, phase or polarization) and serves as a narrowband probe. Both approaches rely on the effects of quantum or optical interference, and are therefore sensitive to noise and de-coherence which often ruin the spectral and temporal integrity of the pulse. Using a narrow slice of the available pulse spectrum as a probe in multiplex CARS also means that higher resolution may only be obtained at the expense of the proportionally lower probe power and correspondingly lower signal.

In this work we show that contrary to the common belief that spectral noise is detrimental to coherent spectroscopic measurements, it can be utilized for improving the resolution, efficiency and robustness against unavoidable degradation of pulse coherence. In our new method of noise auto-correlation spectroscopy with coherent anti-Stokes Raman scattering (NASCARS) the laser-induced molecular vibrations are probed by a broadband pulse with intentionally randomized amplitude and phase. The vibrational resonances result in and are identified through the appearance of intensity correlations in the noisy spectrum of coherently scattered photons. Due to the presence of Raman resonances, the spectral noise of the probe field is transferred to the spectrum of the scattered photons. While completely uncorrelated in the probe, the noise in the anti-Stokes field acquires strong correlations as a result of the molecular vibrational coherence. The latter assures that multiple Raman modes "map" the same realization of the probe noise onto the different spectral regions of the generated anti-Stokes spectrum, as shown schematically in Figure 2.2.1a. An auto-correlation of the noisy anti-Stokes spectrum corresponds directly to the auto-correlation of the Raman mode structure, thus revealing the vibrational beating frequencies of the medium. Even though the probe in NASCARS carries the full available spectral bandwidth of a femtosecond pulse, the resolution is determined by the much smaller frequency correlation length of the introduced noise, $\delta\omega_n$. Utilization of the full bandwidth provides the ability to increase the resolution with no penalty in the available probe power and, therefore, with no direct reduction of the signal level. By its very nature, the method is not sensitive to the quality of the temporal and spectral profile

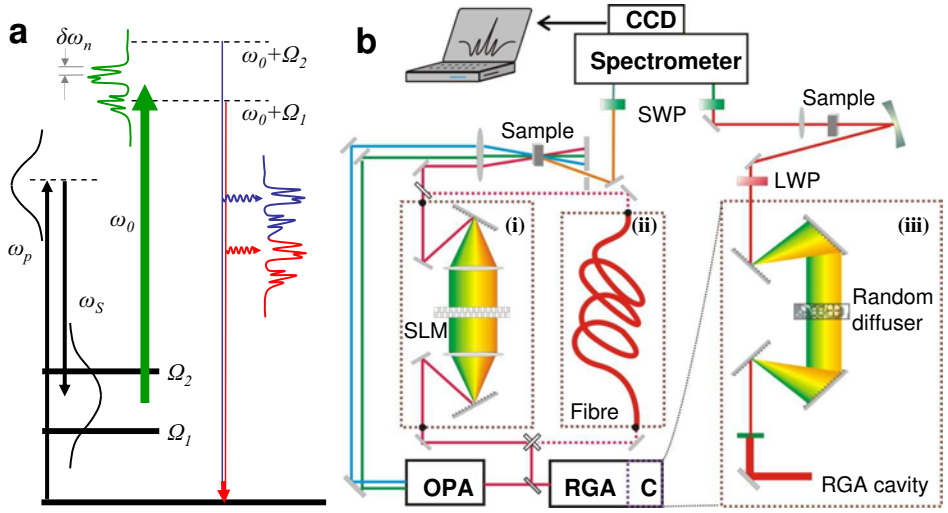


Figure 2.5: Interaction scheme for coherent anti-Stokes Raman scattering (CARS) and experimental arrangement for the detection of NASCARS signal. **a**, Pump and Stokes pulses (black) overlap in time and induce the coherent molecular vibrations. The broadband probe pulse (green) interacting with the vibrational energy levels $\Omega_{1,2}$ generates the anti-Stokes light (red and blue). In NASCARS, the noise in the probe spectrum is imprinted onto the corresponding spectral regions of the anti-Stokes light. **b**, Diagrams of various experimental configurations. In (i), the random spectral noise is applied to the probe pulse by the spatial light modulator (SLM) in the pulse shaper configuration. In (ii), the phase of the probe is randomized due to the inter-modal dispersion of a multi-mode optical fibre. In both cases, the pump and Stokes pulses are generated by the optical parametric amplifier (OPA). In the single-pulse configuration (iii), a diffuser is introduced inside the compressor stage (C) of the regenerative amplifier (RGA) system. Random scattering results in the partial de-coherence of the pulse required by NASCARS. The anti-Stokes spectrum is detected by the CCD-based spectrometer, and the auto-correlation is calculated by the computer. LWP, SWP - long- and short-wave pass filters, respectively.

of the pulses, and can be implemented by simply destroying the coherence of a laser pulse, as demonstrated here.

Noise and fluctuations in resonant fluorescence[17], scattered light[18] and number of trapped ultra-cold atoms[19] have been used to observe statistical properties of a medium but did not provide any spectroscopic information. NASCARS extends the idea of using noise correlations as a diagnostic tool to the domain of coherent nonlinear spectroscopy with ultrashort pulses. Noisy nanosecond lasers have been previously exploited in coherent Raman spectroscopy as a means of achieving time resolution shorter than the duration of the excitation pulses[20, 21]. The method of coherence observation by interference noise (COIN[22]) has been introduced for detecting the decay rates of electronic coherence, and applied to linear spectroscopy with narrow band picosecond pulses and to quantum state holography[23]. Unlike NASCARS, both approaches retrieve spectroscopic data from scanning the time delay between the noisy pulses. Here we show that the availability of a broad spectrum advances the method of noise-assisted spectroscopy towards efficient scan-less single-beam frequency-resolved analysis of molecular vibrations.

Consider the scheme depicted in Figure 2.2.1a with two Raman modes at frequencies $\Omega_1$ and $\Omega_2$ excited by the pump-Stokes pulse pair. The anti-Stokes field $E(t)$, generated by the Raman scattering of the probe field $E_0(t)$, can be expressed as the real part of $E(t) = E_0(t) \cdot e^{-\gamma t}\left[e^{-i\Omega_1 t} + e^{-i\Omega_2 t}\right]$, where for the sake of clarity we have neglected the non-resonant background, and assumed equal strength and decay rate $\gamma$ for both vibrational modes. The experimentally observed anti-Stokes spectrum $I(\omega)$ is the Fourier transform of the field correlation function $G_E(\tau)$, where

$$G_E(\tau) = \int dt E(t)E^*(t-\tau) = G_{\mathcal{E}_0}(\tau)[e^{i\Omega_1\tau} + e^{i\Omega_2\tau}]. \tag{2.5}$$

Here $G_{\mathcal{E}_0}(\tau)$ is the correlation function of the modified input probe field $\mathcal{E}_0 \equiv E_0 \cdot e^{-\gamma t}$, i.e. the probe field multiplied by the exponential decay of

the vibrational coherence. Hence,

$$I(\omega) = \int d\tau e^{-i\omega\tau} G_{\mathcal{E}_0}(\tau)[e^{i\Omega_1\tau} + e^{i\Omega_2\tau}] = \mathcal{I}_0(\omega - \Omega_1) + \mathcal{I}_0(\omega - \Omega_2), \quad (2.6)$$

where $\mathcal{I}_0(\omega - \Omega_{1,2})$ is the spectrum of $\mathcal{E}_0$. Equation (2.6) shows that any amplitude noise in $\mathcal{I}_0$ is mapped onto the corresponding spectral region of the anti-Stokes spectrum $I$ (that is, up-shifted by the corresponding Raman shift $\Omega_{1,2}$ as schematically shown in Fig. a). Averaging over multiple noise realizations, we arrive at the expression for the noise auto-correlation for the measured anti-Stokes spectrum as a function of the frequency shift $\Delta\omega$:

$$\langle G_I(\Delta\omega)\rangle = G_{\mathcal{I}_0} \cdot [2g(\Delta\omega) + g(\Delta\omega + \delta\Omega) + g(\Delta\omega - \delta\Omega)], \quad (2.7)$$

where $\delta\Omega \equiv \Omega_2 - \Omega_1$ is the distance between the vibrational resonances, and we have assumed an uncorrelated probe noise with $G_{\mathcal{I}_0}(\Delta\omega) \equiv G_{\mathcal{I}_0} g(\Delta\omega)$ and $g(\Delta\omega)$ being the line shape function peaked at $\Delta\omega = 0$ and of width $\delta\omega_n$. The two sidebands at $\pm\delta\Omega$ in Eq. 2.7 illustrate the ability of NASCARS to retrieve the vibrational beating frequency from the frequency correlations in the noisy spectrum of the Raman-scattered light, with the resolution determined by the noise correlation length $\delta\omega_n$.

The required amplitude noise in the spectrum of $\mathcal{E}_0$ can be introduced by applying either amplitude or phase noise to the input probe field $E_0$. Numerical simulation of the NASCARS measurement with a phase-randomized probe field is shown in Fig. 2.6. In the time domain, the spectral noise breaks the initial short probe pulse into a long and random sequence of smaller pulses - an "incoherent pulse train" (Fig. 2.6b). In the presence of a long-lived vibrational coherence, this probe train generates a train of the corresponding anti-Stokes pulses. The anti-Stokes train is an exact replica of the original random sequence of the probe pulses with an additional periodic amplitude modulation superimposed on it by the vibrational field of the molecule. It is this amplitude modulation that introduces correlations in the otherwise uncorrelated noise in the observed anti-Stokes spectrum, shown in Fig. 2.6c. High spectral resolution is achieved when the probe train duration

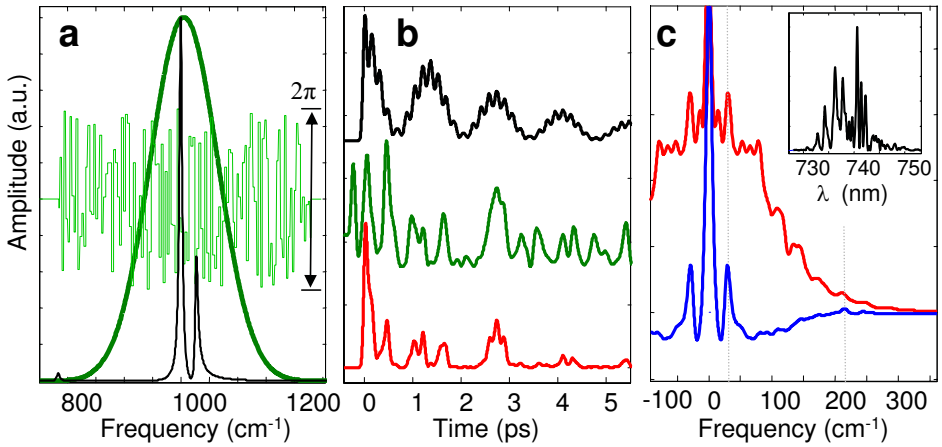


Figure 2.6: Numerical simulations of the noise auto-correlation spectroscopy with CARS. **a**, the frequency bandwidth of the probe pulse, represented by the broad gaussian envelope, is much broader than the width of and the distance between the vibrational resonances of Toluene (black curve). White noise is applied to the spectral phase of the probe pulse via random phase jumps of 0-to-$2\pi$ radians every 1 cm$^{-1}$. **b**, time domain representation of the decaying molecular vibrations (upper black), incoherent probe pulse train obtained by applying the spectral phase noise to the broadband probe (middle green), and the resulting anti-Stokes pulse train (lower red). Being a product of the vibrational amplitude and the probe field amplitude, the output anti-Stokes field acquires spectral correlations due to the periodic vibrational modulation superimposed onto the uncorrelated input noise. **c**, Auto-correlation of the calculated noisy anti-Stokes spectrum (shown in the inset, and exhibiting no clear evidence of the Raman modes) with a single realization of the phase noise (upper red) and after averaging over 100 noise realizations (lower blue). The strong peak at 27 cm$^{-1}$ and weak peak at 218 cm$^{-1}$, marked by the dotted lines, correspond to the beating of the vibrational modes of Toluene at 782, 1000 and 1027 cm$^{-1}$.

is comparable with the decay time of the vibrational coherence.

We first demonstrate the new method by implementing it in a typical multi-color noncollinear BOXCARS geometry[3] (see Fig. 2.2.1b(i)). The setup consisted of a commercial Ti-Sapphire regenerative amplifier providing the probe pulses at a central wavelength of 800nm, and an optical parametric amplifier generating the pump and Stokes pulses at 1111 nm and 1250nm, respectively. All three pulses were focused into a quartz cuvette containing a liquid mixture of Toluene with ortho-Xylene (see **Methods** for details). The anti-Stokes spectrum was measured with a CCD-based spectrometer, while the noise was introduced by means of a home made programmable spectral pulse shaper. The auto-correlation spectrum presented in Fig. 2.7a was averaged over 100 realizations of noise. Well resolved side-bands at $\pm 27$ cm$^{-1}$ and $\pm 49$ cm$^{-1}$ in Fig.  a correspond to the beating frequencies between the strongest excited vibrational modes of the mixed sample. In agreement with our theoretical treatment and numerical simulations, the best performance of NASCARS is obtained with a maximum ($2\pi$ peak-to-peak) phase modulation, while the spectral resolution can be controlled through the pulse shaper by varying the distance between the consecutive phase jumps in the pulse spectrum, $\delta\omega_n$. An easier way of scrambling the probe phase without the shaper is shown in Fig.  2.2.1b(ii). When coupled to a standard multimode fibre, the probe pulse breaks apart into an incoherent pulse train due to the intermodal dispersion, and generates similar auto-correlation spectra.

Numerous applications in vibrational spectroscopy, microscopy and imaging call for a single-pulse technique, recently developed by many groups[11, 12, 24, 25] and based on covering the pump, Stokes and probe wavelengths with a broad spectrum of a single ultrashort pulse. Here we demonstrate a single-pulse NASCARS measurement, based on the following mechanism. If the applied noise introduces only partial de-coherence of the original pulse, the remaining coherent part executes an impulsive pump-Stokes excitation, while the incoherent noisy part of the pulse serves as a probe. To NASCARS advantage, such partial de-coherence can be imposed on a laser beam without an elaborate shaping technology, which typically requires delicate optical alignment, calibration, maintenance, and costly optical components. We

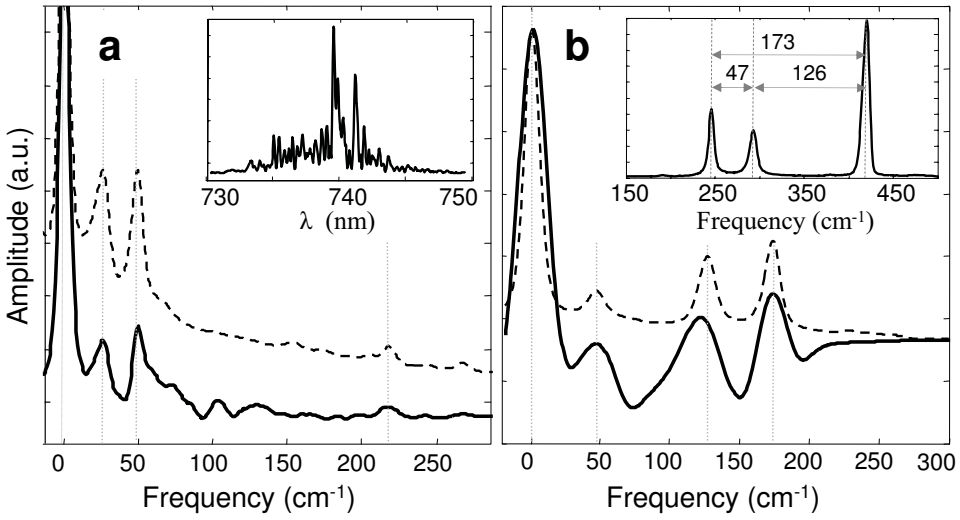


Figure 2.7: Experimental NASCARS spectra (solid) compared with the auto-correlation of the spontaneous Raman spectra obtained by the commercial Raman spectrometer (dashed). **a**, Mixture of Toluene and ortho-Xylene with the relevant Raman shifts of 782, 1000, 1027, 982 and 1049 $cm^{-1}$. Dotted lines point to the strong beating signals at 27, 49 and 218 $cm^{-1}$. The uncorrelated spectral phase noise was introduced to the probe field through the pulse shaper (Fig. 2.2.1b (i)). Anti-Stokes spectrum for a single noise realization is shown in the inset. The observed linewidth is determined by the convolution of the real resonance width of $\sim$3 $cm^{-1}$ and the spectral resolution of the pulse shaper ($\sim$3.5 $cm^{-1}$) which determines the correlation length of the applied spectral noise. **b**, Single-pulse NASCARS results for the sample of liquid $CBrCl_3$. Here, a single ultrashort pulse was focused directly in the medium. A thin sheet of a scattering material was placed inside the compressor stage of the laser system (Fig. 2.2.1b (iii)) to create partial de-coherence of the beam. Vibrational beating at 47, 126 and 173 $cm^{-1}$ is clearly identifiable at the expected locations (dotted lines). The observed peaks are associated with the three Raman modes of $CBrCl_3$ at 246, 293 and 419 $cm^{-1}$, shown on the spontaneous Raman spectrum in the inset.

implemented a single-pulse NASCARS by simply introducing a light scatterer inside the pulse compressor of our laser system (see Fig. 2.2.1b(iii)) and **Methods** section for details). Placed in the way of a spectrally dispersed beam, the scattering element - a single sheet of a standard lens paper - transmits only some frequency components of the pulse while blocking the others. Standard pulse characterization shows that in accord with the aforementioned requirement, the output laser pulse consists of an ultrashort coherent part and a long noisy tail. Statistical averaging over the realizations of noise is performed by moving the scatterer between the consecutive readouts of the anti-Stokes spectrum. The resulting auto-correlation spectrum of $CBrCl_3$, shown in Fig. 2.7b, exhibits three clearly resolved peaks at the expected beating frequencies of the molecule, attesting to the feasibility of the proposed method. Remarkably, the whole setup consists of a single slightly modified light source and a spectrometer, yet the achieved resolution of $20\ cm^{-1}$ surpasses the spectral bandwidth of our pulses ($> 500\ cm^{-1}$) by more than an order of magnitude.

The demonstrated implementation simplicity of noise auto-correlation spectroscopy with broadband pulses positions it as a powerful tool for chemical analysis. In all practical cases, the retrieved auto-correlation of the vibrational spectrum retains the uniqueness of the spectrum itself, and can therefore be used as an excellent fingerprint for molecular identification. As the average difference between the beating frequencies is usually smaller than the average frequency of vibration, the resolving power of NASCARS is lower than that of traditional CARS and may limit its application to relatively simple molecular systems. With no stringent requirements on the quality of the excitation pulse(s), the method may prove especially valuable for the applications in nonlinear microscopy by allowing the delivery of the pulses through the standard high-core-area multi-mode optical fibre, normally prohibited due to the intermodal fibre dispersion. In contrast to multiplex CARS, the pump, Stokes and probe pulses in NASCARS are *all* spectrally broad. As a result, the distribution of the available laser power between these components is independent of the desired spectral resolution and can therefore be adjusted for better performance, e.g. by varying the

applied noise level. By the very nature of random noise, the required averaging can be performed in a quick and robust way. Utilizing pseudo-random phase masks, specially designed for the low correlation background, may further reduce the required amount of averaging. In principle, simultaneous detection of multiple anti-Stokes spectra, observed at different scattering angles and, therefore, corresponding to different noise realizations, should enable a single-shot NASCARS measurement.

### 2.2.2 Methods

The experiments in the multi-color non-collinear geometry (Fig. 2.2.1b(i,ii)) were carried out in a typical CARS setup which consists of a commercial Ti-Sapphire regenerative amplifier (Spitfire, Spectra-Physics, 1 KHz repetition rate, 10 nm spectral bandwidth (FWHM), 2 mJ output pulse power) generating the probe pulses at the central wavelength of 800nm, and an optical parametric amplifier (TOPAS, Light Conversion) generating the pump and Stokes pulses at 1111 nm and 1250nm, respectively. All three pulses of $\sim$10 $\mu$J energy each were focused by a lens (focal length of 500 mm) into a quartz cuvette (5 mm optical path) with the liquid sample, where they overlapped in time and in space (BOXCARS phase-matching geometry). The output anti-Stokes beam was collimated with a 150 mm focal-length lens and coupled into the spectrometer (model 2035, McPhearson) equipped with a CCD camera (iDus DV400, Andor) and providing a spectral resolution of $< 2$ cm$^{-1}$.

In the first configuration (Fig. 2.2.1b(i)), we introduced white noise in the probe pulses using the programmable spectral pulse shaper based on a dual-mask 128-pixel liquid-crystal spatial light modulator (SLM-128, CRI). The resolving power of the shaper was $\sim$3.5 cm$^{-1}$ per pixel, which dictated the smallest frequency correlation length of the applied noise, and therefore determined the spectra resolution of the NASCARS signal. From studying the effects of the phase and amplitude noise independently, we conclude that the phase noise results in superior NASCARS performance. In contrast to the amplitude noise, it does not attenuate the available probe pulse energy

and results in a much smaller temporal overlap of the probe train with the pump-Stokes pulse pair, reducing the non-resonant background and increasing the signal quality.

We also demonstrated one simple way of phase scrambling by replacing the pulse shaper with a 3 meters-long piece of a standard multi-mode fibre of 64 $\mu$m core diameter (Fig. 2.2.1b(ii)). A probe pulse, coupled into the multiple fibre modes, breaks apart into an incoherent pulse train due to the intermodal dispersion. The large number of the available modes and the high sensitivity of the dispersion of each mode to local mechanical stresses in the fibre, enables an easy and efficient way of statistical averaging over the realizations of noise. New realizations of a random probe train are generated by simply moving the fibre between the consecutive data acquisitions. Matching the temporal duration of the output random train to the decay time of the vibrational coherence by choosing an optimal fibre length assures high spectral resolution of the NASCARS measurement.

For the single-pulse experiments we used ultrashort pulses of higher bandwidth from a different femtosecond Ti:Sapphire regenerative amplifier system (Spitfire Pro, Spectra-Physics, 1 KHz repetition rate, 35 nm spectral bandwidth (FWHM), 3 mJ output pulse power). The wavelength of the amplified pulses was centered at 805 nm. The beam was apertured down to the diameter of 0.5 mm before entering the compressor stage of Spitfire Pro. A thin sheet of a light scattering material (optical cleaning tissue, Thorlabs) was fixed on a rigid frame and mounted on a one-dimensional translation stage inside the compressor (Fig. 2.2.1b(iii)). The scatterer was placed after the second reflection from the diffraction grating, i.e. at the location where all spectral components of the pulse are parallel and spatially separated. Different noise realizations in this single-pulse configuration were achieved by moving the scattering sheet perpendicular to the dispersed beam. The energy of the output beam was 10 $\mu$J. A long-wave pass filter (LWP) (LP02-785RU-25, Semrock, cutoff wavelength of 785nm) was used to block the high frequency components of the beam in front of the sample. The laser beam was focused into a quartz cuvette with a liquid sample (5 mm optical path) by a spherical mirror with 300 mm focal length. The transmitted laser

beam was collimated with a lens (150 mm focal length) and, after passing a short wave pass filter (SWP) (SP01-785RU-25, Semrock, cutoff wavelength of 785nm), coupled into the spectrometer (model 2035, McPhearson) equipped with a CCD camera (iDus DV400, Andor). The resolving power of the spectrometer in this case was 1.3 $cm^{-1}$.

In all our experiments, each measured anti-Stokes spectrum corresponded to a different noise realization. After normalization, each two consecutive spectra were subtracted from one another to remove the non-resonant background. An auto-correlation of the differential spectrum represented the result of a single NASCARS measurement. The statistical averaging of the auto-correlation was performed over 100 noise realizations.

# Bibliography


[1] D. Oron, N. Dudovich, D. Yelin, and Y. Silberberg, Physical Review Letters **88** (2002).

[2] D. Pestov, R. K. Murawski, G. O. Ariunbold, X. Wang, M. C. Zhi, A. V. Sokolov, V. A. Sautenkov, Y. V. Rostovtsev, A. Dogariu, Y. Huang, et al., Science **316**, 265 (2007).

[3] A. M. Zheltikov, Journal of Raman Spectroscopy **31**, 653 (2000).

[4] J. X. Cheng and X. S. Xie, Journal of Physical Chemistry B **108**, 827 (2004).

[5] M. O. Scully, G. W. Kattawar, R. P. Lucht, T. Opatrny, H. Pilloff, A. Rebane, A. V. Sokolov, and M. S. Zubairy, Proceedings of the National Academy of Sciences of the United States of America **99**, 10994 (2002).

[6] C. H. R. Ooi, G. Beadie, G. W. Kattawar, J. F. Reintjes, Y. Rostovtsev, M. S. Zubairy, and M. O. Scully, Physical Review A **72** (2005).

[7] J. X. Cheng, A. Volkmer, L. D. Book, and X. S. Xie, Journal of Physical Chemistry B **106**, 8493 (2002).

[8] M. Schmitt, G. Knopp, A. Materny, and W. Kiefer, Chemical Physics Letters **270**, 9 (1997).

[9] T. Lang, K. L. Kompa, and M. Motzkus, Chemical Physics Letters **310**, 65 (1999).

[10] D. Oron, N. Dudovich, and Y. Silberberg, Physical Review Letters **89** (2002).

[11] S. H. Lim, A. G. Caster, and S. R. Leone, Physical Review A **72** (2005).

[12] N. Dudovich, D. Oron, and Y. Silberberg, Nature **418**, 512 (2002).

[13] X. J. G. Xu, S. O. Konorov, S. Zhdanovich, J. W. Hepburn, and V. Milner, Journal of Chemical Physics **126** (2007).

[14] A. M. Weiner, Review of Scientific Instruments **71**, 1929 (2000).

[15] M. Shapiro and P. Brumer, *Principles of the Quantum Control of Molecular Processes* (Wiley, New York, 2003).

[16] D. Meshulach and Y. Silberberg, Nature **396**, 239 (1998).

[17] H. P. Lu and X. S. Xie, Nature **385**, 143 (1997).

[18] W. Schrof, J. F. Klingler, S. Rozouvan, and D. Horn, Physical Review E **57**, R2523 (1998).

[19] T. Rom, T. Best, D. van Oosten, U. Schneider, S. Folling, B. Paredes, and I. Bloch, Nature **444**, 733 (2006).

[20] M. J. Stimson, D. J. Ulness, and A. C. Albrecht, Chemical Physics Letters **263**, 185 (1996).

[21] M. J. Stimson, D. J. Ulness, and A. C. Albrecht, Journal of Raman Spectroscopy **28**, 579 (1997).

[22] O. Kinrot, I. S. Averbukh, and Y. Prior, Physical Review Letters **75**, 3822 (1995).

[23] I. S. Averbukh, M. Shapiro, C. Leichtle, and W. P. Schleich, Physical Review A **59**, 2163 (1999).

[24] B. von Vacano, W. Wohlleben, and M. Motzkus, Journal of Raman Spectroscopy **37**, 404 (2006).

[25] Y. Paskover, I. S. Averbukh, and Y. Prior, Optics Express **15**, 1700 (2007).

# Chapter 3

# Narrowband Spectroscopy by All-optical Correlation of Broadband Pulses

## 3.1 Motivation

In Chapter 2, the method of noise auto-correlation spectroscopy with coherent raman scattering (NASCARS) was introduced. NASCARS can extract the vibrational level spacing through autocorrelations of CARS spectra. The single pulse version of NASCARS method can be performed on a simple experiment setup without a pulse shaper. However, the limitation of NASCARS is obvious: the autocorrelation of the vibrational spectrum is not equivalent to the spectrum itself. It does not reflect absolute locations of the resonances, and the linewidth of the autocorrelation spectrum is often broader than that of the spectrum. In this chapter, the method of narrowband spectroscopy by all-optical correlation of broadband pulses is introduced to give the absolute location of the vibrational levels. This method is based on a cross-correlation optical processing between the CARS signal and a reference pulse of broad bandwidth.

The cross-correlation optical processing is related to sum frequency generation between the CARS field $E_{CARS}(t)$ and a reference field $E_{ref}(t)$. The cross-correlation field $E_{SFG}(t)$ is proportional to the product of the CARS

[0]A version of this chapter is in-press as Stanislav O. Konorov, Xiaoji G. Xu, John. W. Hepburn and Valery Milner "Narrowband Spectroscopy by All-optical Correlation of Broadband Pulses", in *Physical Review A*

field and the reference field

$$E_{SFG}(t) \propto E_{CARS}(t) \cdot E_{ref}(t) \tag{3.1}$$

The CARS field $E_{CARS}(t)$ is proportional to the product between the vibrational coherence R(t) and the probe pulse field $E_{pr}(t)$

$$E_{CARS}(t) \propto E_{pr}(t) \cdot R(t) \tag{3.2}$$

One can combine expressions (3.1) and (3.2), and the order of multiplication can be regrouped into:

$$E_{SFG}(t) = R(t) \cdot [E_{pr}(t) \cdot E_{ref}(t)] \tag{3.3}$$

The time domain spectrum of the cross-correlation signal is obtained through Fourier transform.

$$E_{SFG}(\omega) = R(\Omega) \otimes fft\{[E_{pr}(t) \cdot E_{ref}(t)]\}[\omega] \tag{3.4}$$

Following the same line of reasoning as in section 5.1, the efficiency of the information transfer from the vibrational coherence R(t) is affected by the temporal shape of $[E_{pr}(t) \cdot E_{ref}(t)]$. The desirable pulse product $[E_{pr}(t) \cdot E_{ref}(t)]$ in the time domain should have a long duration so as to overlap with the duration of R(t). In the frequency domain, the Fourier transform of pulse pairs $[E_{pr}(t) \cdot E_{ref}(t)]$ should give a narrow band frequency component. In this chapter, two broad band pulses $E_1$ and $E_2$ that can generate a sum-frequency spectrum with only one narrow band frequency component is defined as a conjugate pulse pair. The ideal mathematical definition is $\delta(\omega) \equiv E_1(\omega) \otimes E_2(\omega)$.

A simple realization of such a conjugate pair can be found by creating chirped pulses. If the probe pulse and reference pulse contains the same amount of chirp but with opposite sign, the products of $[E_{pr}(t) \cdot E_{ref}(t)]$ will show long time duration and a narrow frequency bandwidth in the frequency domain. Experimentally, one pulse from a conjugate pair is used

as a probe pulse, then other pulse can be used to perform sum frequency generation with the CARS field and the sum frequency spectrum should reflect the profile of the vibrational coherence $R(\Omega)$.

Because creating such a conjugate pulse pair needs two pulse shapers, which inevitably increases experimental complexity, a further investigation was made to find a self-conjugate pulse i.e. $[E_{pr}(t) \equiv E_{ref}(t)]$. Such a pulse should satisfy the requirement of having a long duration of $E_{pr}^2(t)$ and a narrow bandwidth in the second harmonic spectrum. The self-conjugate pulse is used as both the probe pulse in the CARS generation and the reference pulse in the sum frequency generation.

One type of spectral phase pattern that is particularly useful on generating a narrow band second harmonic spectrum is the anti-symmetric spectral phase:

$$\phi(\omega_c + \Delta) = -\phi(\omega_c - \Delta) \tag{3.5}$$

with $\omega_c$ being the pulse center. Such pulse shapes has been systematically studied by Dantus and coworkers [1, 2]. The generation of narrow band frequency component of $E_{pr}(t) \cdot E_{pr}(t)$ in the frequency domain can be understood by the following derivation.

The frequency domain spectrum of the field product $E_{pr}(t) \cdot E_{pr}(t)$ is equivalent to the second harmonic generation expression (3.6)

$$E_{SHG}(\omega) = \int_{-\infty}^{\infty} E_{pr}(\Omega) E_{pr}(\omega - \Omega) d\Omega \tag{3.6}$$

The spectrum of $E_{SHG}$ at the frequency of $2\omega$ is

$$E_{SHG}(2\omega) = \int_{-\infty}^{\infty} |E_{pr}(\Omega)| \cdot |E_{pr}(2\omega - \Omega)| e^{i\Phi} d\Omega \tag{3.7}$$

with $e^{i\Phi}$ as the phase term, it is the sum of spectral phase $\Phi(2\omega) = \phi(\Omega) + \phi(2\omega - \Omega)$. With the condition that the spectral phase of the probe pulse satisfies $\phi(\omega_c + \delta) = -\phi(\omega_c - \delta)$ for all $\Delta$, it is not hard to find that the phase term $\Phi = 0$ when $\omega = \omega_c$ and $\Delta = \Omega - \omega_c$. With the spectral phase term $\Phi$ equal to zero at the center of SFG spectrum $2\omega_c$, the integral of the expression (3.7) reaches its maximal value, giving a peak in the spectrum.

The anti-symmetric spectral phase pattern provides a peak at twice the central frequency.

However, having the anti-symmetric spectral phase pattern is not the only requirement for the self-conjugate pulse. A pulse that has anti-symmetric spectral phase pattern can also have other frequency components in the second harmonic spectrum. An extreme case is the transform-limited pulse. With the spectral phase equals zero, the transform-limited pulse trivially satisfies the requirement set by expression (3.5). But the second harmonic spectrum of the transform-limited pulse has a broad peak rather than a narrow peak. To further narrow down the peak of the second harmonic, the spectral phase modulation based on noise was investigated. When the uncorrelated high amplitude spectral noise is introduced into the pulse in addition to the anti-symmetric spectral phase requirement, the second harmonic spectrum is narrowed. However, due to the finite pixel number of the pulse shaper, even with the anti-symmetry spectral phase restriction, random noise patterns often create residual peaks beside the central peak in the second harmonic spectrum. To remove the residual peaks in the second harmonic spectrum, the genetic algorithm optimization was further used.

The genetic algorithm (GA) has been used in many applications in chemical physics[3, 4]. It uses the experiment or process output as a fitness value, optimizing input parameter sets to find the best fitness value through hybridization of multiple best parameter sets. With the utilization of the pulse shaper, the spectral phase of a broad band pulse can be used as input parameters, and GA can search the best available phase pattern to fulfill a given task. The optimization on the narrow central peak in the second harmonic spectrum can then be addressed through a GA optimization.

The experiment started with the measurement of the probe pulse spectrum. Then, a computer-run GA optimization searching for the good quality self-conjugate probe pulse was carried out. Then the pulse shaper tailored the phase shape of the probe pulse according to the GA output. The CARS signal was generated by pump/Stokes and probe pulses and collimated to generate the sum frequency signal in a nonlinear crystal. As the article section shows, the sum frequency spectrum showed the exact spectrum of the

vibrational coherence $R(\Omega)$.

The method of "narrowband spectroscopy by all-optical correlation of broadband pulses" can achieve a good resolution vibrational spectrum while using all broad band pulses. Comparing to NASCARS, the method gives the spectrum of the vibrational resonances rather than the autocorrelation of the spectrum. The resolution of this method is limited by the bandwidth of the central peak in the second harmonic spectrum of the optimized self-conjugate probe pulse. It is not limited by the broad bandwidth of the probe pulse. However, this method requires additional experiment instruments on generating the SFG signal when compared to a typical multiplex CARS setup. The current intensity of the generated SFG signal is lower than the direct CARS signal by two orders of magnitude, which is due to the low conversion efficiency of the nonlinear crystal. With better non-linear crystal, the signal strength can be further improved.

## 3.2 Experimental Technique Considerations

In addition to a typical BOXCARS geometry CARS setup (figure 1.23), the optical processing of CARS requires additional experimental setup for sum frequency generation. The generated CARS signal has to be mixed with the reference pulse in a nonlinear crystal. Nonlinear mixing is usually done with high intensity pulses. Due to the weak intensity of CARS signal, it requires careful work to achieve the spatial overlapping between CARS signal and the reference probe pulse. The spatial overlapping of weak pulses was facilitated by using a small pin hole mounted on a two dimensional adjustable translation stages. Excitation pulses were adjusted to pass through the pin hole. A typical surveillance camera behind the pin hole was used to monitor the laser beam position.

The thickness of the nonlinear crystal is also a concern for the intensity of the SFG signal. The choice is primarily between the efficiency and distortion. Thicker crystals give higher conversion efficiency, but are more limited in phase matching conditions than thinner crystals. Both $30\mu m$ and $100\mu m$ type-I BBO crystal were used in the experiment. The thin $30\mu m$ crystal is

insensitive to crystal angle on sum frequency generation but gives low signal strength due to a short interaction length. The $100\mu m$ type-1 BBO gives good conversion efficiency but require adjustment on the crystal orientation. In the experiment demonstration, the $100\mu m$ crystal was used. The detailed calculation can be carried use the equation (1.51) in section 1.3.

To reduce the dispersion that comes from light passing through lenses, mirrors were used as the collimating and focusing element in the CARS generation and sum frequency generation. To compensate the group velocity dispersion, the beam-split reference probe pulse went through an identical sample cell. The dispersion compensation techniques was found to be able to improve signal to noise ratio for the final sum-frequency spectrum.

## 3.3 Method Content

### 3.3.1 Overview

High peak power ultrafast lasers are widely used in nonlinear spectroscopy but often limit its spectral resolution because of the broad frequency bandwidth of ultrashort laser pulses. Improving the resolution by achieving spectrally narrow excitation of, or emission from, the resonant medium by means of multi-photon interferences has been the focus of many recent developments in ultrafast spectroscopy. We demonstrate an alternative approach, in which high resolution is exercised by detecting narrow spectral correlations between broadband excitation and emission optical fields. All-optical correlation analysis, easily incorporated into the traditional spectroscopic setup, enables direct, robust and simultaneous detection of multiple narrow resonances with a single femtosecond pulse.

### 3.3.2 Content

With recent advances of ultrafast laser sources, featuring high optical field amplitudes at low average power, coherent nonlinear spectroscopy with femtosecond (fs) pulses has been recognized as a promising tool for time-resolved chemical analysis [5–7], remote sensing of complex molecules [8, 9] and non-

invasive imaging of biological objects [10–12]. Due to the broad spectral width of ultrashort pulses, femtosecond spectroscopy often lacks spectral resolution. The latter can be recovered by complementing the frequency resolved measurement with the time-delay scanning [13, 14], or by combining the broadband fs excitation with the narrowband probing by picosecond pulses from a separate laser source [15] or a spectral slice of a femtosecond source [16, 17] ("multiplex CARS"). Alternatively, higher resolution can also be achieved without resorting to narrowband pulses and without the time-consuming delay scans. As many nonlinear optical methods involve interferences between multiple photons of different frequencies from under the same pulse bandwidth, improving the resolution is possible by controlling these interferences with spectral pulse shaping [18]. Spectral resolution, significantly better than the broad bandwidth of ultrashort laser pulses, has been achieved in second harmonic generation [19], multi-photon absorption [1, 20, 21] and coherent Raman scattering [22, 23] of shaped femtosecond pulses.

In this work we focus on Coherent Anti-Stokes Raman Scattering (CARS) which has become a popular method in nonlinear optical spectroscopy and microscopy because of its high sensitivity to molecular structure [24]. In CARS, two laser photons, "pump" and "Stokes", excite the coherent molecular vibrations, which then scatter a third, "probe", photon generating the anti-Stokes signal. Despite the broad spectrum of the femtosecond pump and Stokes pulses, their collective two-photon field can be spectrally narrowed by means of the pulse chirping [25] or shaping [22], providing selectivity of Raman excitation. On the other hand, shaping of the probe pulse have been used for narrowing the spectrum of the anti-Stokes emission [23]. In both cases, the spectral line narrowing is a result of a delicate interference of the input fields inside the Raman medium. As such, it is sensitive to the proper choice of the pulse shapes, non-resonant background and interferometrically stable time delays.

In the recently demonstrated method of noise-autocorrelation spectroscopy [26], we have eliminated the requirement of an accurate pulse shaping, while achieving high spectral resolution without delay scanning and bandwidth

multiplexing. The method is based on the detection of optical field correlations in the coherently scattered light. The correlations are induced by the vibrational resonances, and therefore carry the information about the Raman spectrum of the medium. The auto-correlation of the Raman spectrum has been extracted via computer post-processing of the measured data, which involved numerical correlation analysis with averaging over multiple noise realizations.

Here, we show that spectral correlations in the coherently scattered broadband anti-Stokes radiation can produce a narrowband optical Raman spectrum similar to that obtained with spontaneous Raman or multiplex CARS, yet without the narrowing of the pulse bandwidth. We take advantage of the possibility to detect optical correlations between two broadband pulses by means of the non-resonant interferences in the sum-frequency generation (SFG) of those pulses in the external nonlinear crystal [27]. We start with the two pulses (hereafter called "conjugate" probe, $E_{pr}$, and reference, $E_{ref}$) designed to exhibit narrow single-peak SFG spectrum,

$$E_{pr+ref}(\Omega) \propto \left| \int E_{pr}(\omega) E_{ref}(\Omega - \omega) d\omega \right|^2 \propto \delta(\Omega - \omega_c), \tag{3.8}$$

where $\delta$ is the Dirac $\delta$-function and $\omega_c$ represents the central frequency of the probe/reference SFG spectrum. The probe pulse is then scattered off the molecular vibrations, generating the anti-Stokes pulse. Finally, the resonance-induced correlations in the anti-Stokes light are optically processed by mixing the CARS signal with the reference pulse. The measured CARS/reference SFG spectrum, $I_{\mathrm{CARS}+ref}(\Omega) \propto |\int E_{\mathrm{CARS}}(\omega) E_{ref}(\Omega - \omega) d\omega|^2$, reflects the narrow vibrational modes of the medium as described below.

In CARS, coherent molecular vibrations are excited by a two-photon field of the simultaneously applied transform-limited pump and Stokes pulses, $E_p$ and $E_S$, respectively (black lines in Fig.3.1(a)). The induced vibrational coherence can be expressed as a product of the excitation spectrum and the spectrum of the Raman modes [14]:

$$R(\Omega) = A(\Omega) \times \left( \sum\nolimits_k C_k(\Omega) + C_{\mathrm{NR}} \right), \tag{3.9}$$

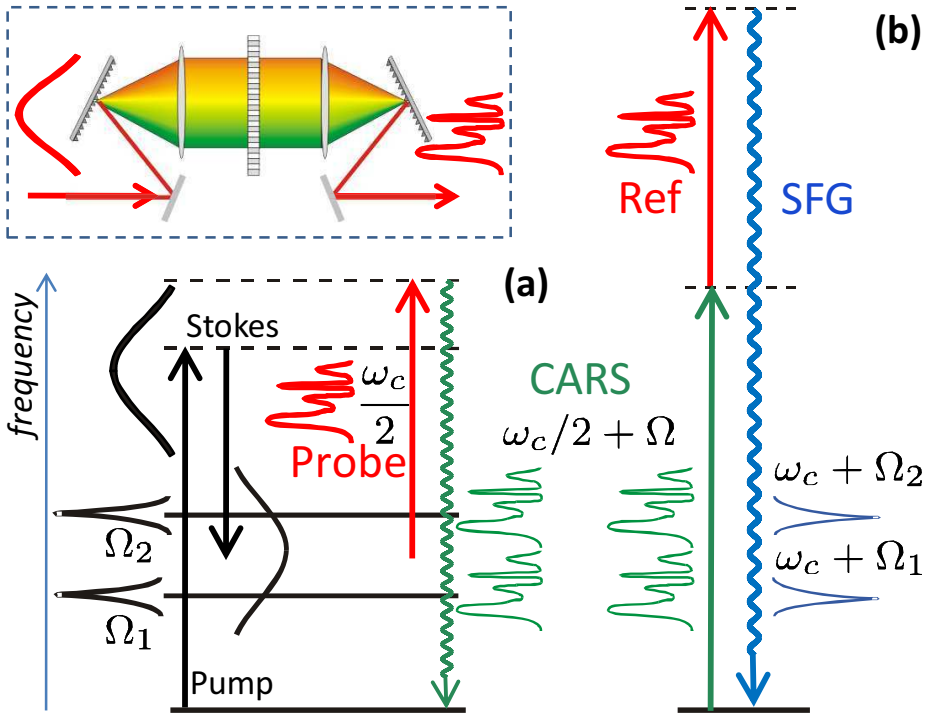


Figure 3.1: (Color online) (a) Schematic representation of the coherent anti-Stokes scattering of the spectrally shaped probe pulse (red) off the molecular vibrations at $\Omega_1$ and $\Omega_2$, induced by the transform-limited pump and Stokes pulses (black). (b) an all-optical retrieval of the narrowband Raman spectrum by means of the sum-frequency mixing of CARS and reference pulses in a separate nonlinear crystal. In this work, reference pulse is a replica of the probe pulse, spectrally shaped by means of the liquid crystal based pulse shaper (inset).

where $A(\Omega) = \int E_p(\omega)E_S(\Omega - \omega)d\omega$, $C_k(\Omega)$ represents the contribution of the $n$th resonance, and the non-resonant background is denoted $C_{\mathrm{NR}}$. Anti-Stokes scattering of the probe field, $E_{pr}$, off the molecular vibrations results in the CARS signal, $E_{\mathrm{CARS}}$, which in the time domain can be written as:

$$E_{\mathrm{CARS}}(t) \propto R(t)E_{pr}(t), \tag{3.10}$$

with $R(t)$ being the Fourier transform of the spectral response, $R(\Omega)$. The sum-frequency generation field of the CARS and reference pulses is, therefore:

$$E_{\mathrm{CARS}+ref}(t) \propto E_{\mathrm{CARS}}(t)E_{ref}(t) = E_{pr}(t)E_{ref}(t)R(t), \tag{3.11}$$

which in the frequency domain corresponds to the convolution of the probe/reference SFG spectrum, $E_{pr+ref}(\omega)$, and the vibrational spectrum of the medium:

$$E_{\mathrm{CARS}+ref}(\omega_c + \Omega) = \int E_{pr+ref}(\omega_c - \Delta)R(\Omega + \Delta)d\Delta. \tag{3.12}$$

Thus, by narrowing the spectrum of $E_{pr+ref}$ (Eq.3.8), one can establish an exact correspondence between $E_{\mathrm{CARS}+ref}(\omega_c + \Omega)$ and $R(\Omega)$, retrieving the Raman frequency shifts directly from the measured SFG signal.

Unlike the all-optical processing used in multiplex CARS and based on the resonant interference between the excited vibrational states and their precise amplitude and phase shaping [28], our approach does not require any prior knowledge on the vibrational frequencies of the molecules. It is also not sensitive to the particular spectral shape of the probe pulses as long as the conjugation condition of Eq.3.8 is satisfied. The conjugate probe and reference pulses can be generated by various means, including simple frequency chirping or frequency down conversion [29]. Here, we employ spectral pulse shaping to create a "self-conjugate" pulse, i.e. a broadband pulse with a narrowband second harmonic, $E_{pr+ref}(\Omega) \rightarrow E_{pr+pr}(\Omega)$. The self-conjugate field serves both as the probe and the reference, thus eliminating the need of dealing with two separate pulses and simplifying the experimental setup. This result, shown schematically in Fig.3.1(b), provides the basis for the experimental method demonstrated in this work.

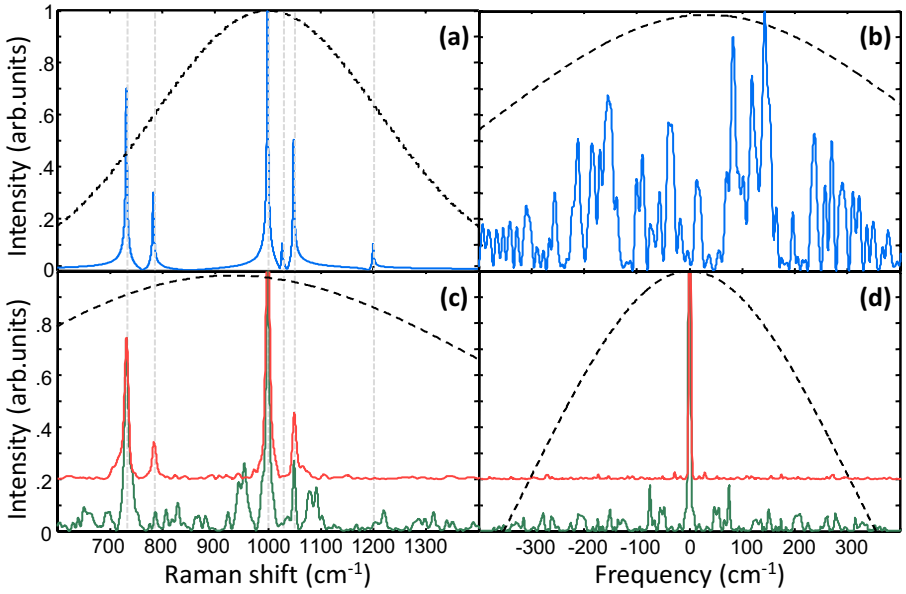


Figure 3.2: (Color online) Numerical simulations of the proposed method. (a) Model spectrum of a toluene/orto-xylene mixture. (b) Calculated CARS spectrum for the case of a pseudo-randomly shaped probe (see text). (c,d) Calculated spectra of the CARS/probe SFG and probe SHG signals, respectively, for the case of the non-optimized (green) and optimized (red) pseudo-random probe shaping. The line width is defined by the frequency resolution of the model pulse shaper (4.7 $cm^{-1}$), rather than by the overall bandwidth of the probe pulse (dashed lines).

Self-conjugate pulses can be generated by shaping the original transform-limited femtosecond pulse with a pseudo-random binary phase mask [30]. As a two-photon process, second harmonic generation (SHG) at any given frequency $\omega_c$ is defined by the interference of multiple photon pairs, whose total frequency adds up to $\omega_c$. For this to result in a narrowband spectrum, the interference must be constructive at $\omega_c$ and destructive everywhere else. The first requirement is known to be satisfied by the condition $E_{pr}(\omega_c/2 - \Delta) = E^*_{pr}(\omega_c/2 + \Delta)$ [20], which can be realized by applying an anti-symmetric spectral phase shaping around $\omega_c/2$. Destructive interference can be achieved by randomizing the spectral phase of the pulse while preserving the anti-symmetric property [30, 31].

Calculations of the sum-frequency mixing of the probe and CARS pulses (Eq.3.12), and its correspondence to the model vibrational spectrum of the medium, are shown in Fig.3.2(a,c). First, an uncorrelated white noise, anti-symmetrized around the central frequency, has been added to the phase of the originally transform-limited probe field through a model pulse shaper. Owing to the presence of Raman resonances and despite the uncorrelated noise in the probe, spectral correlations are created in the CARS field. Though not apparent in the CARS signal itself (Fig.3.2(b)), they produce sharp peaks in the CARS/probe SFG spectrum (Fig.3.2(c)), which can be clearly assigned to the corresponding Raman lines.

Unfortunately, residual correlations in the random phase give rise to the artificial lines and lower signal-to-noise ratio, seen both in the CARS/probe SFG and probe/probe SHG spectra (Fig.3.2(c) and (d),respectively). To improve the quality of the signal, we performed a numerical optimization based on the genetic algorithm search of a pseudo-random binary phase mask (constrained to 0 and $\pi$ radian only [30]) resulting in the narrowest calculated probe SHG spectrum. Due to the finite spectral resolution of the pulse shaper and, therefore, finite width of the optimized SHG, the correspondence between $E_{\mathrm{CARS}+pr}(\omega_c + \Omega)$ and $R(\Omega)$ in Eq.3.12 is not exact. Hence, using the CARS/probe SFG line width as a fitness parameter improved the performance of the method even further, but required *a priori* assumption about the line width of the Raman resonances. The resulting pseudo-random bi-

nary masks were used in the experiments described below.

The experimental setup (Fig.3.3) was based on a standard Ti:Sapphire regenerative amplifier, producing 40 fs probe pulses at the central wavelength of 800 nm and 1 KHz repetition rate. An optical parametric amplifier generated the pump and Stokes beams at 1111 and 1250 nm, respectively. Pre-calculated spectral phase has been applied to the probe pulses by means of a home-made pulse shaper based on a liquid-crystal spatial light modulator (see inset in Fig.3.1) and provided spectral resolution of 10 $cm^{-1}$. Pump, Stokes and probe pulses, about 2 $\mu$J each, have been focused by a silver coated mirror into a quartz cuvette with liquid toluene, where they overlapped in time and space in the standard BOXCARS phase-matching geometry. CARS signal has been then collimated and focused onto a 100 $\mu$m BBO crystal, together with the reference pulse which has been split off the shaped probe pulse in front of the sample. Sum-frequency signal from the nonlinear mixing of the CARS and reference pulses has been coupled into a high-resolution spectrometer equipped with a CCD camera, and typically accumulated for about 1 minute.

Experimental SFG spectra are presented in Fig.3.4(a). The spontaneous Raman spectrum of toluene, measured separately, is shown at the top of the plot for reference. Below it, the two signals with sharp peaks of much narrower width than the bandwidth of the probe pulse, attest to the high resolution of the proposed method. The position of the two peaks of the center curve match the frequencies of the two strong Raman modes of toluene around 1000 and 784 $cm^{-1}$, covered by the broad bandwidth of the pump/Stokes pulse pair. The latter is demonstrated by the observed CARS signal, with and without phase shaping, in plot (b). The apparently random CARS intensity distribution in the shaped case results from the presence of Raman modes and carries the information about their frequencies, which is revealed in the CARS/probe SFG spectrum.

The SFG spectrum at the bottom of Fig.3.4(a) exhibits low signal-to-noise ratio as a result of the lack of the phase mask optimization. An optimized mask has resulted in higher quality spectrum shown in the middle of the plot. Note that the optimization has not been performed during the experiment

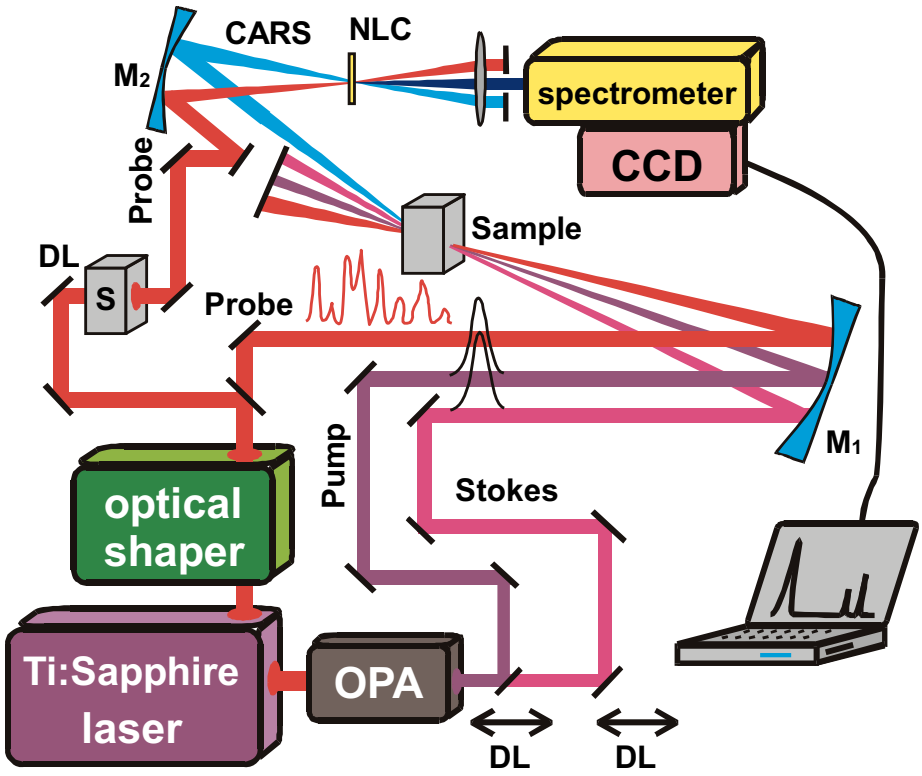


Figure 3.3: Experimental setup. Transform-limited pump and Stokes pulses from an optical parametric amplifier (OPA) and a shaped probe pulse from the pulse shaper are focused on a 5 mm thick sample by a 20 cm focal length mirror ($M_1$). Output CARS pulse is then focused by a similar mirror ($M_2$) on a nonlinear crystal (NLC), together with a replica of the probe pulse, to produce a sum-frequency generation signal, which is detected by a spectrometer (spectral resolution of 0.05 nm). The probe beam, used as a reference, is passed through an identical sample cuvette (S) to compensate the accumulated dispersion of the CARS signal. DL - delay lines.

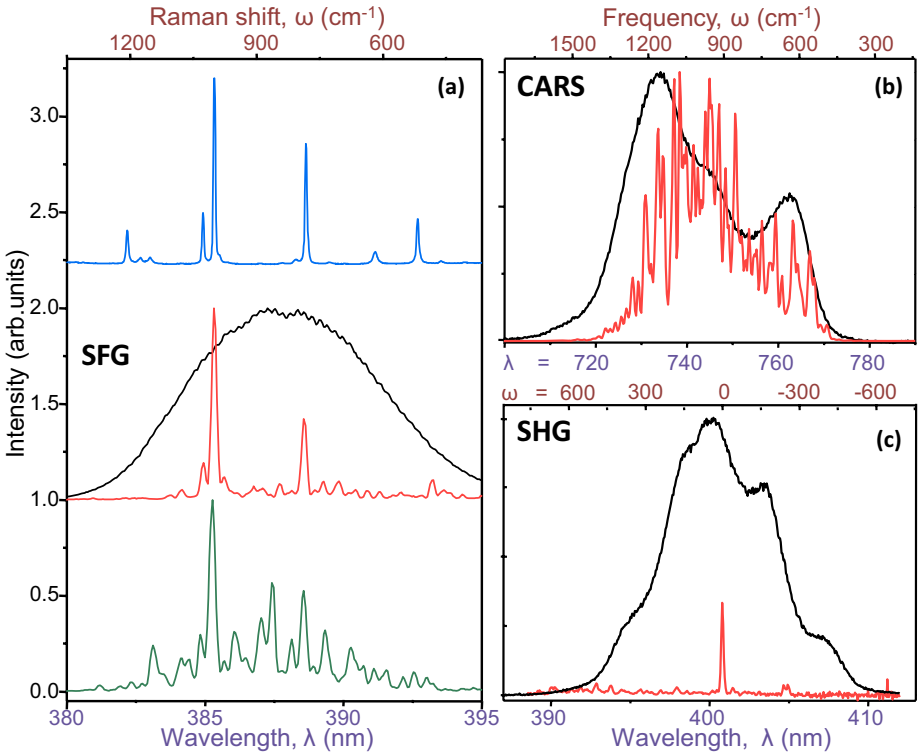


Figure 3.4: (Color online) (a) Experimentally observed CARS/probe SFG spectra (middle and bottom) in comparison to the spectrum of spontaneous Raman scattering (top). Black, green and red curves correspond to the case of unshaped, non-optimized shaped and optimized shaped probe pulse, respectively. (b) CARS spectra for the shaped (red) and unshaped (black) probe pulses. (c) The spectra of the second harmonic of the shaped (red) and unshaped (black) probe pulses.

in an adaptive feedback-controlled fashion, in which the observed spectral contrast would have been used as a fitness parameter. Instead, we have pre-calculated our binary phase masks for the anticipated resonance line width and the measured characteristics of the probe pulse (i.e. its spectral intensity and phase before shaping). The latter proves critical for the quality of the observed SFG signal. We therefore attribute the unequal performance of different masks to the uncertainty in characterizing the probe pulse, which will be improved in the future.

As expected, spectral narrowing of the CARS/probe SFG signal is accompanied by the corresponding narrowing of the probe's second harmonic, shown in Fig.3.4(c). We have found that for our experimental parameters, better peak-to-background contrast in the SFG always corresponds to the better contrast of the SHG peak. The reason for this is the insufficient resolution of our pulse shaper for resolving the line width of the observed Raman modes (10 $cm^{-1}$ vs 3 $cm^{-1}$, respectively). As a result, the optimization is almost insensitive to the width of the resonant lines and works equally well for both the SFG and SHG narrowing. This however, may not be true for the case of higher resolution shaping.

The demonstrated approach presents an alternative to the existing methods of high-resolution Raman spectroscopy with ultrashort pulses, which typically rely on the delay scanning, interferometric stability, or post-processing of the acquired data. All-optical correlation analysis is performed separately from the resonant medium of interest, reducing the sensitivity of the method to non-resonant background, precise time delays, and other laser parameters. The ability to detect Raman peaks directly in the measured SFG spectrum may prove invaluable for the applications in microscopy. For instance, sensitive detection of the integral SFG signal, passed through an appropriate frequency filter, could quickly identify the presence of a certain Raman mode without the need of a spectrometer. Though this type of detection is similar to the traditional spontaneous Raman or multiplex CARS spectroscopy, the proposed method utilizes the whole spectral bandwidth and high peak power of femtosecond pulses, thus suggesting the possibility for higher sensitivity or faster data retrieval. In the proof-of-principle work presented here,

the speed was limited by the low efficiency of the sum-frequency generation. This can be improved by using thicker nonlinear crystals with optimized dispersion properties, and by increasing the power of a reference pulse. Pre-calculated phase masks may enable selective detection of resonances with the specified line width, while avoiding time consuming feedback-controlled optimization.

# Bibliography


[1] I. Pastirk, J. M. Dela Cruz, K. A. Walowicz, V. V. Lozovoy, and M. Dantus, Optics Express **11**, 1695 (2003).

[2] V. V. Lozovoy, B. W. Xu, J. C. Shane, and M. Dantus, Physical Review A **74** (2006).

[3] R. S. Judson and H. Rabitz, Physical Review Letters **68**, 1500 (1992).

[4] A. Assion, T. Baumert, M. Bergt, T. Brixner, B. Kiefer, V. Seyfried, M. Strehle, and G. Gerber, Science **282**, 919 (1998).

[5] T. H. Joo, M. A. Dugan, and A. C. Albrecht, Chemical Physics Letters **177**, 4 (1991).

[6] M. Schmitt, G. Knopp, A. Materny, and W. Kiefer, Chemical Physics Letters **270**, 9 (1997).

[7] T. Lang, K. L. Kompa, and M. Motzkus, Chemical Physics Letters **310**, 65 (1999).

[8] M. O. Scully, G. W. Kattawar, R. P. Lucht, T. Opatrny, H. Pilloff, A. Rebane, A. V. Sokolov, and M. S. Zubairy, Proceedings of the National Academy of Sciences of the United States of America **99**, 10994 (2002).

[9] C. H. R. Ooi, G. Beadie, G. W. Kattawar, J. F. Reintjes, Y. Rostovtsev, M. S. Zubairy, and M. O. Scully, Physical Review A **72** (2005).

[10] A. Zumbusch, G. R. Holtom, and X. S. Xie, Physical Review Letters **82**, 4142 (1999).

[11] E. O. Potma, W. P. de Boeij, P. J. M. van Haastert, and D. A. Wiersma, Proceedings of the National Academy of Sciences of the United States of America **98**, 1577 (2001).

[12] J. X. Cheng and X. S. Xie, Journal of Physical Chemistry B **108**, 827 (2004).

[13] M. Heid, S. Schlucker, U. Schmitt, T. Chen, R. Schweitzer-Stenner, V. Engel, and W. Kiefer, Journal of Raman Spectroscopy **32**, 771 (2001).

[14] X. J. G. Xu, S. O. Konorov, S. Zhdanovich, J. W. Hepburn, and V. Milner, Journal of Chemical Physics **126** (2007).

[15] J. X. Cheng, A. Volkmer, L. D. Book, and X. S. Xie, Journal of Physical Chemistry B **106**, 8493 (2002).

[16] D. Oron, N. Dudovich, and Y. Silberberg, Physical Review Letters **90** (2003).

[17] S. H. Lim, A. G. Caster, and S. R. Leone, Physical Review A **72** (2005).

[18] A. M. Weiner, Review of Scientific Instruments **71**, 1929 (2000).

[19] Z. Zheng and A. M. Weiner, Chemical Physics **267**, 161 (2001).

[20] D. Meshulach and Y. Silberberg, Nature **396**, 239 (1998).

[21] V. V. Lozovoy, I. Pastirk, K. A. Walowicz, and M. Dantus, Journal of Chemical Physics **118**, 3187 (2003).

[22] N. Dudovich, D. Oron, and Y. Silberberg, Nature **418**, 512 (2002).

[23] D. Oron, N. Dudovich, D. Yelin, and Y. Silberberg, Physical Review Letters **88** (2002).

[24] A. M. Zheltikov, Journal of Raman Spectroscopy **31**, 653 (2000).

[25] E. T. J. Nibbering, D. A. Wiersma, and K. Duppen, Physical Review Letters **68**, 514 (1992).

[26] X. G. Xu, S. O. Konorov, J. W. Hepburn, and V. Milner, Nature Physics **4**, 125 (2008).

[27] J.-C. Diels and W. Rudolph, *Ultrashort Laser pulse Phenomena* (Academic Press, 2006), 3rd ed.

[28] D. Oron, N. Dudovich, and Y. Silberberg, Physical Review A **70** (2004).

[29] B. Dayan, A. Pe'er, A. A. Friesem, and Y. Silberberg, Physical Review Letters **93** (2004).

[30] M. Comstock, V. V. Lozovoy, I. Pastirk, and M. Dantus, Optics Express **12**, 1061 (2004).

[31] Z. Zheng and A. M. Weiner, Optics Letters **25**, 984 (2000).

# Chapter 4

# Complete Characterization of Molecular Vibrations using Frequency Resolved Gating

## 4.1 Motivation

As discussed in section 1.3, the purpose of CARS is to prepare the vibrational coherence and recover its information through spectroscopic measurement. However, the vibrational coherence $R(\Omega)$ contains both amplitude and phase information. The traditional CARS methods described in chapter 1.2 and the methods that are presented in chapter 2 and chapter 3 cannot measure the phase of the vibrational coherence. In this chapter, the method of "Complete Characterization of Molecular Vibrations using Frequency Resolved Gating"is presented to experimentally retrieve the phase and amplitude information of the vibrational coherence from CARS spectra.

As described in chapter 2, the method of NASCARS provides a simple way to extract the vibrational spacing of resonances through obtaining the autocorrelation of the vibrational coherence spectrum. In chapter 3, the method of narrowband spectroscopy by all-optical correlation of broadband pulses used optical processing techniques on the broad band CARS signal to

[0] A version of this chapter has been published as Xiaoji G. Xu, Stanislav O. Konorov, Sergey Zhdanovich, John. W. Hepburn and Valery Milner "Complete Characterization of Molecular Vibrations using Frequency Resolved Gating" *Journal of Chemical Physics* Vol. 126 No.9, 2007

obtain the high resolution CARS spectrum. This spectrum contains more information on resonant levels than the autocorrelation of the spectrum. However, neither method can recover phase information. The phase information of the vibrational coherence reflects the excitation conditions as well as the time domain behavior of the prepared vibrational levels. Moreover, as shown in figure 1.10 of section 1.2, with phase information the Fourier transform directly links the complex spectrum of the vibrational coherence with the time domain beating of the vibrational coherence and vice versa. As a property of the Fourier transform, the resolution of the vibrational coherence in the frequency domain is determined by the total duration of the time domain response.

The CARS signal in the frequency domain is the convolution between the probe pulse $E(\omega)$ and the vibrational coherence $R(\Omega)$. The convolution process means that the frequency domain profile of the vibrational coherence is broadened by the probe pulse spectrum. To recover $R(\Omega)$ from the CARS spectrum, one seemingly obvious solution is to perform a reverse operation to the convolution i.e. deconvolution. However, the direct deconvolution process itself is not a mathematically easy question [1]. It requires a high signal to noise ratio spectrum and the exact form of the broadening function i.e. the probe pulse. Moreover, the convolution between $R(\Omega)$ and the probe pulse is done in the complex domain, but the measured CARS spectra do not contain the phase of the anti-Stokes field. This lack of phase information in the CARS field further undermines the feasibility of the direct deconvolution approach.

The cross-correlation frequency resolved optical gating (XFROG) technique was invented by S. Linden et.al.[2] and is based on the pulse characterization technique of frequency resolved optical gating (FROG). It uses a well characterized reference pulse performing sum-frequency generation (SFG) or difference-frequency generation (DFG) with the optical pulse. The SFG or DFG spectra are recorded to form XFROG trace by scanning the time delay between the reference pulse and the unknown pulse. With complete information of the reference pulse, the XFROG algorithm then recovers the amplitude and the phase of the unknown pulses from the recorded data.

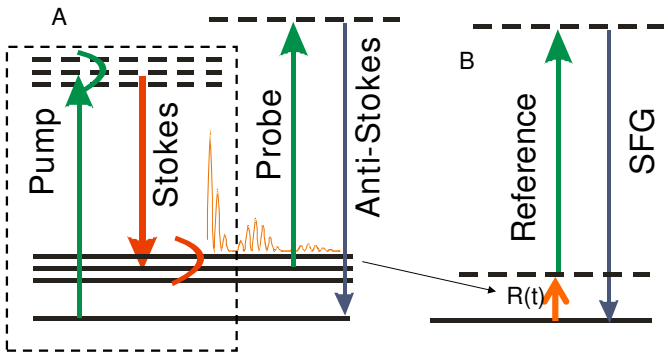


Figure 4.1: Figure A shows the scheme for the CARS process and figure B shows that of SFG. The CARS process and be alteratively regarded as a generalized version of SFG between the vibrational coherence $R(\Omega)$ and the probe field.

As discussed in section 1.3, the coherent scattering step of CARS can be treated as sum-frequency generation between the probe pulse and the vibrational coherence. Correspondence between CARS and SFG is shown in Figure 4.1. The reference pulse in SFG corresponds to the probe pulse in CARS, and the unknown pulse in SFG corresponds to the prepared vibrational coherence. Considering the fact that the mathematical algorithm of XFROG works with sufficient input parameters and data, there is a possibility of extending the XFROG technique to CARS for recovering the profile of $R(\Omega)$.

A method for complete characterization of molecular vibration was proposed based on such reasoning. It requires the experimental characterization of the probe pulse in CARS (corresponding to the reference pulse in the XFROG technique) and scanning the time delay between the probe pulse and the pump/Stokes pair and recording CARS spectra at different time delays. These CARS spectra form a spectrogram with frequency and time delay (corresponding to the XFROG trace). After the CARS spectrogram is obtained, the XFROG algorithm is used to recover the amplitude and the phase of the vibrational coherence.

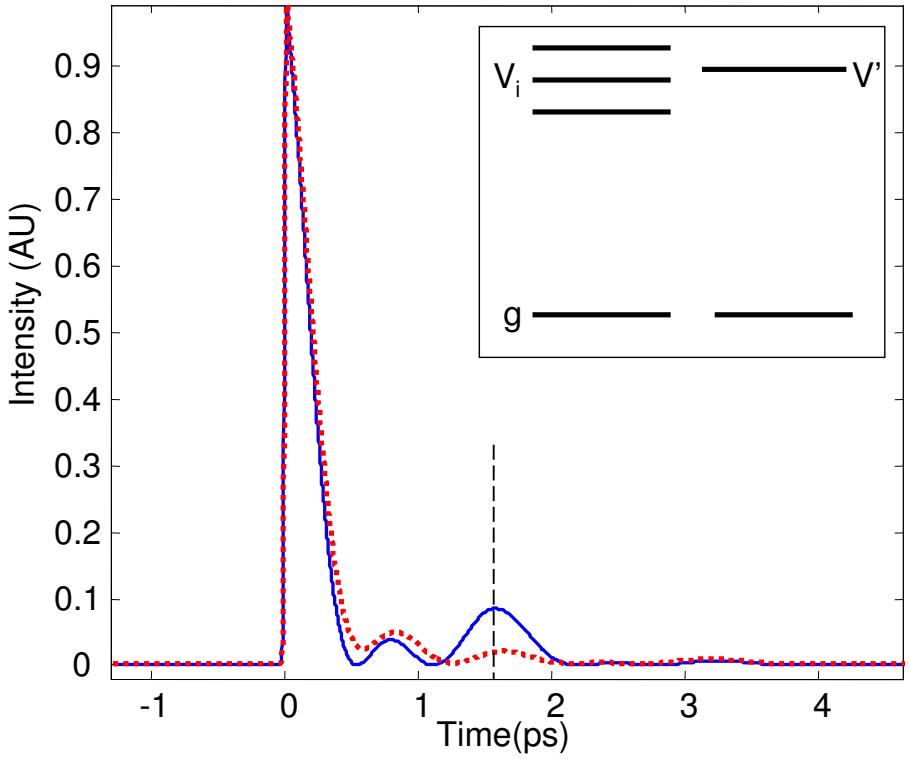


Figure 4.2: The blue continuous curve shows the time beating of a system with 3 excited state levels that are equally spaced. The vibrational beating maximum can be found at 1.6ps (vertical dashed line). The red dashed curve shows the overall beating with another resonant level close to the three level system. Energy levels of the pure sample and the additional component are shown in the inset.

As the following article discusses, the XFROG retrieved vibrational coherence is independent of the properties of the probe pulse, therefore the proposed complete characterization method does not suffer from the intensity vs. resolution dilemma. The retrieved spectrum of the vibrational coherence has good spectral resolution ( $3cm^{-1}$ FWHM resonant peaks are clearly resolved), regardless of the broad bandwidth of the probe pulse ($>200cm^{-1}$). With phase information available, the spectral resolution is determined by the scanning range of time delay. A 10ps scanning range can give $3cm^{-1}$ resolution.

The ability to experimentally obtain the phase of vibrational excited levels is a unique feature that is associated with this approach. With the ability to recover the spectral phase, a demonstration of the ability to separate time domain vibrational beatings from chemical mixtures is also discussed. The current time-resolved CARS methods [3–5] that measure the beating between vibrational levels require pure samples. Additional chemical component in the sample can dramatically change the beating profile due to the interference between resonant levels. For chemical physics experiments that involve utilizations of maxima or minima of vibrational wave packets, the changing of the beating maxima or minima due to the presence of resonance from other chemical component is detrimental. A numerical comparison of vibrational beatings between a "pure" three excited level system of equal spacing and that of a mixture with one additional close resonant level is shown in figure 4.1. The beating maximum of the three level system disappears when the additional level is added. Due to the coherent nature of the beating, simple subtraction of the measured beatings does not solve this problem. If the amplitude of the peak in the vibrational coherence spectrum reflect the excitation strength and Raman cross-section of the resonance, the spectral phase around the peak in the vibrational coherence spectrum reflects the time behavior of the resonance. With the availability of spectral phase of the vibrational coherence in the frequency domain, it is now possible to filter out the additional "impurity" resonances and Fourier transform the remaining spectrum of amplitude and phase to the time domain to reconstruct the beating response of the pure sample. The article section includes

a proof-of-principle experiment on separating the vibrational beatings of mixtures.

## 4.2 Experiment Technique Considerations

The experiment of complete characterization of molecular vibrations can be done based on a time-resolved CARS experiment setup with a pulse shaper for the probe pulse and a spectrometer with CCD. Figure 1.23 of section 1.4 shows the schematic of the setup that is used in this experiment.

The complete characterization of the probe pulse is obtained through the FROG technique described in section 1.4. The accuracy of a vibrational coherence characterization depends on the accuracy of the characterization of the probe pulse. After several trials, pulse shaping of the probe pulse was found to improve the XFROG algorithm retrieval robustness and accuracy. Therefore, a $\pi$ phase step mask or sinusoidal pulse shaping was used on the probe pulse. The procedure for creating and characterizing the probe pulse is first to iteratively use either FROG or MIIPS and the pulse shaper to obtain a transform-limited pulse through spectral phase compensation with the pulse shaper. The FROG technique is then used to characterize the compensated probe pulse, obtaining both the amplitude and phase of the pulse. Then, the pulse shaper introduces the phase function to the compensated probe pulse, and the probe pulse is then used in the CARS process for the spectrogram generation. The discussion about the improvement of XFROG retrieval by pulse shaping of the probe pulse can be found in the published article by Konorov et.al.[6].

The XFROG algorithm is a variation of the FROG algorithm [2, 7]. Figure 4.2 illustrates the operational steps within each iteration. As the figure shows, the XFROG algorithm necessarily requires two inputs: the two-dimensional time-frequency spectrogram $\widetilde{I}_{exp}(\omega, \tau)$ and a well characterized probe pulse $E_{pr}(t)$. An initial guess is not strictly necessary but a close guess to the vibrational coherence can help the retrieval. The first step starts when the characterized probe pulse mathematically generates a two dimensional trace $I(t, \tau)$ from $E_{pr}(t)$ with the probe pulse and the guessed

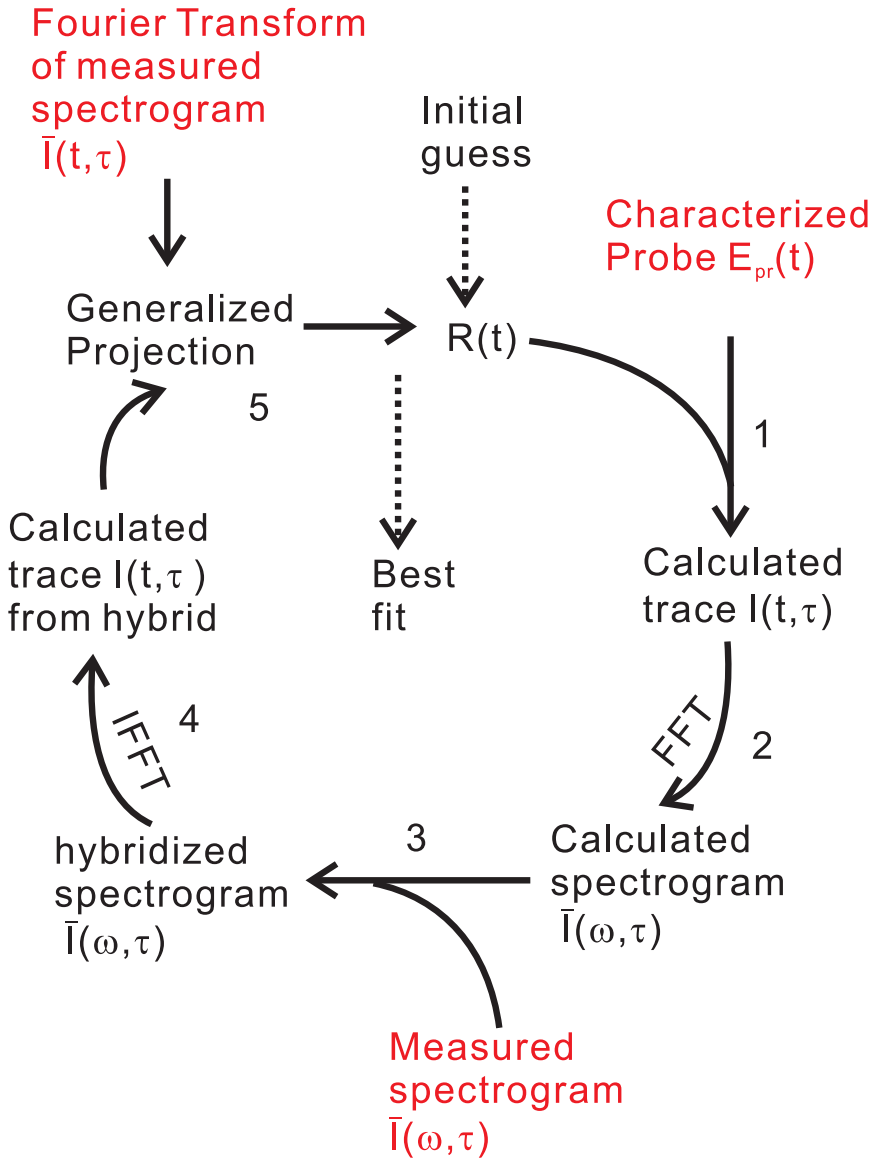


Figure 4.3: This figure shows the operational steps within the XFROG algorithm. The vibrational coherence function is represented by $R(t)$. The probe pulse is in the time domain as $E_{pr}(t)$. $\tau$ is the time delay between the R(t) and probe pulse field. The mathematical steps are denoted as 1 to 5 and explained in text. FFT and IFFT stands for fast Fourier transform and inverse fast Fourier transform respectively.

value of vibrational coherence R(t). Then the trace is Fourier transformed into the frequency domain to obtain calculated spectrogram $\widetilde{I}(\omega,\tau)$. This calculated spectrogram is then "hybridized" with the measured experimental spectrogram $\widetilde{I}_{exp}(\omega,\tau)$. In this hybridization step, the amplitude of the experimental spectrogram gives the amplitude of the hybridized trace and the phase of the calculated spectrogram gives the phase of the hybridized spectrogram. After hybridization, the spectrogram is inverse Fourier transformed back to the time domain to obtain the hybrid trace $\widetilde{I}_{hybrid}(t,\tau)$. This hybrid trace further undergoes the generalized projection step to provide the new generation of guess R(t). The algorithm iterates to find best profile of R(t) that produces the closest trace to the experimental recorded spectrogram.

The metric minimization step is the key to the accuracy of the retrieval. It uses the same generalized projection method that is used in the FROG technique [7]. The procedure of generalized projection is to define a distance metric Z and minimize it with respect to the test field (in the context of this chapter, R(t)). A gradient based minimization [7], is used to obtain next generation of test field:

$$Z = \sum_{i,j=1}^{N} |I^{(}_{exp}t_i,\tau_j) - R(t)E_{pr}(t_i-\tau_j)|^2 \tag{4.1}$$

where $I_{exp}(t,\tau)$ is the experimental trace, $E_{test}(t)$ and$E_{pr}(t)$ are the test field and the well characterized probe field.

In the actual experiment, the XFROG retrieval was done by the FROG3 software (Femtosoft). Since the software was not designed for the purpose of recovering vibrational responses, certain data format adjustment is needed. Appendix C shows the procedure for FROG3 software usage for retrieving the vibrational coherence. Appendix A includes the MATLAB simulation code that can generate the numerical CARS spectrogram and the probe pulse for the test XFROG retrieval.

## 4.3 Method Content

### 4.3.1 Overview

The authors propose a new approach to vibration spectroscopy based on Coherent Anti-Stokes Raman scattering of broadband ultrashort laser pulses. The proposed method reveals both the amplitude and the phase of molecular vibrations by utilizing the cross-correlation frequency resolved optical gating (XFROG) technique. The spectrum of the anti-Stokes pulse is measured as a function of the time delay between the laser-induced molecular vibrations and a well characterized broadband femtosecond probe pulse. The iterative XFROG algorithm provides simultaneous complete characterization of molecular vibrations both in frequency and time domains with high resolution. They demonstrate experimentally the feasibility of proposed method and show one of its potential applications in disentangling the time behavior of a mixture of vibrationally excited molecules. The technique of femtosecond pulse shaping is used for further improvement of accuracy and stability against noise.

### 4.3.2 Content

Coherent Anti-Stokes Raman Scattering (CARS) has been successfully used in spectroscopy and microscopy since the development of tuneable lasers [8, 9]. In CARS, molecular vibrations are coherently excited by the pump and Stokes pulses, and subsequently scatter the probe pulse generating the anti-Stokes signal. The temporal and spectral resolution of CARS spectroscopy is usually limited by the duration of the excitation pulses and their frequency bandwidth, respectively. Narrow bandwidth probe pulses are used in multiplex frequency-resolved CARS (fr-CARS) technique for high spectral resolution [10], whereas broadband femtosecond pulses have been employed in recent developments of time-resolved CARS (tr-CARS) spectroscopy [4, 11].

Since the time duration and the spectral bandwidth of a transform limited laser pulse are inversely proportional to each other, simultaneously

achieving high resolution in both domains requires complementary use of both fr- and tr-CARS [12, 13]. For instance, detection of the quantum beats between various vibrational frequencies of a molecule in the tr-CARS is not sufficient to recover these frequencies unambiguously, especially in the case of a large number of resonances with unknown frequency distribution. Similarly, high-resolution spectral measurement of the anti-Stokes field does not provide sufficient knowledge about the time response of a system. The reason for both shortcomings is the lack of information about the vibrational phase.

The phase of the anti-Stokes field has been recently utilized for significant enhancement of CARS sensitivity by means of interferometric homodyne and heterodyne detection.[14–18] Although the anti-Stokes phase is directly related to the phase of excited vibrational modes through the process of nonlinear frequency mixing, the latter cannot be easily retrieved from the interferometric measurements due to the presence of stochastic experimental noise. Employing spectrally narrow probe pulses (as in Refs. [14, 16]) simplifies the problem but comes at the expense of relatively low probe power and limited frequency resolution. In this paper we show that the cross-correlation frequency resolved optical gating (XFROG) method enables robust and accurate spectral intensity and phase retrieval while using the full spectral bandwidth of the probe pulse. The improved performance of this new method stems not only from the higher available probe power but also from the redundancy of the experimental data due to the utilization of all available spectral components of the probe pulse. In the CARS process, pump pulse $E_p$ and Stokes pulse $E_s$ coherently excite molecular vibrations with a frequency response $R(\Omega)$:

$$R(\Omega) = \left[\sum_n L_n(\Omega) + C_{NR}\right] \cdot \int E_p(\omega')E_s(\omega' - \Omega)d\omega' \qquad (4.2)$$

where $L_n(\Omega)$ and $C_{NR}$ represent the contribution of the n-th resonance and the non-resonant background, respectively. The anti-Stokes field $E_{as}$ is generated as a result of the coherent scattering of the probe pulse $E_{pr}$

from the vibrations of the Raman active medium induced by the pump and Stokes fields:

$$E_{as}(\omega) \propto \int R(\Omega) E_{pr}(\omega - \Omega) d\Omega \tag{4.3}$$

The direct deconvolution of (4.3) for the retrieval of the complex vibrational response $R(\Omega)$ is not feasible because the experimentally measured intensity of the anti-Stokes radiation, $I_{as} \propto |E_{as}(\omega)|^2$, loses the phase of $E_{as}(\omega)$. A similar de-convolution problem occurs in the process of complete temporal and spectral characterization of ultrashort laser pulses,which XFROG was originally developed for [2, 19]. The XFROG iterative algorithm retrieves both the amplitude and phase of an unknown field $E(\Omega) = |E(\Omega)| \cdot e^{i\varphi(\Omega)}$ from its cross-correlation with a well characterized "gate" field $E_g$. The cross-correlation is usually performed by measuring the spectrum of a nonlinear process, such as non-resonant sum frequency generation in a nonlinear crystal,

$$E_{SFG}(\omega) \propto \int E(\Omega) E_g(\omega - \Omega) d\Omega \tag{4.4}$$

To compensate for the missing phase of $E_{SFG}(\omega)$ in the detected intensity $I_{SFG}(\omega)$, XFROG technique introduces the time delay $\tau$ between the unknown pulse $E(\Omega)$ and the gate pulse $E_g$, and applies an iterative retrieval algorithm to the acquired two-dimensional spectrogram $I_{SFG}(\omega, \tau)$. The desired solution $E(\Omega)$ is found by means of the mathematical procedure known as the method of generalized projections [19]. By iteratively projecting onto the well defined constraint sets both in the time and frequency domains, in all practical cases the method leads to a unique solution for $E(\Omega)$. The robustness of the XFROG algorithm stems from the redundancy of the two-dimensional scan which contains (quadratically) more data points than there are unknowns in the sought solution $E(\Omega)$. This high degree of redundancy enables complete reconstruction of $E(\Omega)$ from the measured $I_{SFG}(\omega, \tau)$. The similarity of expressions (4.3) and (4.4) suggests the possibility of de-convolving $R(\Omega)$ by means of the XFROG technique. Indeed, the coherent molecular vibration response $R(\Omega)$ in (4.3) is analogous to the unknown pulse $E(\Omega)$ in (4.4). In the CARS process, these coherent vibrations are "mixed" with the probe pulse to produce the third order polarization

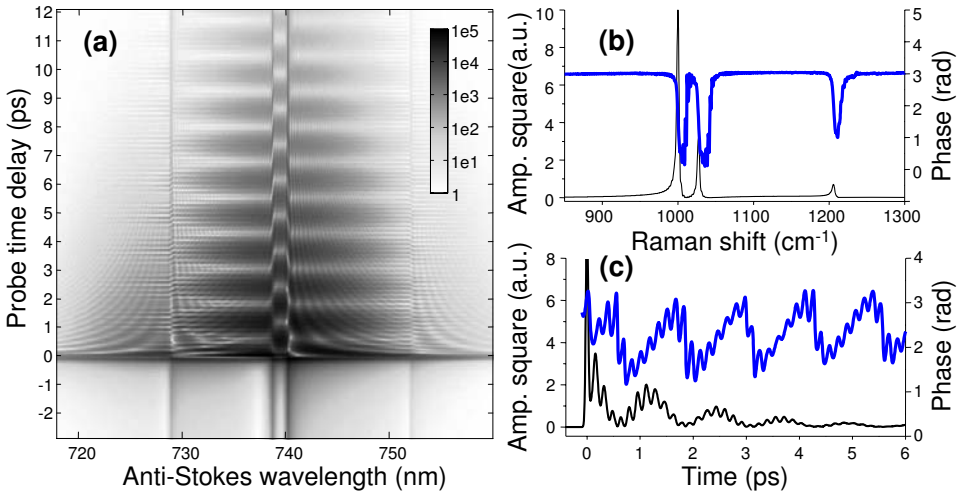


Figure 4.4: (Color online). **(a)** Numerical simulation of the frequency resolved CARS spectrogram for Toluene molecule (log scale). $\pi$-step spectral phase shaping has been applied to a gaussian probe pulse with the spectral bandwidth of 10nm (FWHM), resulting in sharp interference fringes which serve as "frequency markers" for the XFROG retrieval algorithm (see text). **(b,c)** XFROG retrieval of the square of the amplitude (thin black) and the phase (thick blue) of the vibrational response in frequency and time domains, respectively.

which generates the observable anti-Stokes pulse $E_{as}(\omega)$, in direct analogy with the sum frequency generation in a nonlinear crystal. Following this analogy, we introduced the time delay between the pump-Stokes pulse pair and the probe pulse, and applied the iterative XFROG algorithm to the two-dimensional CARS spectrogram $I_{as}(\omega,\tau) \propto |E_{as}(\omega,\tau)|^2$, where

$$E_{as}(\omega,\tau) \propto \int R(\Omega) E_{pr}(\omega-\Omega) e^{-i\Omega\tau} d\Omega \tag{4.5}$$

Numerical simulations of the CARS spectrogram $I_{as}(\omega,\tau)$ for Toluene molecule are shown in fig.4.4(a). We used commercial XFROG software package (FROG3, Femtosoft Technologies) to extract the complex vibrational response $R(\Omega)$ in frequency and time domains, shown in fig.4.4(b)

and fig.4.4(c), respectively. The retrieved positions of the resonances agree with the values used for calculating the spectrogram. The amplitude of each resonant line is determined by the input resonance strength and by the spectral power of the pump-Stokes field correlation at the corresponding resonance frequency. Three resonances at 1000 $cm^{-1}$, 1027 $cm^{-1}$ and 1206 $cm^{-1}$ are clearly resolved. Phase dips at the location of each resonance agree with the assumed Lorentzian model of the resonant molecular response. The latter implies that $C_n(\Omega) = C_n/(\Omega - \Omega_n + i\Gamma_n)$, where $C_n$, $\Omega_n$ and $\Gamma_n$ are the strength, the frequency and the width of the $n$-th resonance.

Our numerical analysis shows that the XFROG algorithm becomes less susceptible to noise with the increased number of sharp features in the input spectrogram [6]. Such features, or "frequency markers", can be introduced by means of the spectral phase shaping of the probe pulse. The latter involves controlled modification of the spectral phase of the pulse by applying an external phase function $\phi(\omega)$ to its spectrum, i.e. $E'_{pr}(\omega) = E_{pr}(\omega) \times e^{i\phi(\omega)}$. A simple, yet very useful, spectral shape consists of a $\pi$ -step at the central frequency of the pulse $\omega_0$. That is, $\phi(\omega) = 0$ if $\omega < \omega_0$, and $\phi(\omega) = \pi$ otherwise. The effect of the $\pi$-step phase shaping on resonantly enhanced multiphoton processes, such as CARS or two-photon absorption, has been thoroughly discussed and exploited in a series of works by Silberberg and co-workers [14, 20]. In the time domain, the $\pi$-step shaping splits an originally transform limited pulse into a pair of phase-coherent pulses. The two corresponding anti-Stokes fields generated by this probe pair interfere as long as the coherent excitation is preserved in the medium due to the presence of vibrational resonances. The interference fringes, seen on the spectrogram as sharp edges along the time axis (fig. 4.4(a)), serve as the frequency markers of the Raman lines and help the XFROG algorithm determine the absolute position of the resonances. We will discuss the performance of different pulse shapes in a follow-up paper [6].

The experimental results of the frequency resolved CARS gating method with the spectrally shaped probe pulse are shown in fig.4.5. We used a commercial Ti-Sapphire regenerative amplifier system (SpitFire, Spectra-Physics) generating pulses of ∼10nm bandwidth (FWHM), a tuneable opti-

cal parametric amplifier (TOPAS, Light Conversion), and a home built pulse shaper based on a liquid crystal spatial light modulator (SLM-128, CRI) and implemented in a commonly used 4f design [21]. The central wavelengths were set to 1111 nm, 1250 nm and 800 nm, for the pump, Stokes and probe pulse, respectively. The pulse shaper was first utilized for flattening the spectral phase of the probe pulse. This transform limited probe was used either directly or after an additional phase shaping was applied by the pulse shaper. Incident pulses with energies lower than $10\mu$J were focused in the BOXCARS phase matching geometry on a liquid sample held in 5 mm optical path quartz cuvette. Low average power pulses are sufficient to generate enough CARS signal because this method utilize full bandwidth of laser as probe pulses. The generated CARS signal was spatially filtered from the residual excitation beams and coupled into a spectrometer with a spectral resolution of 0.05 nm. The time delay $\tau$ between the probe pulse and the pump-Stokes pair was scanned in 20 fs steps.

The results of the XFROG retrieval of the spectral amplitude and phase of the vibrational response $R(\Omega)$ are shown in fig.4.5(b). Confirming our numerical analysis, the experiment shows that the resolution is improved when the shaped probe pulse was used, as opposed to the case of the unshaped transform limited probe [6]. The positions of the three resonance peaks (at 1000 $cm^{-1}$, 1027 $cm^{-1}$ and 1206 $cm^{-1}$) are in good agreement with the reference spectrum of spontaneous Raman scattering shown by the red dashed line. The peak intensities depend on the spectral power density of the pump-Stokes field correlation at the corresponding frequency $\Omega$, as well as the scattering cross section, and are therefore higher at the central frequency of 1000 $cm^{-1}$. The central peak has a FWHM of $\sim$3 $cm^{-1}$, significantly sharper than the bandwidth of our probe pulse of $\sim$170 $cm^{-1}$, and is even comparable to spontaneous Raman spectrum. In the simultaneously retrieved time response shown in fig.4.5(c), coherent oscillations with a period of 160 fs are clearly observed, confirming that the time resolution of the XFROG retrieval is determined by the broad spectral bandwidth of the molecular nonlinear response and the probe pulse bandwidth, rather than by the probe pulse duration which in the case of the $\pi$-step shaping

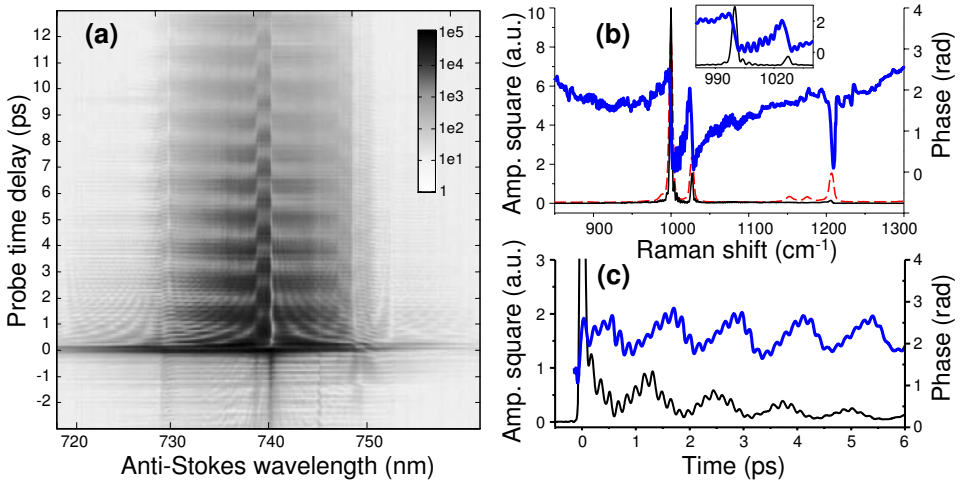


Figure 4.5: (Color online). **(a)** Experimental frequency resolved CARS spectrogram for Toluene sample with the spectrally shaped probe pulse ($\pi-$ *step* at 800 nm, log scale). **(b,c)** XFROG retrieval of the square of the amplitude (thin black) and phase (thick blue) of the vibrational response in frequency and time domains, respectively. Dashed red line in (b) represents the reference spectrum of spontaneous Raman scattering from the same sample. Zoom-in to the central part of the spectrum is shown in the inset in plot (b).

exceeds 500 fs. Spectral phase shifts are observed across each resonant line as expected from the Lorentzian model. The magnitude of the phase shifts is lower than $\pi$ radian due to the presence of the non-resonant background.

Being a result of a coherent process, anti-Stokes fields generated by multiple vibrational resonances interfere and therefore cannot be separated unless both the amplitude and the phase of the total vibrational response are known. The key ability of the proposed method to reveal the phase of molecular vibrations is demonstrated by applying the method to the indirect retrieval of the vibrational response of a molecule from the measured response of its mixture with another molecular species. Such a task would be particularly important if the mixture cannot be separated, and the collective Raman response represents the only available spectroscopic data.

We demonstrate this by retrieving the vibrations of Toluene from the measured CARS spectrogram of its mixture with orto-Xylene as shown in fig.4.6. XFROG retrieval of the time and frequency response of the mixture is shown in plots (a) and (b), respectively. In the absence of the phase information, masking the three main resonances of orto-Xylene at 982 $cm^{-1}$, 1049 $cm^{-1}$ and 1220 $cm^{-1}$ is not sufficient for reconstructing the complex Raman response of Toluene because the inverse Fourier transform from the frequency into the time domain cannot be carried out properly. The availability of the phase in our XFROG retrieval, however, makes this procedure possible. We masked out the three resonances of orto-Xylene in the complex spectrum of the mixture by substituting the amplitude and the phase in their vicinity by a linear slope connecting the two values at the two sides of each resonance (shaded regions in (b)). The Fourier transform of the resulting complex spectrum is compared with the direct XFROG retrieval of the temporal vibrational response of pure Toluene in fig.4.6(a). As shown by the close-up in fig.4.6(c), excellent agreement between the direct retrieval from the pure sample (thin blue) and indirect retrieval from the mixture (thick black) on the time scale of a few picoseconds demonstrates the potential of the proposed technique as a new tool for studying molecular dynamics in complex environments.

The limitations and possible sources of error of the proposed method of XFROG CARS can be seen from the analysis of equations. (4.2) and (4.5). The former assumes that a single vibrational ground state is coupled to a set of excited vibrational levels via nonresonant two-photon transitions by a two-photon field $E_p(t)E_s(t)$. We first note that the complex response $R(\Omega)$ reflects not only the inherent properties of the medium described by the term in the square brackets in Eq. 4.2 but also the field characteristics of the pump and Stokes pulses. For instance, a small residual frequency chirp in the pump-Stokes field correlation can be seen in Fig. 4.5(b) as a small parabolic background. Furthermore, any intermediate one-photon resonance at the pump or Stokes frequency will change the phase and amplitude of $R(\Omega)$. However, owing to the preserved coherence of the excitation, the XFROG retrieval, though more complicated, will properly reflect the

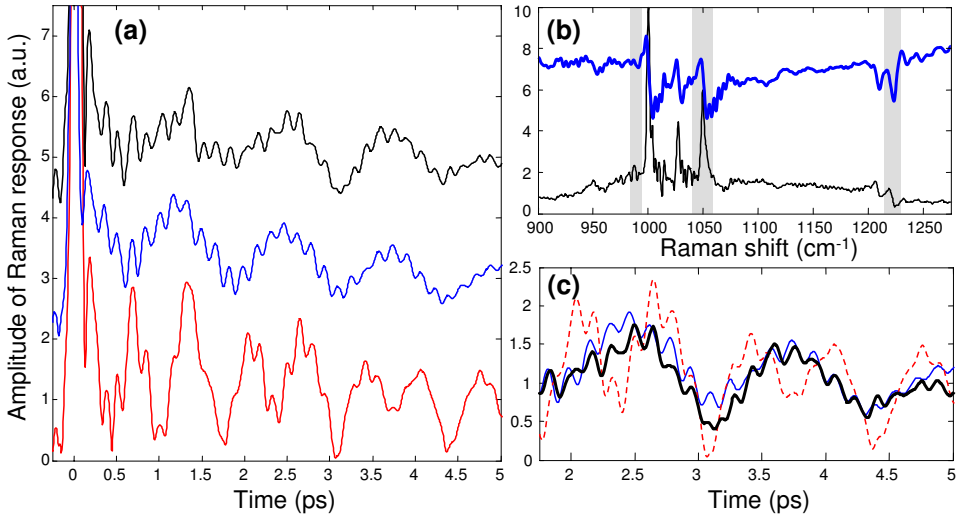


Figure 4.6: (Color online). **(a)** XFROG retrieval of the vibrational oscillations of Toluene (two upper curves, shifted for clarity), and of the mixture of Toluene with orto-Xylene (lower red curve). The two upper curves were obtained by the direct retrieval from pure Toluene (middle blue) and by the indirect reconstruction of the same response from the collective response of the mixture (top black). **(b)** XFROG retrieval of the complex spectrum of the mixture. Both amplitude (thin black) and phase (thick blue) around the three strong resonances of orto-Xylene (shaded rectangles) were masked for the complete reconstruction of the Raman response of Toluene by the Fourier transform of the modified complex spectrum. **(c)** Close comparison of the directly (thin blue) and indirectly (thick black) retrieved vibrational amplitude of Toluene from the pure sample and mixture, respectively. Vibrational response of the mixture is shown by the dashed red curve for reference.

induced molecular vibration. On the other hand, an incoherent mixture of initially populated ground levels will result in faster dephasing of the ensemble-averaged coherences and cause an effective broadening of the vibrational lines. Similar analysis of Eq. 4.5 shows that the XFROG algorithm is applicable only to the case of non-resonant scattering of the probe pulse. Moreover, any discrepancy between the real probe and the one used as an input to the XFROG calculations reduces the accuracy of the amplitude-phase retrieval. We also note that the proposed technique is not limited to the vibrations in the electronic ground state, as it can be used for the analysis of any long-lived vibrations accessible through a two-photon excitation in a general four-wave mixing process. In principle, it can be applied not only to CARS but also to other coherent interaction schemes.

In conclusion, we demonstrated the frequency resolved gating of molecular vibrations as a highly effective and robust method of simultaneous revealing the amplitude and the phase of molecular vibrations. The ability to use full spectral bandwidth of the femtosecond probe pulses, offered by the XFROG CARS, results in higher signal-to-noise ratios, lower required probe power, and high stability against noise. The latter is enhanced by the redundancy of the XFROG retrieval, which is based on simultaneous processing of multiple anti-Stokes signals generated by all spectral components of the probe pulse. Unlike the interferometric methods of phase sensitive detection, the XFROG technique retrieves the phase of molecular vibrations, rather than the phase of the anti-Stokes field. The availability of the vibrational phase provides additional information about the system and extends our capabilities of studying its dynamics. The method is demonstrated experimentally by successfully separating temporal Raman responses of two mixed molecular species without physically separating the mixture. The utilization of femtosecond pulse shaping technique further improves the performance of this method.

# Bibliography


[1] J. K. Kauppinen, D. J. Moffatt, H. H. Mantsch, and D. G. Cameron, Applied Spectroscopy **35**, 271 (1981).

[2] S. Linden, H. Giessen, and J. Kuhl, Physica Status Solidi B-Basic Research **206**, 119 (1998).

[3] M. Schmitt, G. Knopp, A. Materny, and W. Kiefer, Journal of Physical Chemistry A **102**, 4059 (1998).

[4] T. Lang, K. L. Kompa, and M. Motzkus, Chemical Physics Letters **310**, 65 (1999).

[5] G. Knopp, I. Pinkas, and Y. Prior, Journal of Raman Spectroscopy **31**, 51 (2000).

[6] S. O. Konorov, X. G. Xu, R. F. B. Turner, M. W. Blades, J. W. Hepburn, and V. Milner, Optics Express **15**, 7564 (2007).

[7] K. W. Delong, D. N. Fittinghoff, R. Trebino, B. Kohler, and K. Wilson, Optics Letters **19**, 2152 (1994).

[8] W. M. Tolles, J. W. Nibler, J. R. McDonald, and A. B. Harvey, Applied Spectroscopy **31**, 253 (1977).

[9] J. X. Cheng and X. S. Xie, Journal of Physical Chemistry B **108**, 827 (2004).

[10] J. X. Cheng, A. Volkmer, L. D. Book, and X. S. Xie, Journal of Physical Chemistry B **106**, 8493 (2002).

[11] M. Schmitt, G. Knopp, A. Materny, and W. Kiefer, Chemical Physics Letters **270**, 9 (1997).

[12] M. Heid, S. Schlucker, U. Schmitt, T. Chen, R. Schweitzer-Stenner, V. Engel, and W. Kiefer, Journal of Raman Spectroscopy **32**, 771 (2001).

[13] B. D. Prince, A. Chakraborty, B. M. Prince, and H. U. Stauffer, Journal of Chemical Physics **125** (2006).

[14] D. Oron, N. Dudovich, and Y. Silberberg, Physical Review Letters **89** (2002).

[15] D. L. Marks, C. Vinegoni, J. S. Bredfeldt, and S. A. Boppart, Applied Physics Letters **85**, 5787 (2004).

[16] S. H. Lim, A. G. Caster, and S. R. Leone, Physical Review A **72** (2005).

[17] M. Cui, J. P. Skodack, and J. P. Ogilvie, Biophysical Journal pp. 197A–197A (2007).

[18] E. O. Potma, C. L. Evans, and X. S. Xie, Optics Letters **31**, 241 (2006).

[19] K. W. Delong, R. Trebino, J. Hunter, and W. E. White, Journal of the Optical Society of America B-Optical Physics **11**, 2206 (1994).

[20] N. Dudovich, B. Dayan, S. M. G. Faeder, and Y. Silberberg, Physical Review Letters **86**, 47 (2001).

[21] A. M. Weiner, Review of Scientific Instruments **71**, 1929 (2000).

# Chapter 5

# Background-free Coherent Raman Spectroscopy by Detecting the Spectral Phase of Molecular Vibrations

## 5.1 Motivation

CARS spectroscopy has many advantages over spontaneous Raman spectroscopy such as high signal strength, low fluorescence background and directional signals. However, the disadvantage of high non-resonant background in CARS limits its application. Due to the universal existence of $\chi^{(3)}$, CARS has non-resonant Four-Wave-Mixing background independent of the presence of resonances. The problems are twofold for CARS with broad band pulses. Firstly, the presence of non-resonant background at the same frequency as the resonances creates the dispersive line profiles in the vibrational coherence $R(\Omega)$. For CARS methods with narrow band probing, where the CARS spectrum reflects the profile of $R(\Omega)$, dispersive profiles complicate peak fitting. In addition, for CARS methods with broad band probing, the frequency components in the CARS spectrum can come from both resonant contributions and non-resonant response of different frequencies. This is shown in figure 5.1, where the broadband probe pulse links

[0] A version of this chapter has been published as Xiaoji G. Xu, Stanislav O. Konorov, John. W. Hepburn and Valery Milner "Background-free Coherent Raman Spectroscopy by Detecting the Spectral Phase of Molecular Vibrations" *Optics Letters* vol. 33 page 1177-1179. 2008

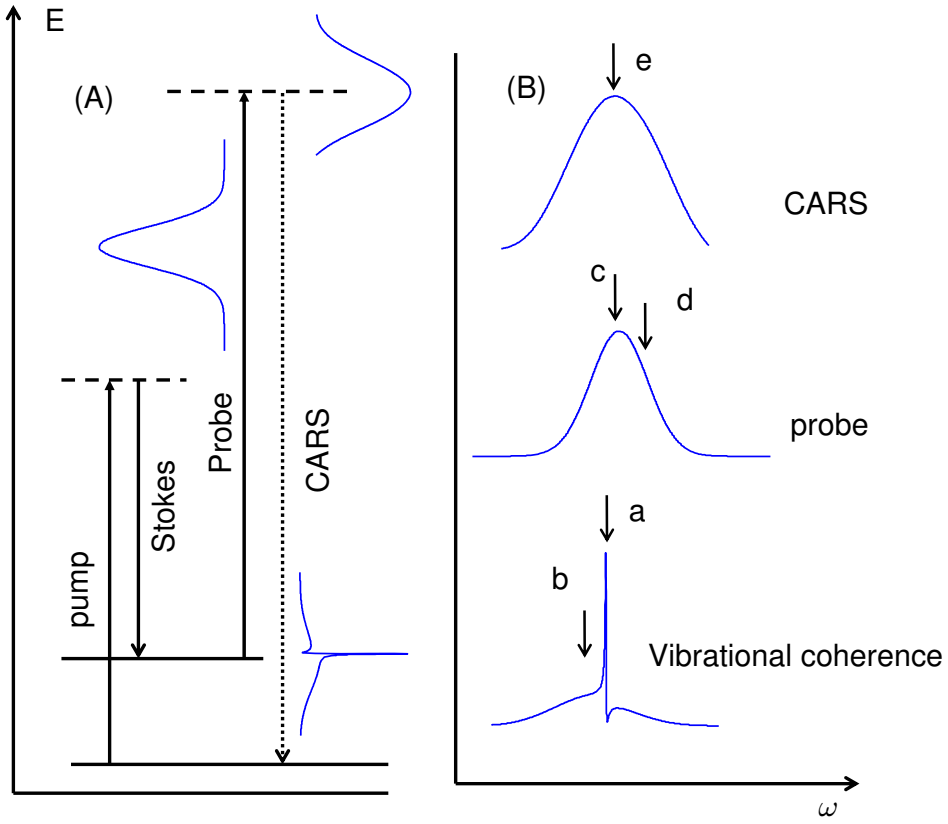


Figure 5.1: The energy level diagram is shown in figure (A). The convolution effect of CARS signal with high non-resonant background and broad band probing is shown in figure (B). The frequency contribution from resonance (a) (specified by an arrow) interacts with frequency component (c) from a broad band probe pulse and contributes to the CARS frequency at location e. However the non-resonant response at position (b) interacts with frequency component (d) and also contributes to the same CARS signal at (e).

both resonant level and non-resonant response to the same frequency component in the CARS spectrum. This problem can also be regarded as a continuation of the convolution problem that is discussed in chapter 4. The non-resonant response adds a background to the vibrational coherence $R(\Omega)$ and this background participates in the convolution process with a broad band probe pulse.

For CARS techniques with narrow-band probe pulses, i.e. multiplex CARS, polarization has been used to remove the non-resonant signal contribution [1, 2], based on a small angle polarization difference between resonant CARS and non-resonant background. This method works in such a way that the polarizer is orthogonal to the polarization of non-resonant FWHM signal, so the optical signal passing through the polarizer is purely from the resonant CARS signal. However, the polarization difference of the resonant CARS signal and the non-resonant FWM signal is often about 5-10°. When blocking the non-resonant signal, the majority of resonant signal is also blocked, therefore the utilization of polarization filtering leads to severe attenuation of the resonant signal. Broad band time-resolved CARS, on the other hand, can avoid non-resonant background quite easily if the short duration probe pulse is properly time-delayed with respect to the excitation pair. However, as mentioned in the discussion in section 1.2, time-resolved CARS gives only the vibrational level spacing of the sample.

To solve the non-resonant background problem in CARS with broad band pulses, a spectral phase approach based on complete characterization of molecular vibrations was proposed and demonstrated [3]. The complete characterization of molecular vibrations technique can effectively remove the convolution effect introduced by the broad band probe pulse, therefore solving the convolution problem between the resonant spectra and non-resonant background. In addition to the application of complete characterization of molecular vibrations method, this chapter solves the non-resonant background problem of CARS by detecting the spectral phase. When the non-resonant background is high, the retrieved spectral phase profile of the vibrational coherence is a good approximation of the spectrum of vibrational resonances.

The spectral phase $\Phi$ of the vibrational coherence $R(\Omega)$ is related to the ratio between the imaginary part of $R(\Omega)$ and the real part of $R(\Omega)$ by $\arctan[\frac{Im(R(\Omega))}{Re(R(\Omega))}]$. As discussed in section 3.2.1 and shown figure 1.16, the imaginary part of $R(\Omega)$ reflects the profile of the vibrational resonances of the sample. The real part of $R(\Omega)$, however, comes from both the real part of the resonance and non-resonant background. The overall spectrum of $R(\Omega)$ often has dispersive profiles. As equation 1.41 shows, the non-resonant background adds a real number $C_{nR}$ to $R(\Omega)$. When the non-resonant background is high, the real part of $R(\Omega)$ is going to reflect primarily the high value of the non-resonant contribution, whereas the imaginary part of $R(\Omega)$ remains the same. As a result, the spectral phase $\Phi$ can be approximated by $\frac{Im(R(\Omega))}{Re(R(\Omega))}$. Now the $Re(R(\Omega))$ is primarily $C_{nR}$ times a field correlation factor $A(\Omega)$. Consequently, the spectral phase $\Phi$ of the vibrational coherence $R(\Omega)$ reflects the imaginary part of the vibrational coherence divided by the field correlation $A(\Omega)$ and gives the profile of the vibrational resonances.

A point worth noting about this spectral phase approach is the ratio between the non-resonant background and the resonant contribution. For the spectral phase to have similar profile as the imaginary part of the the vibrational coherence, the non-resonant background should be high, at least comparable to the strength of the resonant response. The comparison of the spectral phase and the total spectrum of $R(\Omega)$ is shown in figure 5.2. When the non-resonant background is high (100% in figure 5.2(A) and 50% in (B)) the spectral phase reflects the peak profile of the resonances. When the the non-resonant background is low (10% in figure 5.2(C) the spectral phase shows severe distortion comparing to profile of the vibrational resonance as shown in figure 5.2(D). This means when non-resonant background is low, the spectral phase of $R(\Omega)$ cannot be safely used as the profile of the vibrational resonance. A practical estimation on the threshold non-resonant background to resonant response ratio is 50%; if the non-resonant background is about 50% of the strength of resonant response, the spectral phase approach can be used and peaks on the spectral phase has correct linewidths and relevant intensity to that of the vibrational resonances. If the non-resonant background is low, the linewdith and intensity shows severe distortion that

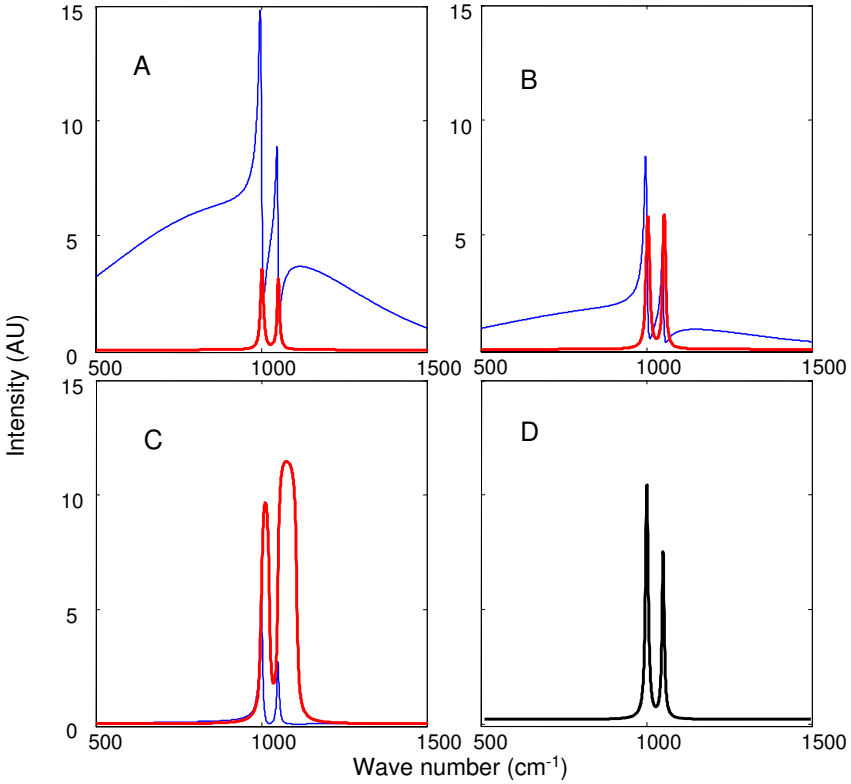


Figure 5.2: Figure A, B and C show the comparisons between spectral phase (red thick line) and total intensity (blue thin line) of $R(\Omega)$. (A) the non-resonant background has the same peak value as the resonant response. (B) the non-resonant background has 50% peak value as the resonant response. (C) the non-resonant background has 10% peak value as the resonant response. Figure (D) is the plot of the imaginary part of resonant response that corresponds to vibrational resonances.

cannot be taken as the indication of linewdith and intensities of vibrational resonances. However, when the non-resonant background is low, the total spectrum of the vibrational coherence can be directly used as the spectrum of the vibrational resonances and there is no need to use the proposed spectral phase approach method. In CARS experiments of condensed phase samples, the non-resonant background depends on the properties sample. Toluene, a commonly used strong Raman active sample, has an estimated ratio of 20% between the strength of non-resonant response and that of the resonant response. For other sample, this ratio can be assumed to be higher than that of toluene.

The spectral phase approach is an effective way of removing high non-resonant background of CARS. It is an application of complete characterization of molecular vibration method. It is specifically useful for those samples that have high non-resonant background. Unlike the polarization techniques, the spectral phase approach detects all the CARS signals. Therefore it can be applied to samples with low total signal. The article section is going to show expression derivations and experiment demonstrations in detail.

## 5.2 Method Content

### 5.2.1 Overview

The authors propose and demonstrate a new approach to subtracting high non-resonant background in coherent anti-Stokes Raman Scattering (CARS) spectroscopy. The method is based on the retrieval of the spectral phase of molecular vibrations using the technique of frequency resolved optical gating of Raman scattering. In the presence of high non-resonant background, the retrieved phase corresponds directly to the background-free spectrum of the coherent Raman response.

### 5.2.2 Content

Since its discovery [4, 5], coherent anti-Stokes Raman scattering (CARS) has been widely used for vibrational spectroscopy. In recent years, CARS

spectroscopy has attracted significant attention because of its applications in biological imaging [6, 7] and chemical diagnosis [8]. However, the often present instantaneous non-resonant background interferes with and typically dominates the much weaker resonant response, making an accurate retrieval of the CARS spectrum difficult. Commonly employed polarization filtering, though successful in removing the non-resonant signal [1, 2], significantly attenuates resonant contribution thus reducing the signal-to-noise ratio. An alternative approach based on heterodyne detection [9–12] comes at the expense of high experimental complexity and requires interferometrical stability of optical components. The non-resonant background can also be eliminated by properly delaying the probe pulse in time resolved CARS [13, 14]. This method, however, is susceptible to imperfect spectral phase of the excitation pulses. Here, we present a simple and robust experimental approach which enables an accurate retrieval of the coherent Raman spectrum in the presence of high non-resonant response.

Coherent anti-Stokes Raman scattering is a four-wave-mixing process, in which the coherent vibrational response $R(\Omega)$ is excited by the two-photon field $A(\Omega)$ of the pump and Stokes photons:

$$R(\Omega) = \left[\sum_k \frac{C_k}{\Omega - \Omega_k - i\Gamma_k} + C_{\mathrm{NR}}\right] \times A(\Omega), \tag{5.1}$$

where

$$A(\Omega) = \int E_p(\omega') E_S^*(\omega' - \Omega) d\omega'. \tag{5.2}$$

Vibrational coherence is prepared when the pump and Stokes excitation fields, $E_p(\omega)$ and $E_S(\omega)$, respectively, overlap temporally and spatially on a Raman active sample. Equation (5.1) assumes a Lorentzian resonant response with $\Omega_n$, $\Gamma_n$ and $C_n$ being the position, linewidth and strength of the $k-$th resonance, whereas $C_{\mathrm{NR}}$ represents the non-resonant contribution. CARS signal, $E_{\mathrm{CARS}}$, results from the scattering of the probe pulse, $E_{pr}(\omega)$, off the excited vibrational coherence $R(\Omega)$. In the case of spectrally broad pulses, this can be expressed as a field correlation in the frequency

domain:

$$E_{\mathrm{CARS}}(\omega) \propto \int R(\Omega) E_{pr}(\omega - \Omega) d\Omega \tag{5.3}$$

The non-resonant background $C_{\mathrm{NR}}$ is a real number which can be assumed frequency-independent across the excitation bandwidth. The coherent nature of the vibrational response results in the interference of the resonant and non-resonant terms in the scattering process described by Eq. (5.3). Figure 5.3 shows the numerical simulation of both the squared amplitude ($|R(\Omega)|^2$) and phase ($\Phi(\Omega)$) of the complex vibrational response based on the spectroscopic data for azobenzene. As seen in Fig. 5.3(a), high non-resonant background distorts the lineshape of the small resonance around 1319 $\mathrm{cm}^{-1}$ into a characteristic dispersion profile. Such distortion represents a common problem both in narrowband and broadband CARS experiments as it creates ambiguity in the peak fitting and complicates the comparison between the coherent and spontaneous Raman spectra, often required for line identification. Here, we present an alternative approach to subtracting high non-resonant background in CARS spectroscopy.

The spectral phase of $R(\Omega)$ can be expressed as

$$\Phi(\Omega) = \arctan \frac{Im(R(\Omega))}{Re(R(\Omega))} \approx \frac{Im(R(\Omega))}{Re(R(\Omega))}, \tag{5.4}$$

where the approximate equality holds in the limit of $Im(R(\Omega)) << Re(R(\Omega))$. As seen from Eq. 5.1, this limit is reached in the case of high non-resonant response, i.e. when $C_{\mathrm{NR}} >> C_k/\Gamma_k$, and transform-limited excitation, i.e. when the pump-Stokes field correlation $A(\Omega)$ is a real quantity. Neglecting the real part of the resonant response, outweighed by $C_{\mathrm{NR}}$, we arrive at:

$$\Phi(\Omega) \approx \left[ \sum_k \frac{C_k \Gamma_k}{(\Omega - \Omega_k)^2 + \Gamma^2} \right] / C_{\mathrm{NR}}. \tag{5.5}$$

Hence, the resonant Raman spectrum, represented by the sum in the square brackets, is directly proportional to the spectral phase $\Phi(\Omega)$. This correspondence can be seen in comparing the spectral phase with the Raman spectrum in the numerically simulated cases of strong and zero non-resonance back-

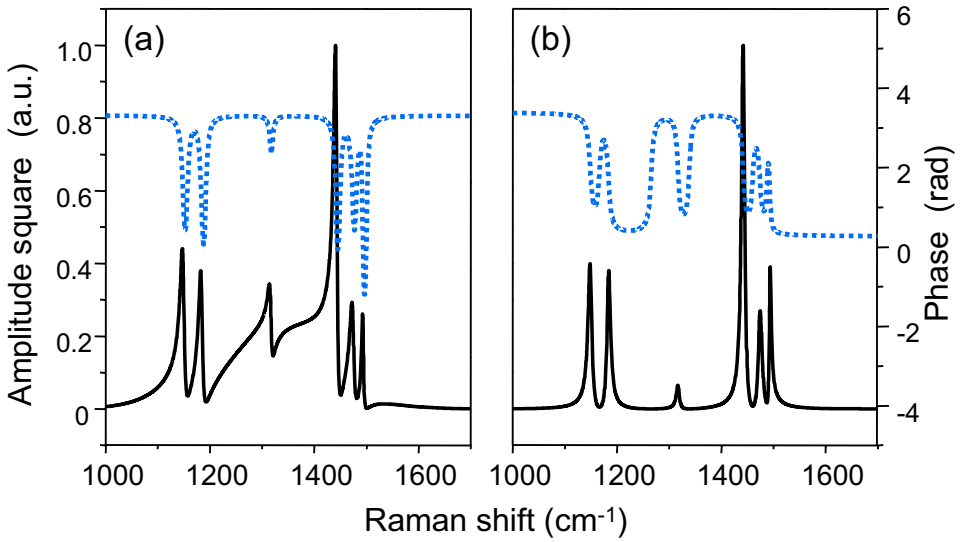


Figure 5.3: (Color online) Numerical simulation of the squared amplitude (solid black) and phase (dashed blue) of coherent vibrational response of azobenzene with (**a**) and without (**b**) high non-resonant background excited by the pump and Stokes pulses of 130 fs duration (FWHM). The similarity between the phase in (a) and amplitude in (b) is the key point exploited in our approach to background subtraction.

ground (Figs. 5.3(a) and 5.3(b), respectively). Note, that as long as the excitation field $A(\Omega)$ is real, its spectral profile does not enter the proportionality between the spectral phase and the Raman spectrum (Eq. (5.5)). Therefore, the relative strength of various Raman modes, $C_k$, is properly reflected in $\Phi(\Omega)$, regardless of their spectral overlap with the excitation profile $A(\Omega)$. This property makes the spectral phase more convenient quantity than the imaginary part of $R(\Omega)$ which, being proportional to $A(\Omega)$, favors the central part of the excitation spectrum.

Detecting the spectral phase of the vibrational response $R(\Omega)$ is not a trivial task. One way of extracting the vibrational phase from the time- and frequency-resolved CARS measurements has been recently demonstrated by our group [3]. The method utilizes the retrieval algorithm of cross-correlation frequency resolved optical gating (XFROG) applied to the ex-

perimentally measured two-dimensional time-frequency CARS spectrogram. Here, we implement the XFROG-CARS technique for efficient background subtraction from the experimentally detected vibrational spectrum of azobenzene.

Because of the gas sample that we used in this work, the experiment was carried out with a regenerative Ti-Sapphire amplifier (Spitfire, Spectra-Physics, pulse duration of 130 fs (FWHM), 1 kHz repetition rate) which provided 800nm wavelength probe pulses, and an optical parametric amplifier (TOPAS, Light Conversion) generating the pump and Stokes pulses at the wavelength of 1080nm and 1270nm, respectively. All laser beams were focused with a 50 cm focal-length lens to overlap in the BOXCARS phase-matching geometry [15] inside a gas cell filled with azobenzene and heated to $\approx$ 500 K (vapor pressure 18kpa). The anti-Stokes beam was spatially filtered and coupled into a spectrometer (McPherson 2035) with a CCD detector (Andor iDus 401DV). Two-dimensional CARS spectrograms were recorded by detecting the anti-Stokes spectrum while scanning the time delay between the probe and synchronized pump-Stokes pulse pair by a motorized translation stage. The total recording time of one spectrogram ranges from two to ten minutes, depending on the required resolution and limited by the sensitivity of the detector. A typical experimental spectrogram is shown in figure 5.4. Excited Raman modes result in the long tail on the picosecond time scale, while the instantaneous non-resonant response contributes to the sharp spike(s) at three pulses overlap. The spectrograms were used as an input to the commercial XFROG software (FROG3, FemtoSoft) for the retrieval of the amplitude and phase of the vibrational response $R(\Omega)$ as described in reference [3].

To improve the performance of the XFROG technique, the probe pulses were spectrally shaped with a home made pulse shaper based on a liquid crystal spatial light modulator. The pulse shaper was used for flattening the spectral phase of the probe pulse. Sinusoidal phase modulation was then applied to the transform limited probe by means of the same pulse shaper, resulting in a rich interference pattern in the measured two-dimensional CARS spectrogram (Fig. 5.4). Detailed discussion on this shaping can be

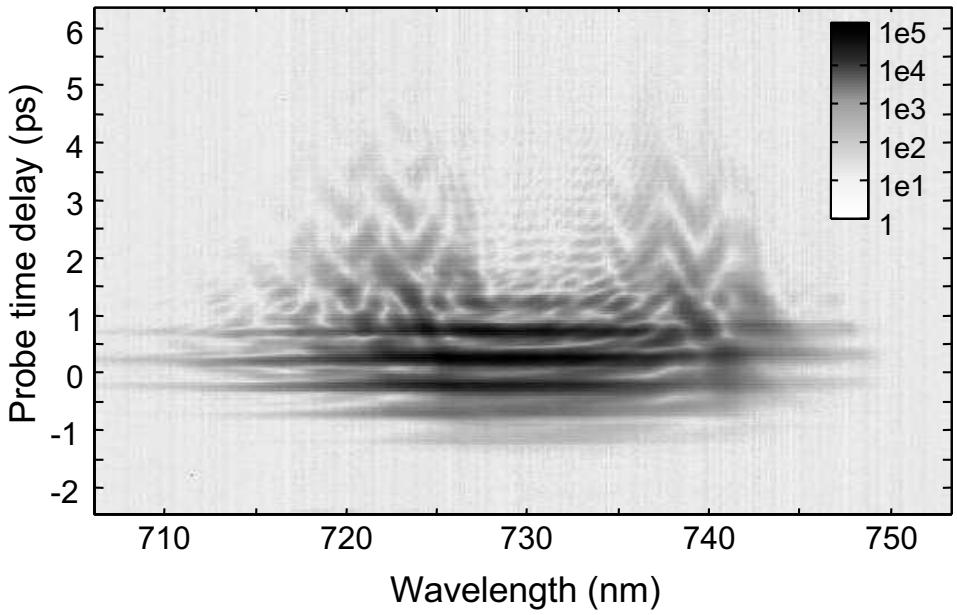


Figure 5.4: Experimentally observed time-frequency CARS spectrogram of azobenzene. (Details see text)

found in our earlier paper [16].

The results of the XFROG processing of the recorded CARS spectrogram are shown in Fig. 5.5(a). As reflected by the big pedestal around the center of the pump-Stokes excitation spectrum ($\sim 1300$ cm$^{-1}$), the vibrational response of azobenzene exhibits strong non-resonant background in this spectral region. Hence, the small resonance around 1319 cm$^{-1}$ assumes a characteristic dispersive profile. On the other hand, the retrieved spectral phase of $R(\Omega)$ shows much better correspondence to the locations and lineshapes of the Raman peaks, as illustrated in Fig. 5.5(b). Here, the smoothly changing baseline has been removed from the retrieved $\Phi(\Omega)$. The curvature of this baseline reflects the residual frequency chirp of the pump-Stokes convolution field (see Eq. (5.2)). As a result, different parts of the vibrational spectrum are excited at slightly different time moments. In direct analogy to chirp photon field, this results in an effective chirp of the coherent vibrational response which appears as a parabolic offset to $\Phi(\Omega)$.

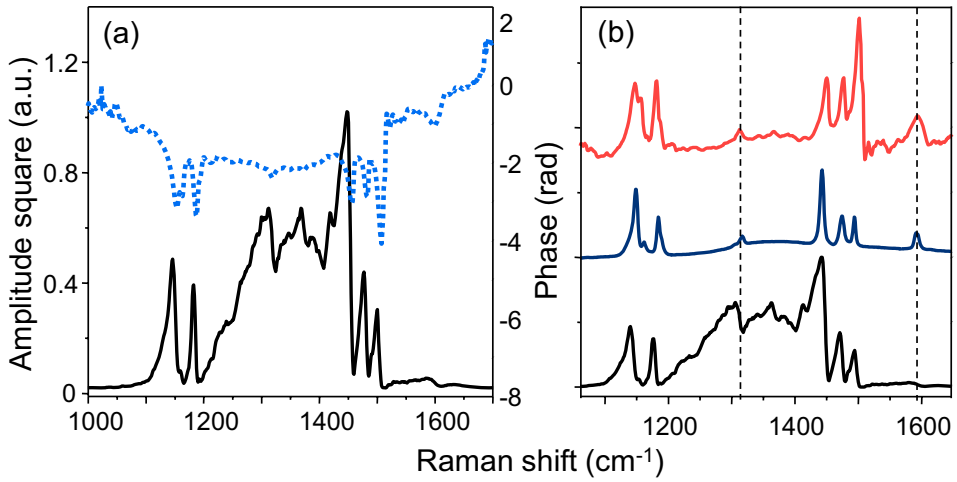


Figure 5.5: (Color online) (**a**) XFROG retrieval of the squared amplitude, $|R(\Omega)|^2$ (solid black), and phase, $\Phi(\Omega)$ (dashed blue), of the coherent Raman response of azobenzene. Sharp dips in the spectral phase correspond to the Raman resonances. Smooth parabolic baseline indicates the residual frequency chirp of the pump-Stokes pulses. (**b**) The retrieved spectral phase (upper red) in comparison with the spontaneous Raman spectrum (middle blue) and the squared amplitude of the vibrational response $R(\Omega)$ (lower black). The background-free spectral phase better reflects the small peaks at 1317 $cm^{-1}$ and 1591 $cm^{-1}$ (dashed lines), whereas $|R(\Omega)|^2$ shows dispersive profiles on top of the strong non-resonant background.

Such phase curvature can be easily subtracted by performing a separate characterization of the excitation pulses and compensated.

After the removal of the slow varying baseline, the retrieved spectral phase shows close resemblance to the spontaneous Raman spectrum, as illustrated in fig. 5.5(b). Our spectral phase approach demonstrates good sensitivity by revealing the 1591 $cm^{-1}$ peak on the far side of the excitation band. As expected, the spectral resolution is defined by the length of the time-delay scan rather than the probe bandwidth (the latter being about 130 $cm^{-1}$). Note, that although the approximation of high non-resonant background invoked in this work is not necessarily valid across the whole spectrum, the agreement between the retrieved spectral phase, $\Phi(\Omega)$, and

the reference spectrum of spontaneous Raman is very satisfactory. The deviations can be seen in the incorrect relative strength of the side peaks (e.g. 1493 $cm^{-1}$) whose amplitude is comparable to that of the non-resonant background.

In conclusion, we have demonstrated a new approach to remove high non-resonant background in CARS spectroscopy, based on the detection of the spectral phase of the vibrational response by means of the recently developed XFROG-CARS technique. The method proves applicable as long as the non-resonant response is comparable to or stronger than the amplitude of Raman resonances. The suggested technique does not require narrowband probing, and does not rely on polarization filtering or optical interferometry. In principle, it can be implemented in the collinear geometry and utilized in CARS microscopy, if the acquisition time is shortened to within practical limits.

# Bibliography


[1] J. X. Cheng, L. D. Book, and X. S. Xie, Optics Letters **26**, 1341 (2001).

[2] N. I. Koroteev, M. Endemann, and R. L. Byer, Physical Review Letters **43**, 398 (1979).

[3] X. J. G. Xu, S. O. Konorov, S. Zhdanovich, J. W. Hepburn, and V. Milner, Journal of Chemical Physics **126** (2007).

[4] P. D. Maker and R. W. Terhune, Physical Review **137**, A801 (1965).

[5] W. M. Tolles, J. W. Nibler, J. R. McDonald, and A. B. Harvey, Applied Spectroscopy **31**, 253 (1977).

[6] J. X. Cheng and X. S. Xie, Journal of Physical Chemistry B **108**, 827 (2004).

[7] N. Dudovich, D. Oron, and Y. Silberberg, Nature **418**, 512 (2002).

[8] D. Pestov, R. K. Murawski, G. O. Ariunbold, X. Wang, M. C. Zhi, A. V. Sokolov, V. A. Sautenkov, Y. V. Rostovtsev, A. Dogariu, Y. Huang, et al., Science **316**, 265 (2007).

[9] S. Constantine, Y. Zhou, J. Morais, and L. D. Ziegler, Journal of Physical Chemistry A **101**, 5456 (1997).

[10] B. von Vacano, T. Buckup, and M. Motzkus, Optics Letters **31**, 2495 (2006).

[11] E. O. Potma, C. L. Evans, and X. S. Xie, Optics Letters **31**, 241 (2006).

[12] S. H. Lim, A. G. Caster, and S. R. Leone, Physical Review A **72** (2005).

[13] C. C. Hayden and D. W. Chandler, Journal of Chemical Physics **103**, 10465 (1995).

[14] S. O. Konorov, R. F. B. Turner, and M. W. Blades, Applied Spectroscopy **61**, 486 (2007).

[15] A. C. Eckbreth, Applied Physics Letters **32**, 421 (1978).

[16] S. O. Konorov, X. G. Xu, R. F. B. Turner, M. W. Blades, J. W. Hepburn, and V. Milner, Optics Express **15**, 7564 (2007).

# Chapter 6

# Conclusion

This thesis has introduced new techniques of coherent anti-Stokes Raman spectroscopy with broad band pulses: the NASCARS method, the method of optical correlation of broad band pulses, the method of complete characterization of molecular vibration and the spectral phase approach of background free CARS. These methods stress different aspects of CARS and can be used under different conditions.

All the methods discussed in this thesis are based on the coherent property of CARS. The coherence between the vibrational levels adds correlation patterns to the noisy probe pulse, from which the vibrational resonance spacing can be extracted through spectral autocorrelation. In this way, the method of NASCARS was invented and demonstrated (chapter 2). The method of NASCARS can be implemented with collinear geometry in addition to the proof-of-principle experiment of non-collinear geometry. The single pulse version of NASCARS in collinear geometry offers a simple way of obtaining the vibrational level spacing of low wavenumber resonances without pulse shaping. In a broader perspective, the approach of tracking correlations within a coherent process can be an interesting topic. Considering CARS as one special type of resonant four-wave-mixing processes, possible applications of the noise correlations on general resonant four-wave-mixing can be an attractive field to explore. Since the method does not require exact shaping of the pulse, and noise that the light field gains during propagation actually helps recovering the vibration level spacing, it may have applications in the vibrational spectroscopy of high scattering media.

While the NASCARS method can only recover the vibrational level spacing of the resonances, the method of optical correlation of broad band pulse is able to obtain the high resolution spectrum (chapter 3). The correlation of

spectral components in a broad band pulse is now processed optically. The probe pulse of an optimized noise pattern is used to generate CARS signal and serve as an optical processing pulse in the sum frequency generation. The underlying novelty of this method is the introduction of conjugate pulse pairs. The proof-of-principle experiment was done with a pulse shaper to create a self-conjugate probe pulse. For the potential future development of this method, it would be attractive to find a universal way of creating a conjugate pulse for a given probe pulse and use it as a separate reference pulse. The phase-conjugate technique [1] is worth investigation.

The complete characterization of molecular vibration method (chapter 4) is different from the previously discussed two methods in that it stresses the recovery of maximal information from the laser induced coherent vibrations. As a result, it can not only obtain the spectrum of vibrational resonances but also the spectral phase. It achieves this complete characterization by a time-frequency two-dimensional scan. The ability to measure the phase of the vibration is the primary advantage of this method. As the experimental results demonstrate, the complete characterization approach can achieve much better spectral resolution than the probe pulse bandwidth. This is because for a coherent property, the frequency domain and time domain response are connected directly by the Fourier transform. With phase information available, the resolution on the frequency domain can be improved by increasing the range of the time domain measurement and vice versa, therefore the duration or bandwidth of the probe pulse is not a limitation. This is an effective solution to the "resolution vs. intensity" dilemma that discussed in section 1.2. Since the phase property is of central interest for coherent control, the ability to measure phase becomes a clear advantage. The direct potential application of this method would be tracking the amplitude and phase of arbitrary vibrational excitation. Since CARS is a special type of resonant four-wave-mixing, there is no reason that this complete characterization method cannot be applied to other type of resonant four-wave-mixing that may involve an electronically excited state, especially under the strong field condition. Due to the limited time span of my PhD study, there are other possible energy schemes (see figure 6.1) of complete characterization

of electronic excited states, which are waiting to be explored. From the perspective of data interpretation, the availability of both amplitude and phase of a coherent vibration allows a reconstruction of CARS response at any frequency or time resolution (see appendix D). In addition, this method can be used to characterize those population transfer technique such as Stimulated Raman adiabatic passage (STIRAP)[2] and the piecewise adiabatic passage technique[3]. For example, the aim of both STIRAP and piecewise adiabatic passage is to robustly transfer the complete population from the ground state to the excited via a real but not populated intermediate state through a special time ordered stimulates Raman process, that can fit into a CARS scheme (see figure 6.2) to use the complete characterization technique of XFROG. Monitoring the amplitude and phase evolution during the STIRAP process can help optimize parameters or even improve the adiabatic passage method itself.

The spectral phase approach (chapter 5) to recover the background free Raman spectrum under high non-resonant background conditions is an application of the method of complete characterization of molecular vibration. The non-resonant background is the factor that seriously limits the general application of CARS. The spectral phase approach can solve the high non-resonant background problem. The currently limitation of this approach is the overall operation time, since it involves a time delay scanning. If the time scan can be further improved by using a fast time delay device, the potential development of this spectral phase approach can be the field of micro-spectroscopy or even vibrational imaging of especially interested material of non-resonant background.

The methods presented in this thesis are improvement on one or another aspect of CARS. With the availability of coherent broad band laser, the ability of pulse shaping and characterization, there are certainly other possibilities of improvement on CARS along those fruitful lines of research.

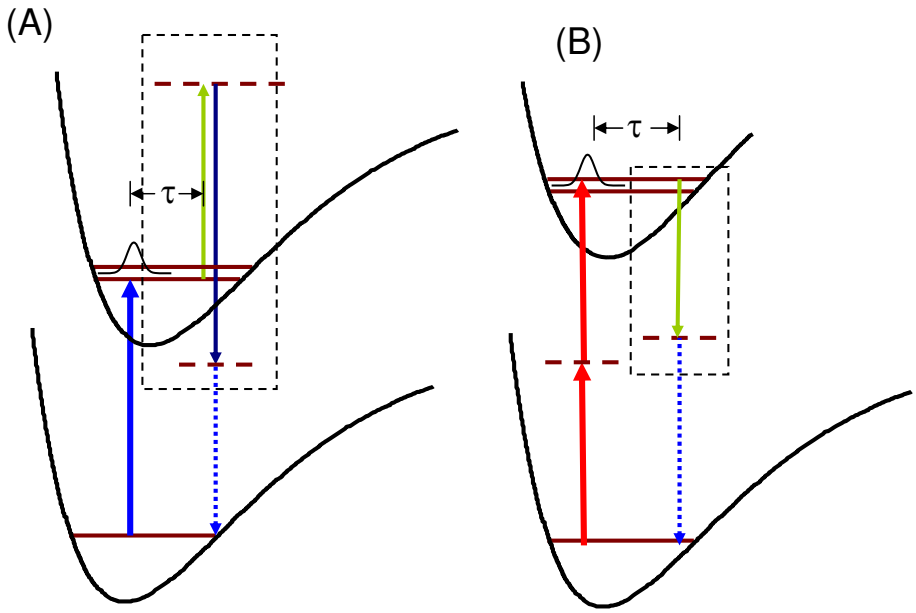


Figure 6.1: (A) shows one variation of complete characterization scheme to a one-photon allowed electronic level, with one excitation pulse and two probing pulses (shown inside the dashed box) to obtain the spectrogram for XFROG retrieval. (B) shows a variation of complete characterization scheme to a two-photon allowed electronic level. (Probe pulse is shown in dashed box).

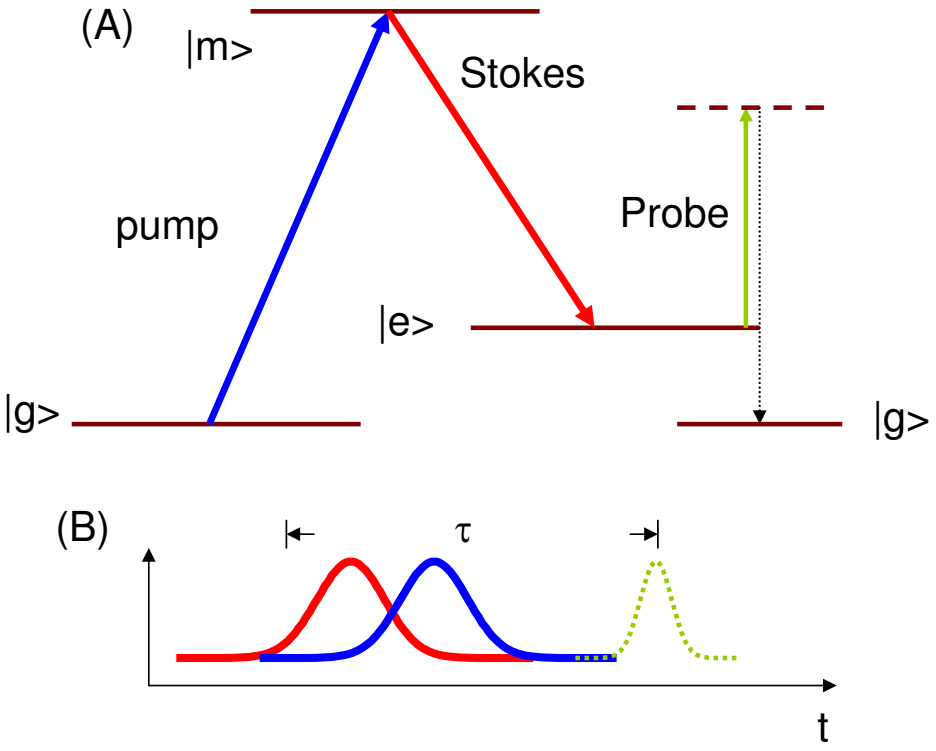


Figure 6.2: (A) shows the scheme of a combination of STIRAP with the complete characterization method. Two high intensity pulses transfer the population to the excited state, a weak intensity probe pulse tracks the actual transfer process in time. (B) shows the time ordering of the involved pulses.

# Bibliography

[1] E. M. Vogel, M. J. Weber, and D. M. Krol, Physics and Chemistry of Glasses **32**, 231 (1991).

[2] K. Bergmann, H. Theuer, and B. W. Shore, Reviews of Modern Physics **70**, 1003 (1998).

[3] E. A. Shapiro, V. Milner, C. Menzel-Jones, and M. Shapiro, Physical Review Letters **99** (2007).

# Appendix A

# MATLAB Simulation code of CARS

This appendix contains simulation code in MATLAB that we used for CARS signal simulation. MATLAB is a widely used scientific calculation platform. It was purchased from Mathwork. We used version 7.2 for our simulation.

The first program is to numerically generate optical pulse that can be used in subsequent CARS process simulations.

## A.1 Generate Pulse

The program A.1 calls function shaper.m to perform pulse shaping function.

## A.2 Pulse Shaping

The program A.2 is the content of shaper.m file for introducing spectral phase and amplitude shaping to the numerical created pulses.

## A.3 CARS Process Simulation

The program A.3 is the actual script that simulates the CARS process with shaped numerical pulses.

The MATLAB script A.3 is capable of simulating CARS spectrum of three pulses. If one wants to simulate a single pulse CARS, a simple way is to use same pulse parameters in all three pulses, and perform proper background subtraction. For the clarity of this thesis, possible variations of this simulation script are not included in this appendix.

**Program A.1** MATLAB program that generates E field of a pulse

```
function [pulsew pulset]=generate_pulse(centerw,FWHM,shaping,shapr,delay)

% output pulsew and pulset are the pulse field in frequency
%domain (wave number) and time domain (picosecond)input variable
%centerw is the central frequency of the broad band pulse, FWHM
% is the width at full width half maximum, shaping is the shaper
% mask, it contains both amplitude and phase two rows e.g.
% shaping=[ones(1,640);[pi*ones(1,320) zeros(1,320)]],
% it also can be one row which corresponds to spectral phase only
%e.g. shaping=[pi*ones(1,320) zeros(1,320)];
%it is in the shaper pixel.
%shapr is the shaper number which predefined
% in shaper_parameter.dat file
% delay is the time delay factor in picosecond

global point step;
start=centerw-point*step/2;
enda=centerw+point*step/2;
z=linspace(start,enda,point);
sizen=size(shaping);
% the following script is to make it adaptive to amplitude
%and phase or phase only shaping
if sizen(1)==1
    if isequal(max(shaping),min(shaping))
        phasew=0;else
        phasew=shaper(z,shaping,shapr);
    end
    amplitude=1;
else
    ampshaping=shaping(1,:); phaseshaping=shaping(2,:);
    if or(min(ampshaping)<0,max(ampshaping)>1)
        disp('amplitude mask out of bound.')
    end
    if isequal(max(phaseshaping),min(phaseshaping))
        phasew=0;amplitude=shaper(z,ampshaping,shapr);
        % here it call the shaper.m function, to shaper
    else
        phasew=shaper(z,phaseshaping,shapr);
        amplitude=shaper(z,ampshaping,shapr);
    end
end
```

```
delayfactor=2*pi*z*delay/1e12*3e10;
% here the time delay is done via the linear phase shift
% according to Fourier transform
pulsew=amplitude.*exp(-(z-centerw).^2/1.414/FWHM^2)
       .*exp(i*(phasew+delayfactor));
pulset=fftshift(fft(fftshift(pulsew)));
end
```

**Program A.2** MATLAB program that serves as pulse shaper.

```
function phasemask=shaper(z,shaping,shapr)
% shaper accept the z as a frequency array index
% (in wave number) and shaping as SLM pixel
% array (e.g. 128 or 640 for CRI SLM )
% The output is the spectral phase mask in the index of z
global p; % global variable p is used to communicate with
 % the pulse shaper setting
pixel=p(shapr,1);startw=p(shapr,2);pixelstep=p(shapr,3);
if isequal(length(shaping),pixel)==0
    disp('Shaper pixel dismatch see check shaper parameter set');
% this is an error handling
end
pixelposition=startw+pixelstep.*(1:pixel);
phasemask=interp1(pixelposition,shaping,z,'nearest',0);

phasemask(find(isnan(phasemask)))=0;
% this line is to remove the NAN in Matlab, replace it with zero

end
```

**Program A.3** MATLAB program that generates CARS.

```
function [spec spwindow probet tstep]=CARS(Stokesshape,delay)
% the output, spec is the CARS spectrum, spwindow is the
%index array of wavenumber that corresponds to the spectrum
% probet and tstep are the probe pulse in time and time step
% that can be used in subsequent XFROG simulation delay is the
% time delay between probe pulse and pump/Stokes pair
% Stokesshape is the pulse shaping on Stokes field,
%it can be replacement with pumpshape or probeshape
global point step p;
global pumpcenter Stokescenter probecenter pFWHM SFWHM prFWHM;
p=importdata('Shaper_parameter.dat');
% Shaper_parameter.dat file in same directory storage the settings
%of shaper, it is actually an array in the format %similar to shaper
%calibration in my actual experiment, e.g. two pulse shapers, 128 pixel
%and 640 pixel format is as follows

%128.0   11604.0 14.0
%640.0   10668.0 3.0
% with pixel number starting wavenumber and pixel size

spcenter=745; spband=50; %spectrometer detection window, spcenter is
%the central wave length, spband is the total CCD bandwidth  all in nm
spwindow=linspace(spcenter-spband,spcenter+spband,2048);
point=40960;step=0.5; % this is the total points in simulation,
%a large number of points reduce the chance of %simulation glitch but
%it also increase calculation time.
tstep=1e12/(point*step*3e10);
pumpcenter=12500;pFWHM=25*16;
    %pump pulse central wave number and FWHM
Stokescenter=1e7/860;SFWHM=25*16;
    %Stokes pulse central wave number and FWHM
probecenter=12500;prFWHM=20*16;
    %probe pulse central wave number and FWHM

% the following matrix is the resonance structure the first
%  row is the % relative resonant strength, second row is the
% resonant position in wave number (Raman shift)
% the third one is line width and the forth one is the
% non-resonant background number
```

```
res=[1 0.4 0.9 0.7;
    1000 1027 782 1206;
    4.5 4.1 3.5 3.5;
    0.005 0 0 0];
pumpshape=zeros(1,128);
         % this is the spectral phase mask for pump pulse
probeshape=[zeros(1,64) pi*ones(1,64)];
        % spectral phase shaper for probe pulse

% note that here the Stokesshape is missing, because
%in this script it is a input parameter
[pumpw pumpt]=generate_pulse(pumpcenter,pFWHM,pumpshape,1,0);
 %128 pixel, 1 corresponds to the firs line on Shaper_parameter.dat
 %file, in my file first line is 128 pixel
[Stokesw Stokest]=generate_pulse(Stokescenter,SFWHM,Stokesshape,2,0);
%2 means 640 pixel SLM
[probew probet]=generate_pulse(probecenter,prFWHM,probeshape,1,delay);
%1 means 128 pixel SLM

tscale=tstep*(-point/2+1:point/2);
convt=pumpt.*conj(Stokest);
convw=fftshift(ifft(fftshift(convt)));
differencew=pumpcenter-Stokescenter;
omg=linspace(differencew-point*step/2+step,
            differencew+point*step/2,point);
resonance=res(1:3,:);
NonR=res(4,1);
Lorentzian=zeros(1,point)+ones(1,point)*NonR;
%NonR is the nonresonance background

for n=1:length(resonance)
    Lorentzian=Lorentzian+resonance(1,n)
                ./(-omg+resonance(2,n)-i*resonance(3,n));
end
vampw=Lorentzian.*convw;
vampt=fftshift(fft(fftshift(vampw)));
CARSt=vampt.*probet;
CARSw=fftshift(ifft(fftshift(CARSt)));
spec=CARSw.*conj(CARSw);
CARScenter=probecenter+pumpcenter-Stokescenter;
CARSscalewn=CARScenter+([-point/2+1:point/2]*step);
CARSscale=1e7./CARSscalewn;
% this is to generate a spectrameter scale
% that come with the CARS spectrum
spec=interp1(CARSscale,spec,spwindow); %fit to spectrometer window
end
```

## A.4 Simulation on XFROG CARS

The "xfrog.dat" and "probefile.txt" are the output files which are already in the required format of FROG3 software.

**Program A.4** MATLAB program that generates time frequency XFROG trace of CARS

```
function output=CARSXFROG(shaping,delay)
global point;
[spec CARSscale probet tstep]=CARS(shaping,0);
lendelay=length(delay);
lenspec=length(spec);
output=zeros(lendelay,lenspec);
fprintf(' 0%%');
for nm=1:length(delay)
    output(nm,:)=CARS(shaping,delay(nm));
    aa=fix(nm/length(delay)*100);
    fprintf('\b\b\b%2d%%',aa);
end
probet=probet(fix(point/2)-2048:fix(point/2)+2047);
tstep=tstep*1e3;
probetfilerange=[-2048:2047]*tstep;
specincr=abs(CARSscale(fix(lenspec/2))
        -CARSscale(fix(lenspec/2)+1));
speccenter=(max(CARSscale)+min(CARSscale))/2;
```

```
prolen=length(probetfilerange);
outputfile=zeros(prolen,5);
outputfile(:,1)=probetfilerange';
% the first column is the time index in femtosecond
outputfile(:,2)=abs(probet).^2;
% the second column is the total
% intensity in time domain of probe pulse
outputfile(:,3)=unwrap(angle(probet));
% the third column is the phase of E field
outputfile(:,4)=real(probet);
 % the fourth column is the real part of the E field
outputfile(:,5)=imag(probet);
% the fourth column is the imaginary part of the E field
Tincr=[delay(2)-delay(1)]*1e3;
fprintf('writing files:\n');
fid = fopen('xfrog.dat', 'wt');
fprintf(fid, '%d %d %12.5f %12.5f %6f \n',
lendelay,lenspec,Tincr,specincr,speccenter);
% this is the header of the XFROG trace as
% the requirement of FROG3 software
% lendelay is the number of delay points,
% lenspec is the number of spectrameter CCD pixel ,
% Tincr is the time step of scanning step
% specincr is the wave length increment of CCD pixel ,
% speccenter is the central wave length of CCD
fclose(fid);
save xfrog.dat output -ascii -append;
fprintf('file xfrog.dat written\n');
save probefile.txt outputfile -ascii -tabs;
fprintf('file probefile.txt written \n');
end
```

# Appendix B

# Alignment of the Pulse Shaper and Calibration of the SLM

## B.1 Alignment of the Pulse Shaper

A low power broad band pulse from a Ti:sapphire oscillator can help the alignment of a pulse shaper. The procedures are as follows:

1. Optical elements on table are placed as figure B.1 shows.

2. The input mirror is adjusted to let the oscillator beam hit the grating. The light beam should pass on top of output-coupling mirror. The beam spot on grating should be at the top as figure 1.30inset (C) dot 1 shows.

3. The grating is mounted a rotational stage. One adjusts the grating angle by rotating the stage to let the dispersed light pass above the intermediate mirror M. Figure B.1 inset (D) shows the relative position. The grating should be placed at exact vertical to the optical table. This can be checked by the dispersed elliptical light patten being parallel to the optical table.

4. The distance of the cylindrical mirror from the grating is adjusted to match the focal length. The cylindrical mirror should collimate the light to a parallel dispersed light belt.

5. The pitch of cylindrical mirror is adjusted for few degrees to make the dispersed light belt hit the intermediate mirror M at the upper part of the mirror as figure B.1 inset (D) dot 2 shows.

6. The intermediate mirror M is set to the let the reflected light enter

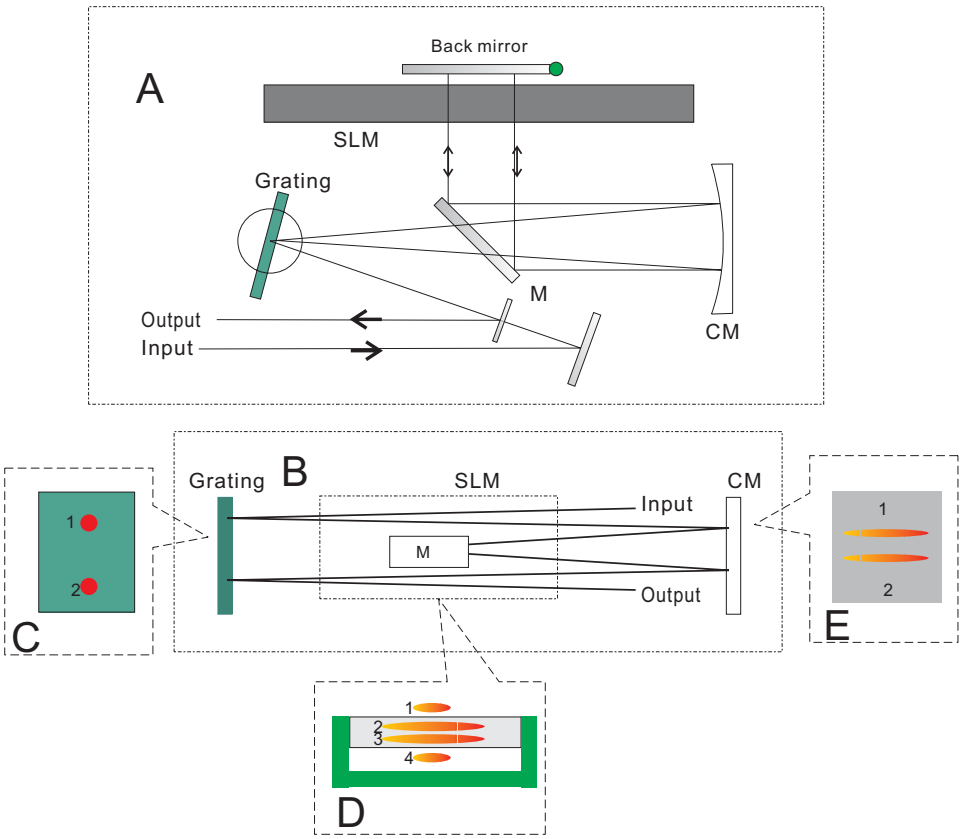


Figure B.1: The above figures show the setup of a folded pulse shaper. The grating on this setup is either 600 or 800groves/mm; cylindrical mirror is $f = 50cm$, and CRI SLM-640 has a window size about 5cm. Figure (A) shows the top view of the pulse shaper. Figure (B) shows the side view of the pulse shaper. Insets (C) to (E) shows the light profile on corresponding optical elements.

the SLM at right angle.

7. The forward/backward and horizontal positions of the SLM are adjusted and an adjustable mirror is mounted behind the SLM to reflect the light belt back to the bottom side of the intermediate mirror M as figure B.1 inset (D) dot 3 shows.

8. The intermediate mirror M should reflect the light to the cylindrical mirror. The mirror behind the SLM have to be adjusted to let the reflected light spot on the cylindrical mirror as figure B.1 inset (E) shows. The Light after the cylindrical mirror are re-focused onto the bottom part of grating. The grating recombines the light into uniform output beam.

After the above alignment, SLM from the pulse shaper is then removed from the optical setup. The output beam is then coupled to an autocorrelator(FR-103, Femtocrhome) and the distance between the cylindrical mirror and the grating is adjusted to minimize the pulse durations while monitoring the autocorrelator. After minimization of the pulse duration, the SLM should be put back to the Fourier plane and the pulse shaper optical alignment is then completed.

## B.2 SLM Voltage to Phase Calibration of CRI-SLM 640 SLM

After the optical path alignment of a pulse shaper, the next step is to obtain the voltage vs. phase relation of the SLM.

Before voltage vs. phase calibration, it is necessary to perform a quick frequency vs. pixel calibration to find out the frequency/pixel correspondence. It can be done as follows:

1. The broad band pulse is aligned into the pulse shaper as appendix B.1 described

2. Arbitrary voltages are set to a serials of pixels.

3. The corresponding dips or spike on spectrum is found and related to the pixels.

4. A linear fit is performed to get the calibration coefficient a and b

with $\lambda = a \cdot n + b$ where $\lambda$ being the light wavelength and n being the pixel number.

With these coefficients obtained, the wavelength of all pixels can be easily calculated. It is used in the subsequent voltage vs. phase calibration.

The fundamental idea on the voltage vs. phase calibration is to scan the voltage of the SLM pixels and measure the transmittance, and the transmittance is used to calculate the phase. A more detail description on nematic liquid crystal SLM on voltage and phase can be found in Juan M Bueno 2000 *J. Opt. A: Pure Appl. Opt.* 2 216-222 . An example transmittance vs. voltage curve is shown as figure B.2 (A). A phase vs. voltage calibration $\phi(v)$ (figure B.2 (B)) can be obtained through calculation.

The two masks of the CRI-SLM 640 have to be calibrated accordingly. The procedure is described as follow: 1. A pair of polarizers is placed at the input and the output of the pulse shaper. The direction of polarization on two polarizers should be set to parallel to the input beam to obtain maximal transmission.

2. The voltage value of the first liquid crystal layer is fixed to certain value (e.g. 1000 voltage count as defined by CRI) and the voltage of the second layer is scanned.

3. The spectra are recorded while the second layer voltage is scanning. The spectrum vs. voltage count is a two dimensional data array. From this array, the transmission vs. voltage curve can be extracted for each frequency.

4. The measured SLM pixel vs. frequency coefficient is used to obtain the transmittance vs voltage curve for each SLM pixel. Figure B.2(A) shows the shape such transmittance vs voltage curve.

5. The peaks and valleys of calibration curves are located. At these locations, calibration curves are cut into segments. Within each segment, one can use the following formula $\phi = 2\arccos(\sqrt{T})$ to convert transmission T into phase.

6 The segments of phase vs voltage curve are connected to get a long range, smooth phase vs. voltage curve as Figure B.2(B) shows. Because the multi-value property of arccos function, adjustment of the integer multiple of $\pi$ is required for a smooth connection of curve segments.

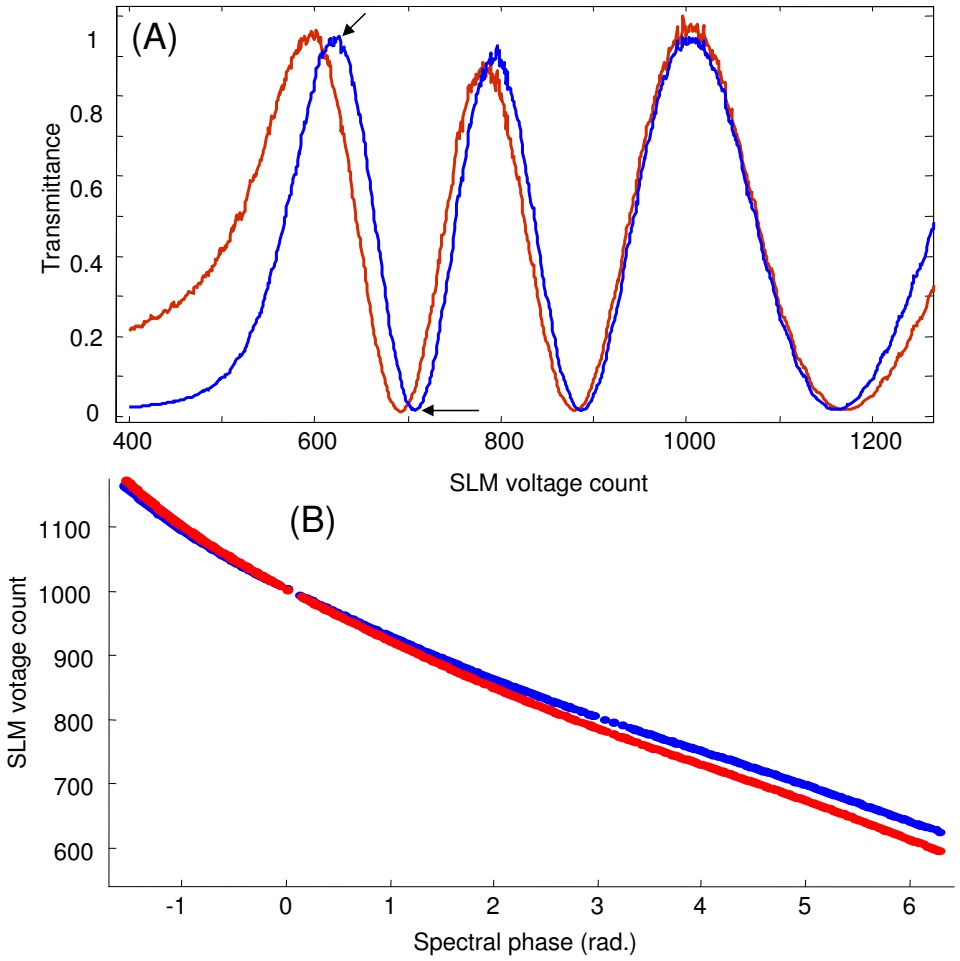


Figure B.2: Figure (A) is the experimental recorded transmittance vs. voltage count curve (CRI SLM-640). The response between maximum and minimum locations (arrows) is used as the total transmission and null transmission to create the phase-voltage response curve shown as figure (B). The blue curve and red in both (A) and (B) correspond to different frequency component of broad band light.

7. The curve can be fitted using a proper continuous function (5th order polynomial was used in the experiment) to obtain the $V_s(\phi, \lambda)$ relation. After curve fitting, one should find the voltage value on the second layer that corresponds to zero phase shift (as calculated by the fitting function).

8. The calculated mask is then applied to the second layer. Then, the voltage value of the first layer and is scanned to obtain a transmittance vs voltage curve similar to that of steps 3 and 4.

9. The voltage vs. phase curve of the first layer is then obtained to calculate the $V_p(\phi, \lambda)$. It is similar to steps from 5 to 7.

Now the calibration curves are obtained for both masks. They are used to convert the phase and amplitude values into voltage counts that can be set directly to two SLM masks. Considering that the voltage vs. phase relation is also wavelength dependent, a computer program was written to do the fitting for the range of pulse shaper light bandwidth.

# Appendix C

# XFROG Retrieval Using FROG3 Software

Due to the requirement on time and expertise on algorithm, I haven't written the XFROG retrieving script, so far FROG3 software (Version 3.2.2 ) has been used to retrieve the vibrational coherence. It was purchased from Femtosoft company (http://www.femtosoft.biz/). FROG3 is a compiled executable program and is useful to retrieval FROG trace as well as XFROG trace in optical field characterization. In order to make it work in vibrational coherence characterization, the data should be organized in correct format.

## C.1 Obtaining and formatting the recorded data

XFROG retrieval requires two sets of data. First data set is used to characterize probe pulse of the CARS. The second data set is the time-frequency CARS spectrogram (also called XFROG trace). The characterization of probe pulse can be done by FROG or MIIPS. Both intensity and phase information of the probe pulse have to be experimentally characterized.

The FROG3 software is used for the actual retrieval. It only accepts data in certain format. The acceptable probe pulse format are five columns, comprised of time scale column, intensity column, phase column, real part column and imaginary part column. The MATLAB simulation program A.4 contains the generation of a numerical probe pulse of acceptable format. Due to the processing ability of FROG3 software, the size of numerical probe pulse is limited to 2048 points (as for FROG3 software ). Too many or too little points both reduce the FROG3 software performance and sometimes

lead to poor algorithm convergence.

The trace data should be a two-dimensional array, with row being spectrum and column representing different time delay. A header file before the data file makes the operation with software simple. The header are an array of numbers: the first one is the number of delay points; the second one is the number of spectrometer CCD pixel; the third one is the time step size in femtosecond; the fourth one being the wave length increment of CCD pixel; the fifth one is the central wavelength of detection CCD. The MATLAB simulation program A.4 provides a functional sample as well.

## C.2 Operation with software

After the installation of FROG3 software, open it and select "run" XFROG (hot key ctrl-x) it will bring a screen like figure C.1

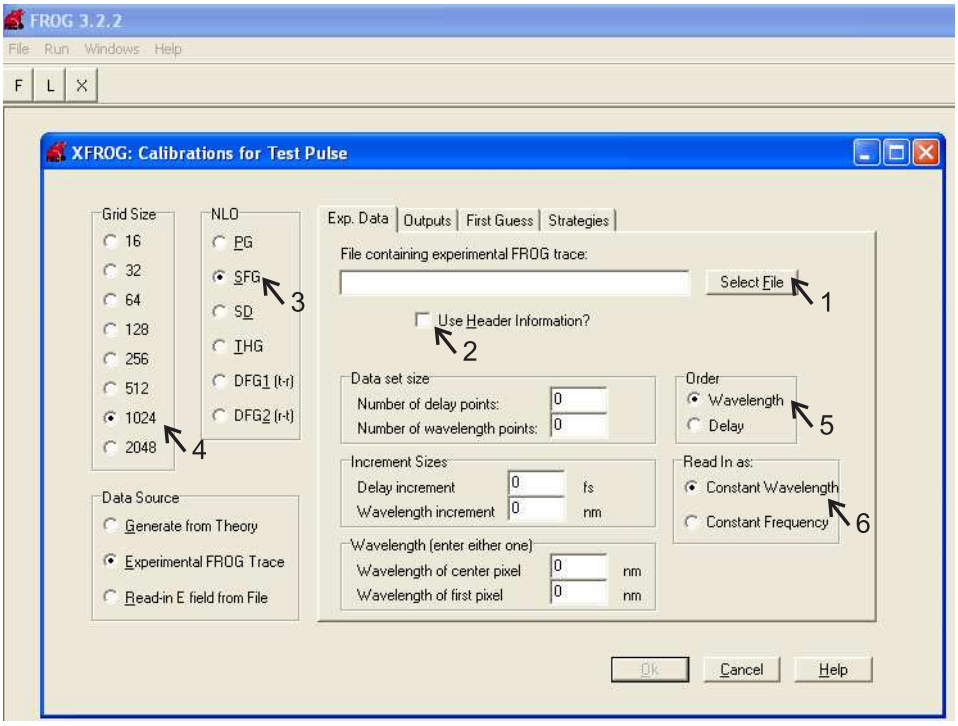


Figure C.1: Experimentally observed time-frequency CARS spectrogram of azobenzene. (Click arrow 1 to select the XFROG (CARS) trace file. Tick the arrow 2 box if the file has header, if not, leave it unchecked and manually input these parameters. Select the settings to "SFG" for XFROG CARS at the arrow 3 position. Arrow 4 position shows the number of points, select it according to data point. A good practice for this experiment record data with points of 256,512 or 1024 points. This can avoid the subsequent interpolation. Arrow 5 and 6 positions are related to the format of trace file. Select "Wavelength" if in the data array row is spectrum otherwise select "Delay". Select "Constant wavelength" if the data is recorded from a spectrometer.

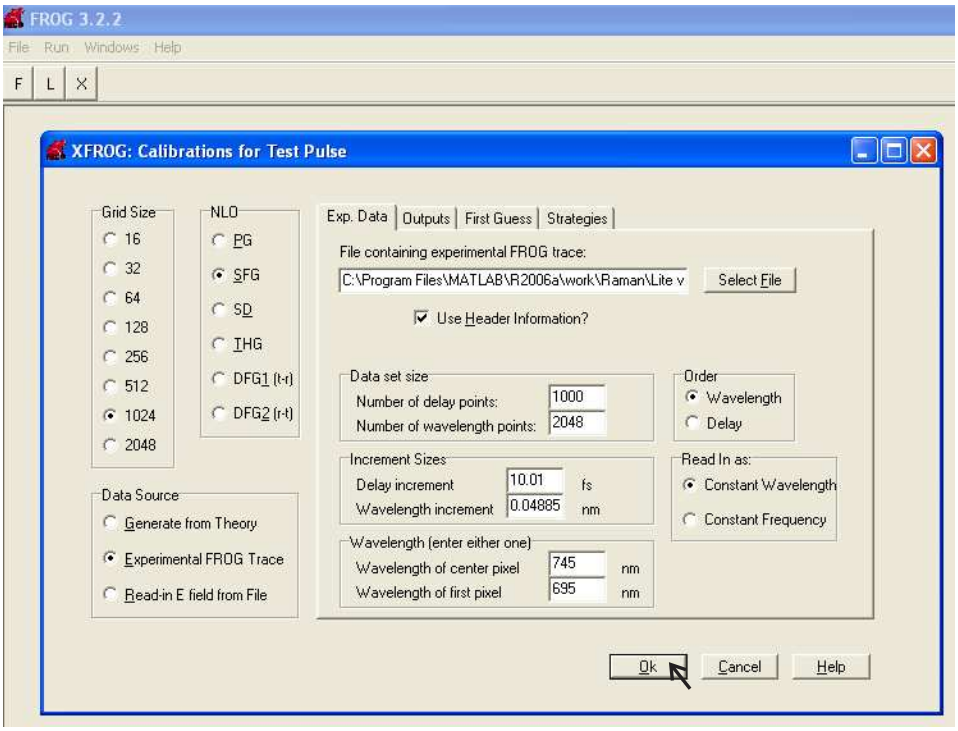


Figure C.2: After all settings correct, click "OK" box to go to next screen. This figure is included as a reference.

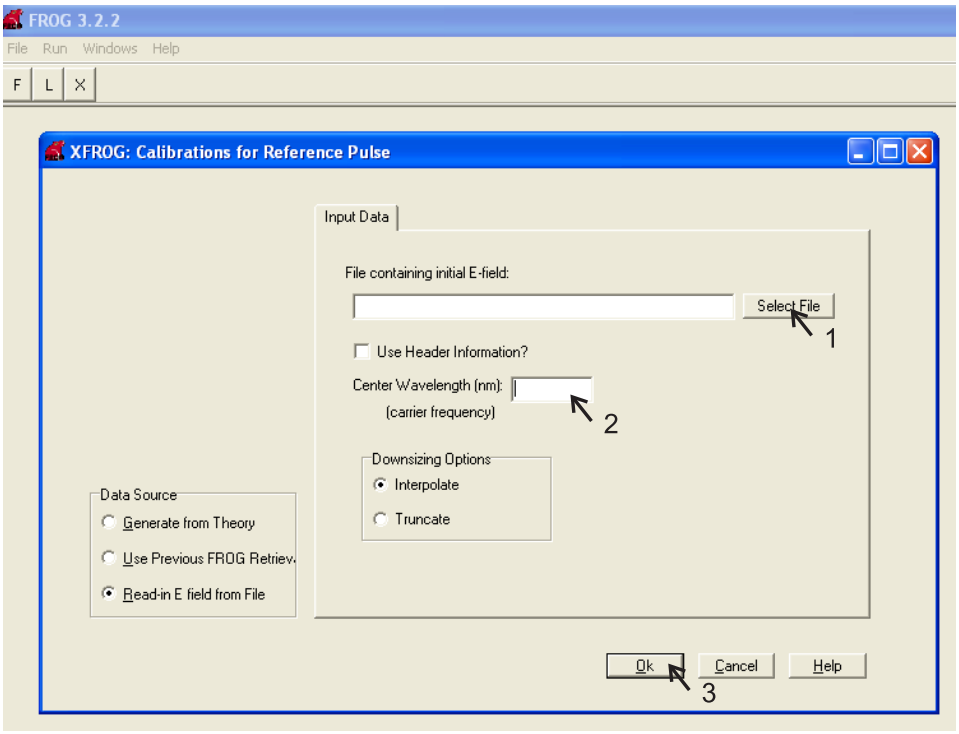


Figure C.3: Select "Read-in E field from file", then select probe file and input the center frequency. The file of the probe field file is in time domain and should not contain fast carrier oscillation.

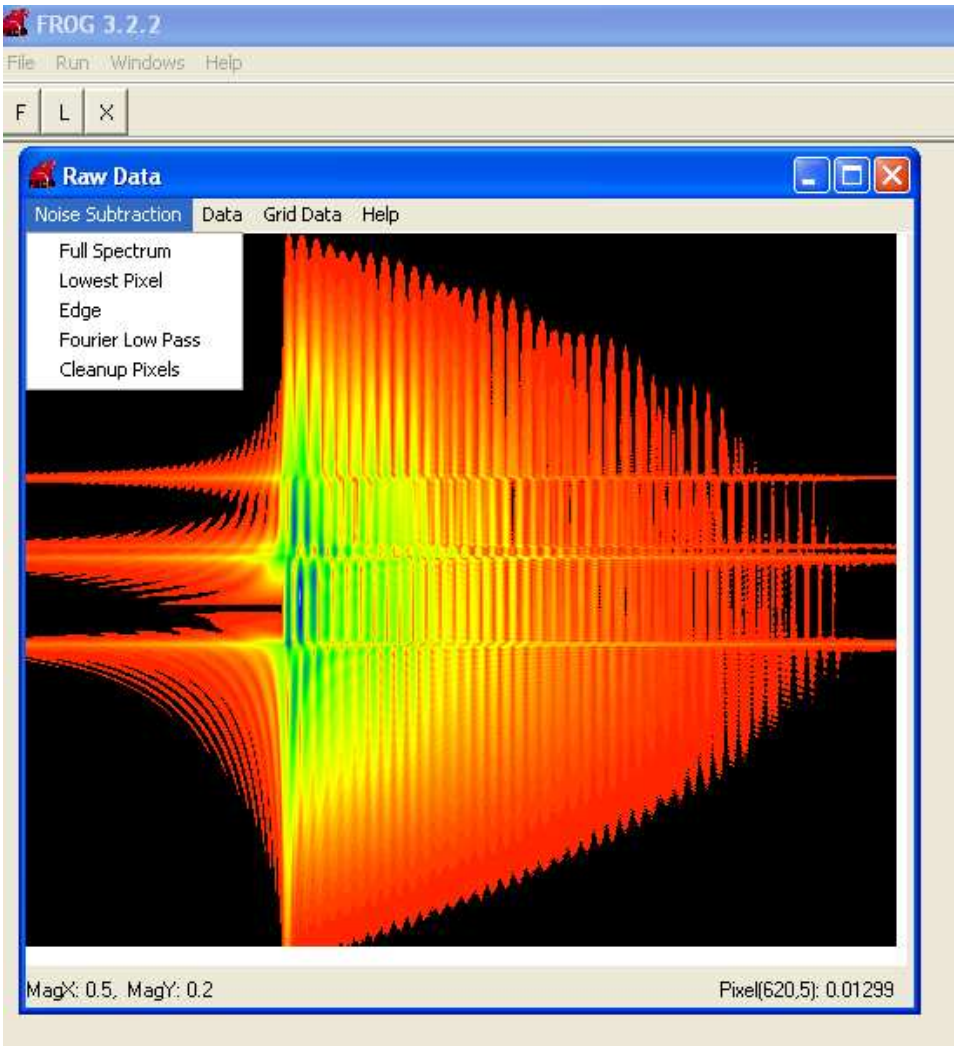


Figure C.4: FROG3loads the trace and display it in logarithmic scale. For experimental recorded trace, it has some noise spot. One can use the five noise subtraction options to reduce noise spot.Note that the edge option potentially can change the relative ratio between highest signal and lowest signal.

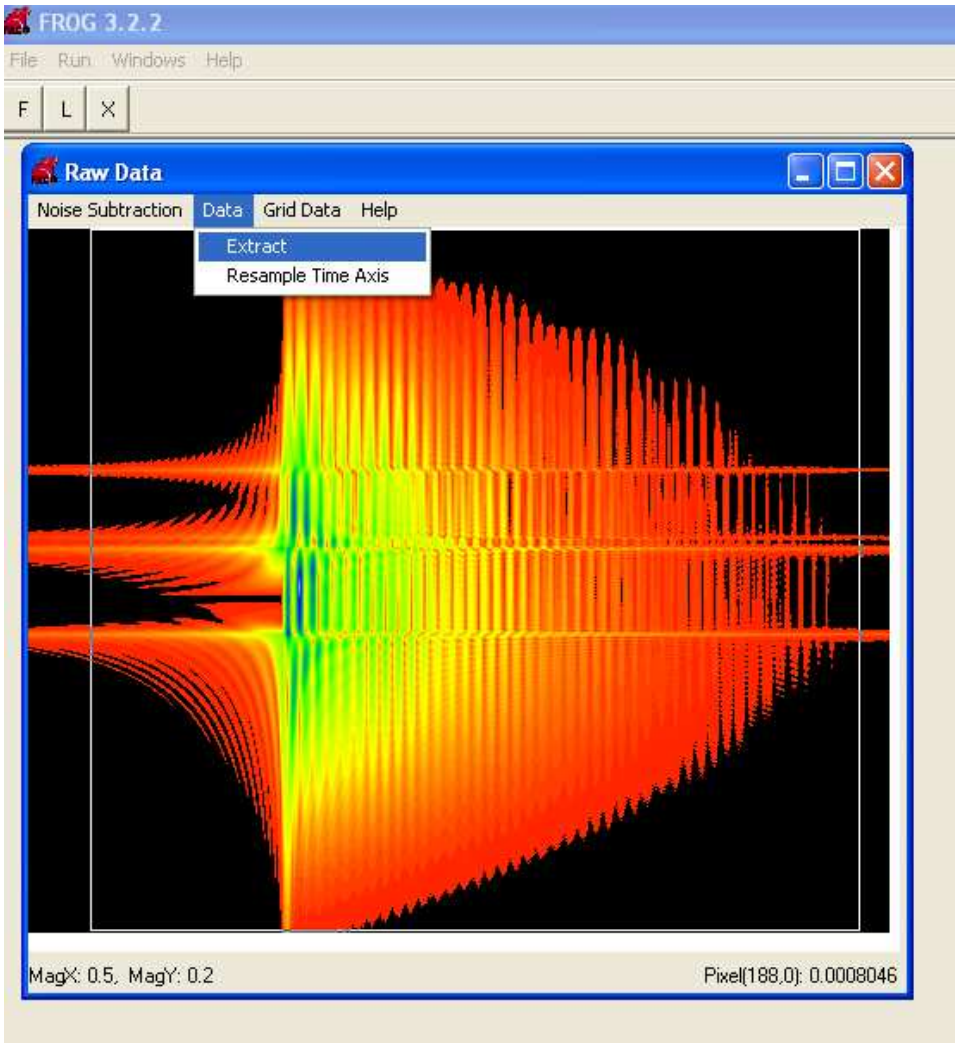


Figure C.5: One can also use the extract function to extract the region of interest. This function is used to cut the residue probe pulse. Then click the "Grid data".

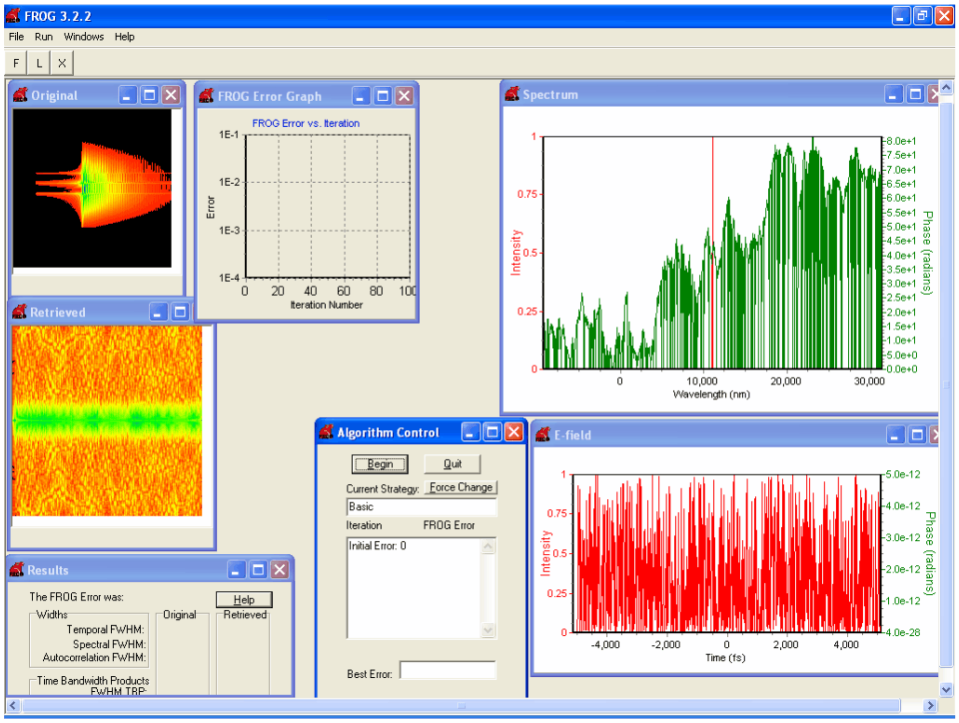


Figure C.6: This screen show the experimental trace and initial guess (as a built-in function of FROG3). Click the "Begin" button to start retrieval.

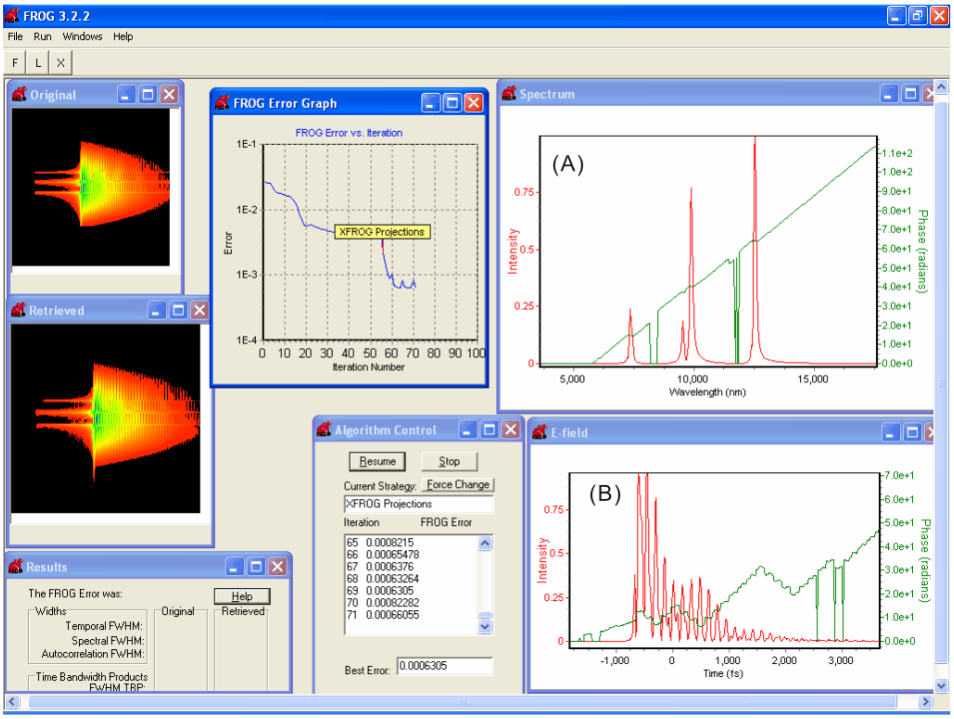


Figure C.7: After certain iterations, it shows convergence, which means the "Retrieved" two dimensional graph is the same as the input "original" spectrogram. It can be stopped or paused. If it is stopped, the retrieved E-field in both frequency and time domain will be saved as file "speck.dat" and "Ek.dat" in the same folder as the trace file. If convergence cannot be achieved, it means the input probe pulse is not accurate or the recorded two-dimensional trace has error. Due to some unknown reasons, the spectral phase of XFROG retrieval has a linear slope, this does not affect data interpretation. It can be trivially removed by linear fitting and subtraction. At the point where corresponding intensity is zero or close to zero, the spectral phase is also give number zero by the software.

# Appendix D

# New Representations of Characterized Vibrational Coherence

This appendix includes a submitted article to Journal of Chemical Physics by our research group with this title.

## D.1 Characterization of Transient Molecular Vibrations on the Way Towards Coherently Controlled Vibrational Target State

Broad spectral width of ultrashort laser pulses has offered new possibilities for coherent control of atomic and molecular quantum states [1]. When a desired target state can be reached via multiple distinguishable paths, control can be implemented by adjusting the spectral components resonant with the corresponding interaction paths. Owing to quantum interferences, one can enhance the amplitude of the target state while suppressing others. In the case of relatively simple systems, the control fields can be calculated *a priori* [2], whereas feedback controlled schemes are employed for controlling more complex systems [3]. Both approaches proved very successful in reaching the target quantum state *at the end* of the laser interaction with atoms or molecules. On the other hand, transient behavior, i.e. the

[0] A version of this chapter is to be appeared in *Journal of Chemical Physics* as Stanislav O. Konorov, Xiaoji G. Xu, John. W. Hepburn and Valery Milner "Characterization of Transient Molecular Vibrations on the Way Towards Coherently Controlled Vibrational Target State"

evolution of the molecular quantum state *during* the interaction with the control field, is rarely considered in the context of coherent control. Such transient dynamics may, however, become important if the intermediately populated quantum states are coupled to the irreversible decay channels, such as photo-ionization, dissociation or chemical reactions [4]. There are two reasons for the transient re-distribution of molecular population among quantum states. In addition to the "control" resonant frequencies, continuous spectrum of an ultrashort pulse contains many off-resonant components which induce population transfer on the time scale inversely proportional to the frequency detuning from the corresponding resonance [2]. The second reason applies to the strong-field regime of interaction, in which the "bare" eigenstates of a free-molecule Hamiltonian are significantly shifted in energy during the interaction with a control field. Though successfully used in the strong-field control schemes [4, 5], these light-induced shifts may result in transient resonances leading to undesired population transfer.

Here we demonstrate tracking of transient vibrational dynamics of a molecule interacting with the control laser field. The latter excites molecular vibration, i.e. a superposition of several vibrational eigenstates, in the ground electronic state via two-photon Raman transition (Fig.D.1). Coherent control of the target vibrational superposition state is executed by shaping the spectrum of the two-photon excitation field in such a way as to suppress the frequencies of certain vibrational transitions, thus leaving those vibrational modes unexcited (e.g. $|b_2\rangle$ state in Fig.D.1). Complete time evolution of the vibrational coherence is detected by means of the cross-correlation frequency resolved optical gating of coherent anti-Stokes Raman scattering (XFROG CARS [6]). We show that even though the final state does not include those vibrational modes whose transition frequencies were blocked in the shaped excitation field, these modes are strongly excited on the intermediate time scale and then de-excited at the end of the interaction. The analysis is possible due to the capability of XFROG CARS to reconstruct molecular coherence with variable time and frequency resolution, without changing the experimental parameters and repeating the experiment.

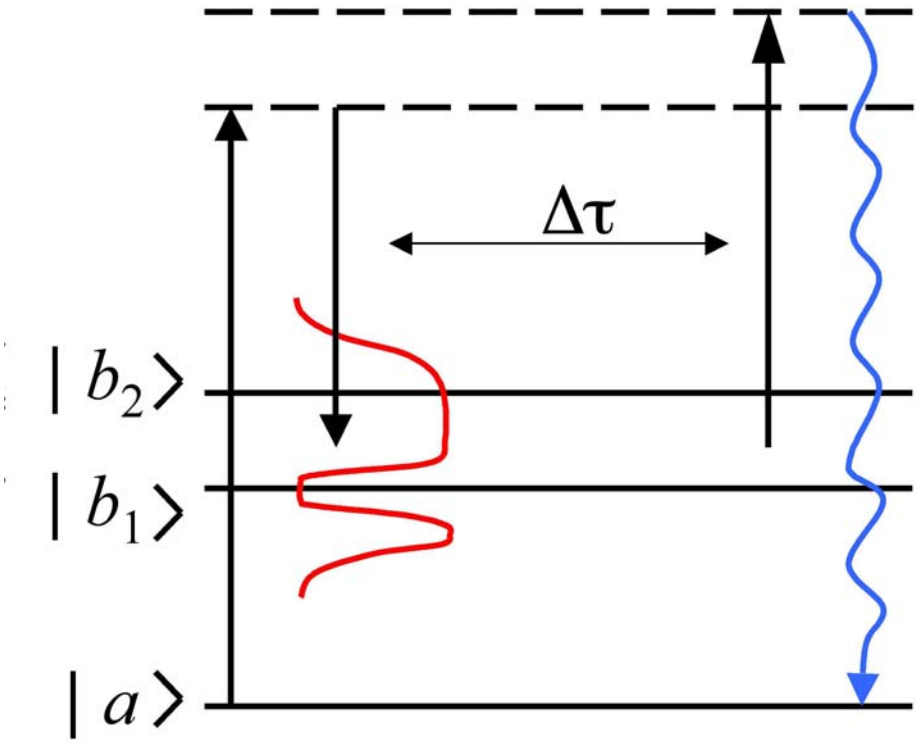


Figure D.1: Energy level diagram and interaction scheme for Coherent anti-Stokes Raman Scattering process with spectrally shaped excitation fields.

In the bare state basis of Fig.D.1, a wavefunction of the $j$-th molecule can be written as:

$$\psi(\mathbf{r}_j, t) = a(t)|a\rangle + \sum_k e^{i(\mathbf{k}_1 - \mathbf{k}_2)\mathbf{r}_j} b_k(t)|b_k\rangle, \tag{D.1}$$

where $a(t)$ and $b_k(t)$ are complex amplitudes of the ground and $k$-th excited state, respectively, for simplicity assumed identical for all molecules in the ensemble. Following the derivation of [7], it can be shown that the amplitude of the coherent anti-Stokes field, emitted in the phase-matching direction, is proportional to the convolution of the probe field amplitude and the resonant molecular response:

$$E_{aS}(\omega) \propto E_{pr}(\omega) \otimes \sum_k \frac{\rho_{ab}^k(\Omega)}{\Omega - \Omega_k + i\gamma_k}, \tag{D.2}$$

where $\rho_{ab}^k(\Omega) \equiv a(\Omega)b_k^*(\Omega)$ represents the vibrational coherence of the $k$-th mode, with $a(\Omega)$ and $b_k(\Omega)$ being the Fourier transformed bare state amplitudes $a(t)$ and $b_k(t)$. The XFROG CARS method enables one to re-construct the complex molecular response $R(\Omega) \equiv \sum_k \rho_{ab}^k(\Omega)/\left[\Omega - \Omega_k + i\gamma_k\right]$ (second term in Eq.D.2) by measuring the two-dimensional spectrogram $I(\omega, \tau) \equiv |E_{aS}(\omega, \tau)|^2$, corresponding to the spectrum of the anti-Stokes field at variable time delays $\tau$ of the probe field [6]. An example of such spectrogram is shown in Fig.D.2. Two-dimensional CARS spectrograms have been widely used in describing coherent molecular dynamics as they provide convenient visualization of both the spectral and temporal features of the molecular response [8, 9]. By experimentally adjusting the probe pulse duration, one can obtain spectrograms exhibiting the desired time and frequency resolution [9]. Shorter probe pulses improve the time resolution at the expense of the spectral one, while longer pulses result in the opposite effect. Here, we take advantage of the capability of XFROG CARS to re-construct the complex-valued response function $R(\Omega)$ after a single two-dimensional scan. Once $R(\Omega)$ is determined, the molecular dynamics can be analyzed with the desired time or frequency resolution by calculating the modulus square of

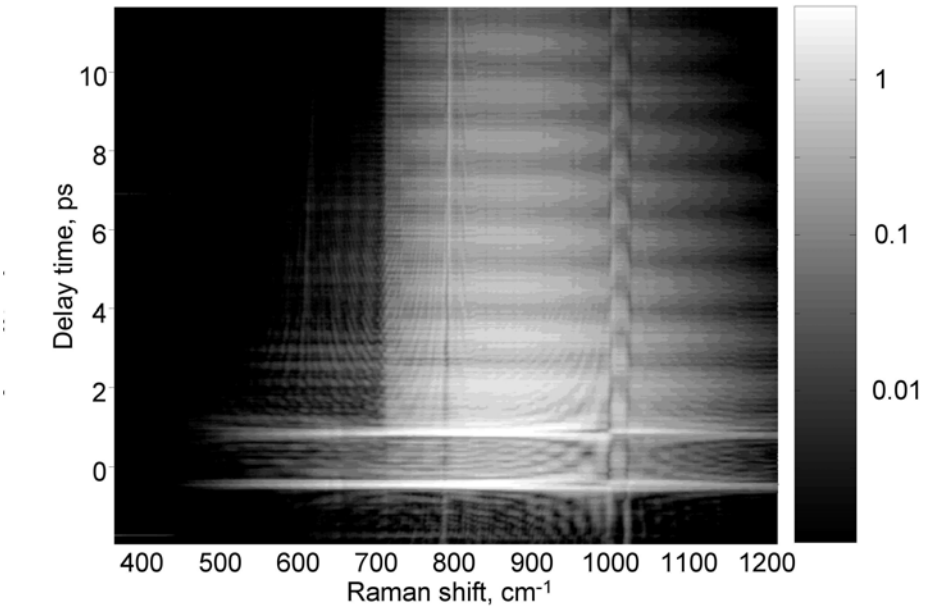


Figure D.2: Experimentally obtained two-dimensial CARS spectrogram. Spectral markers around 782, 1000 and 1027 $cm^{-1}$ indicate positions of Raman lines.

the frequency convolution

$$\tilde{I}(\omega,\tau) \propto \left|\tilde{E}_{pr}(\omega) \otimes R(\Omega)\right|^2 \tag{D.3}$$

with any hypothetical probe field $\tilde{E}_{pr}$, yet without repeating the experiment or changing the experimental parameters of the probe pulses. Below we demonstrate this method by applying it to the analysis of coherently controlled vibrational excitation of toluene.

Our CARS experiments are carried out with the laser system based on a commercial Ti:Sapphire femtosecond amplifier (40 fs, 1 kHz repetition rate) and two optical parametric amplifiers (Fig.D.3), generating pump, Stokes and probe pulses at the central wavelength of 800 nm, 862 nm and 720 nm, respectively. In order to control the molecular vibration excited by the pump-Stokes two-photon field (see Fig.D.1), both pump and Stokes pulses are shaped by means of two separate spectral pulse shapers, implemented in the standard $4f$ geometry [10]. Placing a slit in the Fourier plane of the pump shaper, we narrow its spectral bandwidth to 3 $cm^{-1}$ full width at half maximum (FWHM), much narrower than the frequency separation of the Raman resonances in toluene. With such narrowband pump, the spectral shape of the two-photon excitation field is effectively equivalent to the spectral shape of Stokes pulses. Control of the latter is performed by means of a double-layer spatial light modulator (SLM) in the Fourier plane of the Stokes shaper (PS1 in Fig.D.3). Both the phase and amplitude of Stokes spectrum are controlled with the resolution of 2 $cm^{-1}$. As shown in our earlier work [11], the robustness of the XFROG CARS method can be increased by means of the spectral shaping of probe pulses. To follow that recipe, we use another pulse shaper (PS2 in Fig.D.3) and introduce a sharp phase step of $\pi$ radian in the center of probe spectrum. Pump, Stokes and probe pulses are synchronized in time and focused by means of a silver mirror (focal length of 25 cm) into a 5 mm optical path quarts cuvette with neat toluene. CARS signal is spatially separated from the rest of the beams, and is coupled into a spectrometer equipped with a CCD camera and providing spectral resolution of 1.5 $cm^{-1}$. Two-photon spectrum of the

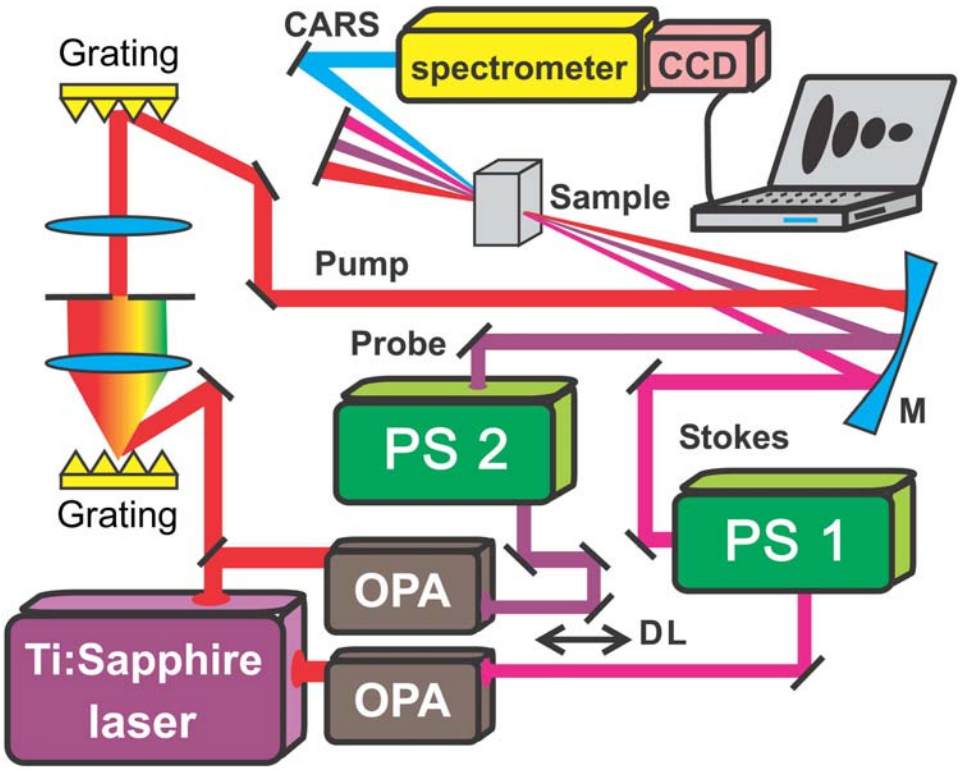


Figure D.3: Experimental setup.

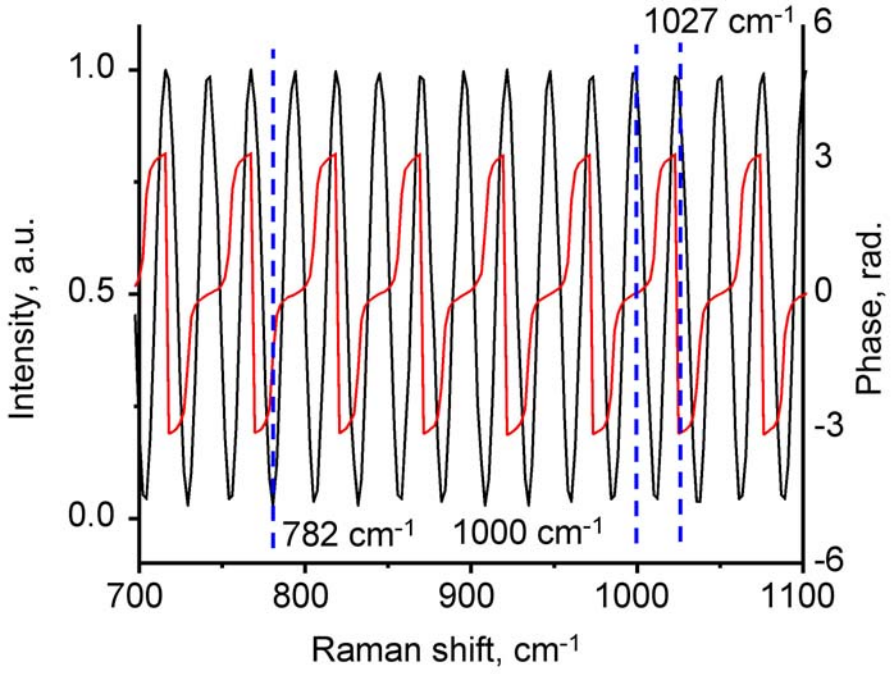


Figure D.4: Amplitude (black) and phase (red) of the spectral shaping applied to Stokes pulses. Raman modes of toluene at 782, 1000 and 1027 $cm^{-1}$ are indicated by dashed blue lines.

pump-Stokes excitation field is centered around 900 $cm^{-1}$ and has a width of about 400 $cm^{-1}$ FWHM. This enables us to excite three strong Raman lines of toluene at 782, 1000 and 1027 $cm^{-1}$. As an example of a simple control scheme of Raman excitation, we suppress the vibrational mode at 782 $cm^{-1}$ by shaping the pump-Stokes field as shown in Fig.D.4. Note that instead of blocking a single spectral component at 782 $cm^{-1}$, we modulate the excitation spectrum periodically in such a way as to have its amplitude maximized at 1000 and 1027 $cm^{-1}$, and minimized at 782 $cm^{-1}$. Upon such shaping, Stokes pulse is split into a sequence of two transform-limited pulses separated by about 1.6 ps. We chose this shaping to make the analysis of the transient dynamics, presented below, more intuitive.

Two-dimensional CARS spectrogram, experimentally measured with all three incident pulses shaped as described above, is shown in Fig.D.2. Bright horizontal lines around -0.6 ps and 1 ps correspond to two transform-limited Stokes pulses separated by $\sim$1.6 ps. Vertical horizontal lines around 782, 1000 and 1027 $cm^{-1}$ are the "spectral markers" of Raman resonances (for more detailed interpretation of the spectrogram, see [11]). To better understand the vibrational dynamics of the system, and the mechanism behind coherent control of the Raman modes, we proceed with the XFROG retrieval of the molecular response to laser excitation [6]. In the frequency domain, the response $R(\Omega)$ shows two strong lines around 1000 and 1027 $cm^{-1}$ (Fig.D.5(a)). The resonance at 782 $cm^{-1}$ is almost completely suppressed due to the missing spectral component at that frequency in the excitation pump-Stokes spectrum. An oscillatory pedestal can be attributed to the non-resonant CARS background which reproduces the spectral shape of the pump-Stokes field (cf. Fig.D.4). Spectral resolution is determined by the maximum time delay between the probe and pump/Stokes pulses.

Knowledge of the spectral phase of the complex-valued $R(\Omega)$ makes it possible to re-construct the temporal response $R(t)$ by means of a straightforward Fourier transform. Shown in Fig.D.5(b), the vibrational response exhibits two distinct excitation peaks corresponding to the overlap of the long pump pulse with a sequence of two transform-limited Stokes pulses. The first pulse excites all three Raman modes. Fast beating at the fre-

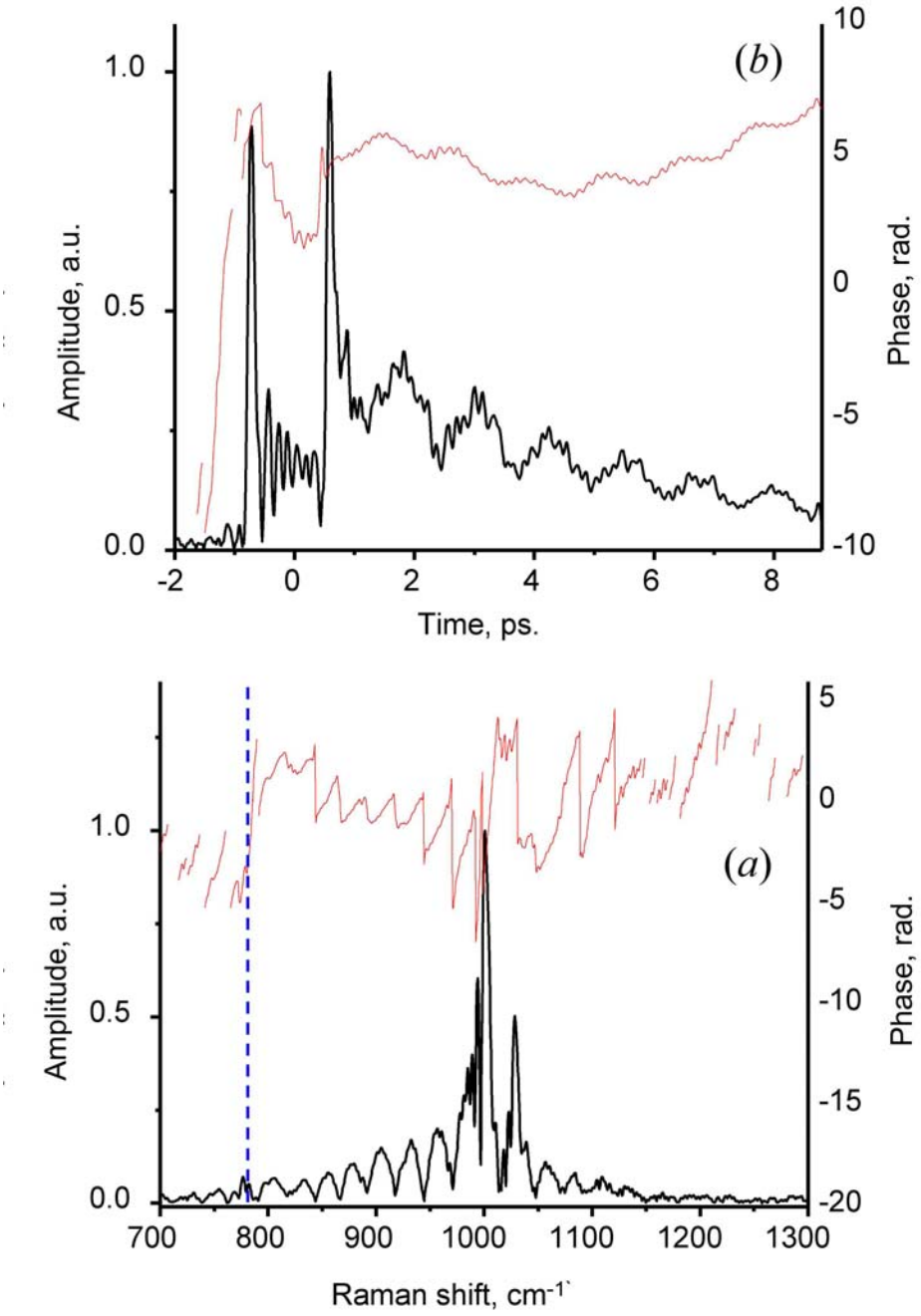


Figure D.5: Amplitude (black) and phase (red) of vibrational response of Toluene in the time (a) and frequency (b) domains.

quency difference between 782 $cm^{-1}$ and 1000, 1027 $cm^{-1}$ is clearly seen until the arrival of the second Stokes pulse. The latter amplifies the vibrations at 1000 and 1027 $cm^{-1}$ and de-excites the vibration at 782 $cm^{-1}$. After the second Stokes pulse, slow beating at the frequency difference between 1000 and 1027 $cm^{-1}$ is well pronounced, while the fast beating with the mode at 782 $cm^{-1}$ is significantly suppressed. Here, the resolution is determined by the spectral bandwidth of the detected CARS signal, rather than the duration of the probe pulse.

Combining the spectral and temporal representations into a single two-dimensional spectrogram often proves more informative, provided that the time and frequency resolution can be adjusted in the desired proportion. Normally, this requires repeating the experiment with a probe pulse of an appropriately chosen duration. Here, we take advantage of the availability of the complex-valued response $R(\Omega)$, retrieved from the experimental data as demonstrated above. We construct the required 2D spectrograms by calculating the frequency convolution (D.3) with a hypothetical transform-limited probe pulse $\tilde{E}_{pr}$ of necessary time duration, limited only by the experimentally achieved time and frequency resolution. In Fig.D.6(a), the spectrogram is calculated with the transform-limited probe pulse of 35 fs length. Fast beating between the mode at 782 $cm^{-1}$ and those at 1000 and 1027 $cm^{-1}$ is clearly resolved between the two Stokes pulses. After the second pulse at around 0.8 ps, fast oscillations disappear almost completely, attesting to the fact that the mode at 782 $cm^{-1}$ has been de-excited, even though the frequency resolution is not high enough to resolve that mode spectrally. Slow beating between the resonances at 1000 and 1027 $cm^{-1}$, enhanced by the second excitation pulse, is clearly visible on a longer time scale.

To analyze the same process with high spectral resolution, we convolve $R(\Omega)$ with a much longer probe pulse of 1 ps length, corresponding to the spectral bandwidth of 15 $cm^{-1}$ (Fig.D.6(b)). This value is dictated by the time delay scanning range of the experimentally obtained CARS spectrogram. Though the time resolution in this case is insufficient to identify the sequence of two Stokes pulses, high spectral resolution provides evidence of

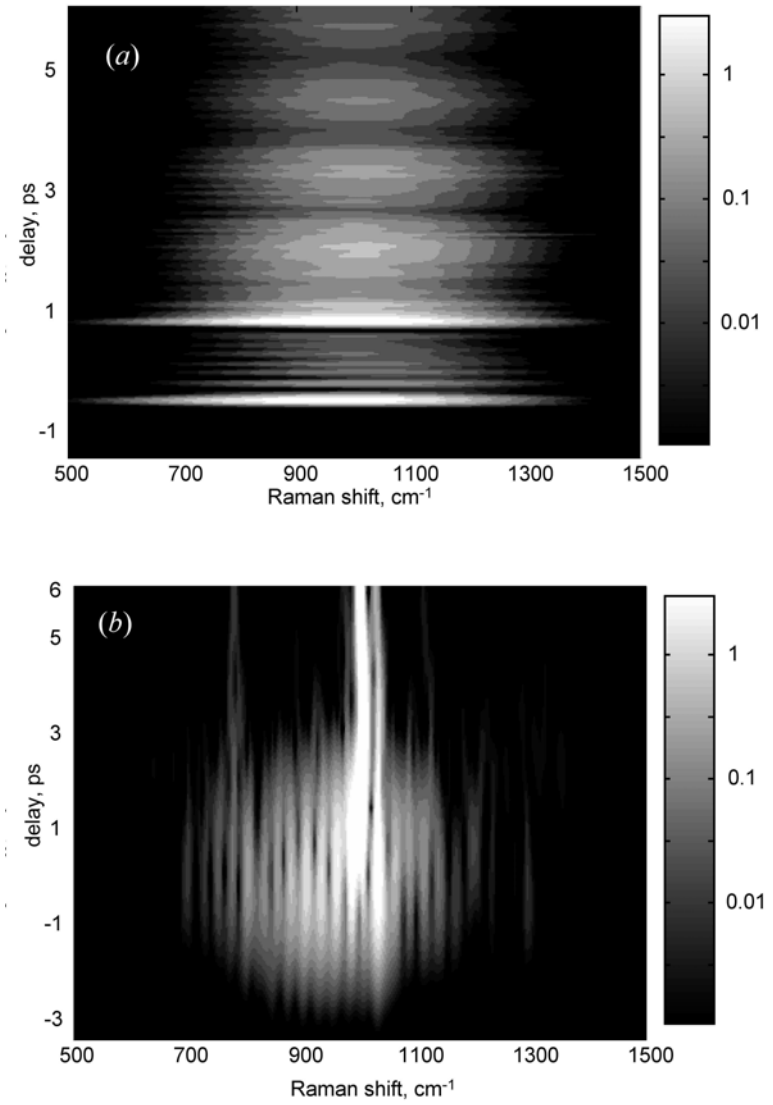


Figure D.6: Calculated two-dimensional CARS spectrograms with high temporal (a) and spectral (b) resolution.

mode amplification (bright vertical lines around 1000 and 1027 $cm^{-1}$) and suppression (week vertical line around 782 $cm^{-1}$). The region between -2 ps and 2 ps represents the dynamics of the system between two Stokes pulses.

In summary, we demonstrate a way of tracking the vibrational dynamics of molecules with variable time and frequency resolution, after performing a single experimental scan of coherent anti-Stokes scattering. The method is based on the XFROG retrieval of the complex-valued vibrational response function. We show the ability to analyze the mechanism behind coherent control of the vibrational response of toluene with shaped excitation pulses. Evolution of the molecular coherence can be followed and interpreted on different time scales and with correspondingly different spectral resolution, yet without repeating the experiment or changing experimental parameters.

# Bibliography


[1] M. Shapiro and P. Brumer, *Principles of the Quantum Control of Molecular Processes* (Wiley, New York, 2003).

[2] N. Dudovich, D. Oron, and Y. Silberberg, Nature **418**, 512 (2002).

[3] A. Assion, T. Baumert, M. Bergt, T. Brixner, B. Kiefer, V. Seyfried, M. Strehle, and G. Gerber, Science **282**, 919 (1998).

[4] B. J. Sussman, D. Townsend, M. Y. Ivanov, and A. Stolow, Science **314**, 278 (2006).

[5] C. Trallero-Herrero, J. L. Cohen, and T. Weinacht, Physical Review Letters **96** (2006).

[6] X. J. G. Xu, S. O. Konorov, S. Zhdanovich, J. W. Hepburn, and V. Milner, Journal of Chemical Physics **126** (2007).

[7] G. I. Petrov, R. Arora, V. V. Yakovlev, X. Wang, A. V. Sokolov, and M. O. Scully, Proceedings of the National Academy of Sciences of the United States of America **104**, 7776 (2007).

[8] B. D. Prince, A. Chakraborty, B. M. Prince, and H. U. Stauffer, Journal of Chemical Physics **125** (2006).

[9] D. Pestov, R. K. Murawski, G. O. Ariunbold, X. Wang, M. C. Zhi, A. V. Sokolov, V. A. Sautenkov, Y. V. Rostovtsev, A. Dogariu, Y. Huang, et al., Science **316**, 265 (2007).

[10] A. M. Weiner, Review of Scientific Instruments **71**, 1929 (2000).

[11] S. O. Konorov, X. G. Xu, R. F. B. Turner, M. W. Blades, J. W. Hepburn, and V. Milner, Optics Express **15**, 7564 (2007).